eman ta zabal zazu

Universidad del País Vasco

Euskal Herriko Unibertsitatea

TAILORING BOMBYX MORI SILK AS MULTIFUCTIONAL MATERIAL FOR ADVANCED APPLICATIONS

Memoria para optar al Grado de Doctor por la Universidad del País Vasco (UPV/EHU) presentada por

Ander Reizabal Lopez-Para

Leioa, Noviembre 2020

Este trabajo de investigación para optar al Grado de Doctor por la Universidad del País Vasco (UPV/EHU) se ha realizado en colaboración entre la Fundación Basque Center for Materials, Applications and Nanostructures (BCMaterials) y el Grupo del Laboratorio de Química Macromolecular (LABQUIMAC) del Departamento de Química Física de la Facultad de Ciencia y Tecnología de la UPV/EHU.

Ambas entidades desean agradecer al Departamento de Desarrollo Económico e Infraestructuras del Gobierno Vasco a través de los Programa ELKARTEK, HAZITEK y PIBA.

Gracias por todo

Resumen

ADAPTACIÓN DE LA SEDA DE *BOMBYX MORY* COMO MATERIAL MULTIFUCCIONAL PARA APLICACIONES AVANZADAS

El planeta tierra y su naturaleza son el sustento de toda vida. Sin embargo, las actividades económicas y el desarrollo social de las últimas décadas han obviado el daño al medio ambiente, llevando a la tierra a límites de agotamiento nunca antes vistos. La sobreexplotación de recursos, la producción insostenible de gases de efecto invernadero, el vertido de productos tóxicos, y la fragmentación del paisaje, entre otras lesiones, han deparado en una grave pérdida de biodiversidad, falta de recursos, aumento de la temperatura global y aumento de los riesgos para la salud, entre otras complicaciones.

Uno de los riesgos más destacados, es la generación de residuos plásticos, cuya estabilidad y uso generalizado, han propiciado su acumulación en zonzas naturales, especialmente, en el océano donde conllevan graves daños a la biodiversidad e indirectamente a toda actividad humana. Además, puesto que los plásticos son sintetizados a partir del petróleo, su uso contribuye al aumento de los daños asociados a los combustibles fósiles, como los vertidos durante su transporte, generación de gases de efecto invernadero durante su combustión, lluvias ácidas, etc.

Entre las posibles alternativas a este problema, desde la ciencia de materiales se plantea el desarrollo de una nueva generación de materiales, capaces de hacer frente a todas las necesidades sociales e industriales desempeñadas actualmente por los plásticos, a la vez que se avanza hacia la sostenibilidad ambiental. En este contexto, se torna necesaria la búsqueda de materiales que sean potencialmente útiles para este cometido. Es decir, materiales cuyas propiedades originales, sean lo suficientemente interesantes como para competir con las propiedades de los plásticos.

los biomateriales se presentan como la opción más interesante, puesto que sus propiedades, desarrolladas durante milenios de selección natural, han confluido en características difícilmente imitables por los procesos sintéticos humanos. Entre sus propiedades más

notables, destacan i) la compatibilidad con tejido humano, lo cual permite usarlos en aplicaciones biomédicas, ii) su capacidad de degradarse en cortos periodos de tiempo y bajo la acción de factores biológicos, lo cual disminuye el impacto ambiental de sus residuos y iii) su disponibilidad natural y condición renovable, lo que contribuye a un modelo más sostenible para obtener recursos y disminuye la probabilidad de que se agoten.

Son varios los biomateriales que generan atención, como la celulosa, la quitina, la gelatina o la seda. Entre ellos, destaca la seda, principalmente por sus innatas propiedades mecánicas (es igual de fuerte que el acero y mucho menos densa), su capacidad para ser disuelta en agua y posteriormente volverse estable, su piezoelectricidad (capacidad de generar señales eléctricas al ser estimulada mecánicamente) y finalmente, la capacidad de ser modificada para adquirir formas y propiedades complejas, que pueden asimilarse a las de los plásticos.

La seda extraída de los capullos producidos por la especie *Bombyx mori* (comúnmente llamados gusanos de seda), merece una especial atención debido a la capacidad de los gusanos de seda para producir grandes cantidades de seda y al conocimiento existente en torno a su cultivo y procesado. Entre los distintos componentes de la seda, destaca la Fibroína, una proteína que compone más del 70% del peso del capullo y que forma las fibras comúnmente empleadas para confeccionar tejidos. Es por ello que la Fibroína ha sido seleccionada como el material base en este estudio.

Con el fin de promover el uso de materiales más sostenibles, el objetivo del trabajo ha sido demostrar la aplicabilidad real de los biomateriales y más en específico de la seda. Para ello, se ha realizado un estudio sistemático para adaptar las propiedades de la Fibroína de Seda (o SF, por su traducción en inglés *Silk Fibroin*), ampliar sus aplicaciones prácticas y así poder emplearla como componente funcional en diversos prototipos.

Como punto de partida, se ha buscado demostrar la aplicabilidad de la Fibroína de seda en la nueva revolución industrial enfocada hacia la interconectividad, más conocida como industria 4.0. En esta revolución, son imprescindibles los dispositivos de monitorización y acción automatizada tales como, i) los sensores, capaces de “leer” una magnitud específica, como la luz, calor o corriente eléctrica; y proporcionar una señal medible y ii) los actuadores, capaces de responder a un estímulo específico para accionar un proceso automatizado. Sin embargo, para confeccionar sensores y actuadores, se requieren

propiedades muy específicas que no posee la Fibroína. Para alcanzarlas, la seda ha sido combinada con nanomateriales en forma de materiales compuestos. La seda actúa como matriz, proporcionando las propiedades estructurales requeridas, mientras que los nuevos materiales actúan como carga, proporcionando las propiedades más específicas. De este modo, se obtendrán materiales que conservan las propiedades propias de la seda, mientras que los nanomateriales aportan nuevas funciones.

Las carga empleadas han sido i) los nanotubos de carbono (CNT, *Carbon Nano Tubes*), ii) nanocables de plata (SNW, *Silver Nano Wires*), iii) nanopartículas de ferrita de cobalto (CFO, *Cobalt Ferrite Nanoparticles*) y iv) líquidos iónicos (IL, *Ionic Liquids*). El procedimiento usado para combinar la SF con las cargas ha consistido en disolver la Fibroína, añadir las cargas y evaporar el disolvente para obtener estructuras laminares y compactas, de cientos de micras de grosor. Las propiedades de los compuestos obtenidos han sido exploradas con el fin de establecer el efecto de las diferentes cargas sobre la Fibroína. Finalmente, las muestras más destacadas, han sido empleadas como componente funcional de diferentes dispositivos. Los resultados más destacables han sido:

i) La adición de CNT permite aumentar progresivamente las propiedades eléctricas (en particular la conductividad eléctrica) de la Fibroína, siendo el umbral de percolación alrededor del 3% en peso de CNT. Las muestras obtenidas además, muestran un comportamiento piezorresistivo (cambian su resistividad eléctrica al ser estimulado mecánicamente) altamente reproducible en correspondencia con la presión aplicada. La sensibilidad obtenida ha sido de aproximadamente 4 MPa^{-1} a pequeñas presiones de 0,11 MPa. Gracias a ello, el compuesto SF/CNT ha sido empleado en la elaboración de un prototipo de sensor de presión.

ii) La adición de SNW ha permitido incrementar la conductividad de la SF, pero además, la morfología de las cargas en combinación con la matriz no conductora, da como resultado la formación de micro-condensadores a lo largo del compuesto, que dota a las muestras de una constante dieléctrica superior a 10 para muestras con SNW del 3% en peso. Además, debido a escasa absorción de la luz por pare de los SNW, los materiales obtenidos presentan transparencia en el rango de luz visible, superior incluso al 25% para cargas de SNW de hasta el 3% en peso. El efecto túnel de los SNW, combinado con el estímulo mecánico dan a las muestras una respuesta piezorresistiva de entre 12 y 26 GPa^{-1} cuando la

presión está entre 0,2 y 0,4 MPa. Finalmente, la combinación de todas las propiedades citadas conduce a muestras con la capacidad de almacenar cargas eléctricas y de este modo generar un voltaje eléctrico por encima de los 3,3 V. Esta capacidad ha dado lugar a la aplicación de los compuestos SF/SNW en un prototipo parta el reconocimiento de objetos.

iii) La incorporación de nanopartículas de CFO conduce a dos efectos significativos: a) un aumento en la respuesta dieléctrica de las muestras, alcanzando valores por encima de 20 en cargas de CFO de 20% en peso; y b) la formación de un compuesto magnético caracterizado por una fuerte respuesta magnética, incluso con una baja adición de nanopartículas: magnetización alrededor de 10 $emu \cdot g^{-1}$ y coercitividad de casi 4 kOe, en cargas de CFO de 20% en peso. Este comportamiento magnético ha dado lugar a la aplicación de los compuestos SF/CFO en el desarrollo de actuadores magnéticos.

iv) La introducción de IL en la matriz de polímero, a) aumenta la conductividad eléctrica e iónica; y b) debido a la plastificación de las estructuras, incrementa la deformación de las muestras a la rotura y disminuye el módulo de Young. La movilidad iónica alcanzada, ha permitido el desarrollo de un actuador de flexión, con una gran respuesta a bajos voltajes aplicados (3 – 5 V). Las respuestas de flexión más altas ($\varepsilon \sim 0.5$), se obtienen para cargas del 40% y del 60%, en voltajes de 5 y 3 V y a una frecuencia de 100 mHz, para los IL [Ch] [DHP] y [Bmim] [C (CN_3)], respectivamente.

Los prometedores resultados obtenidos para todos los nanocompuestos, así como los dispositivos desarrollados, permiten concluir que la combinación de SF con otros materiales es una ruta accesible para el desarrollo de nuevos materiales funcionales.

Como contribución adicional para demostrar la aplicabilidad de biomateriales, la segunda sección del trabajo se ha centrado en explorar como modificar las propiedades de la seda mediante el procesamiento y la morfología. En concreto, se ha estudiado el desarrollo de materiales porosos por su gran utilidad tecnológica. El estudio se ha centrado en tres áreas que tienen como nexo común el uso de materiales porosos en sus dispositivos: biomedicina, energía y medio ambiente. En este contexto, se han diseñado diferentes estructuras porosas de Fibroína y siguiendo distintas rutas de procesado para cada una de las áreas de interés.

i) Mediante electroespining, han sido obtenidos tejidos porosos de Fibroína que, además, al ser combinados con CFO, resultan en estructuras magnéticas capaces de responder a campos magnéticos. De esta forma, ha sido posible no sólo estudiar la capacidad de los tejidos de Fibroína para albergar y favorecer el desarrollo de células óseas, sino también, analizar por vez primera la respuesta celular a la estimulación magnética dinámica. Los resultados obtenidos, muestran que la estimulación dinámica permite mejorar la viabilidad celular, mientras que la morfología tiene un mayor efecto en la proliferación pre-osteoblástica.

ii) Con el objetivo de desarrollar separadores para baterías de Ion-litio, se ha seleccionado un método basado en la adición de pequeñas cargas solubles en agua (sal común) a la Fibroína. De este modo, es posible obtener estructuras compactas que, al ser lavadas únicamente con agua, lixivian la sal originando estructuras porosas. Gracias a la accesibilidad de la sal se ha podido controlar el tamaño y la forma de los poros, así como su cantidad, lo cual ha sido empleado para estudiar el efecto de estos cambios en el funcionamiento de una batería. Los resultados obtenidos, señalan que el separador poroso de Fibroína facilita el transporte de iones de litio a través de la interfaz entre el cátodo y el separador para disminuir la resistencia general de la celda. La mejor capacidad de descarga obtenida ha sido de 89,3 y 131,3 $mAh \cdot g^{-1}$, para 2C y C/8, respectivamente y con un tamaño de poro de entre 250 y 106 µm.

iii) En el último trabajo, se han desarrollado seis estructuras porosas de Fibroína a partir de dos agentes disolventes, $CaCl_2$ y LiBr y tres procedimientos de regeneración diferentes, que incluyen gelificación, secado en frío y espumación de N_2O. Todas las muestras obtenidas muestran valores de porosidad superiores al 94% y una gran estabilidad, lo cual ha permitido estudiar su afinidad hacia contaminantes comunes en el agua, como el cromo y el arsénico. Los resultados obtenidos muestran que las estructuras de seda obtenidas, son capaces de adsorber contaminantes y que dichas capacidades pueden ser amplificadas con el fin de emplear los materiales para la descontaminación de aguas.

Como conclusión general, es posible afirmar que la seda posee un elevado potencial para el desarrollo de dispositivos funcionales. Cabe destacar, la capacidad del procesado y modificación, como herramientas accesibles y sostenibles para el desarrollo de nuevos materiales multifuncionales.

Todavía queda un gran camino para poder aplicar estos biomateriales derivados de la seda comercialmente, pero ha sido demostrado que, a fin de promover la sostenibilidad, el desarrollo y estudio de nuevos biomateriales es una fructífera ruta a seguir.

Abstract

TAILORING BOMBYX MORY SILK AS MULTIFUNCTIONAL MATERIAL FOR ADVANCED APPLICATIONS

Materials support human development. Among the available materials, polymers are nowadays indispensable and practically omnipresent because of their unrivaled properties. Unfortunately, polymers are synthesized from oil, and when they are accumulated in nature, they represent a severe environmental impact.

Among the possible alternatives to this problem, materials science raises the development of a new generation of materials capable of addressing all the social and industrial needs currently performed by plastics, while advancing towards environmental sustainability. In this context, it is necessary to search for materials that are potentially useful for this task. That is, materials whose original properties are interesting enough to compete with the properties of plastics.

Bio-based materials are presented as the most interesting option since their properties, developed over millennia of natural selection, have merged into characteristics that are difficult to imitate by human synthetic processes. Its most notable properties include i) its compatibility with human tissue, which allows its use in biomedical applications, ii) its ability to degrade in short periods of time and under the action of biological factors, which reduces the environmental impact of its waste and iii) its natural availability and renewable condition, which contributes to a more sustainable model to obtain resources and reduces the probability that they will be depleted.

There are several bio-based materials that generate attention, such as cellulose, chitin or gelatin. Among them, silk stands out, mainly for its i) innate mechanical properties (it is even stronger than steel), ii) its ability to be dissolved in water and subsequently become stable, iii) its piezoelectricity (ability to generate electrical signals when mechanically stimulated) and finally, iv) the ability to be modified to acquire complex shapes and properties.

The silk extracted from the cocoons produced by the Bombyx mori species (commonly called silkworms), presents special attention. Especially due to the ability of silkworms to produce large quantities of silk and the existing knowledge surrounding its cultivation and processing. Among the different components of silk, Fibroin, a protein that makes up more than 70% of the weight of the cocoon and that forms the fibers commonly used to make fabrics, stands out. That is why Fibroin has been selected as the base material in this study.

In order to promote the use of more sustainable materials, the objective of the work has been to demonstrate the real applicability of bio-based materials and more specifically of silk. For this, a systematic study has been carried out to adapt the properties of Silk Fibroin (SF), expand its practical applications and thus be able to use it as a functional component in various prototypes.

As a starting point, the aim has been to demonstrate the applicability of silk fibroin in the new industrial revolution focused on interconnectivity, better known as industry 4.0. In this revolution, monitoring devices and automated action are essential, such as i) sensors, capable of "reading" a specific magnitude, such as light, heat or electric current; and providing a measurable signal and ii) the actuators, capable of responding to a specific stimulus to actuate an automated process. However, to make sensors and actuators, very specific properties are required that Fibroin does not have. To achieve them, silk has been combined with nanomaterials in the form of composite materials. The silk will act as a matrix, providing the required structural properties, while the new materials will act as a filler, providing the most specific properties. In this way, materials that preserve the properties of silk will be obtained, with new properties and functions given by nanomaterials.

The used fillers have been i) carbon nanotubes (CNT), ii) silver nanowires (SNW), iii) cobalt ferrite nanoparticles (CFO) and iv) liquid Ionic Liquids (IL). While the procedure used to combine the SF with the charges, has consisted of dissolving the Fibroin, adding the charges and evaporating the solvent to obtain laminar and compact structures, of hundreds of microns thick. The properties of the obtained compounds have been explored in order to establish the effect of the different loads on Fibroin. Finally, the most outstanding samples have been used as a functional component of different devices. The most notable results are described in following.

i) The addition of CNT makes it possible to progressively increase the SF electrical properties (in particular the electrical conductivity), the percolation threshold being around 3% by weight of CNT. The samples obtained also show piezoresistive behavior (their electrical resistivity changes when mechanically stimulated) highly reproducible in correspondence with the applied pressure. The obtained sensitivity has been approximately 4 MPa^{-1} at low pressures of 0.11 MPa. Thanks to this, the SF / CNT nanocomposites has been used in the development of a pressure sensor prototype.

ii) The addition of SNW has allowed to increase the conductivity of the SF. In addition, the morphology of the charges in combination with the non-conductive matrix, results in the formation of micro-capacitors throughout the compound. This provides the samples with a dielectric constant greater than 10 for samples with SNW of 3% by weight. Furthermore, due to the low absorption of light by the SNWs, the obtained materials present transparency in the visible light range, even higher than 25% for SNW loads up to 3% by weight. The tunneling effect of the SNWs, combined with the mechanical stimulus, give the samples a piezoresistive response between 12 and 26 GPa^{-1} when the pressure is between 0.2 and 0.4 MPa. Finally, the combination of all the aforementioned properties leads to samples with the ability to store electrical charges and thus generate an electrical voltage above 3.3 V. This ability has led to the application of SF / SNW compounds in a prototype for objects recognition.

iii) The incorporation of CFO nanoparticles leads to two significant effects: a) an increase in the dielectric response of the samples, reaching values above 20 in CFO loads of 20% by weight; and b) the formation of a magnetic compound characterized by a strong magnetic response, even with a low addition of nanoparticles: magnetization around 10 $emu \cdot g^{-1}$ and coercivity of almost 4 kOe, in CFO loads of 20% by weight. This magnetic behavior has led to the application of SF / CFO compounds in the development of magnetic actuators.

iv) The introduction of IL into the polymer matrix, a) increases the electrical and ionic conductivity; and b) due to the plasticization of the structures, increases the deformation of the samples and reduce Young's modulus. The ionic mobility achieved allowed the development of a bending actuator, with a great response to low applied voltages (3 - 5 V). The highest bending responses ($\varepsilon \sim 0.5$) are obtained for loads of 40% and 60%, at

voltages of 5 and 3 V and at a frequency of 100 mHz, for the IL [Ch] [DHP] and [Bmim] [C (CN_3)], respectively.

The promising results obtained for all nanocomposites, as well as the devices developed, allow us to conclude that the combination of SF with other materials is an accessible route for the development of new functional materials.

As an additional contribution to demonstrate the applicability of bio-based materials, the second section of the work has focused on exploring how to modify the properties of silk through processing and morphology. Specifically, the development of porous materials has been studied due to their great technological utility. The study has focused on three areas with a common nexus, the use of porous materials in their devices: biomedicine, energy and the environment. In this context, different porous structures of Fibroin have been designed by following different processing routes for each of the areas of interest.

i) By electrospining, porous fibroin fabrics have been obtained which, in addition, when combined with CFO, result in magnetic structures capable of responding to magnetic fields. In this way, it has been possible not only to study the capacity of Fibroin tissues to host and promote the development of bone tissue cells, but also to analyze for the first time the cellular response to dynamic magnetic stimulation in SF-base porous materials. The results obtained show that dynamic stimulation improves cell viability, while morphology has a greater effect on pre-osteoblastic proliferation.

ii) In order to develop separators for lithium-ion batteries, a method based on the addition of small water-soluble fillers (common salt) to the Fibroin has been selected. In this way, it is possible to obtain compact structures that, when washed only with water, leach the salt to give porous structures. Thanks to the accessibility of salt, it has been possible to control the size and shape of the pores, as well as their quantity, which has been used to study the effect of these changes on the battery operation. The obtained results indicate that the fibroin porous separator facilitates the transport of lithium ions through the interface between the cathode and the separator to reduce the general resistance of the cell. The obtained best discharge capacity was 89.3 and 131.3 $mAh \cdot g^{-1}$, for 2C and C/8, respectively, and with a pore size of between 250 and 106 µm.

iii) In the last work, six fibroin porous structures have been made from two dissolving agents, $CaCl_2$ and LiBr and three different regeneration procedures, which include gelation, freeze-drying and N_2O foaming. All the obtained samples show porosity values above 94% and great stability, which has made it possible to study their affinity for common contaminants in water, such as chromium and arsenic. The obtained results show that the silk structures are capable of adsorbing pollutants. This capacities can be amplified in order to use the materials for cleaning water.

As a general conclusion, it is possible to affirm that silk has a high potential for the development of functional devices. It is worth highlighting the capacity of processing and modification, as accessible and sustainable tools for the development of new multifunctional porous materials.

There is still a long way to apply bio-based materials commercially, but it has been shown that, in order to promote sustainability, the development and study of new bio-based materials is a route to follow.

The current human lifestyle is leaving a deep mark in nature. Among the different impacts, the massive use of plastics is one of the main alarming issues.

In this section, the main environmental impacts derived from plastics usage are studied, and the proposed routes to minimize them are discussed.

In this sense bio-based materials are proposed as an alternative and among them, Silk Fibroin, a protein material obtained from Bombyx mori, is considered due to its great potential derived from its unique properties.

Chapter. 1

ADVANCED MATERIALS TOWARDS ENVIRONMENTAL SUSTAINABILITY

1.1. ENVIRONMENTAL SITUATION AND CIRCULAR ECONOMY

2020 opened with an alarming message released in the SOER2020 assessment that is an annual report of the European Environmental Agency (EEA) that provides reliable and comparable information that supports European environmental policies: the human lifestyle carries a severe injury to the environment, and soon it will become irreparable[1].

The world is human livelihood, but economic activities and social lifestyles have systematically obviated the environment's damage. The overexploitation of the resources, greenhouse gas emission, toxic product dumping, waste generation, and landscape fragmentation have led to severe biodiversity loss, lack of resources, global temperature rise, and increased human health risk, among other complications[1,2].

The need to act towards a more sustainable socio-economic system has become evident. Thus, it becomes necessary to adopt a conciliatory approach, focused on ensuring the life quality and global economic development while respecting ecological limits.

The circular economy approach accepts the production, distribution, and consumption of goods and services as a fundamental pillar of the economy, as current “linear” economy (***Figure 1.1***). But circular economy building its progress on the need to preserve the environment, establish resource-saving policies and achieve a harmonious balance between economic growth, population, resources, and the environment. In essence, the circular economy is a strategy that tries to mimic the natural fluxes of materials. This approach aims to create a close dynamic where the resources are extracted from nature, processed and used without further environmental impact, and finally, returned to nature by biodegradation (***Figure 1.1***).

To achieve these objectives, the circular economy proposes to join different stakeholders in a collaborative economy, with a single market powered by digital technologies, i.e., Industry 4.0, internet of things, big data, blockchain, and artificial intelligence. These technologies can accelerate circularity by creating a connected structure in where data exchange enables the optimization of all processes. This could reduce the use of unnecessary resources and could make the world less dependent on primary materials. In fact, some studies point out that the gross domestic product (GDP) of the European Union (EU) economy can be reinforced with an increase of around 0.5% by 2030 and 700,000 new jobs[3], by following the principles of the circular economy.

Figure 1. 1. *Materials use in linear economy (above) and circular economy (below)*

To optimize the use of resources and create a close dynamic, resources must be controlled and adapted to social requirements. Resources can be divided into i) natural, extracted directly from nature, like biomass (wood, crops, feed, and plant-based materials), fossil fuels (coal, gas, and oil), metals (such as iron, aluminum, or copper), non-metallic minerals (including sand, gravel, and limestone), water and land; or ii) synthetic, made by chemically changing the natural resources to create new materials. Thus, natural resources provide the foundation for goods, services, and infrastructures.

Among natural resources, two main types can be defined.

i) ***Non-renewable resources*** cannot be produced, regenerated, or reused on a scale that can sustain its consumption rate. These resources often exist in fixed quantities or are consumed much faster than nature can regenerate them. Among non-renewable resources, three main types can be distinguished: fossil fuels, metals, and minerals.

ii) ***Renewable resources***, like solar, wind, hydric, or geothermal powers and bio-based materials (which are intentionally fabricated from natural resources), are regenerated in a shorter time than consumed. Because of their origin and composition, the use of renewable resources does not usually represent a substantial environmental impact.

The materials derived from these resources can be divided into i) recyclable materials, those that can be reused again after their treatment, or ii) non-recyclable materials, which can not be treated to be reused.

The circular economy promotes renewable resources and energies since they are inexhaustible and less pollutant. Contrary, it avoids using synthetic, non-renewable, and non-recyclable materials since they imply significant pollution and finite resource consumption. The essential recyclable resources, like metals and minerals, are redirected towards recycling processes. But highly pollutant resources like fossil fuels and short-time products are avoided. This final point is one of the biggest challenges of environmental neutrality since many plastics are fundamental for current lifestyles but are non-renewable or recyclable.

1.2. PLASTICS DUALITY

Plastics are synthetic materials formed by the linkage of repetitive units (monomer) into macromolecules (polymeric chains) combined with additives (***Figure 1.2***). Plastics cover a wide range of materials (such as polypropylene, polyethylene, polyvinyl chloride, polystyrene, nylon, and polycarbonate), with variable molecular structure and properties. Generally, all plastics share common features, e.g., low cost, facile processability, chemical stability, and low density.

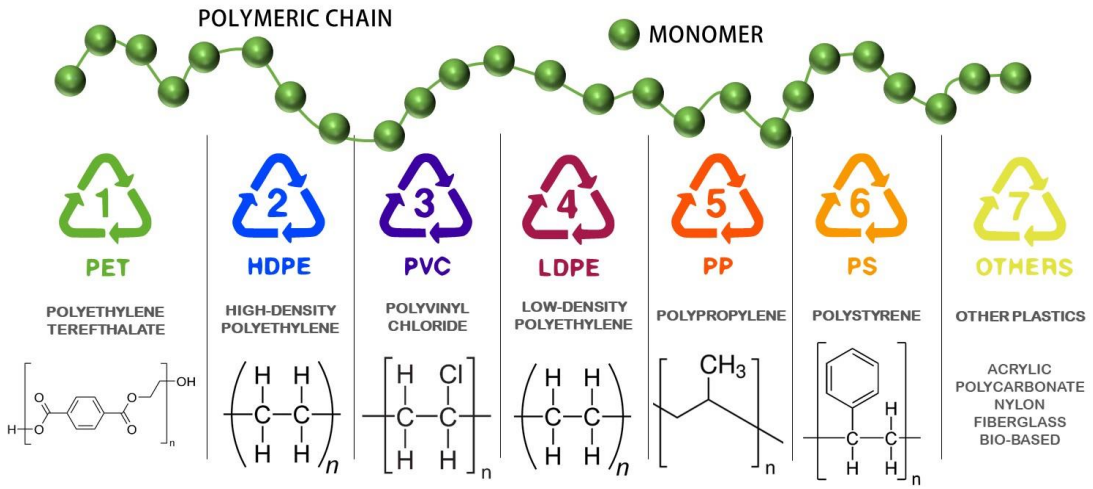

Figure 1. 2. *Polymeric chain graphic representation and main recyclable polymers monomers molecular structure.*

These properties have made them essential for the human lifestyle. In fact, plastics global production grew from 25 million tonnes in 1970 to 359 million tonnes in 2018[4]. A tendency that is expected to double in the next 20 years[2]. Nowadays, the plastics industry generates more than 1.6 million jobs in the EU and provided just in 2018 a turnover of more than 360 billion euros[2]. It places the plastic industry as the 7th in the European industries rank, quite close to pharmaceutical and chemical industries [3].

Unfortunately, plastics consumption involves some social, economic, and environmental impact:

i. Around 95 % of plastics produced in the EU are ***derived from crude oils***[4]. The same tendency is followed worldwide, which corresponds to 4-8 % of global oil consumption[5]. This extrapolates the crude oil environmental impacts to the plastics industry.
   a. ***Depletion:*** crude oil is a non-renewable resource, naturally produced under specific biological actions. The oil reserves are estimated to be around 35 and 1500 billion barrels consumption per year (around 750 per person yearly), which implies a complete reserves depletion in around 50 years[6–8].
   b. ***Extraction:*** The crude oil deposits are accumulated in isolated landscapes, making access difficult for several territories (i.e., around 85 % of total crude oil reserves are nowadays in 10 countries) and generating economic instability[6–8].
      Besides, one of the main oil extraction methods is hydraulic fracturing (also known as fracking). It involves the insertion of large amounts of water and chemicals into the land, leading to environmental and health problems, like chemical contamination of groundwater and accumulation of flammable gases in drinking-water aquifers[9].
   c. ***Refining*** is converting crude-oil into more suitable products for consumption (e.g., plastics precursors: monomers). This process implies a large water consumption and produces solid wastes (i.e., petroleum coke and sludge). Also, nitrogen oxides (NO_x), sulfur dioxide (SO_2), and volatile organic compounds (VOCs) can be generated[10,11]. These releases can cause environmental and social damage[12].
   d. ***Transport*** lead to i) energetic dependence: EU, import more than 50% crude oil and its derivatives (mainly from Russia (almost 30%), Middle East and the Caspian Sea)[13]; ii) Energy consumption. In the EU, crude oil transport represents an average of the travelled distance of 7000 km when crude oil comes from Russia and around 4000 when it comes from the Middle East and the Caspian Sea. In the United States (US),

the crude oil and derivatives transport supposes around 3% of national energy consuption[14]; iii) Non-implicit risk, i.e., accidents and oil spills.

ii. ***Plastics manufacture:*** some of the chemicals released during plastics production are harmful to humans. A low control of production processes or even non-implicit risk can cause this chemical release, representing perjury on human health[15].

iii. ***Plastic waste:*** Plastics are designed to last from less than 1 year to 50 years or more[4], which is, at the same time, their main advantage and disadvantage. As long as plastics are used, their residues are continuously accumulated, representing a substantial social, economic, and environmental risk. In fact, it is estimated an accumulative plastic global generation of 6300 Mt between 1950 and 2015[16]. Several routes have been developed to minimize the impacts of this accumulation, although they do not mitigate the problems:

a. ***Recycling*** is based on giving to waste a second life in an alternative use. Recycling represents the first route for plastics residues. It reduces the total waste, nourishes the industry with new materials for manufacture (i.e., avoids using new raw materials), has the lowest global warming potential, and reduces energy use[17]. To achieve this goal, it is necessary, i) the separation of the different plastics by composition, ii) the extraction of plastics from devices, and iii) the implementation of collection and treatment systems. Nevertheless, to achieve these goals, broad and complex logistic processes are required, that are usually unattainable in many sectors. Besides, although recycling is implemented, it does not ensure great effectiveness. In the EU, only 32.5 % of collected waste was recycled during 2018[4]. Fortunately, recycling it is increasing every year above 1 % [18]. A tendency that grows worldwide since the 90s.

b. ***Thermal destruction*** is oriented towards plastic waste elimination by burning. Although emerging technologies, such as pyrolysis, which extracts fuel from plastic waste, are starting to be employed, incineration is the most used technique[16]. The produced heat can generate electricity, but this requires sophisticated systems, not always available. From plastics incineration, solid dust and gases of different kinds are generated, which result in considerable environmental risk. The incineration always results in the generation of i) greenhouse gases, such as CO_2, ii) carbon monoxide (CO), and iii) dioxin. These substances can be toxic and dangerous for humans and ecosystems health[17]. The incinerated plastic amount was estimated to be ~ 42.6 % in 2018[4]. A value that is decreasing year by year[17].

iv. ***Landfills:*** in 2018, around 25 % of the collected plastic waste in the EU was neither recycled nor incinerated. These remaining residues were accumulated in landfills: a disposal site for materials through burial[4]. But this process requires profound materials management and control of buried conditions. Uncontrolled disposal facilities can lead to severe environmental pollution from toxins lixiviation [19] or discharges.

Despite all the available management techniques, it is still challenging to avoid plastics residues reaching the natural environment. The most worrying ones are the plastic waste inputs from land into the water mass, where plastic waste is accumulated and hardly removed. Oceans' worrying problems must be mentioned because of their large areas, which increase the risk of plastic accumulation. A study of 2015 estimated a plastic waste entrance to oceans of 4.8-12.7 million tons (MT) from the 275 MT of the plastic generated in 192 coastal countries (around 1.7 and 4.6% of total plastics)[20]. The estimations suggest 80 % of the global ocean plastics are originated in land-based sources and the remaining 20 % in marine ones[21]. If current production and waste management trends continue, roughly 12,000 MT of plastic waste will be in landfills or the natural environment by 2050 [16 22]. The main issues derived from this accumulation are:

i. ***Socio-economic impacts:*** Once in the marine environment, due to polymer types and densities, plastics waste can either float or sink, resulting in an accumulation on the sea surface, water column, or even in deep-sea sediments. Highly visible is the surface waste, which, as a direct result, implies visual pollution. Besides, large investments must be done for cleaning and maintaining purposes.

ii. ***Animal impact:*** among the plastics in water lads, the ***l***ess easily detected are the non-floating plastics, which can interact with the living organism. Animals can ingest the plastics [23,24], leading to severe damage or even death to several species. In total, more than 331 different marine species have been documented as having ingested plastics.

iii. ***Bio-accumulation***: Due to photo- and thermal-oxidation, hydrolysis, and microbial activity, plastics become brittle[25]. The environmental processes (e.g., wind, tides, animals) make the brittle plastics fracture forming micrometrical-sized plastic particles. Due to their ingestion by animals, these particles can be integrated within the food chain[26,27,28,29].

iv. ***Environment destabilization***: due to plastics diverse molecular structures, they tend to associate with surrounding molecules (toxic or not), which can be eventually released

into the surrounding, promoting the environment's chemical modification. This modifies several ecological dynamics, directly affecting the species who live there[30] and depleting biodiversity [31,32].

1.3. BIO-BASED MATERIALS.

Nowadays, plastics are irreplaceable materials. However, new approaches that preserve their value and benefits while protecting human and environmental wellness are mandatory. From the point of view of materials science, there are three stages to address this issue: i) production stage and materials design, ii) consumption stage, by modifying usage habits and, iii) refusing stage, where new sustainable or efficient processes for waste recycling or revalorization can be designed.

Since up to 80% of the environmental impacts derived from materials manufacture are determined at the production and design stage[33], actuating in this stage is the best choice to reduce plastic effects. With this regard, it is proposed to develop a new materials generation.

Among different alternatives, the use of bio-based materials, which are materials intentionally made from substances derived from living organisms, has been proposed. Due to this common origin, bio-based materials i) are naturally available, ii) are organic and, consequently, likely to be biodegraded, and iii) have noticeable properties given by natural evolution, which are potentially controllable[34–36].

The potentials advantages of producing and using bio-based materials are:

i. Unmarked production from fossil-fuels, allowing to reduce crude-oils derived damages[37,38].
ii. Natural and renewable origin avoids their depletion[35] and enables manufacture in high enough volumes to support economic demands[39].
iii. Organic structure enables their biodegradation and makes possible the implementation of derived materials in a circular close system [36,39].
iv. Biodegradable nature minimizes the problem of the accumulation in landfills and natural environments. This, at the same time, a) avoids the need of combustion process, which helps to reduce the release of pollutants and derived damages, b) reduces the aesthetic impact, which implies a specific advantage for economic sectors, c) minimizes the assimilation of toxic products and discharge due to their shorter natural durability and iv) decreases bioaccumulation in trophic chains[20,25,30].

v. Novel and promising properties.

Among bio-based materials, those that have attracted significant attention are i) cellulose, used for centuries as wood, paper, and paperboard [40]; ii) alginate and carrageenan, employed in the foods and cosmetics industry as a binder and thickener [41,42]; iii) agar, applied in cuisine for foods elaboration [43] or iv) silk, used for millennia in fabrics [44].

At the moment, it is still insufficient knowledge about how processing affects bio-based materials, how to improve their properties and their potential applicability. In fact, bio-based materials represent e a minimal share of the market, just over 1 % of global plastics production (~ 4 MT per year)[4,16] (***Figure 1.3***). This points out the need to i) search for new bio-based materials, ii) study and control their properties, and iii) develop new components with them to demonstrate their applicability.

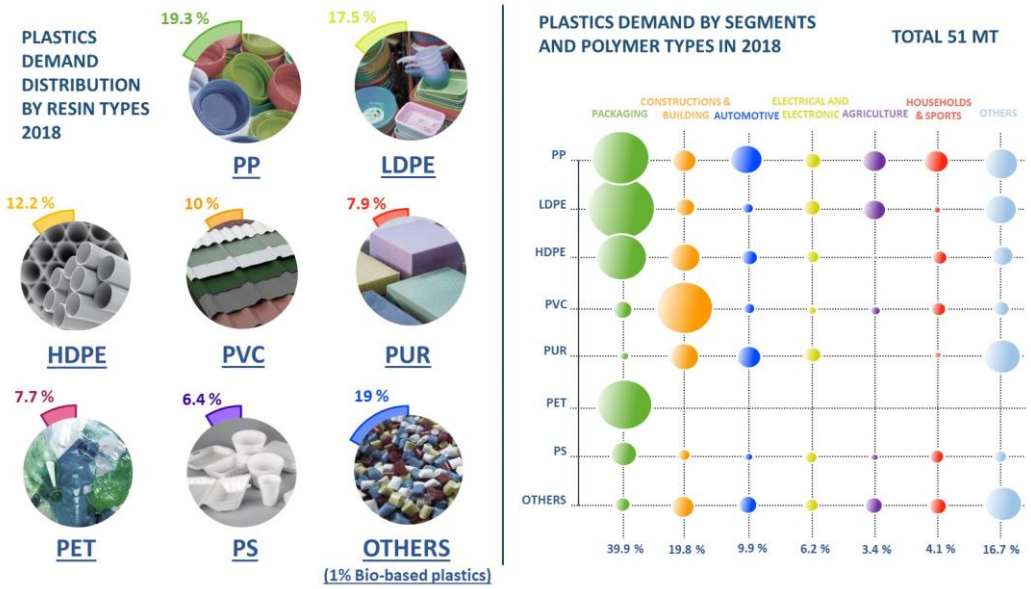

Figure 1. 3. *Plastics global demand by resin (left) and by segment and polymer type (right). From :* [4]

1.4. SILK AS AN ALTERNATIVE

Among available bio-based materials, silk, a macromolecular protein produced in some arthropods' specialized glands, has been the focus of particular interest due to its unique properties[45]. Silk is secreted by some ants, mites, scorpions, and bee's species, but the largest producers are spiders (webs form) and Lepidoptera (moths and butterfly, in cocoons form)[46].

Silk function is mainly structural, acting as a highly stable fiber[47]. Although silk molecular composition slightly varies among different animal species [48], it mainly preserves a similar combination of extremely unusual properties in other natural materials: silk is bio-compatible[49], shows a high tensile strength [50], good elasticity, and excellent resilience[51]. Silk fibers are one of the strongest and toughest materials obtainable in nature [44]. They are estimated to be five to six times lighter than steel while having the same strength [46], and tougher than all existing synthetic fibers, including high-performance polyethylene or Kevlar [52].

From the point of view of materials production, silk is only produced in low amounts in nature and through hardly controllable processes. Therefore, some species have been domesticated to increase their production. The silk obtained from those species is named domesticated silk. To date, from more than 4,000 different silk-producing species, only very few of them have been domesticated and commercially exploited for silk production. The most common ones are *Araneus diadematus* and *Nephila clavipes* Spiders, and *Bombyx mori* and A*ntheraea mylitta* moths. The silk obtained from the rest of the species is commonly named wild silk [53].

Among available domesticated silks, that coming from *Bombyx mori* moth (or silkworm) cocoons aroused the most significant interest because of their high production yields and accessibility. The silkworms are also named mulberry silk because Bombyx mori feeds on mulberry leaves.

1.4.1. SILK HISTORICAL USES: AN ANCIENT MATERIAL

The history of silk and its sericulture began in china, but when it is uncertain. The oldest silk-based material found in China has been dated to about 3600 BC, which places silk production in the Neolithic period[54].

For a long time, silk was only used by the Emperor of China and those very close to him. The restrictions began to vanish gradually, and eventually, production grew to become quite a massive industry. Silk was used for various purposes, from fishing-lines, bowstrings to musical instruments and even writing substrates.

Due to its economic relevance, close to 30 BC, regular commerce began between Romans and Asia. The silk road, a commercial route network connecting Asia with Mongolia, India, Persia, Arabia, Syria, Turkey, Europe, and Africa, opened around the 2nd century AD[55].

Sericulture reached Korea around the year 200 BC, and it was gradually opened by the east. But it would take until after 300 AD before the practice was well established as far away as India. Around the year 550 AD, sericulture opens to the world.

The Mediterranean's silk production began in the 6th century when the silkworm eggs were first smuggled from China by Byzantine monks. It slowly expands, especially in Italy (Piedmont, Lombardía, and Béneto), where the center of European production was established. In this period, Italy became one of the leading world production areas of silk with China and Japan.

Due to technological advances, the silk industry experiences a transformation in the 13th century, mainly due to the knitting wheel invention, which was initially developed for silk processing. In the following hundred years, with the industrial revolution and the consequent increase in per capita income, silk consumption increases extraordinarily. The change was exceptionally sharp, from 1820 until the crisis of 1929, when world silk trade multiplied by twenty, from 2,300 to 47,500 tons per year [56]. By the early 20th century, rapidly industrializing Japan produced as much as 60% of the world's raw silk. In this period, moved by the recently known silk biocompatibility, Joseph Lister introduced the first sterile silk suture into clinical practice [57].

During the Second World War, silk supplied from Japan was cut off, so western countries were forced to find substitutes. Synthetic fibers such as nylon were developed, replacing silk. Even after the war, silk was not able to regain many of the lost markets. After this period, the Republic of China became the world's largest silk producer, with 58,000 tonnes out of world production of 81,000 in 1996 and India at 13,000 tonnes [57].

Following the most actualized data from the International Sericultural Commission[58], the higher production values of SF were reached in 2015 with around 200,000 MT of production. In 2018 the value decreased to 159,648 MT worldwide. The main silk-producing countries in the world are; China (120,000 MT), India (35,260 MT), Uzbekistan (1,800 MT), Thailand, and Vietnam (680 MT each one), and Brazil (650 MT) (2018 data). These values represent a small percentage of the global textile market (less than 0.2%).

1.4.2. SILK POTENTIAL

Due to its properties, silk remains to represent a large textile sector market, demonstrating its considerable potential despite it faces with synthetically designed fibers. The natural

properties of silk made it one of the most priced products worldwide. This represented an ideal chance for the commercial promotion of this material[54 59]. Italy, the leading European silk producer, generated only in 2016 around 870 million Euros in silk-based product export[58].

Due to the low sericulture requirement, silk production has been frequently adopted by regions with lower resources, acting as a profit promoter, and helping society's development. Sericulture has been adapted and improved throughout history, becoming more competitive and successful. Nowadays, investment and technical progress can make still more competitive**.** It is estimated a silk-market global growth of around 8% until 2025, which supposes an increase from 19.7 to around 28 billion US dolars[60].

Also, processing techniques improving and knowledge around silk behaviors could be a great tool in developing new devices based on silk. According to silk potential, some brands (e.g., Adidas and Goodyear) have already released their interest in silk, revealing their plans to use this material in novel applications[61,62].

Silk manufacture has been extended for more than 5,000 years without remarkable environmental impacts, showing the renewable nature of the material and the sustainability of the process**.**

1.5. OBJECTIVES AND STRUCTURE OF THE THESIS

The main goal of the work is to contribute to the promotion of sustainable materials by demonstrating the applicability of silk-based materials. To this, more specific primary and secondary objectives are addressed:

a. To demonstrate the ability of modifications to expand the scope of silk-based material.
    i. Expand the available data around silk-based materials processing and modifications, and more specifically, of Silk Fibroin.
    ii. Enlarge the Silk Fibroin properties through its combination with complementary materials.
    iii. Enlarge the Silk Fibroin scope by studying different processing techniques and their derived effects on Silk Fibroin properties.
b. To demonstrate the functionality of Silk Fibroin in advanced applications.
    i. Study the ability of modified bio-based materials to reach new applications.
    ii. Apply the Silk Fibroin as a functional component of advanced applications.

The thesis structure tracks the followed road to achieving the proposed objectives:

1) Supporting the interest of the searching of a bio-based material with promising original properties (Chapter 1)
   - ➔ The goal is to promote silk as a challenging material with the self-ability to rival with actually used synthetic plastics.
2) Study of the composition and molecular structure of silk (Chapter 2)
   - ➔ The goal is to understand each component's properties and function to select the most promising ones and understand the accessible routes for improvement.
3) Study of viable processing and modification routes. (Chapter 3)
   - ➔ The goal is to identify the most promising processing and modification routes.
4) Improve the main properties of silk to achieve active behaviors (Chapter 4-5)
   i) Demonstrate the functionality of active silk in advanced applications as sensors and actuators. (Chapter 4)
   ii) Silk fibroin/carbon nanotubes as a piezoresistive force sensor (Section 4.1)
   iii) Silk fibroin/silver nanowires as a transparent and flexible sensor (Section 4.2)
   iv) Silk fibroin/cobalt ferrite nanoparticles as a magnetic actuator (Section 4.3)
   v) Silk fibroin / ionic liquids as electrical bending actuator (section 4.4)
   vi) Modify silk morphology and behavior to enable their applicability in different fields. (chapter 5)
   vii) Silk fibroin/cobalt ferrite nanoparticles electrospinning for tissue engineering (section 5.1)
   viii) Silk fibroin membranes as lithium-ion batteries separator (section 5.2)
   ix) Silk fibroin porous structures for heavy metals adsorption (Section 5.3)
5) Conclusion and future trends (Chapter 6)
   i) Summarize the conclusions of the achieved goals. (Section 6.1)
   ii) Identify the challenges for silk and bio-based materials and Show the main focus for future works. (Section 6.2)

1.6. REFERENCES

1. Report of the International Resource Panel. United Nations Environment Programme. *Assessing Global Resource Use*. https://www.resourcepanel.org/reports/assessing-global-resource-use (2017).
2. European Environment Agency. *The European environment - state and outlook 2020: knowledge for transition to a sustainable Europe*. *European Environment* https://www.eea.europa.eu/publications/soer-2020 (2019) doi:10.2800/96749.
3. European Commission. *Impacts of circular economy policies on the labour market*. https://op.europa.eu/en/publication-detail/-/publication/fc373862-704d-11e8-9483-01aa75ed71a1/language-en (2018).
4. PlasticEurope. *Plastics - the Facts 2019*. https://www.plasticseurope.org/es/resources/publications/1804-plastics-facts-2019 (2019).
5. Ellen Macarthur Foundation. *The New Plastics Economy: Rethinking the future of plastics & catalysing action*. https://www.ellenmacarthurfoundation.org/publications/the-new-plastics-economy-rethinking-the-future-of-plastics-catalysing-action (2017).
6. bp. *Statistical Review of World Energy*. https://www.bp.com/en/global/corporate/energy-economics/statistical-review-of-world-energy.html (2020).
7. Worldometer. World Oil Statistics. https://www.worldometers.info/oil/.
8. U.S. Energy Information Administration (EIA). *Short-Term Energy Outlook (STEO)*. https://www.eia.gov/outlooks/steo/report/global_oil.php (2020).
9. Vengosh, A., Jackson, R. B., Warner, N., Darrah, T. H. & Kondash, A. A critical review of the risks to water resources from unconventional shale gas development and hydraulic fracturing in the United States. *Environmental Science and Technology* vol. 48 8334–8348 (2014).
10. Asuquo, F., Morah, F., Nya, A. E. & Ehrhardt, M. Trace metals in crude oils and beach tars from Nigerian coastline. *Indian J. Geo-Marine Sci.* (1995).
11. Haridos, S. Effect of air pollution and its emissions control strategies in petroleum refineries. *J. Ind. Pollut. Control* **33**, 1019–1023 (2017).
12. Morales, M., Gonzalez-García, S., Aroca, G. & Moreira, M. T. Life cycle assessment of gasoline production and use in Chile. *Sci. Total Environ.* **505**, 833–843 (2015).
13. Eurostat. *Shedding light on energy in the EU*. https://ec.europa.eu/eurostat/cache/infographs/energy/bloc-2c.html (2018).
14. Strogen, B. & Horvath, A. Greenhouse Gas Emissions from the Construction, Manufacturing, Operation, and Maintenance of U.S. Distribution Infrastructure for Petroleum and Biofuels. *J. Infrastruct. Syst.* **19**, 371–383 (2013).
15. Shapira, R. & Zingales, L. Is Pollution Value-Maximizing? The DuPont Case. *Natl. Bur. Econ. Res.* **23866**, (2017).
16. Geyer, R., Jambeck, J. R. & Law, K. L. Production, use, and fate of all plastics ever made. *Sci. Adv.* **3**, e1700782 (2017).
17. Our World in Data. FAQs on Plastics. https://ourworldindata.org/faq-on-plastics (2018).
18. PlasticsEurope. Plastics - the Facts 2018. *2018* https://www.plasticseurope.org/es/resources/publications/619-plastics-facts-2018.
19. Asakura, H., Matsuto, T. & Tanaka, N. Behavior of endocrine-disrupting chemicals in leachate from MSW landfill sites in Japan. *Waste Manag.* **24**, 613–622 (2004).
20. Jambeck, J. R. *et al.* Plastic waste inputs from land into the ocean. *Science (80-.).* **347**, 768–771 (2015).
21. Li, W. C., Tse, H. F. & Fok, L. Plastic waste in the marine environment: A review of sources, occurrence and effects. *Science of the Total Environment* vols 566–567 333–349 (2016).
22. Barnes, D. K. A., Galgani, F., Thompson, R. C. & Barlaz, M. Accumulation and fragmentation of

plastic debris in global environments. *Philos. Trans. R. Soc. B Biol. Sci.* **364**, 1985–1998 (2009).

23. Ryan, P. G. Ingestion of Plastics by Marine Organisms. in *Handbook of Environmental Chemistry* vol. 78 235–266 (Springer Verlag, 2019).

24. Digka, N. *et al.* Evidence of ingested plastics in stranded loggerhead sea turtles along the Greek coastline, East Mediterranean Sea. *Environ. Pollut.* **263**, 114596 (2020).

25. Avio, C. G., Gorbi, S. & Regoli, F. Plastics and microplastics in the oceans: From emerging pollutants to emerged threat. *Mar. Environ. Res.* **128**, 2–11 (2017).

26. Villegas, P. J. Challenges to Solve Our Plastic Waste Problems. *Org. Med. Chem.* **7**, (2018).

27. Rochman, C. M. *et al.* Polybrominated diphenyl ethers (PBDEs) in fish tissue may be an indicator of plastic contamination in marine habitats. *Sci. Total Environ.* **476**–**477**, 622–633 (2014).

28. Swan, S. H. Environmental phthalate exposure in relation to reproductive outcomes and other health endpoints in humans. *Environ. Res.* **108**, 177–184 (2008).

29. Thompson, R. C., Moore, C. J., Saal, F. S. V. & Swan, S. H. Plastics, the environment and human health: Current consensus and future trends. *Philosophical Transactions of the Royal Society B: Biological Sciences* vol. 364 2153–2166 (2009).

30. Perkins, S. Plastic waste taints the ocean floors. *Nature* http://www.nature.com/news/plastic-waste-taints-the-ocean-floors-1.16581 (2014) doi:10.1038/nature.2014.16581.

31. Derraik, J. G. B. The pollution of the marine environment by plastic debris: A review. *Marine Pollution Bulletin* vol. 44 842–852 (2002).

32. Gregory, M. R. Environmental implications of plastic debris in marine settings—entanglement, ingestion, smothering, hangers-on, hitch-hiking and alien invasions. *Philos. Trans. R. Soc. B Biol. Sci.* **364**, 2013–2025 (2009).

33. European Commission. Ecodesign Your Future; How Ecodesign can help the environment by making products smarter. https://op.europa.eu/en/publication-detail/-/publication/4d42d597-4f92-4498-8e1d-857cc157e6db/language-en (2012) doi:10.2769/38512.

34. Wool, R. P. & Sun, X. S. *Bio-Based Polymers and Composites*. *Elsevier* (Elsevier Inc., 2005). doi:10.1016/B978-0-12-763952-9.X5000-X.

35. Weber, C. J., Haugaard, V., Festersen, R. & Bertelsen, G. Production and applications of biobased packaging materials for the food industry. *Food Addit. Contam.* **19**, 172–177 (2002).

36. Pawelzik, P. *et al.* Critical aspects in the life cycle assessment (LCA) of bio-based materials - Reviewing methodologies and deriving recommendations. *Resources, Conservation and Recycling* vol. 73 211–228 (2013).

37. Themelis, N. & Mussche, C. Energy and economic value of municipal solid waste (MSW), including non-recycled plastics (NRP), currently landfilled in the fifty states. *Engineering* (2014).

38. Li, C. T., Lee, W. J., Mi, H. H. & Su, C. C. PAH emission from the incineration of waste oily sludge and PE plastic mixtures. *Sci. Total Environ.* **170**, 171–183 (1995).

39. Weiss, M. *et al.* A Review of the Environmental Impacts of Biobased Materials. *J. Ind. Ecol.* **16**, S169–S181 (2012).

40. Fulcher, K. An investigation of the use of cellulose-based materials to gap-fill wooden objects. *Stud. Conserv.* **62**, 210–222 (2017).

41. Gellenbeck, K. W. Utilization of algal materials for nutraceutical and cosmeceutical applications-what do manufacturers need to know? *J. Appl. Phycol.* **24**, 309–313 (2012).

42. Tavassoli-Kafrani, E., Shekarchizadeh, H. & Masoudpour-Behabadi, M. Development of edible films and coatings from alginates and carrageenans. *Carbohydrate Polymers* vol. 137 360–374 (2016).

43. Armisén, R. Agar and agarose biotechnological applications. in *International Workshop on Gelidium* vol. 221 157–166 (Springer Netherlands, 1991).

44. Wideman, T. H., Zautra, A. J. & Edwards, R. R. New Opportunities for an Ancient Material. **154**, 2262–2265 (2014).

45. Zhao, H. F., Li, Y. & Sha, L. Z. Preparation of functional air filter material based on biodegradable fibers and nano titanium dioxide. *Dig. J. Nanomater. Biostructures* **13**, 391–397 (2018).

46. Sun, Q. *et al.* Functional biomaterials towards flexible electronics and sensors. *Biosensors and Bioelectronics* vol. 119 237–251 (2018).

47. Taura, J. R. S. Mechanism of silk processing in insects and spiders. **926**, 1057–1061 (2003).

48. Meinel, L. *et al.* Silk-based biomaterials. *Bone* **39**, 922–931 (2006).

49. Xu, G., Gong, L., Yang, Z. & Liu, X. Y. What makes spider silk fibers so strong? from molecular-crystallite network to hierarchical network structures. *Soft Matter* **10**, 2116–2123 (2014).

50. Cheung, H., Ho, M. & Cardona, F. Natural fibre-reinforced composites for bioengineering and environmental engineering applications. *Compos. Part B Eng.* **40**, 655–663 (2009).

51. Perez-Rigueiro, J., Viney, C., Llorca, J. & Elices, M. Silkworm silk as an engineering material. *J. Appl. Polym. Sci.* **70**, 2439–2447 (1998).

52. Gosline, J. M., Guerette, P. A., Ortlepp, C. S. & Savage, K. N. The mechanical design of spider silks: From fibroin sequence to mechanical function. *J. Exp. Biol.* **202**, 3295–3303 (1999).

53. Tulachan, B. *et al.* Electricity from the silk cocoon membrane. *Sci. Rep.* **4**, 38–42 (2014).

54. Hansen, V. *The Silk Road: A New History*. *Oxford University Press* (2012).

55. Beckwith, C. I. *Empires of the Silk Road: A History of Central Eurasia from the Bronze Age to the Present*. *Princeton University Pres* (2011).

56. Federico, G. *Seda: un producto - mediterraneo*. (1995).

57. Holland, C., Numata, K., Rnjak-Kovacina, J. & Seib, F. P. The Biomedical Use of Silk: Past, Present, Future. *Advanced Healthcare Materials* vol. 8 (2019).

58. International Sericultural Commission. Global Silk Production. *United Nations* http://www.inserco.org/en/statistics (2019).

59. Ebrey, P. B. *The Cambridge Illustrated History of China*. *Cambridge University Press* (2010).

60. Markets, R. and. *Global Silk Market Size, Trends & Forecast (2020 - 2025).* https://www.marketdataforecast.com/market-reports/silk-market (2020).

61. Adidas. Adidas Unveils World's First Performance Shoe Made From Biosteel® Fiber. *adidas AG* https://www.adidas-group.com/en/media/news-archive/press-releases/2016/adidas-unveils-worlds-first-performance-shoe-made-biosteel-fiber/ (2017).

62. Goodyear. The Goodyear reCharge Concept –. https://news.goodyear.eu/the-goodyear-recharge-concept--making-tire-changing-easy-with-customized-capsules-that-renew-your-tires/ (2020).

Silk Fibroin (SF), a protein obtained from *Bombyx mori*, represents one of the most promising choices for developing a more sustainable generation of materials.

To make it real, it is necessary to acquire the ability to control and modify SF's properties. But, this control cannot be reached without a deep understanding of the material.

In the following, the SF molecular structure and organization are described. In addition, the main processing methods are summarized, and their effect on SF structure is studied.

Chapter.2

SILK FIBROIN STRUCTURE AND PROCESSING

Among the available silks types from different arthropods, that produced by *Bombyx mori* moth (also named domesticated silkworm or mulberry silk), represents the most interesting one due to its higher production yield and facility to manufacture.

Four different stages can be differentiated in the silkworm life cycle: moth, egg, larva, and pupa (***Figure 2.1***), but silk is only secreted during the larva or feeding phase, and more specifically at the beginning and the end of five instars through which each larva goes[1]. Silk is only secreted in large quantities at the end of the final instar to form the cocoons[2], a protective covering that shields the silkworm from predator's attacks and the environment while supporting their metamorphosis[3,4]. Thus, cocoons are the main places where *Bombyx mori* silk is obtained. In the following, the silk from cocoons is described.

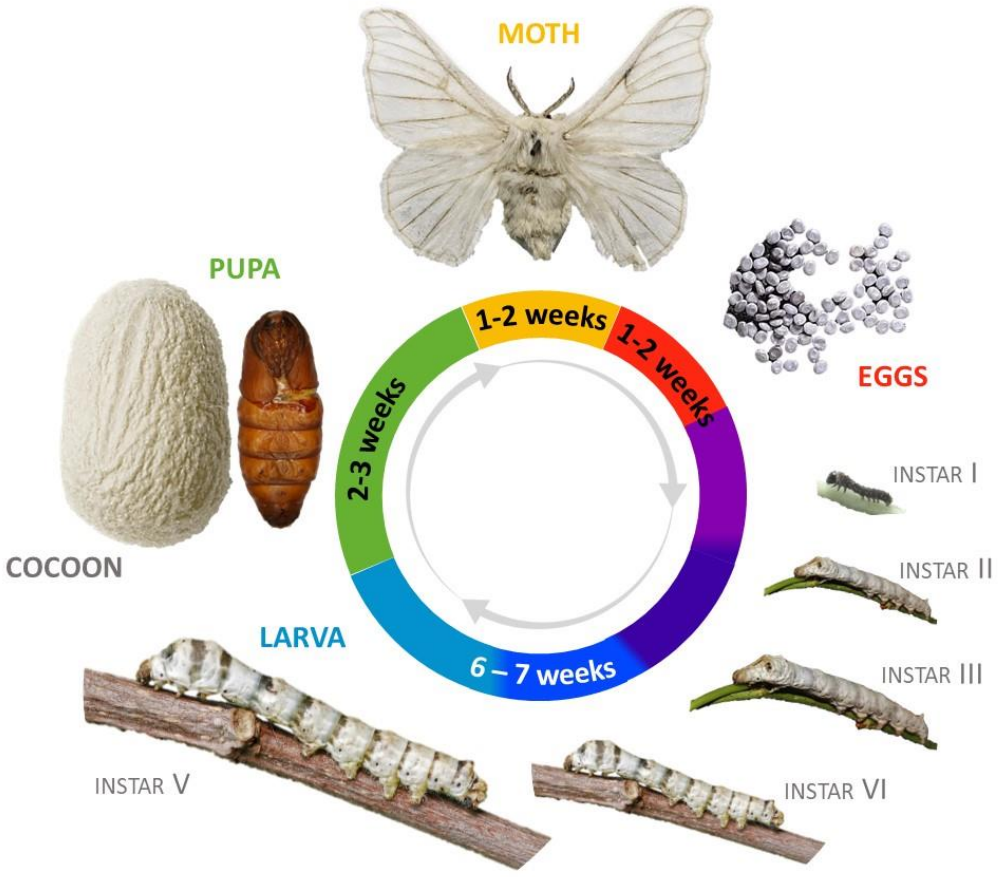

Figure 2. 1. *Bombyx mori lifecycle.*

2.1. SILK COMPOSITION

It is commonly named silk, to the fiber composing the silkworm cocoons. However, this nomenclature does not consider that silk is not a single component since it is made up of several constituents, resulting in a composite material. Each constituent fulfills a particular function and provides specific abilities to the cocoons.

Silkworms produce an aqueous protein solution in two modified salivary glands, which merges in a single duct at the spinneret. Due to physical and chemical processes, each gland's protein-solution coagulates separately in filaments named brins (***Figure 2.2***). The two formed brins are then spun together to form a double-thread core named bave. This is coated with an amorphous protein that wraps it and acts as glue joining fibers to form the cocoon[5]. The cocoons are commonly formed by a single fiber of 700-1500 m long[6,7].

Natural impurities like fat, wax, inorganic salt, and colorants also appear in cocoons. But, due to their low proportion (< 3 %) and scarce industrial interest, these products are commonly discarded during processing[8].

The bave is formed by Silk Fibroin (SF), a protein material that is between 70-80% of cocoon weight[9], with around 65% crystalline region and 35% amorphous[10]. Its function is to provide structural stability and mechanical resistance to the cocoons[11]. The amorphous coating is a protein known as Silk Sericin (SS) and represents 20-30% of cocoon weight. SS acts as an adhesive, holding SF filaments together and maintaining the integrity of the cocoon[9,12]. SF and SS are coupled by Van der Wall dispersive forces and specific interactions mainly dominated by H-bonding[12]. These interactions are facile disrupted that allows to use both materials separately.

As proteins, SF and SS are based on large polyamine acids chains, also known as polypeptides (**¡Error! No se encuentra el origen de la referencia.*2.3***). Each polypeptide is formed by amino acids (monomers) repetition $(–NH–CHR–CO–)_n$, each one linked to the following by peptide bonds (an amide-type bond) formed between carbon (C) of one amino acids and nitrogen (N) of the consecutive (R-C-N-R)). This structure always leads to a chain end with a free amine group ($-NH_2$), named N-terminus, and at the opposite end, a free carboxyl group (-COOH) named C-terminus.

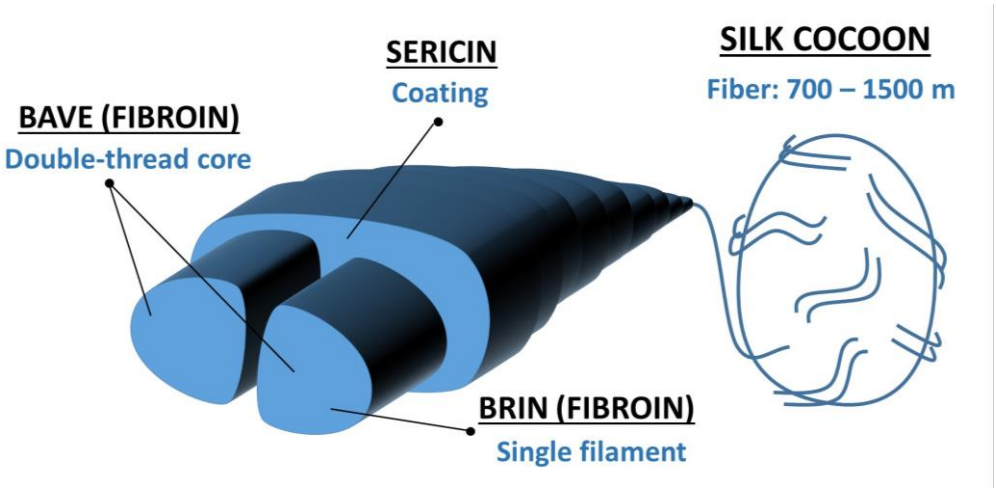

Figure 2. 2. *Graphic representation of silk from cocoons composition and components*

Each repetitive unit of peptide chains shows three functional groups: i) an amine group (-N-H), ii) a carbonyl group (-C=O), and iii) a variable side chain (-R), which gives name to the amino acid (***Figure 2.3***). Each amino acid has unique characteristics because of its R group size, shape, solubility, and ionization properties.

Due to the different roles of SF and SS in the cocoons, their amino acid composition varies. A summary of the amino acids of each component is found in ***Table 2.1***[9,13].

Table 2.1. *Amino acid composition of Bombyx mori Silk fibroin and Sericin (Red highlights: apolar behavior, green highlights: polar behavior)*

Amino Acid	*Symbol*	*Fibroin (%)*	*Sericin (%)*
Glycine (Gly)	*G*	*45*	*14*
Alanine (Ala)	*A*	*29*	*5*
Serine (Ser)	*S*	*12*	*33*
Tyrosine (Tyr)	*Y*	*5*	*3*
Valine (Val)	*V*	*2*	*3*
Aspartic Acid (Asp)	*D*	*1*	*15*
Arginine (Arg)	*R*	*1*	*3*
Glutamic acid (Glu)	*E*	*1*	*8*
Isoleucine (Lle)	*I*	*1*	*1*
Leucite (Leu)	*L*	*1*	*1*
Phenylalanine (Phe)	*F*	*1*	*1*
Threonine (Thr)	*T*	*1*	*8*
Histidine (His)	*H*	*<1*	*1*
Lysine (Lys)	*K*	*<1*	*4*
Proline (Pro)	*P*	*<1*	*1*

Glycine (Gly), Alanine (Ala), Serine (Ser), and Tyrosine (Tyr) are the main components of SF, being more than 90% of the structure. Gly and Ala are predominant, representing around 74% of the total. SS composition, more heterogeneous, contains Serine as the main component (33%) and in the minority Aspartic Acid (Asp), Glycine (Gly), Glutamic acid (Glu), and Threonine (Thr).

Gly and Ala are the simplest amino acids, with a single hydrogen atom (-H) and the methyl group (-CH_3) as its side chain, respectively. Both are hydrophobic non-polar amino acids (***Figure 2.3***). Conversely, the side chains of Ser, Tyr, Asp, Glu, and Thr, contain hydroxyl groups (-OH), which make them polar. Ser has a hydroxymethyl group (-CH_2OH), Tyr a large phenol group (-C_6H_5OH), Asp and Glu have carboxylic groups linked to ethyl and methyl respectively (-CH_2COOH), (-CH_2CH_2COOH) and Thr contains a hydroxyl group linked to a methyl ($CH_2(OH)CH_2$) group[6,14,15]. Due to the hydroxyl groups' reactivity, i) the polar amino acids give water reactivity to the protein and ii) often, due to hydrogen bond interactions with carbonyl groups (-COOH) on adjacent chains, they form hydrogen-bonding networks[6].

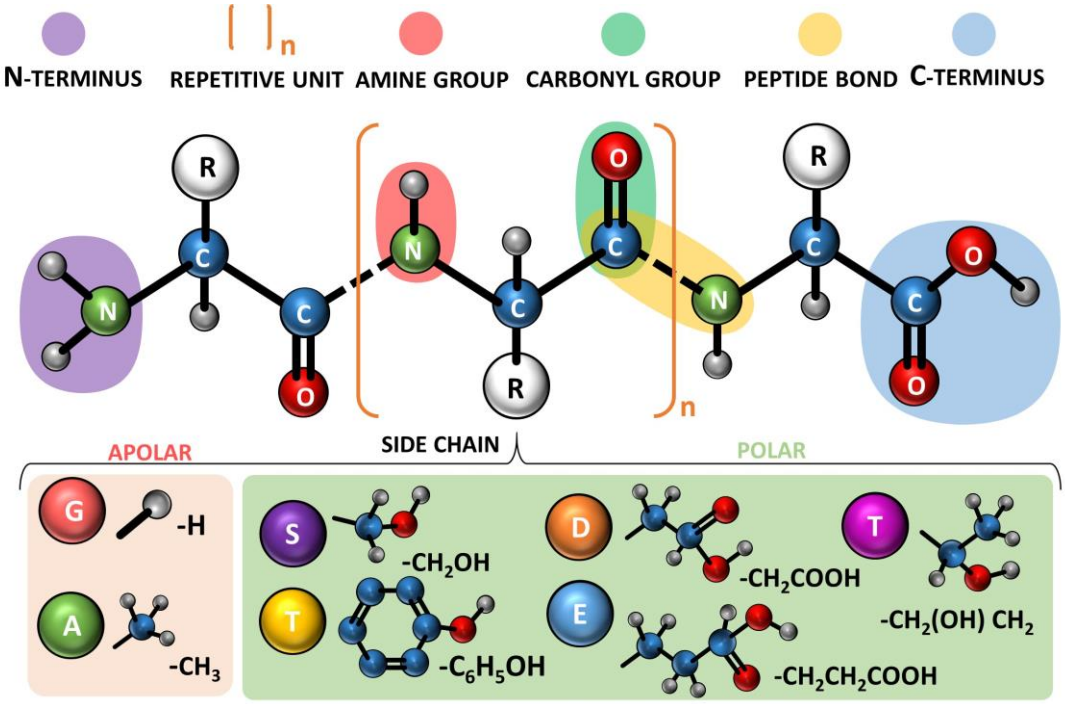

Figure 2. 3. *Graphic representation of polypeptide chain composition (left) and some of the most common side chains of SF and SS (right)*

Amino acids composition, distribution, repetition patterns, and all the non-covalent interactions such as hydrogen bonding, ionic interactions, Van der Waals forces, and hydrophobic packing establish the final properties and behavior of proteins. Thus, the knowledge of protein composition and organization gives a useful tool for designing new materials.

Among the two main silk components, SF has historically deserved significant attention, mainly due to its larger presence inside the cocoon, natural function, and derived self-properties[16–21]. Several methods to process, control, and modify SF in its original shape, and even new morphologies have been developed[22–25]. Also, some promising active properties have been identified, among which piezoelectric response can be highlighted[26–29]. All these factors have located the SF as one of the more promising bio-based materials for new devices development[11,25,30–33]. As a result, SF has been selected as the objective of this study.

2.2. SILK FIBROIN RAW STRUCTURE

2.2.1. PRIMARY STRUCTURE

Silk Fibroin is naturally secreted as a molecular complex, composed of three different protein structures: i) a long polypeptide named Heavy(H)-Chain of 390 KDa, ii) a short polypeptide named Light(L)-Chain of 26 KDa, and iii) a small glycoprotein of 30 KDa known as P25[6]. Both H-Chains and L-Chains are connected by a disulfide bond, while P25 is associated with the chains via non-covalent hydrophobic interactions (***Figure 2.4***).

Quantitatively, H-Chain, L-Chain, and P25 are present in silk fibroin in a molar ratio of 6:6:1, forming the silk fibroin elementary unit $(H_6L_6P25_1)_n$[34]. The amino acid composition of the three components is detailed in ***Table 2.2*** [35,36] [37]. H-Chain composition is 45.9% Gly, 30.3% Ala, 12.1% Ser, 5.3% Thr, 1.8% Val, and only 4.7% of the other amino acid types[35]. As suggested by S. Ha *et al.*[38], the amino acid sequence of H-Chain is ordered on three repetitive motifs: i) $(Gly\text{-}Ala\text{-}Gly\text{-}Ala\text{-}Gly\text{-}Ser)_n$ motifs, ii) Gly-Tyr…Gly-Tyr regular sequences, and iii) Gly-Ala-Ala-Ser structures. Most of these repetitive blocks are linked by 11, Gly-Thr⋯⋯Gly-Thr irregular sequences (commonly composed by 34 residues) immediately followed by Gly-Ala-Gly-Ala-Gly-Ser motifs. This organization acquires a particular relevance during chains secondary folding, as the Gly-Thr⋯Gly-Thr irregular sequences may ease the crystalline organization, possibly due to i) Pro residues, that push

the backbone direction change, and ii) Gly-Thr···Gly-Thr motifs that can interact one each other favoring the chain folding.

In general, H-Chain seems to be based on $(Gly\text{-}X)_n$ hydrophobic motif where X is Ala, Ser, and Tyr in 64-65%, 22-23%, and 10%, respectively. Val and Thr residues contribute to X but only between 1.3 and 2%[35,39]. Thus, the SF consists of 12 hydrophobic and repetitive domains interspersed with 11 hydrophilic less ordered domains[40] (***Figure 2.4***).

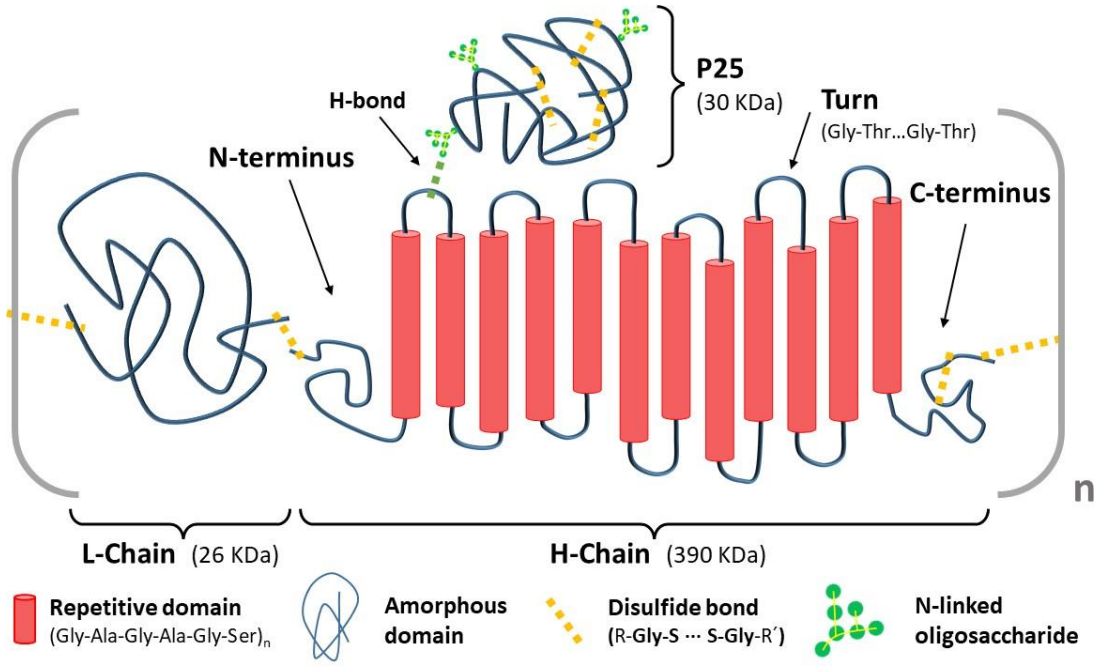

Figure 2. 4. *Graphic representation of SF main components (H-Chain, L-Chain and P25) composition*

C- and N-terminus of H-Chains are entirely based on non-repeating amino acid sequences with many hydrophilic domains, around 60%. Both termini contain Cys residues, two in the N-terminus, and three in the C-terminus [38], which are involved in disulfide bonds (R-S-S-R') that link H- and L-Chains. The non-implied Cys residues of C-terminus for chains linking participate in an internal disulfide linkage[35].

L-Chain is mainly composed of non-repetitive amino acid sequences, with around 47% of hydrophobic residues[38,41]. 15% of these hydrophilic domains are confined into the N-terminal[36]. The hydrophobic/hydrophilic domain relation highly differs between H- and L-Chains, being the hydrophilic domains much higher in L-Chain. This suggests that the L-Chain structure in nature is mainly hydrophilic, although it should show an amphiphilic behaviour due to the hydrophobic domains' presence. Due to this more polar nature, some

works have isolated the smaller L-Chain where chemical modifications are more accessible [42]. The N- and C-terminus of L-Chain have Cys residues that form intermolecular disulfide bonds.

Table 2.2. *SF proteins, amino acid composition.*

Amino Acid	*H-Chain (%)*	*L-Chain (%)*	*P25 (%)*
Alanine (Ala)	*30.3*	*13.5*	*4.4*
Aspartate (Asp)	*0.5*	*7.0*	*6.9*
Asparagine (Asn)	*0.4*	*7.4*	*6.4*
Serine (Ser)	*12.1*	*9.8*	*6.4*
Glycine (Gly)	*45.9*	*9.0*	*4.4*
Glutamic acid (Glu)	*0.6*	*2.0*	*3.4*
Glutamine (Gln)	*0.1*	*6.1*	*3.4*
Isoleucine (Ile)	*0.3*	*8.2*	*6.9*
Valine (Val)	*1.7*	*7.0*	*4.4*
Leucine (Leu)	*0.1*	*7.0*	*9.4*
Arginine (Arg)	*0.3*	*4.1*	*5.9*
Tyrosine (Tyr)	*5.3*	*4.1*	*4.9*
Proline (Pro)	*0.3*	*2.9*	*5.9*
Treonine (Thr)	*0.7*	*2.9*	*7.4*
Pheniolalanine (Phe)	*0.7*	*2.9*	*4.4*
Histidine (His)	*0.1*	*2.1*	*3.4*
Lysine (Lys)	*0.2*	*1.6*	*3.9*
Cisteine (Cys)	*0.1*	*1.2*	*0.5*

The function of L-Chain and intermolecular disulfide bonds seems to be related to i) ensure the intracellular transport of SF during its production in glands and ii) facilitate aqueous SF solution secretion by preventing the H-Chain denaturalization due to excessive crystallization[43]. Thus, disulfide bonds and L-Chain are essential for the secretion of a large amount of fibroin [34].

P25 primary structure consists of alternate hydrophobic and hydrophilic regions with eight Cys residues and three potential N-glycosylation sites. Following these data, K. Tanaka *et al.*[44] found that P25 is a polypeptide chain linked to mannose-type N-linked oligosaccharides associated with the H and L-Chains complex mainly by hydrophobic interactions. M. Ratio *et al.*[34] resolved that the P25 was linked to H-Chain by hydrophobic bonding, while N-linked oligosaccharides also link to H-Chain by hydrogen bonding. Both interactions were found to be required in maintaining the integrity of the elementary unit. However, P25 is stable only during secretion and storage in the gland, and it does not persist after shear and

dehydration during fiber extrusion [45]. Further, the presence of some intramolecular disulfide bonds suggests that P25 is also involved in H-Chains repetitive units folding[44].

Thus, H-Chains are the main components of SF, while L-Chain and P25 structures are mainly required to ensure the correct formation and the integrity of SF fibers.

2.2.2. SECONDARY STRUCTURE

Driven by repetitive domains interactions, SF's folding models are defined:

i. ***α-helix*** is formed by a single polypeptide chain when the carboxylic groups (-C=O) of one amino acid are linked by hydrogen bonding to amino groups (NH) of another amino acid that is three residues further (***Figure 2.5***). As a result, the single-chain adopts a three-dimensional helix conformation where the polypeptide backbone forms the central structure, and the side chains extend outside the helix. When this structure is adopted, all the carboxylic and amino groups of one chain are linked one each other, becoming a stable structure.

ii. ***β-Sheets*** result from several polypeptide chains or/and sections interactions[6,35] in which there, both repetitive and non-repetitive units are implied. In search of the most stable configuration, the non-repetitive units (Gly-Thr⋯Gly-Thr sequences) fold driven by Pro residues and resulting in a 180^{o} bending. The subsequent structures link one repetitive unit with the following, so are named β-turns (***Figure 2.4***). Consequently, the repetitive units get placed in parallel, leading to the formation of a planar and flat two dimensional (2D) sheets where the chain backbone gets placed parallel. The backbone is linked by covalent peptide bonds, in contrast, carboxylic groups and amino groups get linked perpendicularly by H-bonds. This vastly connected configuration leads to highly stable structures (***Figure 2.5***). It is accepted that ordered chain folding follows a regular folding with 12 repetitive motifs linked by 11 non-repetitive β-turns[35] (***Figure 2.4***).

Although both folding models are present in SF, β-Sheets represent a quarter of the structure[45]. Only around 4% of SF is composed of α-helix[46]. The remaining SF is amorphous, although this values may vary depending on the treatment.

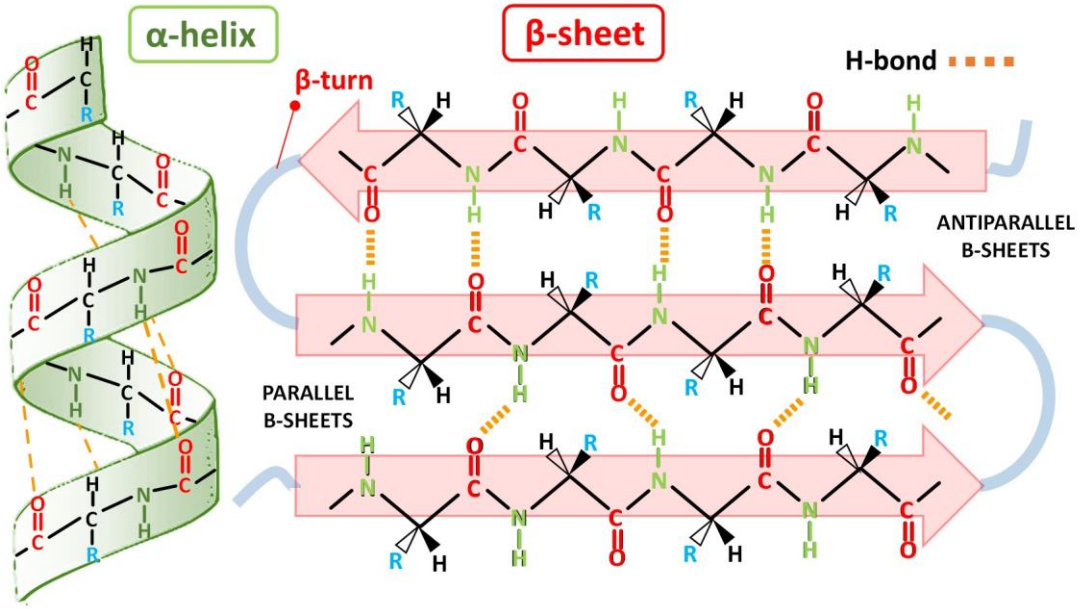

Figure 2. 5. *Graphic representation of α-helix, β-sheets and its two folding models: antiparallel and parallel*

Depending on the relative N- and C- terminus orientation during chains packing, two main conformations are adopted in β-Sheets (***Figure 2.5***):

i. ***Parallel β-Sheets*** are formed when connected chains have the same N- to C- terminus direction. Consequently, polypeptide chains adopt in the plane of the sheet the form of a centrally located 2-fold screw axis bonded by identical hydrogen-bond repeated along the chain axis direction.

ii. ***Antiparallel β-Sheets*** are formed when chains are placed opposite in the N- to C-terminus direction. As a result, chains adopt a double-strand structure interconnected by a set of "small" and "large" pairs of H-bond, repeated along the chain axis direction. This H-bond configuration gives the antiparallel β-Sheet structures the ability to alter its extension while still preserving integrity. This allows a larger geometrical diversity[47]. Parallel sheets commonly lead to planar sheets, while antiparallel sheets can lead to turned configurations, resulting in globular proteins.

The remaining chain sections that are not involved in α-helix neither β-Sheets formation get randomly organized, forming amorphous domains named random coils. Different chains organization implies a variation of SF behavior, thus, the control of structures formation represents a useful tool for the control of SF properties.

Regarding the crystallographic packing of β-Sheets, three main crystalline models can be identified in SF: silk I, silk II, and silk III. Each polymorph results in a specific SF behaviours[48].

i. ***Silk I*** is a metastable configuration, mainly found in aqueous SF before being secreted by the silkworm gland. The aqueous state makes it difficult to define its structure completely. However, it is clear that it i) presents some polypeptide chains order, ii) contains β-turns elements of the appropriate length to form β-Sheets, and iii) displays some hydrogen inter- and intramolecular bonds between adjacent units, mediated by Ser residues[6]. During the silkworm's natural silk spinning process, silk I is the precursor of silk II, so it can be considered that somehow, silk I follows the crystalline structure of β-Sheets without reaching the final close folded state. This lack of order must be associated with the trapped water molecules inside the packed structure, which form polar interactions with polypeptide chains, hindering the formation of close, packed, and stable crystals[49,50]. This lack of protein-protein interactions makes Silk I structures water-soluble and less stable than completely packed ones. Some works have focused on promoting Silk I to regulate the ability of SF based structures to be soluble in water [51]. The main explored techniques for Silk I promotion are: i) drying the aqueous silk directly without further perturbation[52,53], ii) generating foam in aqueous silk fibroin solutions[54], or iii) adding polyalcohol's to silk fibroin aqueous solutions[55].

ii. ***Silk II*** is considered the primary representation of β-Sheets. Silk II is commonly obtained when silk is addressed to extrusion processes, progressive dehydration, shear-induced alignment, salt concentration increase, pH lowering, heat treatment, water annealing, organic solvents treatment, or mechanical strain[48,50,56]. The moisture loss and polypeptide chains compression allow crystalline domains packing aligned with the fiber axis[57]. Several works have been focused on promoting silk II [58], i) by water annealing[50], ii) Ethanol (EtOH), and Methanol (MetOH) exposure[50,59]; iii) autoclaving[50]; iv) casting concentrated silk fibroin solutions (>3%) onto warm substrates (>50 ºC). The same solutions cast onto cold substrate produce silk I or random coil[48]; and v) water vapor annealing. 4 ºC annealing promotes silk I structure, and at 100 ºC, crystallization rates around 60 % are obtained[60].

iii. ***Silk III*** is more uncommon because it is not naturally present in raw SF. Silk III structure is defined as a threefold helical crystalline structure, mostly found in the air-water interface of films prepared without compression. Silk III crystallites, nucleate, and grow

from the water sub-phase based on the symmetry patterns initially established. The left-handed threefold helical conformation separates the hydrophilic serine residues and hydrophobic alanine residues to opposite sides. This allows the chains to behave as polysurfactants[61].

It is essential to notice that SF, as material formed by large macromolecular chains, cannot adopt a perfect crystalline structure with well-defined diffraction patterns, but crystallization is associated with the partial alignment of some domains.

The packing level affect the SF density. The most dense structures are the crystalline units, Silk I show a density of 1.40 $g \cdot cm^{-3}$, while more packed Silk II show a density of 1.45 $g \cdot cm^{-3}$. Because the random coil presence, the density of whole structure decreases to values between 1.31 $g \cdot cm^{-3}$ and 1.325 $g \cdot cm^{-3}$, depending on crystalline domains-random coil ratio[62].

2.2.3. TERTIARY STRUCTURE

During β-Sheets formation, side chains (R) get oriented out of the plane. These non-bonded sections provide new interaction places, where additional β-Sheets can join. This coupling allows the growth of a three dimensional (3D) structure in the z-direction to form the β-crystals.

Among amino acids, the main responsible for β-Sheets linkage are the Ser residues, which interact through their hydroxyl groups with the carbonyl groups on adjacent chains, leading to several planar sheets joints[6,47]. Although Tyr residues can also form the same interactions, their large size implies a steric impediment, which results in the destabilization of crystalline structures and thus, they are not commonly implied[6]. Gly and Ala have low relevance on the β-Sheets joint because of their less reactive side chain.

Due to the repetitive nature of β-Sheets and side chains orientation out of the plane, the Gly side chains of β-Sheets always get oriented towards one single direction. In contrast, the remaining side chains are oriented to the opposite (***Figure 2.6***). This configuration leads to two different disposal models:

i. In the ***polar model***, Gly side chains are always pointing out in one direction. The remaining residues point in the opposite direction. In this crystal growing model, considering Gly side chains' position as the upper side (U) and the opposite as the bottom

side (B), β-Sheets rise following UBUBUB… ordered pattern[35]. As a result of this repetitive pattern, inter-sheet spacing is always the same, 3.5-3.9 Å.

ii. In the ***antipolar model***, conversely, side chains point alternatively up and down across a β-Sheets. In this way, and following the crystal model growing, the antipolar model grows following UBBUBUUB… less ordered pattern. The calculated inter-sheet distances between two Gly faces (UU), Gly-non-Gly (UB), and two non-Gly faces (BB) are 3.5 Å, 3.5 – 3.9 Å, and 5.3 - 5.7 Å, respectively[40]. Due to the lowest order present in the antipolar model, the resulting crystals are less regular, and consequently, β-Sheets adopt a non-defined configuration. This local disorder in the crystal packing increases the fiber's strength by preventing crystals from slipping past each other[6].

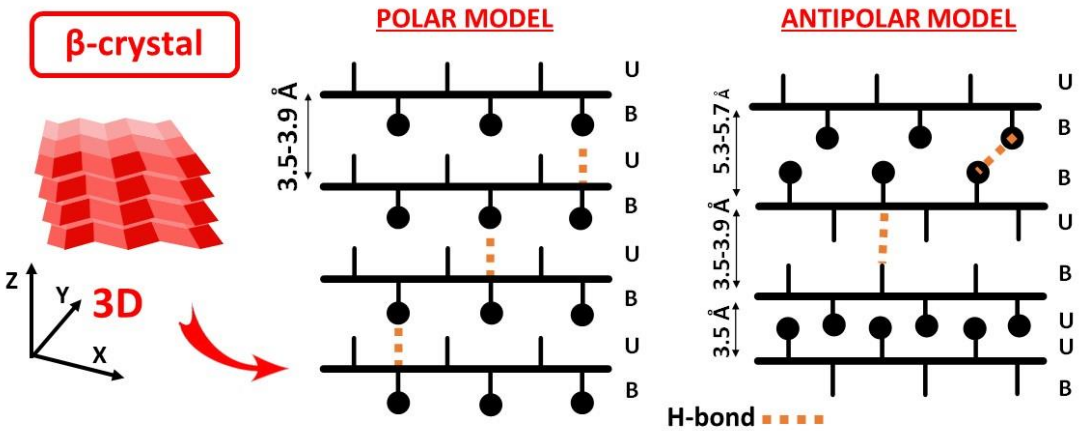

Figure 2. 6. *β-crystals graphic representation and a scheme of polar and antipolar configurations.*

The β-Sheets two folding models and two crystal packing models lead to four differentiated β-crystals arrangements: i) Parallel-Polar, ii) Parallel-Antipolar, iii) Antiparallel-Polar, and iv) Antiparallel-Antipolar. Computational studies, together with Nuclear Magnetic Resonance NMR and X-ray diffraction experimental studies, indicate the antiparallel-antipolar model as the most stable one[6,47,63]. However, to date, there is not yet a real consensus about this arrangement.

2.2.4. QUATERNARY STRUCTURE

In both crystalline and amorphous domain formation, several polypeptide chains sections can participate either from the same chain or even from several chains. Indeed, β-crystals are commonly confluence points. In this way, chains are linked to form a cross-linked structure where β-crystals act as nodes and remaining amorphous domains (random coils) get around, forming a continuous structure[45] (***Figure 2.7***). The same configuration is repeated along with the whole SF structure, promoting the formation of extended cross-linked networks that constitute the quaternary structure. Due to the spinning conditions, the cross-linked configuration is commonly aligned with the longitudinal fiber axis[40].

On a slightly larger scale, the spinning conditions induce the aqueous SF solution to become solid into a nanofibrils of 20-30 nm of diameter[57,64]. Several nanofibrils are formed simultaneously, and all of them become together to form the brins of 10 - 20 µm of diameter[65] (***Figure 2.7***). Strong adjacent interactions are formed between each bin's nanofibrils, resulting in strong friction that avoids sliding. This behavior gives the nanofibrils a crack-stopping property during the deformation of SF fibers, enhancing the strength of silk fibers and improving the mechanical resistance to the whole structure[64].

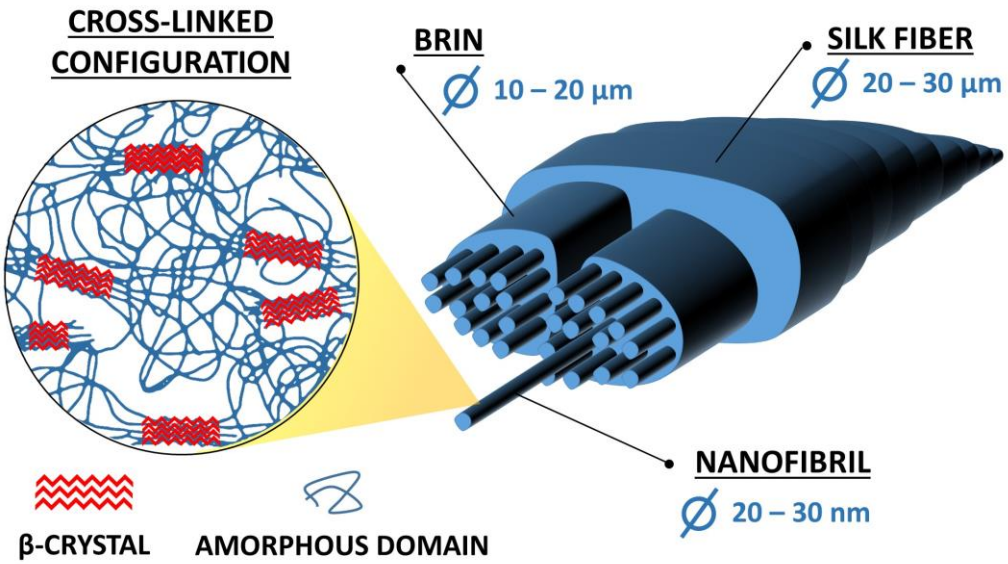

Figure 2. 7. *Graphic representation of silk hierarchical configuration. Left: SF cross-linked configuration. Right: nanofibers < brin < fiber configuration.*

The hierarchical configuration of SF (β-crystals < cross-linked structure < nanofibrils < brins < fiber) contributes to the macroscopic behavior of SF. Thus, the control of crystalline nodes packing, crystallographic model, and crystalline domain size or distribution are useful tools for SF properties tailoring.

2.3. SILK FIBROIN PROCESSING

Silk fibroin processing includes the techniques required to extract SF from the cocoon and generate SF based materials. Four separate steps can define the process: i) degumming, ii) solving, iii) regeneration, and iv) post-processing.

2.3.1. DEGUMMING

The binary composition of raw silk requires the separation of its main components (SF and SS) to obtain neat SF. This isolation process is commonly named degumming. An example of degummed fibers is shown in ***Figure 2.8***.

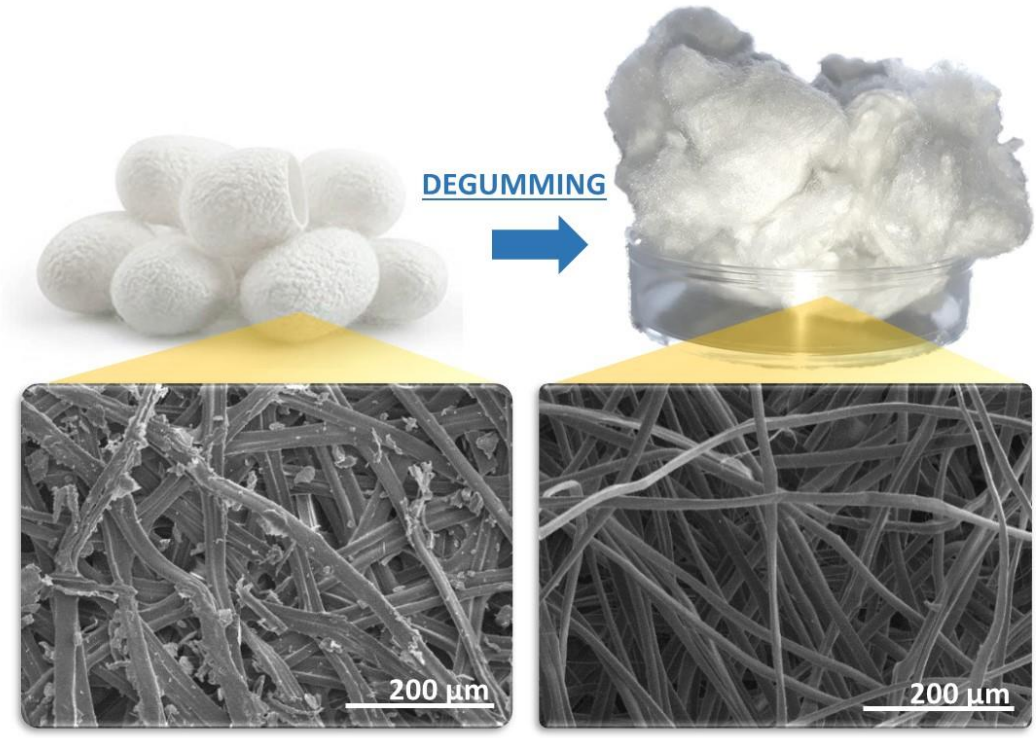

Figure 2. 8. *Silk cocoon degumming example. above: macroscopic appearance before (left) and after (right) cocoon shape loss. Below: SEM images of SF fibers appearance before (left) and after (right) SS (white) removal.*

The simplest method to isolate both components is based on the elimination of one of the components in favor of the other. Due to SS large polar residues, it is soluble in water[66]. Thus, SS elimination is the most exploited procedure for SF isolation. Nevertheless, only the more accessible structures of the SS surface are solubilized in water[67]. Fortunately, it is possible to increase this yield by solubilization in hot water baths, which is the most common and traditional technique[68]. Despite being more effective, not all the SS is degummed, which leaves SF fibers with large SS residues. This degumming is enough for SF-based threads processing. However, there are more demanding applications, such as biomedicine, for which is necessary to extract SS completely because any SS residue could affect the final materials' behavior, varying its crystallization, mechanical and thermal stability[69], cytotoxicity, and biocompatibility[70].

An alternative treatment to improve SS extraction and practically remove it consists of adding pressure to the process. The method is named high temperature and high pressure (HT-HP) degumming [71]. Both degumming processes are only based on water and allow obtaining neat SS in aqueous solution without any additional product.

In search of a completely purified SF, the commonly used degumming methods are i) alkaline degumming [72], ii) urea degumming [73], iii) enzymatic degumming[74–76], and iv) soap degumming[66,77]. Each degumming method affects in a different way SF and the final properties of the material[70]. In the same way, each degumming implies a variable environmental, energetic, and economic cost.

i. ***Alkaline degumming*** efficiently hydrolyses SS with high removing rates[73]. Still, it is a non-specific process that always results in a certain degree of damage to the SF structure. Consequently, the SF average molecular weight (Mw) and derived properties can be reduced[70].
ii. ***Urea degumming*** is gentler with SF, but it needs high urea concentrations to yield a total SF cleaning[78] and can act as an aggressive hydrogen bond breaker (denaturant), altering significantly the overall conformation of protein chains[66]. Also, produced aqueous residues must be treated to avoid environmental problems derived from wastewaters eutrophication problem[79,80].
iii. ***Enzymatic degumming*** removes Sericin by a mild hydrolysis reaction with high efficiency, strong specificity, and low pollution[73]. However, the high cost of most enzymes makes this process unsuitable for large-scale industrial production[68].

iv. ***Soap degumming*** is based on boiling the cocoons in sodium carbonate or sodium phosphate hot aqueous solutions[68,78,81,82]. The standard method consists of boiling the cocoons in Na_2CO_3 hot aqueous solutions. During degumming, the chaotropic agent Na_2CO_3 mainly affects the weaker hydrogen bonds of silk, i.e., those of SS. Na_2CO_3 is adsorbed, making the –COOH in the SS molecules become $–COONa^+$, which enhances their solubility[73]. In general, this method provides good efficiency at low cost, and the used low salt proportions reduce the environmental impact of the process. Results suggest that temperatures lower than 80 ^oC are not enough to remove the SS completely. Temperatures higher than 100 ^oC can damage the fiber surface and produce the polypeptide chain cleavage, resulting in some molecules below 30 KDa[66,70,73,77,78]. Short time degumming processes can remove the SS completely without apparent damage of SF fibers[78], and equally, short contents of Na_2CO_3 have not reported any SF degrading evidence[66,70,73,77,78].

A table summarizing the main degumming methods with an inappreciable effect over SF molecular structure is presented in ***Table 2.3***.

Table 2.3. *Non-damaging degumming methods and main parameters.*

Method	*Agent*	*Concentration (M / wt.%/(g/l))*	*Silk / liquor (w/w)*	*Time (min)*	*Temperature (^oc)*	*SS removal (%)*	*ref*
Hot water	*Water*	-	*1/30*	*5*	*120*	*80*	78
		-	*1/30*	*60*	*100*	*50*	78
Urea	*Urea*	*8*	*1/30*	*10*	*80*	*100*	78
Alkaline	*alkaline water*	-	*1/25*	*30*	*100*	*100*	83
Standard method	*Na_2CO_3*	*~3.7·10-3 / 0.05 / 0.5*	*1/50*	*5*	*100*	*100*	78
		~3.68·10-3 / 0.05 / 0.5	*1/40*	*30*	*100*	*100*	77

Wetting agents and surfactants addition, such as sodium dodecyl sulfate (SDS) and olive oil (Marseille) soap, reduce the surface tension between the cocoons and water and improve the SS extraction[70]. However, their effect has not been deeply studied, and thus are less used.

Alternative methods are infrared heating, plasma pre-treatment, or the use of CO_2 supercritical as solvent[84–86]. However, they present additional complications like fibroin damage, problematic industrial use, low efficiency, and high cost. A new promising method

with high SS extraction yields is the steam treatment. By this method, SF is degummed by using only pressurized water, reducing water pollution and energy consumption[87].

2.3.2. DISSOLVING

SF from degumming can be directly used as a thread in the textile industry and as a suture in biomedicine[40]. Nevertheless, to improve the material processability, SF is commonly dissolved.

Due to its cross-linked structure and β-Sheets packed and resistant configuration, natural SF fibers present high stability versus solvents[88]. Depending on the solvent's ability to dissolve the SF, two main types could be classified: i) those with self-ability to dissolve SF original structure (first step solvents) and ii) those able to dissolve SF only after a pre-dissolution (second step solvents). Four solvent types are commonly used.

i. ***Organic solvents***: They can dissolve SF at room temperature to get extremely stable, transparent, and highly viscose solutions [89] [88] [90]. The most common first step organic solvents are hexafluoro-iso-propanol (HFIP) and N-methyl morpholine N-oxide (NMMO) [88,91,92]. Additional ones, like hexafluoroacetone (HFA), just work like second step solvents[88]. However, organic solvents can destroy the structural hierarchy of natural SF and become toxic the final material[93].
ii. ***Aqueous salt solutions*** are probably the most common ones. The main reason for that could derive from the low environmental impact of salts, their low cost, solving facility, and the ability to dissolve the original SF structure (first step solvent). Their main disadvantage is that salt-based SF solutions require long preparation times since solutions must be dialyzed for several days, and prepared solutions present low stability[88]. In aqueous salts solutions, SF polar interactions are broken due to their interaction with polar and charged groups from salts dissociation. The solvent capacity to denature the SF depends on the ions binding affinity.

The principal used salt solutions are those based on $CaCl_2$ and LiBr aqueous solutions[94–97]. The amount of $CaCl_2$ to completely dissolve SF is quite large. Commonly it is used in a ternary solution combined with Ethanol (EtOH) or Methanol (MetOH), which helps in proteins opening due to its polar nature[89]. Some authors have suggested SF degradation in $CaCl_2$ aqueous solution, but this is only observed at large solution times (> 5-6 h) and high temperatures (> 80 ºC)[98].

iii. ***Acidic solvents*** protonate the amide groups of the polypeptide chain to induce the solvation of the macromolecule[88]. The most common ones are carboxylic acids and trifluoroacetic acid (TFA). However, they are second step solvents and need the previous solubilization and regeneration of SF to dissolve it[99,100]. Although formic acid (FA) is a second step solvent, it is the most employed one. This is probably due to the provided short solving times, small solvent amount requirement, low degradation of molecular structure, low turbidity, solution stability, and self-ability to induce β-crystals into final SF structures[101]. FA presents two dual and opposite functions when dissolving SF due to its high polarity: solvent and crystallizer. Initially, FA penetrates the SF structure and breaks the H-bonds that hold the secondary structure by forming new bonds with SF polar residues, promoting the chain's opening (even the crystalline units) and their conversion to random coil configuration (***Figure 2.9***). At this point, FA molecules are found inside and outside the polypeptide. Due to the polarity of the FA molecules surrounding the SF hydrophobic domains, these are retracted to form small cores with an average hydrodynamic radius (R_H) of 22 nm. FA molecules inside the cores avoid the hydrophobic interactions, preventing their association to form again the cross-linked structure. As a consequence, in presence of FA, SF does not crystallise and remains stable in solution. When FA is removed, both the outer and internal solvent molecules are expelled, enabling the hydrophobic interactions of SF and inducing crystallization[101]. Acids can be combined with salts to induce the SF dissolution as the first step solvent and without damage to the structure[102]. The most used salt-acid combination is the formic acid-$CaCl_2$ solutions (FA/CaCl)[58,102,103], probably because of its selectivity and short processing times.

iv. Less used alternative solvents are the ***ionic liquids*** (ILs)[104], which are first step solvents, and provide tunable solubility, high thermal stability, negligible volatility, and ease solvent recovering. A suitable option for green chemistry[104–107]. Unfortunately, their effect on SF has been slightly studied.

During dissolving, all the SF structures are broken, and only the primary amino acid composition is preserved. Nonetheless, due to the protein-protein self-interactions, during solvent removal, most structures are re-formed on their own (i.e., β-Sheets and cross-linked configurations). The nanofibrils conformation, conversely, is hardly recoverable[90].

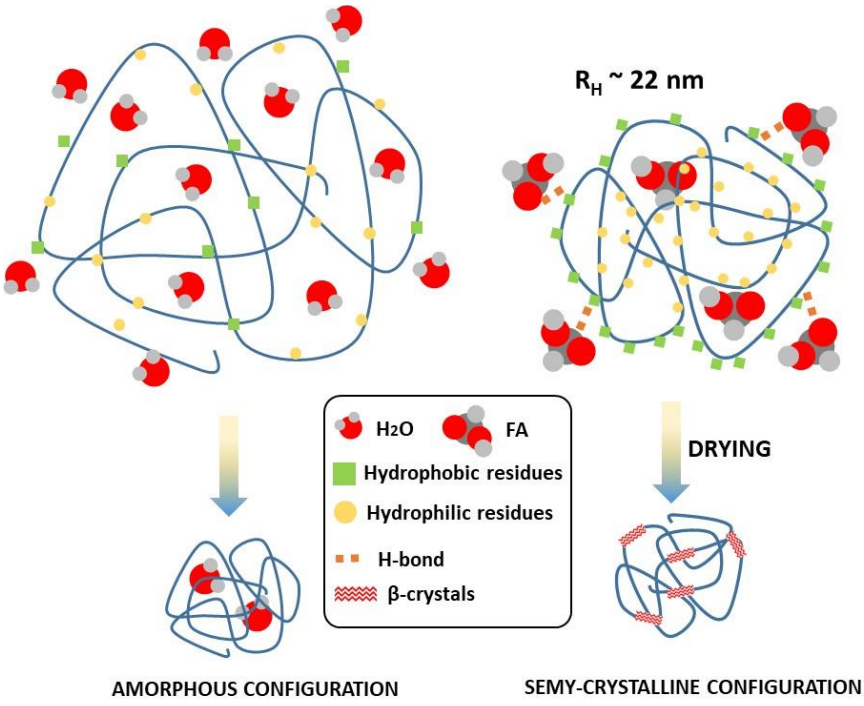

Figure 2. 9. *Silk Fibroin molecular organization under different solution environments: water (left) and formic acid (right)*

2.3.3. REGENERATION

It is named regeneration, to the recovering of the SF secondary structure after its solubilization in a controlled way. Different morphologies of SF can be obtained by following different processing methods. In the following, the most common SF morphologies and how are they obtained is presented.

Film

By simple solvent evaporation, it is possible to obtain SF based 2D structures in the form of film[51,108] (***Figure 2.10***). The standard techniques to achieve this morphology are dry-casting[109], spin-coating[110], layer-by-layer addition[111], and roll-coating[109]. SF concentration, casting temperature, humidity, solution composition, and tuning speed influence the main properties of the film like thickness, crystallinity, mechanical behavior, and optical parameters, among others[23,51,112,113]. Films thickness is highly controllable, and it could vary from a few tens of nanometres to hundreds of microns[23].

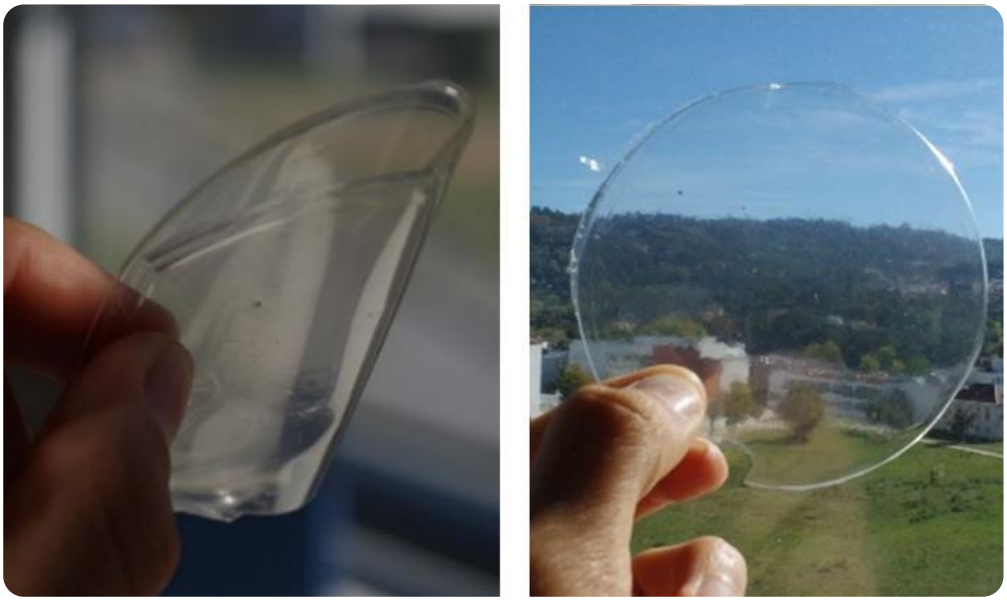

***Figure 2. 10**. SF films with mechanical flexibility and optical transparency.*

In general, the used middle conditions during SF solution casting (room temperature and humidity) results in films with dense and smooth surfaces (roughness below 50 – 60 nm)[114,115], highly transparency (> 90% in the visible region), high refractive index (between 2 and 1 at wavelengths from 500 to 800 nm respectively)[112,113] and interesting wave-guiding properties (~2.8 $dB \cdot mm^{-1}$)[116].

By controlling casting conditions, it is possible to induce changes into films nanostructure[94], increase the ultimate tensile strength[110] and induce mayor β-crystals formation (by using polar solvents or increasing the casting temperature)[117–120].

Crystallinity (β-Sheets content) is one of the more important parameters to control the films' properties since it strongly affects their characteristics. Among the most remarkable effects, it is worth to highlight the influence on water stability, fragility, and mechanical strength.

Gel

As a result of SF precipitation from a poor solvent, a sol-gel transition takes place, where polypeptide macromolecules self-assemble into an interconnected network. The most common and used poor solvent of SF is water. SF aqueous solution is generally obtained when salts from SF aqueous/salts solutions are removed[121]. After SF precipitation, water remains bonded and trapped inside the SF network leading to semi-solid structures named hydrogels[122].

Under middle conditions (room temperature and pressure), the SF aqueous solution's gelation requires long periods, even weeks and months[123]. Nevertheless, variations in concentration and temperature[122], pH[122], the addition of organic and inorganic compounds[124], gases[125], and surfactants[126], could facilitate inter-chains interactions and consequently SF sol-gel transition.

Alcohols are the most commonly used transition throttles, widely used due to their availability, cheapness, and facility to be removed[127,128]. The conformational transition of silk is attributed to alcohol's ability to strip the water molecules that hydrated the packed SF structures, promoting proteins self-interaction and, consequently, forming a cross-linked network. The alcohols induced gelation times are commonly too slow to be applied in fields in which rapid gelation is required. For promoting SF fast gelation, several alternatives have been proposed: i) salts use, such as sodium oleate (SO) and carboxylate salt[129]; ii) redox-type crosslinkers such as epichlorohydrin[130], ethylene glycol diglycidyl ether[131], glutaraldehyde[132], and genipin[133]; iii) enzymatic crosslinkers, such as Tyrosinase[134] and peroxidase [135]; iv) photo-crosslinking [136,137] and v) physical stimulus such us, sonication[138,139], vortexing[140]; freezing-induced self-assemble[141], non-solvent induced phase separation[142], and electrogelation[143].

Fibers – wet spinning

Naturally processed SF fibers are widely used for fabric production. However, their properties and packing mode can be slightly controlled[144]. To regulate these parameters, artificial spinning methods have been developed. The common ones are wet spinning and electrospinning.

Wet spinning is mainly used for obtaining single SF fibers. The process involves extruding a highly concentrated SF solution through a spinneret into a coagulation bath, where SF precipitates, forming one-dimensional fibril structures [144]. The fibers' width can be easily controlled from nanometres to microns, mainly by adapting the spinneret nozzle diameter[145].

Extruding needle dimensions, extruding rate[144] diffusion difference between SF and coagulation bath, and temperature mainly influence the SF final properties of the fibers, e.g., flexibility, water stability, and degradability[146,147].

Concerning the used solvents, spinning from aqueous[144], acidic[147], organic solutions[144], and ionic liquids[107] have been reported. Solvent selection directly defines the coagulation bath

in where SF must be precipitated. To avoid environmentally harmful solvents, fibers from aqueous solutions have been highly studied. In general, the process requires a high SF concentration and the need to add complementary materials to stabilize the solution and avoid SF precipitation (e.g. NaOH addition to increase the total pH and avoid the cross-linked structure formation)[144]. For SF aqueous solutions, the most used coagulation bath is methanol since this solvent favors the formation of crystalline structures and enhanced properties[91,147,148]

Fibers - Electrospinning mats

A mat is a structure formed by non-woven fibers grouped above the others, forming three-dimensional compositions. The quantity of the stacked fiber defines the thickness of the mats. Electrospinning is commonly used to produce the mat. The technique involves applying a high voltage electric field into an SF conductive solution to create a flow that puss the solution through a needle, creating electrically charged microjets (***Figure 2.11***). The jets initially formed by SF solutions are directed through a target and dried during the process, leading to a neat SF fiber, which is collected into the target[149]. When the collector remains static, the fibers are collected in a non-ordered configuration, leading to a mat with fibers in all directions. It is possible to use rotatory collectors to control the fibers' orientation and align them in the rotation direction[150,151] (***Figure 2.11***).

The resulting fibers are cylindrical, uniform, and have smooth surfaces. They also present highly variable diameters from several micrometers to tens of nanometres, depending on the processing conditions[149,152]. These dimensions result in mats with high surface areas per unit mass. Due to the gap formed between deposited fibers, the electrospun SF mats present high porosity values, ranging around 70-75 %[149,153] and with cavities ranging from few nanometers to hundreds of microns[152].

Organic, acidic, and aqueous solvents have been used in non-woven electrospinning mats processing[96,154,155]. The most used one is the formic acid/SF solution, probably due to its high stability, that is of great importance during the time-consuming electrospinning process (hours and even days)[153,154]. As in the wet spinning, some works have focused on SF electrospinning from aqueous solutions[99]but similar difficulties have been found in both cases.

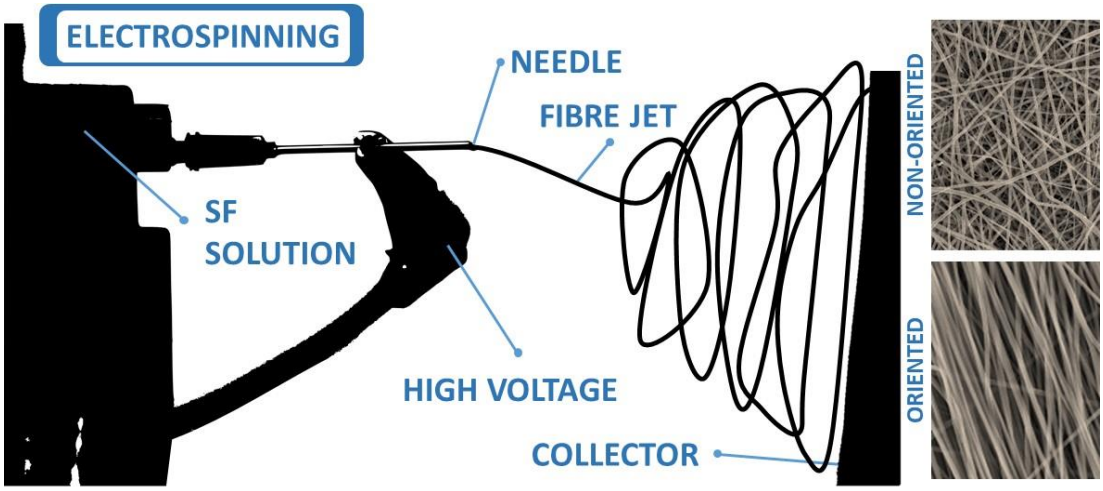

Figure 2. 11. *Graphic representation of electrospinning and SF non-woven mats.*

Porous structures

Three-dimensional structures with high surface area, low density, interconnected internal core, controllable pore characteristics, and able to be processed in a mold can be obtained by inducing pores into SF. Several techniques are available to induce pores in SF, each one with specific implications over final structures[156–158].

i. ***Freeze-drying*** is based on removing the solvent from the SF solution, avoiding the structure's collapse, to get a foamy material where pores are the regions first occupied by solvent (***Figure 2.12***). The process is commonly carried out by freeze-drying, where the solvent is previously frozen and then sublimated under low pressures. Due to solvents' compatibility with the equipment and process facility, freeze-drying is mostly carried out with water as a solvent.

   The use of supercritical CO_2 opens the possibility to develop highly porous structures (90-99% of porosity), with density values around 50 – 60 $mg \cdot ml^{-1}$ and large surface areas (above 400 $m^2 \cdot g^{-1}$) named aerogels [159–161].

ii. ***Porogens*****:** This technique consists of using a material as a sacrificial phase to induce pores into the SF based structure (***Figure 2.12***). The main advantage of this method is the control of pores size and shape, the high porosity level, the facility of processing, and the possibility to use templates. The material final behavior is influenced by SF-porogen relation, solvent, SF concentration, porogens nature, shape, size, content, and templates shape. The more commonly used solvents are aqueous solutions, hexafluoroisopropanol

(HFIP), and FA [162–164]. Sugar crystals and paraffin beads have been used as porogens, although the most commonly used materials to induce porous into SF are salts[158,165,166]. NaCl crystals are the most used ones due to their accessibility, low environmental impact, and facility to be dissolved by water, commonly named salt leaching[162,163]. An alternative way to promote pores into SF structures is by using a sacrificial phase printed by 3D devices[167].

iii. ***Gas foaming:*** This alternative is based on inducing pores by decompressing a highly volatile material diffused in a SF solution[158] (***Figure 2.12***). This method allows the processing of highly porous structures (porosity > 90 %) directly injected in a cavity in a single step. Ammonium bicarbonate particles have been used as volatile materials[158]. However, the most promising method consists of using N_2O gas mixed with SF aqueous solution into a container with a valve to inject the solution directly[168]. In this way, the gas has a double function. On the one hand, it acts as a pressurizing agent and, on the other hand, as a pore inducer.

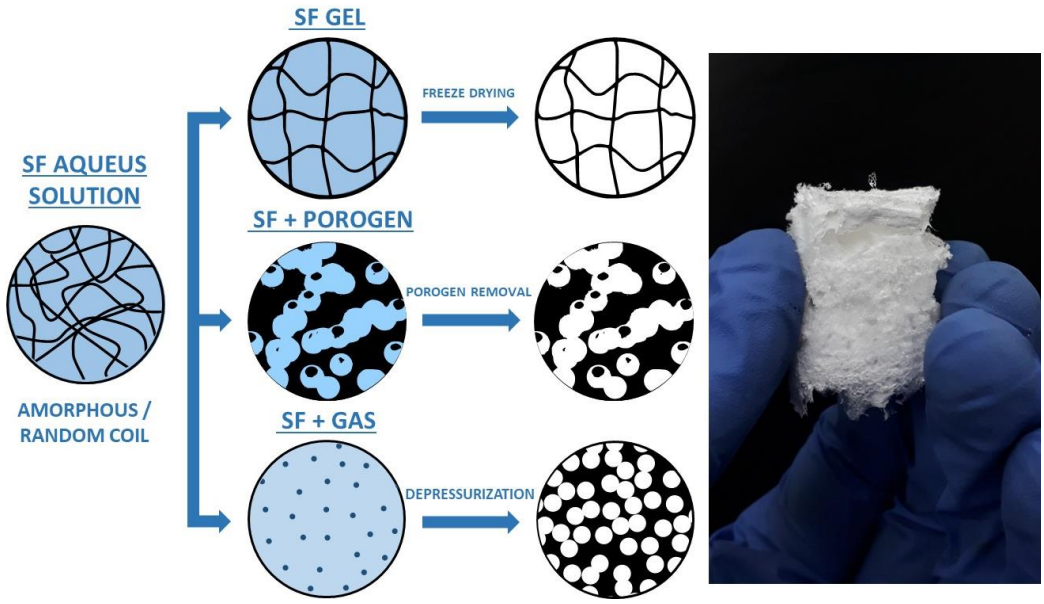

Figure 2. 12. *Left: Scheme of the main techniques to produce SF porous structures. Right: macroscopic appearance of porous SF structures.*

SF particles

Reducing the size of materials represents an interesting field where one material's properties could be expanded to serve in new advanced uses. The main techniques focused on reducing SF materials to microparticles are:

i. **Powdering:** mainly consist of milling and crushing SF solid structures to get micro- and nanoscaled particles. It represents a simple method to obtain small-sized SF structures, commonly ranging between 1-4 μm, depending on milling conditions[169,170]. Due to the low control over the final particles' shape, SF powder generally shows irregular forms with rough surfaces[169,171,172] and displays a high ability to absorb enzymes and for drugs immobilization[171,173].

ii. **Micro/nanospheres** formation is based on carrying the SF original structures into micro and nanoscale by inducing the collapse of solubilized SF into non-solvent[170]. Unlike the wet fiber production, the spheres are induced from low concentrated SF solutions, which lead to non-continuous SF precipitation and, thus, in spheres formation. In general, SF nanospheres from 100 to 400 nm can be obtained[174,175]. The chemical procedures give significant control over particle size, shape, and properties[173]. To induce the desired shape, fast mixing or dropwise mixing and mechanical stirring have been used[173–175]. The obtained spheres are commonly collected by centrifugation.

iii. **Spray drying:** This procedure is based on spraying a SF solution in the air to promote solvent evaporation and origin micrometric SF structures with spherical shape[170]. The spheres are commonly obtained from low concentrated solutions, and in order to allow the complete solvent evaporation, high temperatures are usually used[176]. The principal limitation of this technique is the requirement of a solution without any solid impurities since it could plug the spray nozzle and hinder the process.

iv. **Jet break-up** is based on using a vibrating nozzle at a controlled frequency and amplitude to dispense in a controlled way dissolved SF drops, which are shock-frozen in a liquid nitrogen bath and then freeze dried[170]. Obtained particles are spherical and show a size ranging between 100 μm to 440 μm, depending on the nozzle's diameter. All the spheres show a high porosity level[177].

2.3.4. POST PROCESSING

It is known as post-processing or post-treatment, the set of techniques used to modify SF materials' properties once the other processing steps (degumming, solution, and regeneration) have concluded. Most post-treatments are focused on inducing the transformation of random coils and α-helix into crystalline β-Sheets. The most common post-treatments are:

i. ***Polar organic solvents immersion:*** This is the most used technique and consists of the immersion of SF based materials into a selected organic solvent to induce the transition of the random coil, α-helix, or silk I structure into more stable β-crystals. The most used organic solvents are EtOH and MetOH, mainly because of their accessibility, obtained high conversion ratios (from amorphous to crystalline), rapid transformation (< 30 s), higher hydrophobicity of the samples, and the ability to achieve sterilized samples[145,178,179].

   The SF secondary structure transition promoted by EtOH and MetOH can be described as the result of two complementary processes induced by the solvents high polarity of the solvents. Unlike FA, an alternative polar solvent is also used to promote SF crystalline structures, EtOH and MetOH do not break the SF H-bonds. On the contrary, these alcohols penetrate the SF structure to form new H-bonds with free SF polar residues. The penetration of the organic molecule inside the polypeptide increases the free volume and plasticizes the structure to give to the SF molecules increased mobility for molecular readjustments. This mobility leads to the molecules to adopt the minimum energy conformation, which is the crystalline β-Sheets. Despite adopting the β-Sheets organization, the crystalline units are not completely formed since the organic solvent molecules, and even the remaining water molecules hinder the hydrophobic interactions. During the drying process, the solvents (both polar solvents and water) leave the structure together because of the polar interactions between them, giving the SF free of plasticizing molecules. This SF dehydration derives into an increase of hydrophobic interactions, which lead to chains packing and crystalline domains increase[180]. Due to the strong influence of polarity during this process, the hydrophilic/hydrophobic balance becomes the main parameter. In general, it has been found that EtOH or MetOH concentration around 40– 60% (w/w) (solvent/water) is the most effective relation[180].

ii. ***Stretching***: This technique consists of elongated and aligned SF structures through physical spinning or stretching. The process enhances the chain's packing and the growth of silk II structures in the elongation direction. As a result, mechanical properties about five times higher than those of the original materials are obtained[97,181]. Due to the SF limited elongation ability, stretching is commonly carried out in wet material, enabling the stretch even of 200% of original size [97].

iii. ***Water vapor treatment*** offers a simple and green approach to control the molecular structure of silk biomaterials. Only by annealing the SF structures above their T_g in the

presence of water vapor leads to i) the plasticization of SF due to water penetration and ii) enough thermal energy for large-scale molecular motions[60,182]. As a result, polypeptide structures pack into crystalline domains, reaching crystallinity values up to 60%. At high vapor temperatures, silk II rich structures are obtained, while low-temperature conditions (around 4 °C) lead to α-helix dominated silk I structure[60]. Due to hot water vapor self-ability to avoid microorganisms grow, sterilized samples are obtained [23,183].

iv. ***Thermal annealing*** allows the evaporation of the water inside SF structures. It provides molecular mobility for the self- assembly of hydrophobic domains into a more crystalline structure, rich in β-Sheets. The process requires long times (12 – 24 h) to produce a completely water-stable structure[184]. During this treatment, globular structures are formed, and this generates topographical changes on the surface, influencing the surface nanotopography and increasing the average surface roughness (Ra)[184,185]

2.4. REFERENCES

1. Peng, Z. *et al.* Structural and Mechanical Properties of Silk from Different Instars of Bombyx mori. *Biomacromolecules* **20**, 1203–1216 (2019).
2. Roy, M. *et al.* Carbondioxide gating in silk cocoon. *Biointerphases* **7**, 1–11 (2012).
3. Tulachan, B. *et al.* Electricity from the silk cocoon membrane. *Sci. Rep.* **4**, 38–42 (2014).
4. Zhang, J., Rajkhowa, R., Li, J. L., Liu, X. Y. & Wang, X. G. Silkworm cocoon as natural material and structure for thermal insulation. *Mater. Des.* **49**, 842–849 (2013).
5. Pérez-Rigueiro, J., Viney, C., Llorca, J. & Elices, M. Mechanical properties of single-brin silkworm silk. *J. Appl. Polym. Sci.* **75**, 1270–1277 (2000).
6. Asakura, T., Okushita, K. & Williamson, M. P. Analysis of the Structure of Bombyx mori Silk Fibroin by NMR. (2015) doi:10.1021/acs.macromol.5b00160.
7. Chen, S., Liu, M., Huang, H., Cheng, L. & Zhao, H. Mechanical properties of Bombyx mori silkworm silk fi bre and its corresponding silk fi broin fi lament : A comparative study. **181**, 1–11 (2019).
8. Hardy, J. G. & Scheibel, T. R. Composite materials based on silk proteins. *Prog. Polym. Sci.* **35**, 1093–1115 (2010).
9. Lalit Jajpura, A. R. The Biopolymer Sericin: Extraction and Applications. *J. Text. Sci. Eng.* **05**, 1–5 (2015).
10. Zafar, M. S. & Al-Samadani, K. H. Potential use of natural silk for bio-dental applications. *Journal of Taibah University Medical Sciences* vol. 9 171–177 (2014).
11. Zhu, B. *et al.* Silk Fibroin for Flexible Electronic Devices. *Adv. Mater.* **28**, 4250–4265 (2016).
12. Du, S. *et al.* Interactions between fibroin and sericin proteins from Antheraea pernyi and Bombyx mori silk fibers. *J. Colloid Interface Sci.* **478**, 316–323 (2016).
13. Aramwit, P., Kanokpanont, S., Nakpheng, T. & Srichana, T. The Effect of Sericin from Various Extraction Methods on Cell Viability and Collagen Production. *Int. J. Mol. Sci.* **11**, 2200–2211 (2010).
14. Lloyd-Williams, P., Albericio, F. & Giralt, E. *Chemical Approaches to the Synthesis of Peptides and Proteins*. *Chemical Approaches to the Synthesis of Peptides and Proteins* (CRC Press, 2020). doi:10.1201/9781003069225.
15. McKay, F. C. & Albertson, N. F. New Amine-masking Groups for Peptide Synthesis. *J. Am. Chem. Soc.* **79**, 4686–4690 (1957).
16. Wang, H. *et al.* Ultra-Lightweight Resistive Switching Memory Devices Based on Silk Fibroin. *Small* **12**, 3360–3365 (2016).
17. Wang, C.-H., Hsieh, C.-Y. & Hwang, J.-C. Flexible Organic Thin-Film Transistors with Silk Fibroin as the Gate Dielectric. *Adv. Mater.* **23**, 1630–1634 (2011).
18. Cheung, H., Ho, M. & Cardona, F. Natural fibre-reinforced composites for bioengineering and environmental engineering applications. *Compos. Part B Eng.* **40**, 655–663 (2009).
19. Perez-Rigueiro, J., Viney, C., Llorca, J. & Elices, M. Silkworm silk as an engineering material. *J. Appl. Polym. Sci.* **70**, 2439–2447 (1998).
20. Larson, J. D. *et al.* Enhanced actuation performance of silk-polypyrrole composites. *Mater. Chem. Phys.* **186**, 67–74 (2017).
21. Kaur, J. *et al.* Photoprotection by silk cocoons. *Biomacromolecules* **14**, 3660–3667 (2013).
22. Leem, J. W., Fraser, M. J. & Kim, Y. L. Transgenic and Diet-Enhanced Silk Production for Reinforced Biomaterials: A Metamaterial Perspective. *Annu. Rev. Biomed. Eng.* **22**, 79–102 (2020).
23. Lawrence, B. D., Omenetto, F., Chui, K. & Kaplan, D. L. Processing methods to control silk fibroin film biomaterial features. *J. Mater. Sci.* **43**, 6967–6985 (2008).
24. Koh, L. D. *et al.* Structures, mechanical properties and applications of silk fibroin materials. *Prog.*

Polym. Sci. **46**, 86–110 (2015).

25. Kundu, B. *et al.* Silk proteins for biomedical applications: Bioengineering perspectives. *Prog. Polym. Sci.* **39**, 251–267 (2014).
26. Fukada, E. Piezoelectricity of biopolymers. *Biorheology* **32**, 593–609 (1995).
27. Joseph, J., Singh, S. G., Rama, S. & Vanjari, K. Piezoelectric Micromachined Ultrasonic Transducer Using Silk Piezoelectric Thin Film. **39**, 2018–2021 (2018).
28. Yucel, T., Cebe, P. & Kaplan, D. L. Structural Origins of Silk Piezoelectricity. *Adv. Funct. Mater.* **21**, 779–785 (2011).
29. ANDO, Y. *et al.* Piezoelectricity of oriented silk fibroin films. *Work. Electr. Charg. Dielectr.* (1978).
30. Koh, L.-D. *et al.* Structures, mechanical properties and applications of silk fibroin materials. *Prog. Polym. Sci.* **46**, 86–110 (2015).
31. Wideman, T. H., Zautra, A. J. & Edwards, R. R. New Opportunities for an Ancient Material. **154**, 2262–2265 (2014).
32. Min, K., Kim, S. & Kim, S. Silk protein nanofibers for highly efficient , eco-friendly , optically translucent , and multifunctional air filters. 1–10 (2018) doi:10.1038/s41598-018-27917-w.
33. Rockwood, D. N. *et al.* Materials fabrication from Bombyx mori silk fibroin. *Nat. Protoc.* **6**, 1612–1631 (2011).
34. Inoue, S. *et al.* Silk fibroin of Bombyx mori is secreted, assembling a high molecular mass elementary unit consisting of H-chain, L-chain, and P25, with a 6:6:1 molar ratio. *J. Biol. Chem.* **275**, 40517–40528 (2000).
35. Zhou, C. Z. *et al.* Silk fibroin: Structural implications of a remarkable amino acid sequence. *Proteins Struct. Funct. Genet.* **44**, 119–122 (2001).
36. Yamaguchi, K. *et al.* Primary structure of the silk fibroin light chain determined by cDNA sequencing and peptide analysis. *J. Mol. Biol.* **210**, 127–139 (1989).
37. Chevillard, M., Couble, P. & Prudhomme, J. C. Complete nucleotide sequence of the gene encoding the Bombyx mori silk protein P25 and predicted amino acid sequence of the protein. *Nucleic Acids Res.* **14**, 6341–6342 (1986).
38. Ha, S., Gracz, H. S., Tonelli, A. E. & Hudson, S. M. Structural Study of Irregular Amino Acid Sequences in the Heavy Chain of Bombyx mori Silk Fibroin. 2563–2569 (2005).
39. Zhou, C. *et al.* Fine organization of Bombyx mori fibroin heavy chain gene. **28**, 2413–2419 (2000).
40. Koh, L. D. *et al.* Structures, mechanical properties and applications of silk fibroin materials. *Progress in Polymer Science* vol. 46 86–110 (2015).
41. Huang, Y., Zou, Q., Jia, X. & Ming, S. Differential Expression of microRNA 2b with Potential Target Coding P25 in the Fifth Instar Larvae Posterior Silk Gland of the Silkworm 1. *Mol. Biol.* **45**, 576–581 (2011).
42. Liu, W. *et al.* Precise Protein Photolithography (P 3): High Performance Biopatterning Using Silk Fibroin Light Chain as the Resist. **1700191**, (2017).
43. Tanaka, K., Kajiyama, N., Ishikura, K. & Waga, S. Determination of the site of disul ¢ de linkage between heavy and light chains of silk ¢ broin produced by Bombyx mori. **1432**, 92–103 (1999).
44. Tanaka, K., Inoue, S. & Mizuno, S. Hydrophobic interaction of P25 , containing Asn-linked oligosaccharide chains , with the H-L complex of silk fibroin produced by Bombyx mori. **29**, 269–276 (1999).
45. Drummy, L. F., Farmer, B. L. & Naik, R. R. Correlation of the β-sheet crystal size in silk fibers with the protein amino acid sequence. *Soft Matter* **3**, 877–882 (2007).
46. Lefèvre, T., Rousseau, M. E. & Pézolet, M. Protein secondary structure and orientation in silk as revealed by Raman spectromicroscopy. *Biophys. J.* **92**, 2885–2895 (2007).
47. Salemme, F. R. Structural properties of protein β-sheets. *Prog. Biophys. Mol. Biol.* **42**, 95–133 (1983).

48. Naik, R. R., Drummy, L. F., Phillips, D. M., Stone, M. O. & Farmer, B. L. Thermally Induced α-Helix to β-Sheet Transition in Regenerated Silk Fibers and Films. *Biomacromolecules* **6**, 3328–3333 (2005).

49. Kratky, O., Schauenstein, E. & Sekora, A. A new type of lattice with large periods in silk. *Nature* **165**, 527–528 (1950).

50. Kaplan, D. L. *et al.* Silk I and Silk II studied by fast scanning calorimetry. *Acta Biomater.* **55**, 323–332 (2017).

51. Jin, H. J. *et al.* Water-stable silk films with reduced β-sheet content. *Adv. Funct. Mater.* **15**, 1241–1247 (2005).

52. Cebe, P. *et al.* Water-insoluble silk films with silk I structure. *Acta Biomater.* **6**, 1380–1387 (2009).

53. Iizuka, E. Species specificity of the conformation of silk fibroin in solution. *BBA - Protein Struct.* **160**, 454–463 (1968).

54. He, S. J., Valluzzi, R. & Gido, S. P. Silk I structure in Bombyx mori silk foams. in *International Journal of Biological Macromolecules* vol. 24 187–195 (Elsevier, 1999).

55. Lu, S. *et al.* The influence of the hydrophilic-lipophilic environment on the structure of silk fibroin protein. *J. Mater. Chem. B* **3**, 2599–2606 (2015).

56. Ming, J., Pan, F. & Zuo, B. Influence factors analysis on the formation of silk I structure. *Int. J. Biol. Macromol.* **75**, 398–401 (2015).

57. Hernández Cruz, D., Rousseau, M. E., West, M. M., Pézolet, M. & Hitchcock, A. P. Quantitative mapping of the orientation of fibroin β-sheets in B. mori cocoon fibers by scanning transmission X-ray microscopy. *Biomacromolecules* **7**, 836–843 (2006).

58. Dal Pra, I., Chiarini, A., Boschi, A., Freddi, G. & Armato, U. Novel dermo-epidermal equivalents on silk fibroin-based formic acid-crosslinked three-dimensional nonwoven devices with prospective applications in human tissue engineering/regeneration/repair. *Int. J. Mol. Med.* **18**, 241–247 (2006).

59. Zhou, J. *et al.* Regenerated Silk Fibroin Films with Controllable Nanostructure Size and Secondary Structure for Drug Delivery. (2014) doi:10.1021/am502278b.

60. Hu, X. *et al.* Regulation of silk material structure by temperature-controlled water vapor annealing. *Biomacromolecules* **12**, 1686–1696 (2011).

61. Valluzzi, R., Gido, S. P., Muller, W. & Kaplan, D. L. Orientation of silk III at the air-water interface. **24**, 237–242 (1999).

62. Minoura, N., Tsukada, M. & Nagura, M. Fine structure and oxygen permeability of silk fibroin membrane treated with methanol. *Polymer (Guildf).* **31**, 265–269 (1990).

63. Takahashi, Y., Gehoh, M. & Yuzuriha, K. Structure refinement and diffuse streak scattering of silk (Bombyx mori). **24**, 127–138 (1999).

64. Xu, G., Gong, L., Yang, Z. & Liu, X. Y. What makes spider silk fibers so strong? from molecular-crystallite network to hierarchical network structures. *Soft Matter* **10**, 2116–2123 (2014).

65. Li, G., Liu, H., Li, T. & Wang, J. Surface modification and functionalization of silk fibroin fibers/fabric toward high performance applications. *Mater. Sci. Eng. C* **32**, 627–636 (2012).

66. Jiang, P. *et al.* Tensile behavior and morphology of differently degummed silkworm (Bombyx mori) cocoon silk fibres. **60**, 919–925 (2006).

67. Zhong, J. *et al.* Self-assembly of regenerated silk fibroin from random coil nanostructures to antiparallel β-sheet nanostructures. *Biopolymers* **101**, 1181–1192 (2014).

68. Cao, T. T., Wang, Y. J. & Zhang, Y. Q. Effect of Strongly Alkaline Electrolyzed Water on Silk Degumming and the Physical Properties of the Fibroin Fiber. *PLoS One* **8**, (2013).

69. Ki, C. S., Um, I. C. & Park, Y. H. Acceleration effect of sericin on shear-induced β-transition of silk fibroin. *Polymer (Guildf).* **50**, 4618–4625 (2009).

70. Allardyce, B. J. *et al.* The impact of degumming conditions on the properties of silk films for biomedical applications. *Text. Res. J.* **86**, 275–287 (2016).

71. Production method of water soluble sericin. (2003).

72. Teh, T. K. H., Toh, S. L. & Goh, J. C. H. Optimization of the silk scaffold sericin removal process for retention of silk fibroin protein structure and mechanical properties. *Biomed. Mater.* **5**, (2010).

73. Wang, Z., Yang, H., Li, W. & Li, C. Effect of silk degumming on the structure and properties of silk fibroin. *J. Text. Inst.* **110**, 134–140 (2019).

74. Nakpathom, M., Somboon, B. & Narumol, N. *Papain enzymatic degumming of thai Bombyx mori silk fibers. Journal of Microscopy Society of Thailand* vol. 23 https://www.researchgate.net/publication/228483054 (2009).

75. Cao, T. T. & Zhang, Y. Q. Processing and characterization of silk sericin from Bombyx mori and its application in biomaterials and biomedicines. *Mater. Sci. Eng. C* **61**, 940–952 (2016).

76. Kim, J., Kwon, M. Y. & Kim, S. Biological Degumming of Silk Fabrics with Proteolytic Enzymes. *J. Nat. Fibers* **13**, 629–639 (2016).

77. Dou, H. & Zuo, B. Effect of sodium carbonate concentrations on the degumming and regeneration process of silk fibroin. *J. Text. Inst.* **106**, 311–319 (2015).

78. Yamada, H., Nakao, H., Takasu, Y. & Tsubouchi, K. Preparation of undegraded native molecular fibroin solution from silkworm cocoons. *Mater. Sci. Eng. C* **14**, 41–46 (2001).

79. Xu, W., Wu, Z. & Tao, S. Urea-Based Fuel Cells and Electrocatalysts for Urea Oxidation. *Energy Technology* vol. 4 1329–1337 (2016).

80. Hamonts, K. *et al.* Influence of soil bulk density and matric potential on microbial dynamics, inorganic N transformations, N2O and N2 fluxes following urea deposition. *Soil Biol. Biochem.* **65**, 1–11 (2013).

81. Hu, X. *et al.* Determining Beta Sheet Crystallinity in Fibrous Proteins by Thermal Analysis and Infrared Spectroscopy. *APS* J34.010 (2007).

82. Lee, J. H., Song, D. W., Park, Y. H. & Um, I. C. Effect of residual sericin on the structural characteristics and properties of regenerated silk films. *Int. J. Biol. Macromol.* **89**, 273–278 (2016).

83. Wang, H. Y. & Zhang, Y. Q. Effect of regeneration of liquid silk fibroin on its structure and characterization. *Soft Matter* **9**, 138–145 (2013).

84. Gupta, D., Agrawal, A., Chaudhary, H., Gulrajani, M. & Gupta, C. Cleaner process for extraction of sericin using infrared. *J. Clean. Prod.* **52**, 488–494 (2013).

85. Long, J. J., Wang, H. W., Lu, T. Q., Tang, R. C. & Zhu, Y. W. Application of low-pressure plasma pretreatment in silk fabric degumming process. *Plasma Chem. Plasma Process.* **28**, 701–713 (2008).

86. Lo, C.-H. & Chao, Y. Degumming of Silk Fibers by CO2 Supercritical Fluid. *J. Mater. Sci. Chem. Eng.* **05**, 1–8 (2017).

87. Wang, R. *et al.* Degumming of raw silk via steam treatment. *J. Clean. Prod.* **203**, 492–497 (2018).

88. Structure and solubility of natural silk fibroin. *Russ. J. Appl. Chem.* **79**, 869–876 (2006).

89. Shen, T. *et al.* Dissolution behavior of silk fibroin in a low concentration CaCl2-methanol solvent: Frommorphology to nanostructure. *Int. J. Biol. Macromol.* **113**, 458–463 (2018).

90. Ling, S. *et al.* Polymorphic regenerated silk fibers assembled through bioinspired spinning. *Nat. Commun.* **8**, (2017).

91. Zhao, C., Yao, J., Masuda, H., Kishore, R. & Asakura, T. Structural characterization and artificial fiber formation ofBombyx mori silk fibroin in hexafluoro-iso-propanol solvent system. *Biopolymers* **69**, 253–259 (2003).

92. Yao, J., Masuda, H., Zhao, C. & Asakura, T. Artificial spinning and characterization of silk fiber from bombyx mori silk fibroin in hexafluoroacetone hydrate. *Macromolecules* **35**, 6–9 (2002).

93. Shen, T. *et al.* Dissolution behavior of silk fibroin in a low concentration CaCl2-methanol solvent: From morphology to nanostructure. *Int. J. Biol. Macromol.* **113**, 458–463 (2018).

94. Zhou, J. *et al.* Regenerated silk fibroin films with controllable nanostructure size and secondary structure for drug delivery. *ACS Applied Materials and Interfaces* vol. 6 21813–21821 (2014).

95. Zhang, H. *et al.* Preparation and characterization of silk fibroin as a biomaterial with potential for drug delivery. 1–9 (2012).

96. Pignatelli, C. *et al.* Electrospun silk fibroin fibers for storage and controlled release of human platelet lysate. *Acta Biomater.* **73**, 365–376 (2018).

97. Lu, Q. *et al.* Silk self-assembly mechanisms and control from thermodynamics to kinetics. *Biomacromolecules* **13**, 826–832 (2012).

98. Cho, H. J., Ki, C. S., Oh, H., Lee, K. H. & Um, I. C. Molecular weight distribution and solution properties of silk fibroins with different dissolution conditions. *Int. J. Biol. Macromol.* **51**, 336–341 (2012).

99. Kishimoto, Y., Kobashi, T., Yamanaka, S. & Morikawa, H. Comparisons Between Silk Fibroin Non-Woven Fabrics Electrospun Using Aqueous and Formic Acid Solution. **4037**, 0–21 (2017).

100. Zhang, X. *et al.* Production of silk sericin/silk fibroin blend nanofibers. *Nanoscale Res. Lett.* **6**, 1–8 (2011).

101. Um, I. C., Kweon, H. Y., Lee, K. G. & Park, Y. H. The role of formic acid in solution stability and crystallization of silk protein polymer. *Int. J. Biol. Macromol.* **33**, 203–213 (2003).

102. Um, I. C., Kweon, H. Y., Park, Y. H. & Hudson, S. Structural characteristics and properties of the regenerated silk fibroin prepared from formic acid. *Int. J. Biol. Macromol.* **29**, 91–97 (2001).

103. Yue, X. *et al.* A novel route to prepare dry-spun silk fibers from CaCl2-formic acid solution. *Mater. Lett.* **128**, 175–178 (2014).

104. Lozano-Pérez, A. A. *et al.* Production of silk fibroin nanoparticles using ionic liquids and high-power ultrasounds. *J. Appl. Polym. Sci.* **132**, 1–8 (2015).

105. Xie, H. & Li, S. Chitin and chitosan dissolved in ionic liquids as reversible sorbents of CO 2 {. 630–633 (2006) doi:10.1039/b517297g.

106. Silva, S. S. *et al.* Silk hydrogels from non-mulberry and mulberry silkworm cocoons processed with ionic liquids. *Acta Biomater.* **9**, 8972–8982 (2013).

107. Phillips, D. M. *et al.* Regenerated silk fiber wet spinning from an ionic liquid solution. 4206–4208 (2005) doi:10.1039/b510069k.

108. Rujiravanit, R., Kruaykitanon, S., Jamieson, A. M. & Tokura, S. Preparation of Crosslinked Chitosan/Silk Fibroin Blend Films for Drug Delivery System. *Macromol. Biosci.* **3**, 604–611 (2003).

109. Jia, X. *et al.* A Biodegradable Thin-Film Magnesium Primary Battery Using Silk Fibroin-Ionic Liquid Polymer Electrolyte. *ACS Energy Lett.* **2**, 831–836 (2017).

110. Jiang, B. C. *et al.* Mechanical Properties of Robust Ultrathin Silk Fibroin Films **. 2229–2237 (2007) doi:10.1002/adfm.200601136.

111. Huang, L., Li, C., Yuan, W. & Shi, G. Strong composite films with layered structures prepared by casting silk fibroin-graphene oxide hydrogels. *Nanoscale* **5**, 3780–3786 (2013).

112. Lee, M., Jeon, H. & Kim, S. A highly tunable and fully biocompatible silk nanoplasmonic optical sensor. *Nano Lett.* **15**, 3358–3363 (2015).

113. Asha, S., Sangappa, Y. & Ganesh, S. Tuning the refractive index and optical band gap of silk fibroin films by electron irradiation. *J. Spectrosc.* **2015**, (2015).

114. Qin, X. *et al.* Silk fibroin and ultra-long silver nanowire based transparent, flexible and conductive composite film and its Temperature-Dependent resistance. *Int. J. Optomechatronics* **13**, 41–50 (2019).

115. Zhang, X. *et al.* Thiolation and characterization of regenerated Bombyx mori silk fibroin films with reduced glutathione. *BMC Chem.* **13**, 1–9 (2019).

116. Kujala, S., Mannila, A., Karvonen, L., Kieu, K. & Sun, Z. Natural Silk as a Photonics Component : a Study on Its Light Guiding and Nonlinear Optical Properties. *Nat. Publ. Gr.* 1–9 (2016) doi:10.1038/srep22358.

117. Motta, A., Fambri, L. & Migliaresi, C. Regenerated silk fibroin films: Thermal and dynamic mechanical analysis. *Macromol. Chem. Phys.* **203**, 1658–1665 (2002).

118. Peng, Q., Shao, H., Hu, X. & Zhang, Y. Role of humidity on the structures and properties of regenerated silk fibers. *Prog. Nat. Sci. Mater. Int.* **25**, 430–436 (2015).

119. Hu, X., Kaplan, D. & Cebe, P. Effect of water on the thermal properties of silk fibroin. *Thermochim. Acta* **461**, 137–144 (2007).

120. Reizabal, A. *et al.* Optimized silk fibroin piezoresistive nanocomposites for pressure sensing applications based on natural polymers. *Nanoscale Adv.* **1**, 2284–2292 (2019).

121. Xiong, R., Grant, A. M., Ma, R., Zhang, S. & Tsukruk, V. V. Naturally-derived biopolymer nanocomposites: Interfacial design, properties and emerging applications. *Materials Science and Engineering R: Reports* vol. 125 1–41 (2018).

122. Matsumoto, A. *et al.* Mechanisms of silk fibroin sol-gel transitions. *J. Phys. Chem. B* **110**, 21630–21638 (2006).

123. Yin, Z. *et al.* A silk fibroin hydrogel with reversible sol-gel transition. *RSC Adv.* **7**, 24085–24096 (2017).

124. Im, D., Kim, M., Yoon, Y. & Park, W. Gelation Behaviors and Mechanism of Silk Fibroin According to the Addition of Nitrate Salts. *Int. J. Mol. Sci.* **17**, 1697 (2016).

125. Floren, M. L., Spilimbergo, S., Motta, A. & Migliaresi, C. Carbon dioxide induced silk protein gelation for biomedical applications. *Biomacromolecules* **13**, 2060–2072 (2012).

126. Wu, X. *et al.* Sodium dodecyl sulfate-induced rapid gelation of silk fibroin. *Acta Biomater.* **8**, 2185–2192 (2012).

127. Kaewprasit, K., Kobayashi, T. & Damrongsakkul, S. Thai silk fibroin gelation process enhancing by monohydric and polyhydric alcohols. *Int. J. Biol. Macromol.* **118**, 1726–1735 (2018).

128. Yao, M., Su, D., Wang, W., Chen, X. & Shao, Z. Fabrication of Air-Stable and Conductive Silk Fibroin Gels. *ACS Appl. Mater. Interfaces* **10**, 38466–38475 (2018).

129. Yang, Y. *et al.* Sodium oleate induced rapid gelation of silk fibroin. *J. Biomater. Sci. Polym. Ed.* **29**, 1219–1231 (2018).

130. Lee, M. S., Seo, S. R. & Kim, J. C. A β-cyclodextrin, polyethyleneimine and silk fibroin hydrogel containing Centella asiatica extract and hydrocortisone acetate: Releasing properties and in vivo efficacy for healing of pressure sores. *Clin. Exp. Dermatol.* **37**, 762–771 (2012).

131. Ak, F., Oztoprak, Z., Karakutuk, I. & Okay, O. Macroporous silk fibroin cryogels. *Biomacromolecules* **14**, 719–727 (2013).

132. Srisawasdi, T., Petcharoen, K., Sirivat, A. & Jamieson, A. M. Electromechanical response of silk fibroin hydrogel and conductive polycarbazole/silk fibroin hydrogel composites as actuator material. *Mater. Sci. Eng. C* **56**, 1–8 (2015).

133. Elliott, W. H. *et al.* Silk Hydrogels of Tunable Structure and Viscoelastic Properties Using Different Chronological Orders of Genipin and Physical Cross-Linking. *ACS Appl. Mater. Interfaces* **7**, 12099–12108 (2015).

134. Das, S. *et al.* Bioprintable, cell-laden silk fibroin-gelatin hydrogel supporting multilineage differentiation of stem cells for fabrication of three-dimensional tissue constructs. *Acta Biomater.* **11**, 233–246 (2015).

135. Partlow, B. P. *et al.* Highly tunable elastomeric silk biomaterials. *Adv. Funct. Mater.* **24**, 4615–4624 (2014).

136. Kim, H. H., Kim, J. W., Choi, J., Park, Y. H. & Ki, C. S. Characterization of silk hydrogel formed with hydrolyzed silk fi broin- methacrylate via photopolymerization. **153**, 232–240 (2018).

137. Applegate, M. B. *et al.* Photocrosslinking of Silk Fibroin Using Riboflavin for Ocular Prostheses. *Adv. Mater.* **28**, 2417–2420 (2016).

138. Wölfl, M., Kuball, J., Eyrich, M., Schlegel, P. G. & D, P. Sonication-Induced Gelation of Silk Fibroin for Cell Encapsulation. *Cytometry* **73**, 1043–1049 (2009).

139. Su, D., Jiang, L., Chen, X., Dong, J. & Shao, Z. Enhancing the Gelation and Bioactivity of Injectable

Silk Fibroin Hydrogel with Laponite Nanoplatelets. *ACS Appl. Mater. Interfaces* **8**, 9619–9628 (2016).

140. Yucel, T., Cebe, P. & Kaplan, D. L. Vortex-induced injectable silk fibroin hydrogels. *Biophys. J.* **97**, 2044–2050 (2009).

141. Li, X. *et al.* Soft freezing-induced self-assembly of silk fibroin for tunable gelation. *Int. J. Biol. Macromol.* **117**, 691–695 (2018).

142. Kasoju, N., Hawkins, N., Pop-Georgievski, O., Kubies, D. & Vollrath, F. Silk fibroin gelation via non-solvent induced phase separation. *Biomater. Sci.* **4**, 460–473 (2016).

143. Lu, Q. *et al.* Silk fibroin electrogelation mechanisms. *Acta Biomater.* **7**, 2394–2400 (2011).

144. Zhu, Z., Imada, T. & Asakura, T. Preparation and characterization of regenerated fiber from the aqueous solution of Bombyx mori cocoon silk fibroi. *Mater. Chem. Phys.* **117**, 430–433 (2009).

145. Yang, M., Kawamura, J., Zhu, Z., Yamauchi, K. & Asakura, T. Development of silk-like materials based on Bombyx mori and Nephila clavipes dragline silk fibroins. *Polymer (Guildf).* **50**, 117–124 (2009).

146. Um, I. C. *et al.* Wet spinning of silk polymer: I. Effect of coagulation conditions on the morphological feature of filament. *Int. J. Biol. Macromol.* **34**, 89–105 (2004).

147. Fu, C., Shao, Z. & Fritz, V. Animal silks: Their structures, properties and artificial production. *Chem. Commun.* 6515–6529 (2009) doi:10.1039/b911049f.

148. Ha, S. W., Tonelli, A. E. & Hudson, S. M. Structural studies of Bombyx mori silk fibroin during regeneration from solutions and wet fiber spinning. *Biomacromolecules* **6**, 1722–1731 (2005).

149. Min, B. M. *et al.* Electrospinning of silk fibroin nanofibers and its effect on the adhesion and spreading of normal human keratinocytes and fibroblasts in vitro. *Biomaterials* **25**, 1289–1297 (2004).

150. Panda, N., Bissoyi, A., Pramanik, K. & Biswas, A. Development of novel electrospun nanofibrous scaffold from P. ricini and A. mylitta silk fibroin blend with improved surface and biological properties. *Mater. Sci. Eng. C* **48**, 521–532 (2015).

151. Bhattacharjee, P. K. *Electrospinning and Polymer Nano fibers : Process Fundamentals*. *Comprehensive Biomaterials II* vol. 5 (Elsevier Ltd., 2017).

152. Yin, C., Jatoi, A. W., Bang, H., Gopiraman, M. & Kim, I. S. Fabrication of silk fibroin based three dimensional scaffolds for tissue engineering. *Fibers Polym.* **17**, 1140–1145 (2016).

153. Ki, C. S., Gang, E. H., Um, I. C. & Park, Y. H. Nanofibrous membrane of wool keratose/silk fibroin blend for heavy metal ion adsorption. *J. Memb. Sci.* **302**, 20–26 (2007).

154. Zhou, W., He, J., Cui, S. & Gao, W. Preparation of electrospun silk fibroin/Cellulose Acetate blend nanofibers and their applications to heavy metal ions adsorption. *Fibers Polym.* **12**, 431–437 (2011).

155. Baek, D. H., Ki, C. S., Um, I. C. & Park, Y. H. Metal ion adsorbability of electrospun wool keratose/silk fibroin blend nanofiber mats. *Fibers Polym.* **8**, 271–277 (2007).

156. Wang, Y., Blasioli, D. J., Kim, H. J., Kim, H. S. & Kaplan, D. L. Cartilage tissue engineering with silk scaffolds and human articular chondrocytes. *Biomaterials* **27**, 4434–4442 (2006).

157. Kim, U. J., Park, J., Joo Kim, H., Wada, M. & Kaplan, D. L. Three-dimensional aqueous-derived biomaterial scaffolds from silk fibroin. *Biomaterials* **26**, 2775–2785 (2005).

158. Nazarov, R., Jin, H. J. & Kaplan, D. L. Porous 3-D scaffolds from regenerated silk fibroin. *Biomacromolecules* **5**, 718–726 (2004).

159. Marin, M. A., Mallepally, R. R. & McHugh, M. A. Silk fibroin aerogels for drug delivery applications. *J. Supercrit. Fluids* **91**, 84–89 (2014).

160. Maleki, H., Montes, S., Hayati-Roodbari, N., Putz, F. & Huesing, N. Compressible, Thermally Insulating, and Fire Retardant Aerogels through Self-Assembling Silk Fibroin Biopolymers Inside a Silica Structure - An Approach towards 3D Printing of Aerogels. *ACS Appl. Mater. Interfaces* **10**, 22718–22730 (2018).

161. Mitropoulos, A. N. *et al.* Noble metal composite porous silk fibroin aerogel fibers. *Materials (Basel).* **16**, 894 (2019).

162. Mano, J. F. *et al.* Macro/microporous silk fibroin scaffolds with potential for articular cartilage and meniscus tissue engineering applications. *Acta Biomater.* **8**, 289–301 (2011).

163. Studart, R. *et al.* Silk fibroin scaffolds with inverse opal structure for bone tissue engineering. 2074–2084 (2016) doi:10.1002/jbm.b.33737.

164. Wibowo, U. A. *et al.* Development of salt leached silk fibroin scaffold using direct dissolution techniques for cartilage tissue engineering. *Int. J. Adv. Sci. Eng. Inf. Technol.* **9**, 810–815 (2019).

165. Li, Z. *et al.* Fabrication , characterization , and in vitro evaluation of biomimetic silk fibroin porous scaffolds via supercritical CO 2 technology. *J. Supercrit. Fluids* **150**, 86–93 (2019).

166. Du, L. *et al.* Hierarchical macro / micro-porous silk fibroin scaffolds for tissue engineering. *Mater. Lett.* **236**, 1–4 (2019).

167. Chen, C. H. *et al.* Cartilage tissue engineering with silk fibroin scaffolds fabricated by indirect additive manufacturing technology. *Materials (Basel).* **7**, 2104–2119 (2014).

168. Maniglio, D., Bonani, W., Migliaresi, C. & Motta, A. Silk fibroin porous scaffolds by N2O foaming. *J. Biomater. Sci. Polym. Ed.* **29**, 491–506 (2018).

169. Xiao, S., Wang, Z., Ma, H., Yang, H. & Xu, W. Effective removal of dyes from aqueous solution using ultrafine silk fibroin powder. *Adv. Powder Technol.* **25**, 574–581 (2014).

170. Xu, Z., Shi, L., Yang, M. & Zhu, L. Preparation and biomedical applications of silk fibroin-nanoparticles composites with enhanced properties - A review. *Mater. Sci. Eng. C* **95**, 302–311 (2019).

171. Yoshimizu, H. & Asakura, T. Preparation and characterization of silk fibroin powder and its application to enzyme immobilization. *J. Appl. Polym. Sci.* **40**, 127–134 (1990).

172. Rajkhowa, R., Wang, L. & Wang, X. Ultra-fine silk powder preparation through rotary and ball milling. *Powder Technol.* **185**, 87–95 (2008).

173. Zhang, Y. Q. *et al.* Formation of silk fibroin nanoparticles in water-miscible organic solvent and their characterization. *J. Nanoparticle Res.* **9**, 885–900 (2007).

174. Hofmann, S. *et al.* Silk fibroin as an organic polymer for controlled drug delivery. *J. Control. Release* **111**, 219–227 (2006).

175. Kumar, S. & Singh, S. K. Fabrication and characterization of fibroin solution and nanoparticle from silk fibers of Bombyx mori. *Part. Sci. Technol.* **35**, 304–313 (2017).

176. Hino, T., Tanimoto, M. & Shimabayashi, S. Change in secondary structure of silk fibroin during preparation of its microspheres by spray-drying and exposure to humid atmosphere. *J. Colloid Interface Sci.* **266**, 68–73 (2003).

177. Wenk, E., Wandrey, A. J., Merkle, H. P. & Meinel, L. Silk fibroin spheres as a platform for controlled drug delivery. *J. Control. Release* **132**, 26–34 (2008).

178. Kweon, H. Y. & Park, Y. H. Structural and conformational changes of regenerated Antheraea pernyi silk fibroin films treated with methanol solution. *J. Appl. Polym. Sci.* **73**, 2887–2894 (1999).

179. Lammel, A. S., Hu, X., Park, S. H., Kaplan, D. L. & Scheibel, T. R. Controlling silk fibroin particle features for drug delivery. *Biomaterials* **31**, 4583–4591 (2010).

180. Li, M., Tao, W., Kuga, S. & Nishiyama, Y. Controlling molecular conformation of regenerated wild silk fibroin by aqueous ethanol treatment. *Polym. Adv. Technol.* **14**, 694–698 (2003).

181. Huang, J. W. *et al.* Tissue performance of bladder following stretched electrospun silk fibroin matrix and bladder acellular matrix implantation in a rabbit model. *J. Biomed. Mater. Res. - Part A* **104**, 9–16 (2016).

182. Marelli, B., Brenckle, M. A., Kaplan, D. L. & Omenetto, F. G. Silk Fibroin as Edible Coating for Perishable Food Preservation. *Nat. Publ. Gr.* 1–11 (2016) doi:10.1038/srep25263.

183. Wang, Y. *et al.* In vivo degradation of three-dimensional silk fibroin scaffolds. *Biomaterials* **29**, 3415–3428 (2008).

184. Geão, C. *et al.* Thermal annealed silk fi broin membranes for periodontal guided tissue regeneration. *J. Mater. Sci. Mater. Med.* (2019) doi:10.1007/s10856-019-6225-y.

185. Drummy, L. F., Phillips, D. M., Stone, M. O., Farmer, B. L. & Naik, R. J. Thermally induced α-helix to β-sheet transition in renegated silk fibers and films. *Biomacromolecules* **6**, 3328–3333 (2005).

In the road to make Silk Fibroin (SF) a multifunctional material, some features must be considered. Among others, the physical-chemical properties deserve special attention since they define the material potential.

In the following, SF's original properties and their variations after processing are described. In addition, with the aim to expand its applicability, the particular routes to modify those properties will be explored.

Finally, the fundamental application areas of SF and the challenges for further applications will be analyzed.

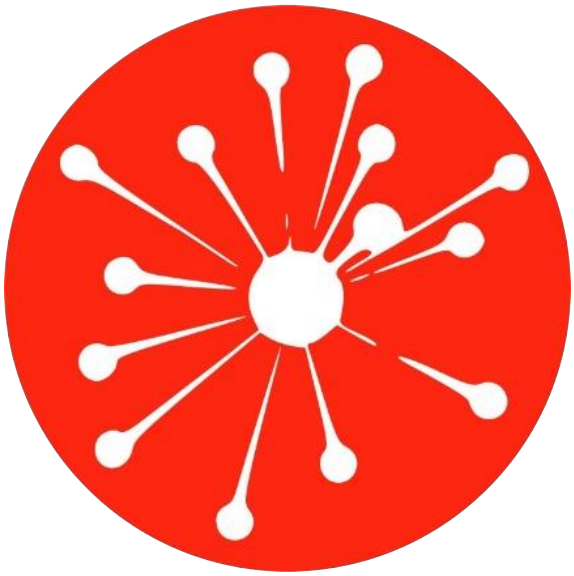

Chapter.3

THE PATH TO MULTIFUNCTIONAL SILK

3.1. SILK FIBROIN PROPERTIES

Due to natural selection, *Bombyx mori* cocoons have developed several promising properties for silkworm's survival (***Figure 3.1***). Among these properties, two main types can be differentiated: passive and active ones.

Passive properties are characterized by the lack of regulation since they continuously control and maintain the biological conditions that silkworm survival requires. Among the passive characteristics are found the mechanical properties, water and light protection, thermal regulation[1,2], gas selective permeability[3], antibacterial[4] and UV-protection[5,6], among others[7].

Active properties control the metamorphosis through a connexion between cocoon and pupa. This connexion is regulated through electrical stimuli, which are originated in the cocoons and directly travel to the pupa brain[8,9].

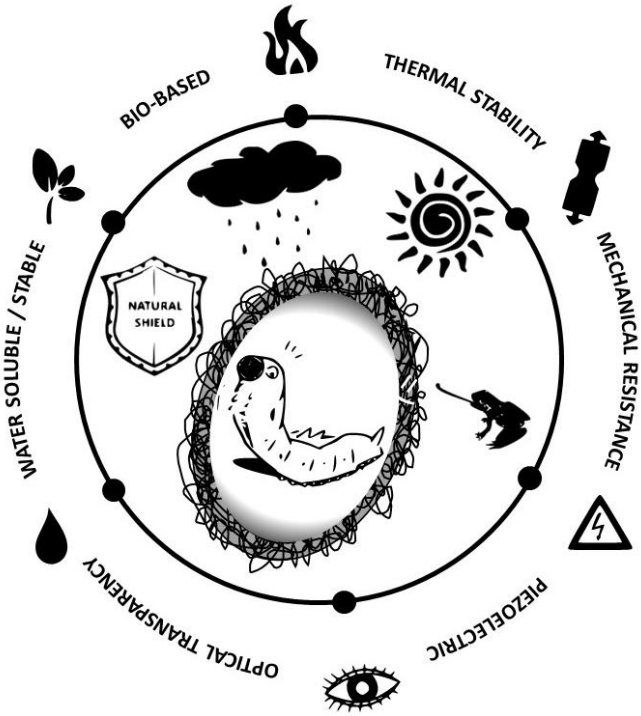

Figure 3. 1. *Graphic representation of SF natural functions as part of the cocoon.*

As a composite material, cocoon properties mainly derive from the specific properties of its components, materials interfacial compatibility, materials shape, cocoon's packing, and the interaction with the environment. But, as Silk Fibroin (SF) is the main component of silk cocoons, it clusters almost all the cocoon properties.

In the following, the original properties of raw SF fibers are described. Due to the strong effect of processing on the SF final behavior, the main regenerated structures' properties are also considered.

3.1.1. HIGROSCOPIC PROPERTIES

The polar residues present in SF (mostly Ser and Tyr) have a strong affinity to water, even to the water molecules present in the air. This makes the SF a hygroscopic material, able to absorbs and holds water molecules inside. Due to the compact structure of crystalline domains and the higher content of hydrophobic residues, water penetration is restricted. Thus, water is mainly retained on more hydrophilic amorphous domains. Due to the high crystalline content of naturally spun SF fibers, there is not practically water in their inside[10] (below 5%). On the contrary, in SF processed materials, the significant amorphous domain presence enables water penetration, leading to water amounts between 4 and 10 % of total weight[11].

Depending on SF-water molecules interaction, absorbed water can be classified as i) non-bonded water, which is unbound water that has the same transitions temperatures as bulk water and could be easily removed by vacuum or dry environments; and ii) bound water, which results from the strong SF-water interaction, and thus is hardly removed.

The water molecules' interaction with the SF amorphous regions disrupts the amide-amide hydrogen bonds between protein residues, increasing the free volume, and allowing their unrestricted movement[12]. The result is a more plasticized material with important implications on the rest of the properties[13] (***Figure 3.2***):

i. An increase in the mobility of the polypeptide chains promotes hydrophobic interactions and, thus, crystalline domains formation[10].
ii. Plasticization results in polypeptide chains' thermal relaxation. The modification being proportional to the bonded water trigger a constant decrease of the material's strength. As a consequence, at high water values, the SF becomes completely malleable. This enables the deformation of SF to obtain macroscopically modified new materials, even with new functionalities. After bonded water is lost, SF materials recover their original properties, making the state reversible[14] (***Figure 3.2 bottom***).

iii. Due to the limited hydrophilic bonding points for water molecules, as water content increases, the amount of bonded molecules decreases, allowing easier water removal as water content increases[10].

iv. The increase in molecular free volume increases the whole structure mobility, which results in a gradual reduction of the glass transition temperature as the time that moisture level increases[12]. At high water loadings, an abrupt toughness decreasing occurs.

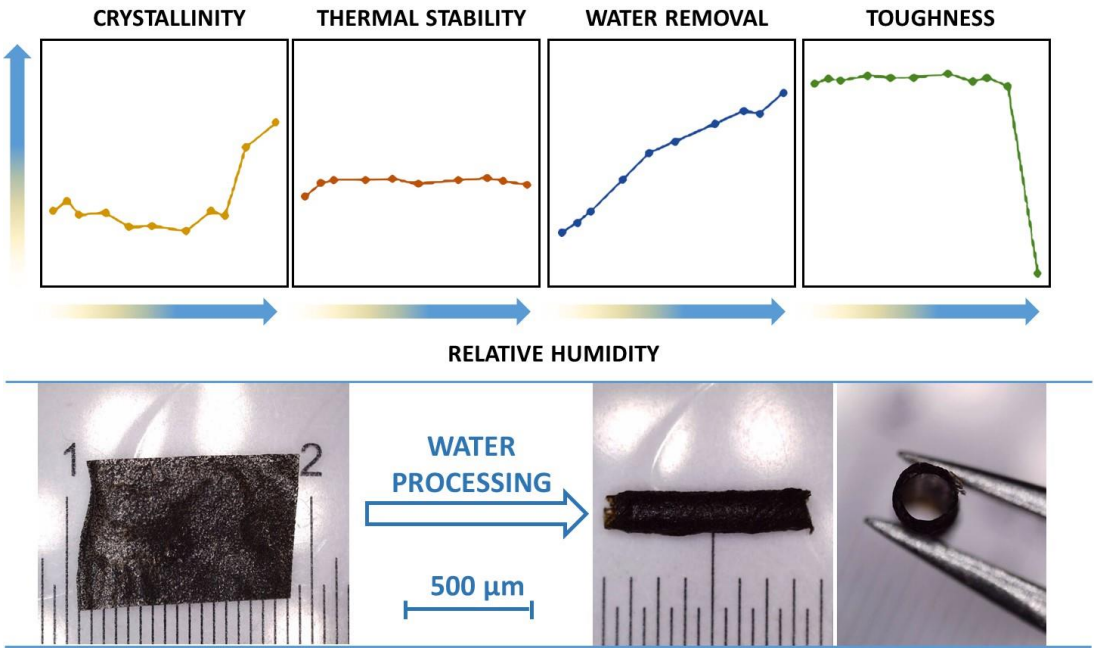

Figure 3. 2.*Above: SF properties as a function of relative humidity (ref: [170]). Below: SF films morphological adaptation through water plasticisation. (black coloration has been applied to easily observe the SF films)*

3.1.2. GAS BARRIER

The cocoon offers a physically isolated space where the pupa carries out its metabolic functions, including breathing. Consequently, the cocoon membrane can regulate the diffusion of gases, such as CO_2, N_2, O_2, and water vapor. This ability has been proven to result from cocoons composition, silk weave, shape, and components behavior[3,15–18].

Calcium oxalate hydrate crystals, mainly found in some cocoons composition, have a particular function in this process. However, due to different environmental conditions and even the human selection processes, the *Bombyx mori* lacks these crystals[3,16]. As a result, *Bombyx mori* cocoons do not preserve the most gas barrier abilities found in other silkworm species[15].

Despite this lack, the studies carried out in this regard with *Bombyx mori* silk point out the ability of SF films and coatings to act as gas barrier structures. SF can allow or hinder gasses permeation according to the β-Sheets content. In particular, O_2, CO_2, and N_2 gases' ability to be permeated through SF decrease as β-sheets content increses[17,18]. This effect has been ascribed to: i) the packed composition of crystals, which restricts molecular dynamics, and ii) the decreased water content due to crystal's hydrophobic nature, which hinders the diffusivity of water-soluble gases[17,18].

3.1.3. THERMAL PROPERTIES

To understand the complete thermal behavior of SF, several features are comprised:

Thermal stability:

Thermal stability is defined as weight loss during thermal annealing. SF loss the non-bonded water between 30 and 150ºC[19]. Bonded water begins to be eliminated above 100ºC, but it is wholly removed above 160ºC – 170ºC[13,19].

Once the water has been completely removed, SF remains stable until 280- 290 °C, where polypeptide chains start degrading due to the side chains and amino acid residues breakdown, and peptide bonds cleavage[20,21].

In a second degradation step, thermal decomposition of peptides occurs, producing a weight loss of around 50%. The heating environment influences this final degradation: under non-oxidative atmospheres, the peptides pyrolysis behave; when oxygen is present, peptides combustion occurs[21]. Due to the low presence of inorganic compounds in SF, above 700ºC negligible SF residues left.

Thermal transitions

The water content inside de material and the crystallinity strongly influence the SF thermal transitions.

At water freezing temperatures (-60 to 0 °C) in hydrated samples, a first relaxation related to the hydrogen bond formed between water and SF amino acids C=O and N-H groups can be observed. This is denoted as β-relaxation.

Around 60 ºC, SF displays a second endothermic relaxation (α'-relaxation), usually related to an increase of the amorphous domain motion (low-temperature glass transition)[12,13]. However, since it disappears on dehydrated samples, it has also been associated with protein-

water bonding rupture and the consequent motion increase of water molecules [19,22]. In any case, the α'-relaxation induces a molecular motion increase and a partial thermoplasticity of SF materials [14]. It is possible to control this α'-relaxation through the water content inside the material[12]. Around 170 ºC, the bound water is completely removed, and SF undergoes a real glass transition known as α-relaxation[19].

Around 140 ºC, the intramolecular hydrogen bonds of α-helices start to break[19]. Above the glass transition temperature (T_g), and until to reach around 214 ºC, the released chains from α-helices and mobile non-crystalline domains (random coils) start packing and adopt the lowest energy configuration by cold crystallization, it is the β-crystals. The process is revealed as an exothermic peak, and it implies the stabilization of the whole structure[14,23]. Finally, SF shows an endothermic peak around 325 ºC ascribed to the thermal decomposition of fibroin chains[23,24].

Some authors have reported an endothermic transition at 130 °C assigned to the melting temperature (T_m) of the α-helix conformation[25].

Thermal diffusivity

To protect the pupa during the metamorphosis, SF behaves as a thermal insulator[26]. This is related to SF thermal diffusivity values (measured by direct contact method) around 1.6 x 10^{-7} $m^2 \cdot s^{-1}$ [27]. The diffusivity can be controlled through crystallinity since it was shown to be reduced below 1 x 10^{-7} $m^2 \cdot s^{-1}$ in samples with high β-sheets content[27].

3.1.4. MECHANICAL PROPERTIES

Cocoon prevent physical damage to the pupa[28]. This has derived in quite interesting mechanical properties. Silk is the lightest among natural fibers, but its tensile strength is superior to many biomaterials (e.g., cotton and polylactic acid (PLA)). Besides, it is stronger than an equal thickness of steel wire. Natural SF fibers show: i) a maximum elongation (ε_{max}) between 13 and 14%; ii) elastic modulus (E) between 15 and 18 GPa iii) yield strength (σ_y) around 230 ± 10 MPa; iv) tensile strength (σ_u) between 620 MPa and 760 MPa, and v) average shear modus(G) of 3.0 ± 0.8 GPa. All these properties are quite constant among different cocoons. Fracture properties, conversely, are poorly reproducible due to microstructural defects present along the fibers [29,30].

This unusual combination of strength and toughness and the excellent ability to absorb energy at high loading speed rates distinguish SF from other natural and synthetic fibers. The properties are even comparable to those shown by some high-performance fibers, like nylon or Kevlar (***Table 3.1***) [31,32].

Table 3.1. *Mechanical properties of SF and other fiber like materials*

Sample	*Density(g/cm^3)*	*ε_{max} (%)*	*E (GPa)*	*σ_u (MPa)*	*Ref*
SF - bin	*1.17*	*13 - 14*	*15 -18*	*620 - 760*	[29,33]
SF- film	-	-	*3.9 +- 00.7*	*47.2 +- 6.4*	[34]
SF-Film, water annealed	-	-	*1.9 +- 0.5*	*67.7 +- 11.7*	[34]
SF-Film, MeOH	-	-	*3.5 +- 0.9*	*58.8 +- 16.7*	[34]
SF–water electrospinning	-	*9.6*	-	*130*	[35]
SF–FA electrospinning, MeOH	-	*29.3*	-	*980*	[35]
Bone	-	*3*	*20*	*160*	[36]
PLA- sheet	-	*2 - 6*	*1– 4*	*47 - 72*	[36,37]
Nylon - fibre	*2.35*	*18*	-	*950*	[38]
Cotton	*1.5 – 1.6*	*3 - 10*	*5.5 – 12.6*	*287 - 597*	[39]
Kevlar - fiber	*2.15*	*2.7*	*130*	*3600*	[36,38]
High-tensile steel	*8.05*	*0.8*	-	*1500*	[38]
Wool		*24 - 68*	*1.8×10^{-4}– $4.6\ 10^{-2}$*	*0.9 -7.4*	[39]

SF mechanical properties are mainly derived from the hierarchical composition and molecular structure of the fibers [40]:

i. The strongly interconnected nanofibrils prevent slipping when SF fibers are subjected to mechanical stress and prevent the total failure when a segment is broken by sharing its loaded force with surrounding segments[41].
ii. β-crystals hold the cross-linked section together, act as independent force loader, dividing the total force among all nodes, and transmitting the loaded force to surroundings ones[41].

The loss of this hierarchical configuration may cause some changes in the mechanical properties of the materials. The most common one is the loss of nano-fibrils configuration during the dissolving process. This, because of its complexity, is hardly recovered after the SF regeneration process. Two main approaches have been followed to avoid this problem: i) the first and less destructive one is based on preserving the SF hierarchy by using partial

solving techniques[42] and ii) the second approach is based on recovering the hierarchical configuration by using additive manufacturing techniques (i.e., direct printing, or electrospinning) which allow the replication of the original nanofibrils [24,43].

Fortunately, most of the mechanical properties of Silk are dominated by its cross-linked configuration, which can be mainly controlled during the regeneration process[39,44]. The behavior of cross-linked configuration under tensile load respond to the following steps (***Figure 3.3***):

i. SF amorphous domains firstly support the force. This causes the non-crystalline domain to unravel, which results in elastic and recoverable deformation.
ii. Once the amorphous domains are wholly unraveled, the tension is translated to the nodes (β-crystals), which, due to their strong packing level, cannot be deformed[39].
iii. When the loading force exceeds the tension supported by β-crystals, some are broken, leading to the structure's plastic deformation. Due to the cross-linked configuration, the previously loaded force by broken β-crystals is loaded by surrounding β-crystals.
iv. Finally, the load force causes the filature of remaining β-crystals, leading to the final breakdown of the structure.

β-crystals domains arrangements, size, and orientation also influence the mechanical properties:

i. ***Arrangement***: parallel β-sheets show larger mechanical resistance than antiparallel ones. Thus, the stability provided to the whole structure is higher when antiparallel β-crystallites are promoted[39].
ii. ***Size***: β-crystallites confined to a few nanometres can achieve higher strength, stiffness, and toughness than larger β-crystallites. The reported dimensions of β-crystallites for optimal mechanical properties are between 2–4 nm along chain direction and 1–2 nm along the strand axis[39].
iii. ***Orientation:*** a higher orientation of β-crystallites along the fiber axis contributes to a higher breaking stress[39].

In this sense, it is worth highlighting that considerable differences are found for regenerated SF according to the followed processing conditions. Some examples of SF mechanical properties variation with processing have been collected in ***Table 3.1.***

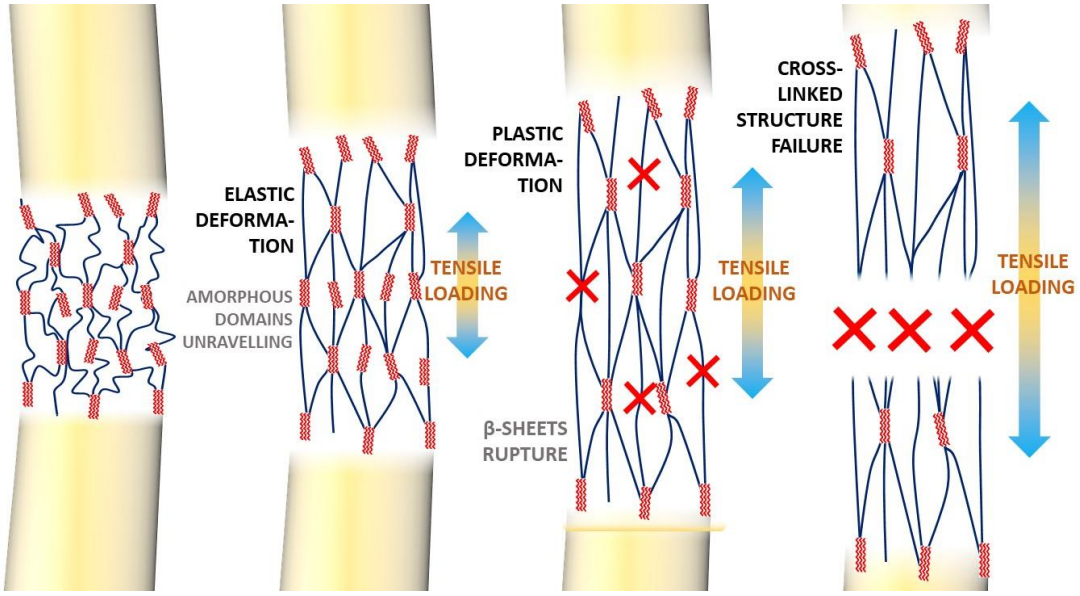

Figure 3. 3. *Graphic representation of SF molecular arrangement under tensile loading*

3.1.5. OPTICAL PROPERTIES

Silk fibers have been historically appreciated for their natural brightness and lustrous appearance. These properties are directly derived from the ability of silk fibers surface to reflect and scatter the light.

However, the interest of SF in the optics field is mainly focused on processed SF materials. An important parameter that dictated the SF performance in this context is the refractive index[11], which compares the variation of the light's speed when it passes from vacuum to another material or between two phases. This variation mainly depends on the fluctuations in composition, packing density (volume effect), and the scattering promoted by internal defects[45].

SF films and fibers deserve particular interest among SF regenerated materials for the optical purpose because of their high visible-light transparency (>95%), low absorbance along the UV-Vis region, and high refractive index [46,47,48,49]. Also, SF films show low roughness and can be patterned, enabling modifying light behavior in SF's contact.

Processed SF films and wet fibers only display light absorption at 300 nm, which is assigned to $\pi \rightarrow \pi^*$ transition of the Tyr, Phe, and Try residues of the molecular chain. Electronic irradiation can decrease the energy required for the optical transition since it causes the

creation of carbonyl groups and moves the absorption bandgap (located at around 4.18 eV) towards longer wavelengths[49]

The SF refractive index, which is 1.566 (at 550 nm) and 1.543 (at 630 nm), can be easily modified by the regeneration process[11]. The main influencing parameter is the packing level of SF structures, which is related to:

i. ***Water content***: The plasticized structures increase the free volume and thus, decrease their packing level. For a 5% variation in water content, a variation of about 0.01 in the refractive index can be expected
ii. ***Crystallinity***: Due to the β-crystals higher packing level, the light passage is hindered, increasing the material refractive index. On the contrary, amorphous domains present a lower molecular density, which results in a decrease in the refractive index [11]. By increasing β-crystals content, a maximum increase of around 0.005 is observed.

It is also possible to adjust the SF refractive index through electromagnetic irradiation and the consequent structural modifications of the samples[49]. In all cases, it has been observed a good reproducibility of SF optical parameters as long as processing conditions remain unalterable[11,50].

3.1.6. ELECTRIC PROPERTIES

The molecular structure of SF lacks charge transfer complexes capable of carrying electrical charges. Consequently, in dry conditions, SF presents a very high electrical resistance and behaves like an insulator[12]. However, SF is commonly presented as a water-protein complex due to its hygroscopic behavior, which presents relatively low electrical resistivity values [51]. This phenomenon has been related to two effects derived from water penetration inside SF[12,52]:

i. ***Ionic conductivity*** is related to the liberation of charge carriers (e.g., Na, K, and Cl), which are naturally founded inside SF. The SF conductivity values in a hydrated state are around 350 µS with a total amount (dissolved ionic carriers) of around 150 ppm[12]
ii. ***Water-mediated proton hopping*** is related to hydrated protein's ability to exhibit electronic and electrochemical activity due to protons dynamics[52].

The increased mobility of polypeptide chains in a hydrated state enables the different domains' polarization under an electric field. The SF main polarizable units are:

i) ***Non-crystallizable parts*** (random coils, turns, and side-chain groups) have a residual dipole moment.

ii) ***α-helix***, have a net dipole moment along the longitudinal axis due to its spiral structure and the alignment of peptide dipoles (C=O and N-H) parallel to the helical axis.

iii) ***Parallel β-sheets*** have a net dipole moment along the β -strand direction because the peptide dipoles orientation in angle with the strand direction, which avoids their mutual canceling and generates a dipole moment; and finally,

iv) ***Antiparallel β-sheets*** have a cero dipole moment because the peptide dipole moments perpendicular to the strand direction are mutually canceled. Each peptide unit of SF has a dipole moment of ∼3.5D. Thus, for example, α-helix, with 10 residues and almost 100% of peptide dipoles pointing along the direction of the helical axis, has a net dipole moment of 34D[19].

Due to the polarizable domains size and low mobility, as frequency increases, dipoles' ability to be oriented in the applied field direction decreases[19]. Commonly, SF shows a dielectric constant (e') around 1.84 at 50 kHz of frequency and gradually decreases to e' = 0.5 at 5 MHz [53].

Thermo-electrical behavior

The silk cocoon membrane has an inherent ability to sense the change of many environmental conditions. Any change in temperature or humidity is translated as electrical signals from cocoon to pupa, as current flow across the silk cocoon [8]. This effect is ascribed to the SF ability to modulate the mobility of the water molecules by temperature, affecting in this way, the conductivity behavior of SF. It has been observed that the electron mobility of SF is almost constant in the temperature range of 10–40ºC, but it exhibits a sharp rise at temperatures above 40 ºC, mostly around 50 ºC – 60 ºC. This is related to the molecular dynamics increase inside the SF, either for amorphous domain motion increase (glass transition) or for the higher mobility of water molecules [12,13,22].

Piezoelectricity

Piezoelectricity is the inherent ability of certain materials without a center of symmetry to convert mechanical energy into electrical energy (direct piezoelectric effect) or vice versa (inverse piezoelectric effect).

Silk II crystals have a monoclinic unit cell, while Silk I crystallize in an orthorhombic one. The lack of center of symmetry in both crystalline units suggests that SF presents piezoelectricity, independently of the crystalline polymorphism in the protein [54]. On the contrary, the Silk I structure has a lower degree of orientation and does not yield a strong piezoelectric effect.

It was hypothesized that when shear forces are applied in the plane of the β-sheet, they could result in intra- and inter-chain slide within pleated β-sheet domains and a subsequent rotation of amide dipoles, leading to an internal polarization. While an isotropic distribution of β-sheet crystal domains would lead to a cancellation of internal polarizations, the uniaxial orientation of crystal domains could facilitate a net polarization[55]. With water, the internal rotation of dipoles is more accessible, and the relaxation time required for the rotation is shorter[55].

The piezoelectric effect in bundles of silk fibers was firstly observed in 1956 and set at d_{14}= ~1 pC/N [56], comparable to that of the quartz crystal (~2 pC/N) [55]. The same behavior was then observed in oriented films of SF elongated three times as large as the original length, d_{14}= ~3 pC/N [57]. A strain of 0.04 % at 0.5 Hz resulted in a shear piezoelectric polarization value of ±10 pC and a potential difference of ± 20 mV. These values may be sufficient to affect cell behavior[57], and are comparable with the absolute d_{14} values reported previously from highly piezoelectric biopolymers (e.g., oriented collagen, 2–3 pC/N, and cellulose, 0.4–0.9 pC/N), and oriented films of synthetic polypeptides, including polyalanine (~ 1 pC/N) and poly-γ-methyl-L-glutamate (~ 2 pC/N)[58]. Furthermore, to achieve these values, SF must be subjected to low frequency (0.5 Hz) compared to that in the majority of previous reports (10 Hz). The d_{33} piezoresponse of SF has been later set at 56 pm/V in ultra-smooth (2.8 nm) and thin films prepared by spin coating and photolithography [59–61].

3.1.7. BIOCOMPATIBILITY

When the biocompatibility of biomaterials is mentioned, it is usually referred to as two aspects: the material compatibility with cells and the lack of adverse effects derived from the secondary products of degradation. The lack of biocompatibility derives in a hypersensitive response of the organism and consequent inflammation of tissues.

Because of its protein structure, SF shows natural compatibility with human tissues. The small polypeptide chains and peptides derived from SF degradation do not cause a great

hypersensitive response in the organism, and consequently, SF is considered as a biocompatible material[62,63].

Nevertheless, when Silk was used for the first time in biomedicine as a suture, reactions ranging from hypersensitivity to acute and chronic inflammatory processes were found[64]. Subsequent research showed that in the absence of Sericin, SF fibers demonstrate a minimal inflammatory tissue reaction[36]. Interestingly, SS by itself has shown to be minimally inflammatory [65]. Thus, the use of Silk as a biomaterial requires the complete separation of these two main proteins [66].

Nowadays, some SF-based materials, such as surgical scaffold and injectable implants [67], are approved by The United States Food and Drug Administration (FDA). These materials have been successfully applied for clinical purposes [68,62].

3.1.8. BIODEGRADABILITY

Biodegradability is the ability of a material to be degraded under biological action. In the case of Silk, this process implies, i) the loss of the original properties of the material and ii) at the chemical level, the progressive rupture of polypeptide chains, leading to simpler and more stable forms. The most common degradation products of Silk are small polypeptide sections and amino acids[63], while the most simpler and definitive compounds are CO_2 (oxidized form), CH_4 (in a reduced form), or a mixture of both.

In nature, the cocoons have been adapted to remain stable and without further degradation for long periods. Humidity, light or temperature, can affect the SF protein structure, inducing polypeptide chains, oxidation, hydrolysis scission, and rearrangements[69,70]. Due to this change of composition, aged samples show a progressive loss of their main properties, including weight loss [70]. The SF degradation rate mainly depends on the environmental conditions, material shape (fiber, film, sponge), and the structural composition (i.e., secondary units composition, crystalline domains content, crystal structures organization) [71]. The control of these parameters allows a certain control of the degradation through processing. Due to its cross-linked nature and the consequent heterogeneity in chains packing mode, the SF degradation behaves in a heterogeneous way, in which the amorphous sections, more opened and accessible, are commonly the first degraded ones [72]. This makes possible to regulate the SF degradation by controlling β-sheet content and amorphous domains organization degree [70].

From a biomedical point of view, SF is defined by the USP (US pharmacopeia) as non-degradable. This is because it retains the majority of its tensile strength beyond 60 days *in-vivo*. Nevertheless, this does not mean that SF is non-degradable under body environmental conditions since around 1-year *in-vivo* the SF loses the majority of its tensile strength. Besides, SF fails to be recognized in biomedical implants within two years after the implantation[73,74].

As a protein, silk fibroin is mainly susceptible to biological degradation by proteolytic enzymes[75–77], which produce amino acids as final waste[63]. The more studied enzymes for SF degradation are protease, α-chymotrypsin, and collagenase. Their effect on the reduction of SF molecular weight follows the order protease < collagenase < α-chymotrypsin [75]. Proteolytic enzymes induce a noticeable decrease of SF samples weight and degree of polymerization. Chymotrypsin enzymes, on the contrary, have been used to degrade amorphous regions of fibroins to obtain highly crystalline SF [78].

The silkworm, Bombyx mori, produces a protease inhibitor in the silk gland embedding it within the cocoon for protection against premature proteolytic degradation. Generally, this 6kDa trypsin inhibitor is isolated during cocoons degumming[79].

SF also can be degraded by other non-natural ways s, such as gamma radiation, which directly affects the decreasing tensile strength of the fibroin fibers [80].

3.2. SILK FIBROIN MODIFICATION

SF properties could limit its use as multifunctional material. Nevertheless, modification can enhance SF's physicochemical properties or even allow the incorporation of new functionalities[81–83].

3.2.1. PHYSICAL MODIFICATIONS

SF physical modifications do not involve the use of chemical reagents, which avoids residual contamination. Physical modification techniques are simple, have low energy consumption, and are suitable for the treatment of large quantities of material. This makes physical modifications sustainable techniques with high potential for their scale-up in industry.

UV treatment

Due to its organic polypeptide structure, rich in bonds and atoms with nonbonding electron pairs, such as oxygen or nitrogen, SF strongly absorbs the light below 200 nm wavelengths [83] (UV light). This energetic light absorption leads the polypeptide chains to split, forming microspores and free radicals, which may further react with the oxygen to form highly reactive excited oxygen and oxygen-containing polar hydroxyl (-OH) and carbonyl (-C-O) groups [84].

Due to the loss of energy of absorbed photons as a consequence of the breakage of chemical bonding, the light penetration is mainly limited to about 50–100 nm depth. Consequently, the applicability of this technique is limited to superficial treatments, with negligible losses in weight, crystallinity, and mechanical properties of the bulk material[84].

UV treatment is a low-cost technique that is highly useful to modify the adhesion properties of SF, to increase its wickability, and reduce wetting, even at short exposure times, without affecting SF bulk properties[85]. On the other hand, it must be taken into account for further applications that UV treatment increases the yellowness index of SF due to the oxidation of amino acid residues, especially glycine, alanine, serine, and tyrosine [86].

Ozone treatment

Ozone, an unstable allotrope of oxygen, has been used as an oxidizing agent of Silk due to its strong oxidation potential (2.07 V) and reactivity to some of the majoritarian amino acids of SF, e.g., glycine, alanine, serine, and tyrosine[83,86]. The main effects of ozone over SF are:

i. The breakage of polypeptide chains due to oxidizing conditions[87]. As a consequence, the secondary and tertiary folding is affected, and the crystallinity is decreased[88].
ii. Weight loss due to removing the produced gaseous products such as ammonia, carbon dioxide, aldehyde, ketones, and nitrates [86].
iii. The decrease in breaking strength, elongation, and flexural rigidity due to the reorganization of the peptides derived from chains breaking?¿, and weight loss[86].
iv. Transformation of amino acids (more than 40% for tyrosine) into secondary products: i) Glycine, alanine, and serine, form 3,4-dihydroxyphenylalanine and chromophoric products; ii) cysteine form kynurenine, and iii) serine and glutamic acid form tryptophan and nitrates [86].

v. Increase in yellowness index of SF due to generated chromophoric products containing carbonyl groups [86].
vi. In the presence of water, Silk is powerfully attacked by ozone and becomes acidic and sticky [86].

Ozone treatments consume low energy and water amounts, they require short processing times and reduce the environmental impact, particularly chemical oxygen demand[89]. Ozone treatment can also be applied for both superficial and bulk treatments. The treated structures gain antimicrobial activity [88].

Plasma treatment

Plasma is a materials state formed by applying an electric discharge into a conventional gas, which induces the gas ionization. This excited state evokes the formation of free electrons, ions, and molecule fragments, which in contact with a target material, can initiate reactions via physical bombardment and plasma polymerization [83].

As the plasma treatment only modifies the outermost thin layer of the surface, it is commonly considered surface functionalization, keeping the bulk material unchanged [87].

Plasma could be based on several gases [83], being the most common for SF treatment: oxygen (O_2), nitrogen (N_2), argon (Ar), ammonia (NH_2), sulfur dioxide (SO_2), methane (CH_4), and air[87,90–94]. The effects of plasma over SF strongly differs depending on the employed gas in the plasma.

i. O_2 plasma treatment hydrolyses the SF surface inducing the breaking of surface polypeptide chains, saving the bulk behavior. Due to chain hydrolysis, an increase of roughness and a derived increase of hydrophobicity is observed [87,93].
ii. Ar plasma has been shown to produce a hydrophilic surface with a decreased contact angle, without any apparent effect on surface morphology. However, a certain increase of roughness and pore size is observed, which effectively enhances the cellular adhesion and chondrogenic differentiation of chondrocytes [91].
iii. NH_3 plasma treatment was used to produce amino groups on the SF materials surface [92], while SO_2 plasma treatment was used to link sulfonic groups ($-SO_3^-$) covalently. Also, SO_2 plasma treatment shown the formation of sulfur at a higher oxidation state, assigned to sulfur atoms bonded to two or three oxygen atoms such as sulfone (R-S(=O)(=O)-R'), sulfonate ($R-SO_3^-$) or sulfonic acid ($S(=O)_2(OH)$), being sulfur form 70.89% of total [92].

iv. Air plasma treatment changes the hydrophobic nature of SF into hydrophilic and significantly decreased the contact angle [90]. Plasma treatment is an environmentally friendly process that requires low chemical consumption and avoids waste production[83].

3.2.2. CHEMICAL FUCTIONALIZATIONS

Chemical modifications are usually required to achieve more specific modifications. Due to the diversity of chemical groups present on silk polypeptides (-CH_2, -OH, -NH_2, among others), several chemical modifications are possible[95]. However, the number of amino acids that can be modified under mild conditions is relatively short, resulting in low modification or harsh conditions requirement[96]. Fortunately, the intrinsic properties of SF allow its modification under various harsh conditions, including organic solution, high temperature and pressure, and the presence of catalysts and initiators. Further, these chemical reactions with SF solutions or even solid structures allow bulk or superficial treatment, depending on the modification objective [81].

pH effect

Among chemical modifications, pH is one of the main routes for SF control. pH affects, i) the SF solutions behavior (solubility, stability, turbidity, and viscosity, among others); ii) the size, shape, secondary structure, and zeta potential of silk particles [97,98] and iii) the self-assembly of polypeptide chains and gelation dynamics [99].

The strongest effect of pH over SF is observed in aqueous solutions, where pH variations can induce completely opposed molecular behaviors. In proteins, when pH is at the isoelectric point (pI), the net charge is zero, positive when pH is below the pI, and negative when pH is above the pI [100]. It is not possible to provide a single pI value for the whole SF since it is composed of different sections with variable polypeptide compositions. The SF H-Chain is the main component of the structure and, thus, it mainly influences SF behavior. H-Chain can be decomposed into four different sections depending on the amino acid presence and their distribution: N-terminus (pI = 4.6), C-terminus (pI = 10.5), hydrophobic repetitive units (not charged), and hydrophilic linkers (pI = 4) [97,101]. Depending on each section charge, SF behaves differently (***Figure 3.4***):

i. At low pH (pH > 5), as it happens in silkworm glands before silk-spinning[102], C-terminus are negatively charged while the other sections remain unchanged. The C-terminus minimum charge is found at pH 4 and minor values [97,98]. Consequently, at acidic pH, the

H-chains electrostatic repulsion is mainly suppressed, allowing the free packing of the structure.

ii. At neutral pH, negative charges slightly predominate over the positive charges. This situation leads to chain sections to gather, making the structure adopt a semi-compact conformation, leading to molecular aggregates[103]. However, the low charge that dominates the structure is not strong enough to induce fast hydrophobic domains interactions. This is why SF requires a considerable period to become gel at a neutral aqueous solution [97,98].

iii. At high pH (pH > 8), the H-chain sections except the C-terminus are negatively charged, resulting in repulsive forces that induce the polypeptide to adopt elongated conformations. Locating the amino acids maximum charge at values above pH 9 [98].

These three states have broad implications over SF processing, functions, and applications.

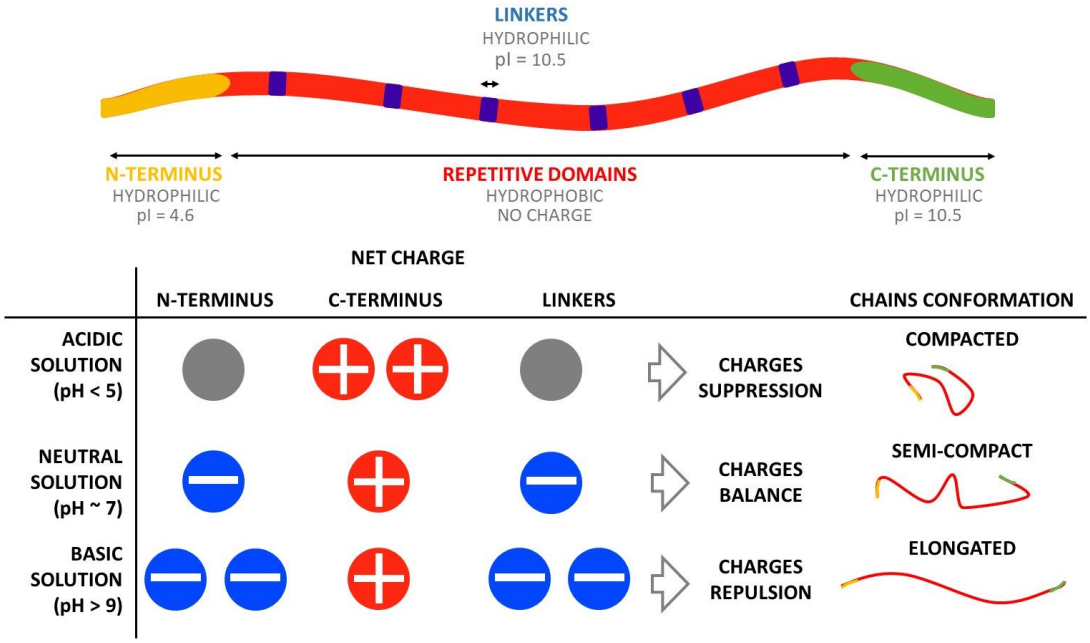

Figure 3. 4. *H-Chain conformation as a function of the pH of SF aqueous solution.*

Coupling reactions

Among chemical modifications of SF, functionalization includes the set of techniques/procedures that allow introducing single functional groups or small molecules into SF structure. The new residues, in general, slightly modify SF properties and bring new active groups [104–106].

Coupling reactions are specifically focused on introducing new functional groups or structures into SF but using a secondary molecule that participates as a mediator linking SF and the target structure. SF residues modified by coupling reactions are not majoritarian, and they always remain below 5% of the total. The most common coupling reaction for SF are:

i. ***Cyanuric chloride-activated coupling*** allows the introduction of molecules bearing nucleophilic hydroxyl or amino functional groups into SF structure by using cyanuric chloride ($N_3C_3Cl_3$) as a mediator by reaction with the phenolic hydroxyl group of tyrosine (~ 5 % of polypeptide chains) and the amino groups of Lysine (<1% of the total)[107]. Cyanuric chloride-activated coupling is based on a two-step process, performed in an aqueous environment and basic conditions [107]. The process implies in a first step the attachment to cyanuric chloride of a selected molecule, generally polyethylene glycol (PEG) [108], lactose derivatives [109], and oligosaccharides [81]. In a second step, the complex molecule-cyanuric chloride is attached to SF (***Figure 3.5***)

ii. ***Carbodiimide coupling*** allows the coupling of SF carboxylic groups with molecules containing primary amines through carbodiimides as mediators[110,111]. 1-ethyl-3-(3-(dimethylamino)propyl) carbodiimide (EDC) is the most commonly used carbodiimide for SF modification since it is water-soluble [112], have low toxicity, and only generates water-soluble urea residues [113]. Due to the middle conditions of the reaction (neutral pH and room temperature), SF's molecular disruption is avoided [112]. As it can be carried out in solution, it allows the SF solutions treatment to obtain modified bulk structures[114,115].

iii. ***Glutaraldehyde*** (GTA) has been commonly used to modify the amine-containing amino acids of SF [107]. GTA is linked to polypeptides through its two aldehyde groups (-CHO) to form bonds similar to Schiff bases ($R_1R_2C=N-R_3$) [116]. In GTA mediated reaction, the most reactive residue of SF is the lysine with is less than 1% of total polypeptides. GTA is used as a fixing agent for biological tissues, as its two aldehyde groups can generate the non-specific cross-linking of structures through several amines linking [81]. GTA has been used as a stabilizing agent for several SF mixtures [116,117], and even to induce SF films' conformational transition from random coils to β sheets [118]. Although it can be used in solution, it is commonly applied as a vapor for treatment because it is easy to control and avoid the collapse of sensible morphologies [116]. This makes GTA treatment useful for SF solutions and even the treatment of SF solid structures [119].

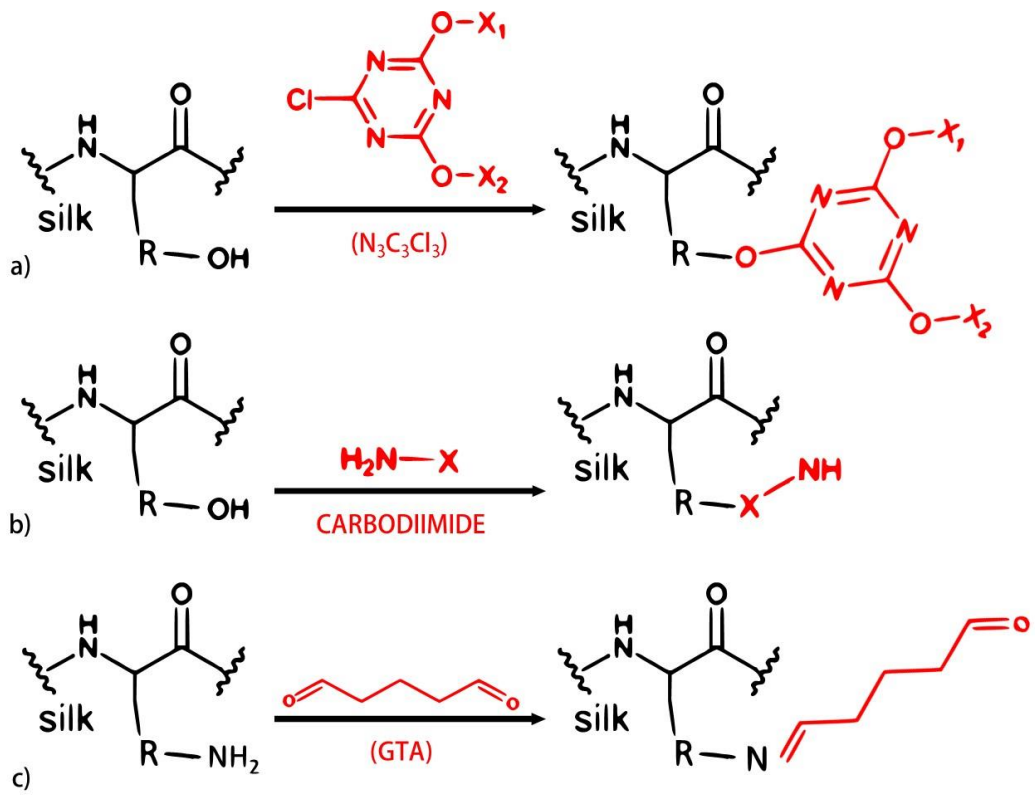

Figure 3. 5. *Examples of a)* ***Cyanuric chloride****-activated coupling, b)* ***Carbodiimide coupling*** *and c)* ***Glutaraldehyde*** *mediated coupling reactions on SF.*

Single functionalizations

Single modifications are a set of procedures focused on introducing new functional groups into SF structure. Unlike coupling reactions, single functionalization does not use intermediate molecules. In general, the introduction of these new groups does not induce strong effects on SF properties. Most of these routes have been followed to increase the bonding points where coupling reactions will proceed later. The most common single modification are:

i. ***Diazonium coupling reaction:*** some SF chemical modifications (such as carbodiimide coupling methods) imply a coupling of several molecules with SF carboxylic acid residues [110,111]. However, only ~1% of the total amino acid content of the SF is composed of aspartic and glutamic acid residues, thereby limiting the extent of functionalization.
The diazonium coupling reaction implies the modification of tyrosine residues, which are ~5% of SF's total amino acid content, to use these new functional groups for carbodiimide coupling methods and in this way increase almost by 3 the amount of functional

group[120,121]. Also, tyrosine residues are distributed throughout the protein sequence, allowing a homogeneous distribution of modifications along with the scaffold protein.

Diazonium coupling reaction involves an electrophilic aromatic substitution reaction between the tyrosine phenolic (φOH) side chains and a diazonium salt ($R{-}N_2^+X^-$). It results in an azobenzene derivative (***Figure 3.6***) [104,107].

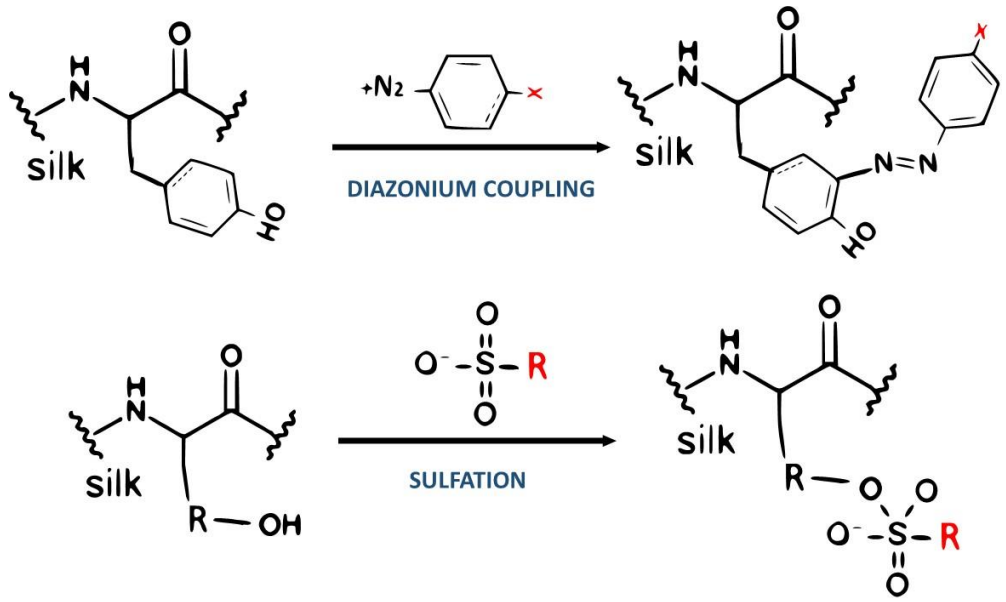

Figure 3. 6. *Functionalization routes for Silk Fibroin. Above: aromatic substitution reaction between the Tyr and a diazonium salt resulting in an azobenzene derivative, Below: incorporation of sulphated groups into SF hydroxyl groups, c) modification of hydroxyl groups and the amine groups, by carboxylic acid and d) introduction of sulfhydryl groups into primary amine groups.*

The reaction that takes place in middle conditions provided a rapid development, adaptability, and high modification level (yielding above 70% of the total), and thus, it represents a suitable SF modification strategy. Besides, the mild conditions of the method allow the recovering of above 90% of the material. Surface and bulk treatments can incorporate small molecules with various non-natural functional groups into SF, including sulfonic acids, carboxylic acids, ketones, and alkanes[104,107].

ii. ***Sulfation*** provides a useful tool to incorporate negatively sulfated groups into SF [122,123]. The process, commonly mediated by immersing an SF structure into heat chlorosulfonic acid solution, allows the replacement of hydroxyl groups (-OH) of tyrosine and serine residues by sulfone group ($R\text{-}SO_2\text{-}OH$) [122]. The process that reaches modification values of around 6% of the total implies certain SF backbone hydrolysis [124]. Further, the negative

charge of incorporated sulfone groups allows the adsorption of positive molecules [122,123] (***Figure 3.6***).

iii. ***Arginine masking*** complies the use of 1,2-cyclohexandione under basic aqueous conditions to modify arginine residues of SF (<1% of the total residues) in the form of uncharged imidazolidinone products [107].

iv. ***Carboxylation*** implies the modification of SF hydroxyl groups (-OH) of the serine and threonine residues and the amine groups of the lysine, arginine, and histidine residues by carboxylic acid (-COOH) functional groups[125]. The most common process uses a succinic anhydride bath as a modifying agent, which avoids the strong degradation of SF structures and provides reaction yields that can reach 90% of the total [96,125]. (***Figure 3.7***)

v. ***Thiolation*** implies the introduction of sulfhydryl groups (-SH) into primary amine groups of SF. The process requires the use of 2-iminothiolane (2-IT) and 4-dimethylaminopyridine (DMAP) in solutions mixed with SF solutions [126,127] (***Figure 3.7***).

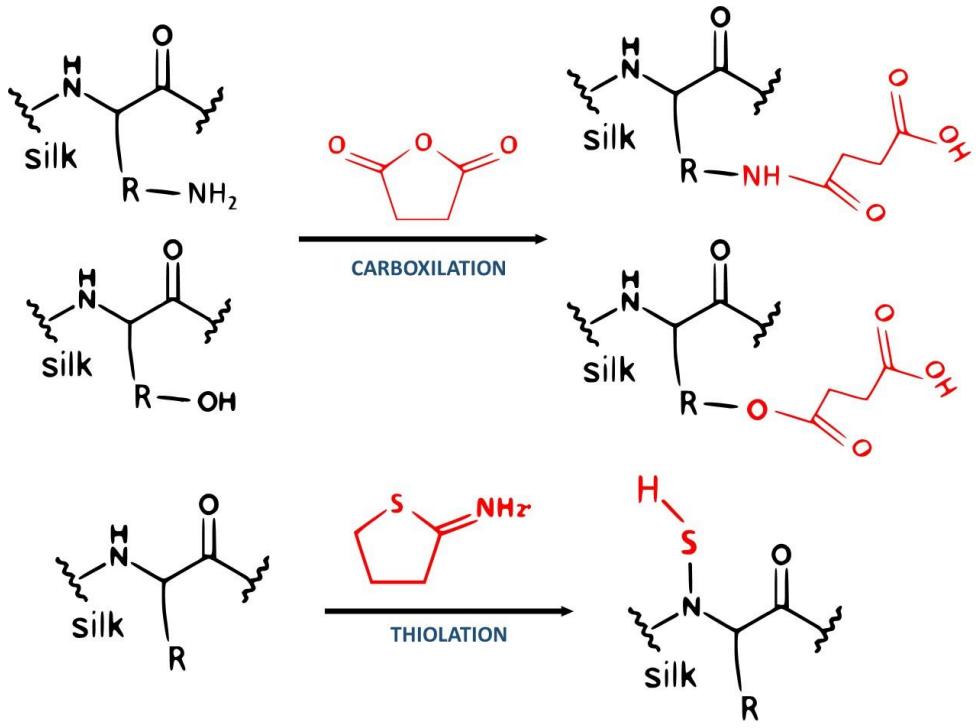

Figure 3. 7. *Functionalization routes for Silk Fibroin. Above: modification of hydroxyl groups and the amine groups, by carboxylic acid. Bottom: introduction of sulfhydryl groups into primary amine groups.*

Grafting

In polymeric structures, grafting refers to the introduction of shorter polymeric chains (grafts) into the backbone of the principal chains. The process adds new functionalities while keeping the intrinsic polymer properties unchanged[128,82]. Silk fibroin can be grafted by natural or synthetic polymers[129,130], inorganic mineralization agents (hydroxyapatites) [131,132], or drugs [133,134].

Grafting of SF has been performed through various routes such as laccase-mediated graft polymerization [135], enzymatic deposition [131], free radical initiation [136], thermal-induced ester formation [134], esterification of tyrosine [133], and hydrothermal reaction [132].

The objectives of grafting are mainly focused on i) improving SF main properties, such as electrical conductivity [137], flexibility [135] or water swelling ability [138]; ii) increase SF potentiality for biomedicine through controlling SF drug loading and release ability [133] or increase the bioactivity [137] among others: and iii) endow SF with new functional groups or structures useful for the design of alternative materials with novel properties [138]. A summary of some of the most relevant SF grafting processes reported between 2005 and 2020 have been collected in ***Table 3.2.***

3.2.3. COMPOSITE MATERIALS

Within SF self-properties, and even though those properties able to acquire through physical and chemical modifications, there exist several behaviors that SF is not able to reach. In this context, SF's combination with one or more materials of a different nature is an interesting alternative. This combination leads to a composite material where both components' properties are combined in a single element. Among the available options to combine SF with complementary materials, three main alternatives have been explored in the last years:

i. ***Particle-reinforced composite materials***: are composite materials based on particles of one material (fillers) dispersed into a second material. Commonly, due to its mechanical resistance, flexibility, and optical properties, SF behaves as collector material, gathering complementary particles inside. Thus, in general, it is considered that SF behaves like a matrix when it represents more than 50 wt. % of the material or binder, when its content is lower than 50 wt. % of the composite[139,140].
ii. ***Long fiber-reinforced composite materials*** are composite materials based on fiber- or wire-like fillers dispersed into a matrix. Due to the large aspect ratios of fillers, these are

commonly oriented towards the mechanical reinforcement of a polymeric resin. Due to the large mechanical properties of raw Silk and its fiber-like configuration, SF has been widely applied as fillers in this type of composite material[31].

iii. ***Structural composite materials*** properties depend on the design and geometry of the structural elements. Unlike the other two types, structural composite materials are not commonly integrated between them, although they form a single structure[139].

Table 3.2. *SF grafting examples*

Graft	*Matrix*	*Method*	*Application*	*Ref*
b-cyclodextrin citrate	*SF*	*Thermal induced ester formation*	*Drug delivery – control drugs loading and release*	134
Carboxyl-terminated polyethylene glycol	*SF*	*In solution*	*improve flexibility*	135
Polypyrrole	*SF-g-cPEG*	*Enzymatic (laccase) graft*	*achieve electrical conductivity*	135
Poly(g-methacryloxypropyl trimethoxysilane)	*SF- with vinyl groups*	*vinyl double bond mediated by AIBN initiator*	*Improve hard and brittle composites limits*	137
Poly(4-methacryloyloxyethyl trimellitate anhydride)	*SF*	*free radical initiation*	*improve the bioactivity*	136
Acrylamide and acrylic acid	*SF*	*Solution*	*add new functional groups*	138
Poly(acrylamide-co-acrylic acid)	*acrylated SF*	*Solution*	*improve swelling ability and wound dressing ability*	138
Steroids	*SF*	*Esterification of tyrosine residues*	*controlled release of anticancer drug*	133
Methacrylamide	*SF*	*Hydrothermal reaction 82oC*	*Make SF more stable toward alkaline hydrolysis*	132

A wide range of functional materials can be combined with Silk, including quantum dots[141], metal and inorganic particles[142], and ionic liquids[143]. The properties, shape, and size of added materials vary from macro metric structures (i.e., sandwich composites) to nanoparticles. The use of SF as a matrix allows the combination of SF chemical-physical properties (i.e., mechanical resistance and flexibility, thermal stability, gas permeability, and optical transparency, among others) with the new properties of the complementary materials. This

can endow composites with ionic and electrical conductivity[144,145], magnetic behavior[146] or antibacterial capacities[147], among other properties.

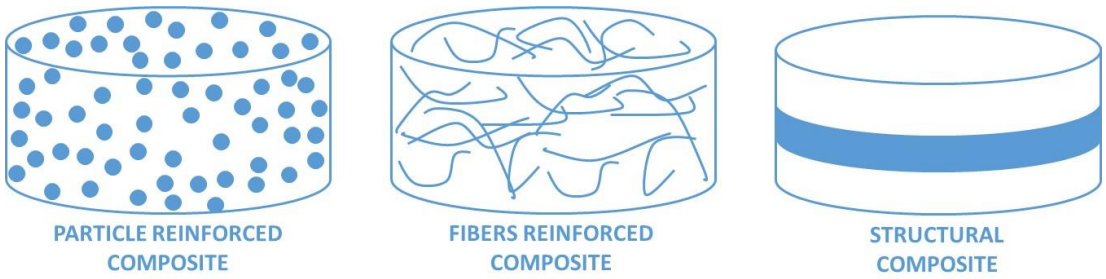

Figure 3. 8. *Graphic representation of different composite types.*

The use of micro- and nanoparticles for composites preparation is of particular interest because i) it eases the homogenous distribution of fillers along with SF structures, ii) allows their use in small-sized applications, and iii) enables their use in complementary processing techniques where large scale particles cannot be used (i.e., additive manufacturing, screen printing, ..).

Usually, the incompatibility between materials can hinder the development of a composite material. Non-compatible materials could result in large interphases or even in the impossibility of composites production. As a result, several properties, especially those related to mechanical behavior, could be compromised. In composite materials production, the compatibility between materials would be a priority. However, it is also possible to combine non-compatible materials with SF through SF physical and chemical modifications, which endow SF with the necessary active groups that ease the process [83].

3.2.4. IN-VIVO MODIFICATIONS

As Silk comes from a living organism, an alternative treatment to modify SF properties is based on the control of silk producer: the silkworm. Two differentiated approaches have been applied to this purpose.

Feeding modifications

As a living organism, silk producers have specific diets. In particular, silkworms are characterized because they only feed on mulberry leaves. Consequently, several

modification techniques have focused on introducing into the mulberry leaves (directly or indirectly) several products that cannot be metabolized by silkworms and finish into the silk glands. When Silk is spun, this product is dragged with the fibers leading to materials with new properties. Further, alternative feeding with artificial diets prepared from commercially available mulberry leaf powder has also been investigated. The main products given to silkworms have been dyes, organic molecules (i.e., hexaphenylsilole)[148] inorganic particles (i.e., Cu, Fe, TiO2 nanoparticles and rare earth) [149–151], carbonaceous materials (i.e., carbon nano-dots, graphene and carbon nanotubes) [152,153], and much more[154].

The feeding approach has emerged as a greener modification since it represents a reduction in processing resources, such as chemical, water, and energy. Also, the products incorporated through feeding have shown stronger interactions with SFs, low interference with SF intrinsic properties, and the ability to preserve the original fiber's hierarchical structure. Furthermore, the feeding strategy enables the large-scale production of high-performance modified SF, with low production costs [154].

Genetic modifications

Genetic engineering, or transgenesis, is presented as an alternative to providing Silk with unique biophysical and biochemical properties. The technique is based on using silkworms as host to introduce alternative genes (vectors), resulting in modifications of silkworm characteristics and silk [155].

Among the genetic modification kinds of silkworms that are nowadays accessible, they are notice worth:

i. The possibility to influence the secreted silk composition. In this way, fibers of neat SF can be directly obtained from the silkworm, reducing the time and energy and chemical consumption for its extraction[155].
ii. Recently, silk fibers with enhanced antibacterial properties and fluorescence were obtained by incorporating green fluorescent proteins (GFP) and antimicrobial peptides (cecropin) into silkworm[156]. This approach shows a large scale production of antibacterial Silk with low-cost production [155].
iii. By introducing PiggyBac (pBac)-mediated germline, it has been possible to generate different silkworm transgenic lines able to overexpress in the Silk Cec B 1 or Mor AMPs, to obtain Silk with improved antimicrobial properties and able to inhibit the bacterial growth of the Gram-negative E. coli [157].

However, because of the novelty of this technique and its socio-biological implications, the real advantages of using genetically modified SF are still unexplored. Properties of the modified samples, such as cytotoxicity, allergenic, or therapeutic effects, need to be thoroughly investigated in vitro and in-vivo to ascertain its safety and suitability. Nonetheless, genetic modifications to enhance silk-based components paves the way for tailoring high requirements material [158].

3.3. SILK FIBROIN APPLICATIONS

Thanks to its advanced properties, silk-based fabrics still represent a large economic sector, being part of some of the most prized textile products. SF fibers have led to turn the Silk into a quality standard, and consequently, thousands of products worldwide try to replicate its properties in search of the highest quality values[39].

Out of its more common applications, SF is further applied. Silk has been used as a suture for biomedical applications, mainly because of high strength, low bacterial adherence, durability, and biocompatibility. Claudius Galenus, a Roman (c. 131 to c. 211 AD), was the first to document a potential medical application of the silk threads as a suture for tendons in his book *De Methodo Medendi* (150 AD). However, it wasn't until 1869 when *Joseph Lister* introduced the first sterile silk suture into clinical practice. After this, the evolution of silk applications was ralentised[159] and almost passed another century, for the first patent of Silk, Ethicon Inc. (NJ, USA), in the 1960s, that dealt with the use of coated SF fibers to reduce the limpness, fraying and unwanted capillary action of non-treated silk sutures.

With the XX century entrance, the chemical industry strengthening and the desire to replicate silk properties (that ended with rayon, nylon, and Kevlar fibers creation) carried new silk processing advances. The first Silk based glue was patented in 1986, followed by the first patent for a silk-based porous scaffold in 1987s, and by several new patents in the 90s (e.g., powdered Silk for wound dressings; reconstituted silk films and molded gels for skin, blood vessel, and corneal coatings; and colloidal Silk for consumption in medicine)[159].

Nowadays, the main new application fields of SF are (***Figure 3.9***):

i. ***Tissue engineering:*** Silk processability allows to design SF based porous structures/scaffolds able to meet the requirements for cellular growth. Processing enables the control of the shape and size of the materials and their pores connectivity and content. The additional silk biocompatibility and controlled degradability make SF a promising

material to mimic the human body's cell tissue, including bone, vascular, neural, skin, cartilage, ligaments, tendons, cardiac, ocular, and bladder [39,160].

ii. ***Therapeutic agent carrier:*** i) the SF heterogeneous chemical structure with various functional groups; ii) its water processability and its ability to become a water-stable structure without chemical use; iii) the chance to control SF based structures shape and configuration; iv) the robust capabilities of SF based materials to absorb polar solvents as well as, other therapeutic agents with variable chemical structure; v) the controllable crystallinity and cross-linking level that enables the control of absorbed agents loading and release; vi) and its biocompatibility, have become SF the ideal material to act as drug delivery vehicles of a wide range of therapeutic agents [39,161]. In this context, SF has been applied as films, scaffolds, and particles, among others, for cancer therapy[161,162], grow factors release[62], proteins, and small molecules delivery[68], among others.

iii. ***Optics, photonics, electronics, and energy:*** i) The ability of Silk to become almost transparent to the visible light; ii) its mechanical robustness and flexibility and, iii) the control of its geometries and topologies from patterning techniques and novel advanced manufacturing process and, iv) its controllable electrical conductivity; have opened new application areas for SF. Especially for regenerated fibers, coatings, and self-standing films to be used as photonic components (i.e., light-guiding applications)[163], optical sensing[45], dielectric gate[164], circuits printing[165] and energy generation, among others[166–168].

All the described properties are compatible between them, allowing the design of SF-based structures where several properties could converge (i.e., optically transparent fiber for light guiding, dielectric devices for biocompatible electronic components, among others). Consequently, SF based optical and optoelectrical devices have been widely used for sensing or measuring in biomedical applications[169].

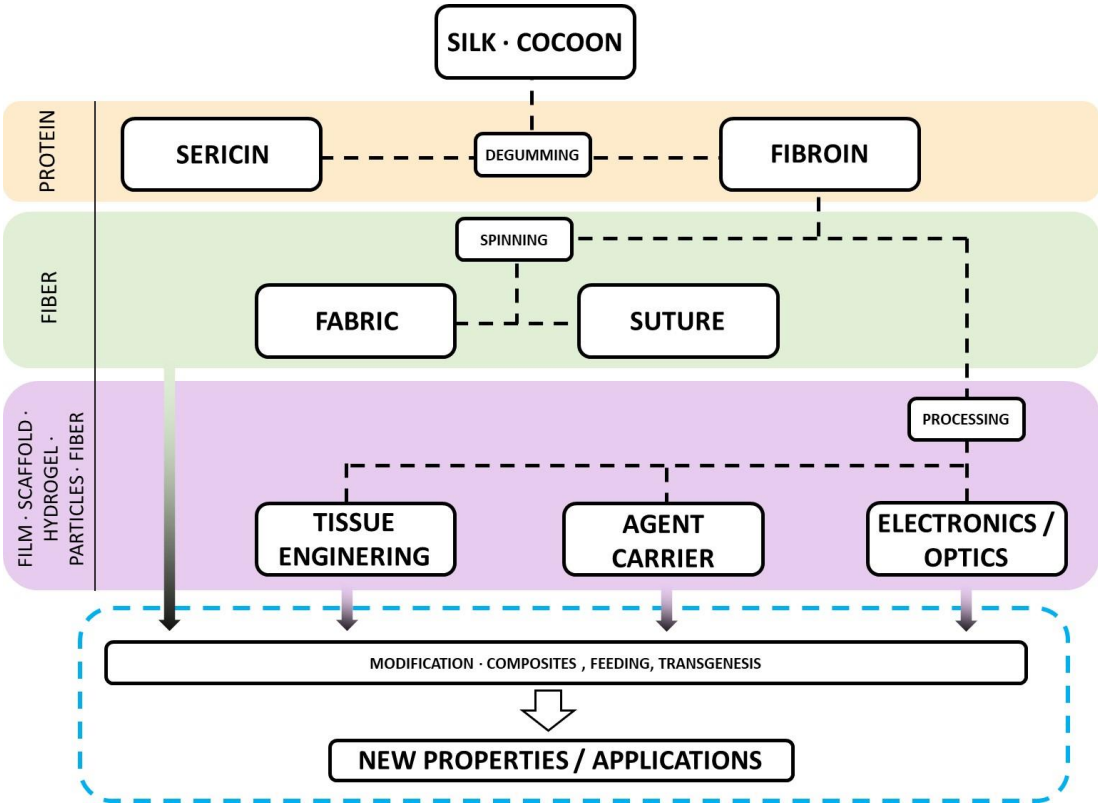

Figure 3. 9. *Scheme of silk common processing and applications*

3.4. REFERENCES

1. Ishay, J. S. & Barenholz-Paniry, V. Thermoelectric effect in hornet (Vespa orientalis) silk and thermoregulation in a hornet's nest. *J. Insect Physiol.* **41**, 753–759 (1995).
2. Zhang, J., Rajkhowa, R., Li, J. L., Liu, X. Y. & Wang, X. G. Silkworm cocoon as natural material and structure for thermal insulation. *Mater. Des.* **49**, 842–849 (2013).
3. Roy, M. *et al.* Carbondioxide gating in silk cocoon. *Biointerphases* **7**, 1–11 (2012).
4. Kaur, J., Rajkhowa, R., Afrin, T., Tsuzuki, T. & Wang, X. Facts and myths of antibacterial properties of silk. *Biopolymers* **101**, 237–245 (2014).
5. Kusurkar, T. S. *et al.* Fluorescent silk cocoon creating fluorescent diatom using a "water glass-Fluorophore ferry. *Sci. Rep.* **3**, 1–8 (2013).
6. Daimon, T. *et al.* The silkworm Green b locus encodes a quercetin 5-O-glucosyltransferase that produces green cocoons with UV-shielding properties. *Proc. Natl. Acad. Sci. U. S. A.* **107**, 11471–11476 (2010).
7. Zhang, J. *et al.* Mechanical properties and structure of silkworm cocoons: A comparative study of Bombyx mori, Antheraea assamensis, Antheraea pernyi and Antheraea mylitta silkworm cocoons. *Mater. Sci. Eng. C* **33**, 3206–3213 (2013).
8. Tulachan, B., Srivastava, S., Kusurkar, T. S. & Sethy, N. K. The role of photo-electric properties of silk cocoon membrane in pupal metamorphosis : A natural solar cell. *Nat. Publ. Gr.* 1–9 (2016) doi:10.1038/srep21915.
9. Rahmathulla, V. K. Management of climatic factors for successful silkworm (Bombyx mori L.) crop and higher silk production: A review. *Psyche (London)* (2012) doi:10.1155/2012/121234.
10. Yazawa, K., Ishida, K., Masunaga, H., Hikima, T. & Numata, K. Influence of Water Content on the β-Sheet Formation, Thermal Stability, Water Removal, and Mechanical Properties of Silk Materials. *Biomacromolecules* **17**, 1057–1066 (2016).
11. Perotto, G. *et al.* The optical properties of regenerated silk fibroin films obtained from different sources. *Appl. Phys. Lett.* **111**, 103702 (2017).
12. Tulachan, B. *et al.* Electricity from the silk cocoon membrane. *Sci. Rep.* **4**, 38–42 (2014).
13. Hu, X., Kaplan, D. & Cebe, P. Effect of water on the thermal properties of silk fibroin. *Thermochim. Acta* **461**, 137–144 (2007).
14. Marelli, B. *et al.* Programming function into mechanical forms by directed assembly of silk bulk materials. *Proc. Natl. Acad. Sci. U. S. A.* **114**, 451–456 (2017).
15. Blossman-Myer, B. & Burggren, W. W. The silk cocoon of the silkworm, Bombyx mori: Macro structure and its influence on transmural diffusion of oxygen and water vapor. *Comp. Biochem. Physiol. - A Mol. Integr. Physiol.* **155**, 259–263 (2010).
16. Horrocks, N. P. C., Vollrath, F. & Dicko, C. The silkmoth cocoon as humidity trap and waterproof barrier. *Comp. Biochem. Physiol. - A Mol. Integr. Physiol.* **164**, 645–652 (2013).
17. Marelli, B., Brenckle, M. A., Kaplan, D. L. & Omenetto, F. G. Silk Fibroin as Edible Coating for Perishable Food Preservation. *Nat. Publ. Gr.* 1–11 (2016) doi:10.1038/srep25263.
18. Choi, M., Heo, J., Kim, H., Kang, S. W. & Hong, J. Control of gas permeability by transforming the molecular structure of silk fibroin in multilayered nanocoatings for CO2 adsorptive separation. *J. Memb. Sci.* **573**, 554–559 (2019).
19. Yu, L., Hu, X., Kaplan, D. & Cebe, P. Dielectric relaxation spectroscopy of hydrated and dehydrated silk fibroin cast from aqueous solution. *Biomacromolecules* **11**, 2766–2775 (2010).
20. Porter, D., Vollrath, F., Tian, K., Chen, X. & Shao, Z. A kinetic model for thermal degradation in polymers with specific application to proteins. *Polymer (Guildf).* **50**, 1814–1818 (2009).
21. Sionkowska, A. & Płanecka, A. Preparation and characterization of silk fibroin/chitosan composite sponges for tissue engineering. *J. Mol. Liq.* **178**, 5–14 (2013).

22. Guan, J., Porter, D. & Vollrath, F. Thermally induced changes in dynamic mechanical properties of native silks. *Biomacromolecules* **14**, 930–937 (2013).

23. Motta, A., Fambri, L. & Migliaresi, C. Regenerated silk fibroin films: Thermal and dynamic mechanical analysis. *Macromol. Chem. Phys.* **203**, 1658–1665 (2002).

24. Zhang, F. *et al.* Silk dissolution and regeneration at the nanofibril scale. *J. Mater. Chem. B* **2**, 3879–3885 (2014).

25. Shen, T. *et al.* Dissolution behavior of silk fibroin in a low concentration CaCl2-methanol solvent: From morphology to nanostructure. *Int. J. Biol. Macromol.* **113**, 458–463 (2018).

26. Fuente, R., Mendioroz, A. & Salazar, A. Revising the exceptionally high thermal diffusivity of spider silk. *Mater. Lett.* **114**, 1–3 (2014).

27. Morikawa, J. *et al.* Silk fibroin as a water-soluble bio-resist and its thermal properties. *RSC Adv.* **6**, 11863–11869 (2016).

28. Shao, Z. & Vollrath, F. Surprising strength of silkworm silk. *Nature* **418**, 741 (2002).

29. Pérez-Rigueiro, J., Viney, C., Llorca, J. & Elices, M. Mechanical properties of single-brin silkworm silk. *J. Appl. Polym. Sci.* **75**, 1270–1277 (2000).

30. Chen, S., Liu, M., Huang, H., Cheng, L. & Zhao, H. Mechanical properties of Bombyx mori silkworm silk fi bre and its corresponding silk fi broin fi lament : A comparative study. **181**, 1–11 (2019).

31. Mohd Ishak, Z. A. & Mat Taib, R. Multifunctional polymer composites using natural fiber reinforcements. in *Multifunctionality of Polymer Composites: Challenges and New Solutions* 71–101 (Elsevier Inc., 2015). doi:10.1016/B978-0-323-26434-1.00003-9.

32. Kawauchi, T. & Takeichi, T. Polybenzoxazine/polysiloxane hybrids. in *Handbook of Benzoxazine Resins* 415–428 (Elsevier, 2011). doi:10.1016/B978-0-444-53790-4.00068-0.

33. Chen, S., Liu, M., Huang, H., Cheng, L. & Zhao, H.-P. Mechanical properties of Bombyx mori silkworm silk fibre and its corresponding silk fibroin filament: A comparative study. *Mater. Des.* **181**, 108077 (2019).

34. Jin, H. J. *et al.* Water-stable silk films with reduced β-sheet content. *Adv. Funct. Mater.* **15**, 1241–1247 (2005).

35. Fu, C., Shao, Z. & Fritz, V. Animal silks: Their structures, properties and artificial production. *Chem. Commun.* 6515–6529 (2009) doi:10.1039/b911049f.

36. Meinel, L. *et al.* Silk-based biomaterials. *Bone* **39**, 922–931 (2006).

37. Jiang, B. C. *et al.* Mechanical Properties of Robust Ultrathin Silk Fibroin Films **. 2229–2237 (2007) doi:10.1002/adfm.200601136.

38. Hsia, Y., Gnesa, E., Jeffery, F., Tang, S. & Vierra, C. Spider Silk Composites and Applications. (1996).

39. Koh, L. D. *et al.* Structures, mechanical properties and applications of silk fibroin materials. *Progress in Polymer Science* vol. 46 86–110 (2015).

40. Loh, Q. L. & Choong, C. Three-dimensional scaffolds for tissue engineering applications: Role of porosity and pore size. *Tissue Eng. - Part B Rev.* **19**, 485–502 (2013).

41. Xu, G., Gong, L., Yang, Z. & Liu, X. Y. What makes spider silk fibers so strong? from molecular-crystallite network to hierarchical network structures. *Soft Matter* **10**, 2116–2123 (2014).

42. Ling, S., Kaplan, D. L. & Buehler, M. J. Nanofibrils in nature and materials engineering. *Nat. Rev. Mater.* **3**, 1–15 (2018).

43. Sommer, M. R., Schaffner, M., Carnelli, D. & Studart, A. R. 3D Printing of Hierarchical Silk Fibroin Structures. *ACS Appl. Mater. Interfaces* **8**, 34677–34685 (2016).

44. Cheng, Y. *et al.* On the strength of β-sheet crystallites of Bombyx mori silk fibroin. *J. R. Soc. Interface* **11**, (2014).

45. Hey Tow, K. *et al.* Exploring the Use of Native Spider Silk as an Optical Fiber for Chemical Sensing. *J. Light. Technol.* **36**, 1138–1144 (2018).

46. Applegate, M. B., Perotto, G., Kaplan, D. L. & Omenetto, F. G. Biocompatible silk step-index optical waveguides. **6**, 641–643 (2015).

47. Chow, D. M. *et al.* Shedding light on the optical properties of spider silk fiber. in *2015 IEEE Photonics Conference, IPC 2015* 333–334 (Institute of Electrical and Electronics Engineers Inc., 2015). doi:10.1109/IPCon.2015.7323526.

48. Parker, B. S. T. *et al.* Biocompatible Silk Printed Optical Waveguides. 2411–2415 (2009) doi:10.1002/adma.200801580.

49. Asha, S., Sangappa, Y. & Ganesh, S. Tuning the refractive index and optical band gap of silk fibroin films by electron irradiation. *J. Spectrosc.* **2015**, (2015).

50. Applegate, M. B. *et al.* Photocrosslinking of Silk Fibroin Using Ribofl avin for Ocular Prostheses. 2417–2420 (2016) doi:10.1002/adma.201504527.

51. ELECTRICAL COXDUCTIOS I S TEXTILES. I The Dependence of the Resistivity* of Cotton, Silk and Wool on Relative Humidity and Moisture Content. **94**, (1924).

52. Oshida, I., Ooshika, Y. & Miyasaka, R. Proton Transfer in Hydrogen Bond and Its Participation in Φ-Electron Systems. *J. Phys. Soc. Japan* **10**, 849–859 (1955).

53. Ranjana, R. *et al.* Fabrication and characterization of conductive silk fibroin–gold nanocomposite films. *J. Mater. Sci. Mater. Electron.* **5**, (2019).

54. Sencadas, V. *et al.* Nano Energy Electroactive properties of electrospun silk fi broin for energy harvesting applications. *Nano Energy* **66**, 104106 (2019).

55. Wideman, T. H., Zautra, A. J. & Edwards, R. R. Structural Origins of Silk Piezoelectricity. **154**, 2262–2265 (2014).

56. On the piezoelectric effect of silk fibers.

57. ANDO, Y. *et al.* Piezoelectricity of oriented silk fibroin films. *Work. Electr. Charg. Dielectr.* (1978).

58. Fukada, E. Piezoelectricity of biopolymers. *Biorheology* **32**, 593–609 (1995).

59. Joseph, J., Singh, S. G., Rama, S. & Vanjari, K. Leveraging Innate Piezoelectricity of Ultra-Smooth Silk Thin Films for Flexible and Wearable Sensor Applications. **17**, 8306–8313 (2017).

60. Joseph, J. *et al.* Silk Piezoelectric Thin Films : Materials to Devices. 31–33 (2016).

61. Joseph, J., Singh, S. G., Rama, S. & Vanjari, K. Piezoelectric Micromachined Ultrasonic Transducer Using Silk Piezoelectric Thin Film. **39**, 2018–2021 (2018).

62. Li, Z. H., Ji, S. C., Wang, Y. Z., Shen, X. C. & Liang, H. Silk fibroin-based scaffolds for tissue engineering. *Front. Mater. Sci.* **7**, 237–247 (2013).

63. Cao, Y. & Wang, B. Biodegradation of silk biomaterials. *Int. J. Mol. Sci.* **10**, 1514–1524 (2009).

64. Peleg, H., Rao, U. & Emrich, L. An Experimental Comparison of Suture Materials for Tracheal and Bronchial Anastomoses. *Thorac. Cardiovasc. Surg.* **34**, 384–388 (1986).

65. Mandal, B. B., Priya, A. S. & Kundu, S. C. Novel silk sericin/gelatin 3-D scaffolds and 2-D films: Fabrication and characterization for potential tissue engineering applications. *Acta Biomater.* **5**, 3007–3020 (2009).

66. Kundu, B. *et al.* Silk proteins for biomedical applications: Bioengineering perspectives. *Prog. Polym. Sci.* **39**, 251–267 (2014).

67. Altman, G. H., Horan, R. L., Weitzel, P. & Richmond, J. C. The use of long-term bioresorbable scaffolds for anterior cruciate ligament repair. *J. Am. Acad. Orthop. Surg.* **16**, 177–187 (2008).

68. Mottaghitalab, F., Farokhi, M., Shokrgozar, M. A., Atyabi, F. & Hosseinkhani, H. Silk fibroin nanoparticle as a novel drug delivery system. *Journal of Controlled Release* vol. 206 161–176 (2015).

69. Chelazzi, D., Badillo-Sanchez, D., Giorgi, R., Cincinelli, A. & Baglioni, P. Self-regenerated silk fibroin with controlled crystallinity for the reinforcement of silk. *J. Colloid Interface Sci.* **576**, 230–240 (2020).

70. Vilaplana, F., Nilsson, J., Sommer, D. V. P. & Karlsson, S. Analytical markers for silk degradation: comparing historic silk and silk artificially aged in different environments. *Anal. Bioanal. Chem.* **407**,

1433–1449 (2015).

71. Kino, R. *et al.* Biodegradation of multilayer silk fibroin and Hydroxyapatite composite material. in *Polymer Preprints, Japan* vol. 54 5042 (Trans Tech Publications Ltd, 2005).

72. Rockwood, D. N. *et al.* Materials fabrication from Bombyx mori silk fibroin. *Nat. Protoc.* **6**, 1612–1631 (2011).

73. Horan, R. L. *et al.* In vitro degradation of silk fibroin. *Biomaterials* **26**, 3385–3393 (2005).

74. Zhu, Z. H., Lu, X. & Zhou, X. H. Study on improving biodegradation process of regenerated silk fibroin fiber. *Adv. Mater. Res.* **175**–**176**, 266–271 (2011).

75. Li, M., Ogiso, M. & Minoura, N. Enzymatic degradation behavior of porous silk fibroin sheets. *Biomaterials* **24**, 357–365 (2003).

76. Saunders, R. M., Conner, M. A. & Kohler, E. M. The Digestion of Silk Fibroin by Rat. *J. Sericultural Sci. Japan* **60**, 402–403 (1991).

77. Guoding Chen, Arai, M. & Hirabayashi, K. Isolation of tyrosine from silk fibroin by enzyme hydrolysis. *J. Sericultural Sci. Japan* **65**, 182–184 (1996).

78. Arai, T., Freddi, G., Innocenti, R. & Tsukada, M. Biodegradation of bombyx mori silk fibroin fibers and films. *J. Appl. Polym. Sci.* **91**, 2383–2390 (2004).

79. Kurioka, A., Yamazaki, M. & Hirano, H. Primary structure and possible functions of a trypsin inhibitor of Bombyx mori. *Eur. J. Biochem.* **259**, 120–126 (1999).

80. Kojthung, A. *et al.* Effects of gamma radiation on biodegradation of Bombyx mori silk fibroin. *Int. Biodeterior. Biodegrad.* **62**, 487–490 (2008).

81. Chen, J., Venkatesan, H. & Hu, J. Chemically Modified Silk Proteins. *Adv. Eng. Mater.* **20**, 1–14 (2018).

82. Lin, N. *et al.* Functionalization of Silk Fibroin Materials at Mesoscale. 1–18 (2016) doi:10.1002/adfm.201603826.

83. Li, G., Liu, H., Li, T. & Wang, J. Surface modification and functionalization of silk fibroin fibers/fabric toward high performance applications. *Mater. Sci. Eng. C* **32**, 627–636 (2012).

84. Periyasamy, S., Gulrajani, M. L. & Gupta, D. Preparation of a multifunctional mulberry silk fabric having hydrophobic and hydrophilic surfaces using VUV excimer lamp. **201**, 7286–7291 (2007).

85. Periyasamy, S., Gupta, D. & Gulrajani, M. L. Nanoscale surface roughening of mulberry silk by monochromatic VUV excimer lamp. *J. Appl. Polym. Sci.* **103**, 4102–4106 (2007).

86. Sargunamani, D. & Selvakumar, N. A study on the effects of ozone treatment on the properties of raw and degummed mulberry silk fabrics. **91**, 2644–2653 (2006).

87. Eren, H. A. EFFECTS OF PLASMA AND OZONE TREATMENTS ON TENSILE AND WHITENESS PROPERTIES OF 100 % SILK. **20**, 43–56 (2015).

88. Bayraktar, O. & Özyıldız, F. Use of ozone for the preparation of functional silk fibroin-based biomaterial loaded with bioactive compounds for biomedical applications. *Ozone Sci. Eng.* **00**, 1–12 (2018).

89. Eren, H. A. & Anis, P. Surface Trimer Removal of Polyester Fibers by Ozone Treatment. *Text. Res. J.* **79**, 652–656 (2009).

90. Uchida, R. *et al.* Effect of plasma-irradiated silk fi broin in bone regeneration. *J. Biosci. Bioeng.* **118**, 333–340 (2014).

91. Sook, H., Hwan, Y., Seok, C., Park, J. & Kyun, D. Surface & Coatings Technology Enhanced chondrogenic responses of articular chondrocytes onto porous silk fi broin scaffolds treated with microwave-induced argon plasma. *Surf. Coat. Technol.* **202**, 5794–5797 (2008).

92. Gu, J., Yang, X. & Zhu, H. Surface sulfonation of silk fibroin film by plasma treatment and in vitro antithrombogenicity study. **20**, 199–202 (2002).

93. Jeong, L. *et al.* Plasma-treated silk fibroin nanofibers for skin regeneration. *Int. J. Biol. Macromol.* **44**,

222–228 (2009).

94. Li, G., Liu, H., Li, T. & Wang, J. Surface modification and functionalization of silk fi broin fi bers / fabric toward high performance applications. *Mater. Sci. Eng. C* **32**, 627–636 (2012).

95. Li, G. *et al.* Silk-Based Biomaterials in Biomedical Textiles and Fiber-Based Implants. *Adv. Healthc. Mater.* **4**, 1134–1151 (2015).

96. Heichel, D. L. & Burke, K. A. Enhancing the Carboxylation Efficiency of Silk Fibroin through the Disruption of Noncovalent Interactions. *Bioconjug. Chem.* **31**, 1307–1312 (2020).

97. Terry, A. E., Knight, D. P., Porter, D. & Vollrath, F. pH induced changes in the rheology of silk fibroin solution from the middle division of Bombyx mori silkworm. *Biomacromolecules* **5**, 768–772 (2004).

98. Lammel, A. S., Hu, X., Park, S. H., Kaplan, D. L. & Scheibel, T. R. Controlling silk fibroin particle features for drug delivery. *Biomaterials* **31**, 4583–4591 (2010).

99. Matsumoto, A. *et al.* Mechanisms of silk fibroin sol-gel transitions. *J. Phys. Chem. B* **110**, 21630–21638 (2006).

100. Shaw, K. L., Grimsley, G. R., Yakovlev, G. I., Makarov, A. A. & Pace, C. N. The effect of net charge on the solubility, activity, and stability of ribonuclease Sa. *Protein Sci.* **10**, 1206–1215 (2001).

101. Foo, C. W. P. *et al.* Role of pH and charge on silk protein assembly in insects and spiders. *Appl. Phys. A Mater. Sci. Process.* **82**, 223–233 (2006).

102. Ha, S. W., Tonelli, A. E. & Hudson, S. M. Structural studies of Bombyx mori silk fibroin during regeneration from solutions and wet fiber spinning. *Biomacromolecules* **6**, 1722–1731 (2005).

103. Cho, H. J., Ki, C. S., Oh, H., Lee, K. H. & Um, I. C. Molecular weight distribution and solution properties of silk fibroins with different dissolution conditions. *Int. J. Biol. Macromol.* **51**, 336–341 (2012).

104. Murphy, A. R., John, P. S. & Kaplan, D. L. Modification of silk fibroin using diazonium coupling chemistry and the effects on hMSC proliferation and differentiation. *Biomaterials* **29**, 2829–2838 (2008).

105. Serban, M. A. & Kaplan, D. L. PH-sensitive ionomeric particles obtained via chemical conjugation of silk with poly(amino acid)s. *Biomacromolecules* **11**, 3406–3412 (2010).

106. Love, C. J., Serban, B. A., Katashima, T., Numata, K. & Serban, M. A. Mechanistic Insights into Silk Fibroin's Adhesive Properties via Chemical Functionalization of Serine Side Chains. *ACS Biomater. Sci. Eng.* **5**, 5960–5967 (2019).

107. Murphy, A. R. & Kaplan, D. L. Biomedical applications of chemically-modified silk fibroin. *J. Mater. Chem.* **19**, 6443–6450 (2009).

108. Gotoh, Y., Tsukada, M. & Minoura, N. Chemical Modification of Silk Fibroin with Cyanuric Chloride-Activated Poly(ethylene glycol): Analyses of Reaction Site by 1H-NMR Spectroscopy and Conformation of the Conjugates. *Bioconjug. Chem.* **4**, 554–559 (1993).

109. Gotoh, Y., Niimi, S., Tamura, K., Akahira, R. & Inamura, M. Comparative study between lactose-silk fibroin conjugates and extracellular matrices as a substrate for the culture of human induced pluripotent stem cell-derived hepatocytes. *Biomed. Mater. Eng.* **31**, 35–45 (2020).

110. Bhattacharjee, P., Fernández-Pérez, J. & Ahearne, M. Potential for combined delivery of riboflavin and all-trans retinoic acid, from silk fibroin for corneal bioengineering. *Mater. Sci. Eng. C* **105**, 110093 (2019).

111. Abbott, A., Oxburgh, L., Kaplan, D. L. & Coburn, J. M. Avidin Adsorption to Silk Fibroin Films as a Facile Method for Functionalization. *Biomacromolecules* **19**, 3705–3713 (2018).

112. Mojarradi, H. *Coupling of substances containing a primary amine to hyaluronan via carbodiimide-mediated amidation*. http://www.teknat.uu.se/student.

113. Park, S. N., Park, J. C., Kim, H. O., Song, M. J. & Suh, H. Characterization of porous collagen/hyaluronic acid scaffold modified by 1-ethyl-3-(3-dimethylaminopropyl)carbodiimide cross-linking. *Biomaterials* **23**, 1205–1212 (2002).

114. Zhang, X. *et al.* Thiolation and characterization of regenerated Bombyx mori silk fibroin films with reduced glutathione. *BMC Chem.* **13**, 1–9 (2019).

115. Zhang, X. *et al.* Surface modification of Bombyx mori silk fibroin film via thiol-ene click chemistry. *Processes* **8**, 1–9 (2020).

116. Mohammadzadehmoghadam, S. & Dong, Y. Fabrication and characterization of electrospun silk fibroin/gelatin scaffolds crosslinked with glutaraldehyde vapor. *Front. Mater.* **6**, 1–12 (2019).

117. Zhu, B. *et al.* Optimization of Glutaraldehyde Vapor Treatment for Electrospun Collagen/Silk Tissue Engineering Scaffolds. *ACS Omega* **2**, 2439–2450 (2017).

118. Wang, Y. X., Qin, Y. P., Kong, Z. J., Wang, Y. J. & Ma, L. Glutaraldehyde cross-linked silk fibroin films for controlled release. in *Advanced Materials Research* vols 887–888 541–546 (Trans Tech Publications Ltd, 2014).

119. Qiao, F. *et al.* Silk fibroin-coated PLGA dimpled microspheres for retarded release of simvastatin. *Colloids Surfaces B Biointerfaces* **158**, 112–118 (2017).

120. Gotoh, Y., Tsukada, M., Minoura, N. & Imai, Y. Synthesis of poly(ethylene glycol)-silk fibroin conjugates and surface interaction between L-929 cells and the conjugates. *Biomaterials* **18**, 267–271 (1997).

121. Yang, Y., Chen, J., Migliaresi, C. & Motta, A. Natural Fibrous Protein for Advanced Tissue Engineering Applications: Focusing on Silk Fibroin and Keratin. *Adv. Exp. Med. Biol.* **1249**, 39–49 (2020).

122. Ding, X. *et al.* Trilayered sulfated silk fibroin vascular grafts enhanced with braided silk tube. *J. Bioact. Compat. Polym.* **31**, 613–623 (2016).

123. Yi, S. *et al.* Scalable fabrication of sulfated silk fibroin nanofibrous membranes for efficient lipase adsorption and recovery. *Int. J. Biol. Macromol.* **111**, 738–745 (2018).

124. Zhu, Y., Yu, X., Zhang, T., Li, P. & Wang, X. Biomimetic sulfated silk nanofibrils for constructing rapid mid-molecule toxins removal nanochannels. *J. Memb. Sci.* **598**, 117667 (2020).

125. Heichel, D. L. & Burke, K. A. Dual-Mode Cross-Linking Enhances Adhesion of Silk Fibroin Hydrogels to Intestinal Tissue. *ACS Biomater. Sci. Eng.* **5**, 3246–3259 (2019).

126. Monteiro, N. *et al.* Immobilization of bioactive factor-loaded liposomes on the surface of electrospun nanofibers targeting tissue engineering. *Biomater. Sci.* **2**, 1195–1209 (2014).

127. Laomeephol, C. *et al.* Exploring the gelation mechanisms and cytocompatibility of gold (III)-mediated regenerated and thiolated silk fibroin hydrogels. *Biomolecules* **10**, 1–14 (2020).

128. Hossain, M. R., Mallik, A. K. & Rahman, M. M. Fundamentals of chitosan for biomedical applications. in *Handbook of Chitin and Chitosan* 199–230 (Elsevier, 2020). doi:10.1016/b978-0-12-817966-6.00007-8.

129. Xu, Y. *et al.* Structure and properties of silk fibroin grafted carboxylic cotton fabric via amide covalent modification. *Carbohydr. Polym.* **161**, 99–108 (2017).

130. Bhattacharjee, P., Naskar, D., Maiti, T. K., Bhattacharya, D. & Kundu, S. C. Journal of Colloid and Interface Science Non-mulberry silk fibroin grafted poly (Є -caprolactone)/ nano hydroxyapatite nanofibrous scaffold for dual growth factor delivery to promote bone regeneration. *J. Colloid Interface Sci.* **472**, 16–33 (2016).

131. Bhattacharjee, P., Naskar, D., Maiti, T. K., Bhattacharya, D. & Kundu, S. C. Investigating the potential of combined growth factors delivery, from non-mulberry silk fibroin grafted poly(ε-caprolactone)/hydroxyapatite nanofibrous scaffold, in bone tissue engineering. *Appl. Mater. Today* **5**, 52–67 (2016).

132. Taddei, P. & Tsukada, M. Stability toward alkaline hydrolysis of B . mori silk fibroin grafted with methacrylamide. 731–739 (2016) doi:10.1002/jrs.4892.

133. Quiñones, J. P., Roschger, C., Zierer, A., Peniche, C. & Brüggemann, O. Steroid-grafted silk fi broin conjugates for drug and agrochemical delivery. *Eur. Polym. J.* **119**, 169–175 (2019).

134. Mehraz, L., Nouri, M. & Namazi, H. Electrospun silk fibroin / β -cyclodextrin citrate nanofibers as a

novel biomaterial for application in controlled drug release. *Int. J. Polym. Mater. Polym. Biomater.* **0**, 1–11 (2018).

135. Yuan, J., Wang, L., Xu, B. & Wang, P. Enzymatic deposition of PPy onto cPEG-grafted silk fibroin membrane to achieve conductivity †. 7042–7050 (2020) doi:10.1039/d0nj00772b.

136. Korematsu, A., Furuzono, T. & Yasuda, S. Nano-scaled hydroxyapatite / polymer composite III . Coating of sintered hydroxyapatite particles on poly (4-methacryloyloxyethyl trimellitate anhydride) -grafted silk fibroin fibers. **6**, 67–71 (2005).

137. Furuzono, T. & Kishida, A. Nano-scaled hydroxyapatite / polymer composite I . Coating of sintered hydroxyapatite particles on grafted silk ® broin ® bers through chemical bonding. **5**, 19–23 (2004).

138. Majumder, S. *et al.* Zinc Oxide Nanoparticles Functionalized on Hydrogel Grafted Silk Fibroin Fabrics as E ffi cient Composite Dressing.

139. Gibson, I. & Rosen, D. *Additive Manufacturing Technologies*.

140. Cheung, H., Ho, M. & Cardona, F. Natural fibre-reinforced composites for bioengineering and environmental engineering applications. *Compos. Part B Eng.* **40**, 655–663 (2009).

141. Nathwani, B. B., Jaffari, M., Juriani, A. R., Mathur, A. B. & Meissner, K. E. Fabrication and characterization of silk-fibroin-coated quantum dots. *IEEE Trans. Nanobioscience* **8**, 72–77 (2009).

142. Kim, H., Che, L., Ha, Y. & Ryu, W. Mechanically-reinforced electrospun composite silk fibroin nanofibers containing hydroxyapatite nanoparticles. *Mater. Sci. Eng. C* **40**, 324–335 (2014).

143. Goujon, N., Wang, X., Rajkowa, R. & Byrne, N. Regenerated silk fibroin using protic ionic liquids solvents: Towards an all-ionic-liquid process for producing silk with tunable properties. *Chem. Commun.* **48**, 1278–1280 (2012).

144. Niu, Y. *et al.* Enhancing neural differentiation of induced pluripotent stem cells by conductive graphene/silk fibroin films. *J. Biomed. Mater. Res. Part A* **106**, 2973–2983 (2018).

145. Jia, X. *et al.* A Biodegradable Thin-Film Magnesium Primary Battery Using Silk Fibroin-Ionic Liquid Polymer Electrolyte. *ACS Energy Lett.* **2**, 831–836 (2017).

146. Karahaliloğlu, Z., Yalçın, E., Demirbilek, M. & Denkbaş, E. B. Magnetic silk fibroin e-gel scaffolds for bone tissue engineering applications. *J. Bioact. Compat. Polym.* **32**, 596–614 (2017).

147. Ribeiro, M. *et al.* Antibacterial silk fibroin/nanohydroxyapatite hydrogels with silver and gold nanoparticles for bone regeneration. *Nanomedicine Nanotechnology, Biol. Med.* **13**, 231–239 (2017).

148. Zhan, Q. *et al.* Super-strong and uniform fluorescent composite silk from trace AIE nanoparticle feeding. *Compos. Commun.* **21**, 100414 (2020).

149. Wu, G. H. *et al.* Robust composite silk fibers pulled out of silkworms directly fed with nanoparticles. *Int. J. Biol. Macromol.* **104**, 533–538 (2017).

150. Cai, L., Shao, H., Hu, X. & Zhang, Y. Reinforced and ultraviolet resistant silks from silkworms fed with titanium dioxide nanoparticles. *ACS Sustain. Chem. Eng.* **3**, 2551–2557 (2015).

151. Zheng, X. *et al.* Intrinsically Fluorescent Silks from Silkworms Fed with Rare-Earth Upconverting Phosphors. *ACS Biomater. Sci. Eng.* **4**, 4021–4027 (2018).

152. Fan, S. *et al.* Super-strong and Intrinsically Fluorescent Silkworm Silk from Carbon Nanodots Feeding. *Nano-Micro Lett.* **11**, (2019).

153. Wang, Q., Wang, C., Zhang, M., Jian, M. & Zhang, Y. Feeding Single-Walled Carbon Nanotubes or Graphene to Silkworms for Reinforced Silk Fibers. *Nano Lett.* **16**, 6695–6700 (2016).

154. Ramos, N. *et al.* Toward Spinning Greener Advanced Silk Fibers by Feeding Silkworms with Nanomaterials. *ACS Sustain. Chem. Eng.* **8**, 11872–11887 (2020).

155. Leem, J. W., Fraser, M. J. & Kim, Y. L. Transgenic and Diet-Enhanced Silk Production for Reinforced Biomaterials: A Metamaterial Perspective. *Annu. Rev. Biomed. Eng.* **22**, 79–102 (2020).

156. Li, Z. *et al.* Construction of transgenic silkworm spinning antibacterial silk with fluorescence. *Mol. Biol. Rep.* **42**, 19–25 (2015).

157. Saviane, A. *et al.* Intrinsic antimicrobial properties of silk spun by genetically modified silkworm strains. *Transgenic Res.* **27**, 87–101 (2018).

158. Koh, L.-D. *et al.* Advancing the frontiers of silk fibroin protein-based materials for futuristic electronics and clinical wound-healing (Invited review). *Mater. Sci. Eng. C* **86**, 151–172 (2018).

159. Holland, C., Numata, K., Rnjak-Kovacina, J. & Seib, F. P. The Biomedical Use of Silk: Past, Present, Future. *Advanced Healthcare Materials* vol. 8 (2019).

160. Kundu, B., Rajkhowa, R., Kundu, S. C. & Wang, X. Silk fibroin biomaterials for tissue regenerations. *Adv. Drug Deliv. Rev.* **65**, 457–470 (2013).

161. Jastrzebska, K. *et al.* Silk as an innovative biomaterial for cancer therapy. *Reports Pract. Oncol. Radiother.* **20**, 87–98 (2015).

162. Elahi, M., Ali, S., Tahir, H. M., Mushtaq, R. & Bhatti, M. F. Sericin and fibroin nanoparticles—natural product for cancer therapy: a comprehensive review. *Int. J. Polym. Mater. Polym. Biomater.* **0**, 1–14 (2020).

163. Kujala, S., Mannila, A., Karvonen, L., Kieu, K. & Sun, Z. Natural Silk as a Photonics Component : a Study on Its Light Guiding and Nonlinear Optical Properties. *Nat. Publ. Gr.* 1–9 (2016) doi:10.1038/srep22358.

164. Wang, C.-H., Hsieh, C.-Y. & Hwang, J.-C. Flexible Organic Thin-Film Transistors with Silk Fibroin as the Gate Dielectric. *Adv. Mater.* **23**, 1630–1634 (2011).

165. Hota, M. K., Bera, M. K., Kundu, B., Kundu, S. C. & Maiti, C. K. A Natural Silk Fibroin Protein-Based Transparent Bio-Memristor. 4493–4499 (2012) doi:10.1002/adfm.201200073.

166. Wen, D. L. *et al.* Printed silk-fibroin-based triboelectric nanogenerators for multi-functional wearable sensing. *Nano Energy* **66**, 104123 (2019).

167. Liu, C. *et al.* Toward large-scale fabrication of triboelectric nanogenerator (TENG) with silk-fibroin patches film via spray-coating process Chaoran. *Nano Energy* **41**, 359–366 (2017).

168. Tao, H. materials-A. road to sustainable high technology, Kaplan, D. L. & Omenetto, F. G. Silk materials - A road to sustainable high technology. *Adv. Mater.* **24**, 2824–2837 (2012).

169. Fan, S. N. *et al.* Silk materials for medical, electronic and optical applications. *Science China Technological Sciences* vol. 62 903–918 (2019).

170. Yazawa, K., Ishida, K., Masunaga, H., Hikima, T. & Numata, K. Influence of Water Content on the β-Sheet Formation, Thermal Stability, Water Removal, and Mechanical Properties of Silk Materials. *Biomacromolecules* **17**, 1057–1066 (2016).

This chapter is a first approach to explore the potential of Silk Fibroin (SF) as functional material. Focused on the incoming technological and industrial transition (Industry 4.0), SF has been used to develop sensors and actuators.

To enlarge its original properties SF has been used as matrix to hold fillers of different nature: i) electrical conductive, carbon nanotubes (CNT), ii) electrical conductive and optically transparent, silver nanowires (SNW), iii) magnetic, cobalt ferrite nanoparticles (CFO) and iv) ionic conductive, ionic liquids (IL).

The properties of obtained composites have been explored in order to establish the effect of the different fillers on the SF matrix. The most outstanding samples, have been finally used as functional component of different devices i) piezoresistive force sensors (SF/CNT), ii) object recognition device (SF/SNW), iii) magnetic actuator (SF/CFO) and iv) bending actuator (SF/IL)

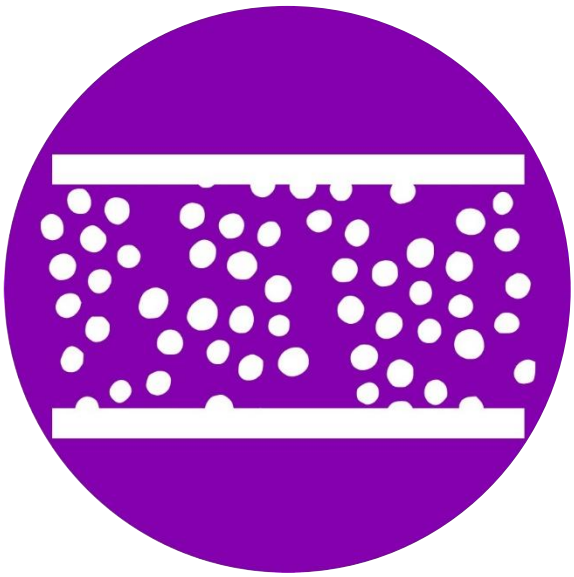

Chapter.4

ACTIVE SILK FIBROIN FOR SENSORS AND ACTUATORS

The control of coal combustion around the XVII century end led to a profound change of society by incorporating mechanical traction instruments into production lines. This process was known as the first industrial revolution (Industry 1.0) ***(Figure 4.1***). At the end of the XVIV century, the industrial organization and the formation of assembly lines took with him the second industrial revolution (Industry 2.0). The development of electronics, computing, and automated production along the XX century, brought the third industrial revolution (Industry 3.0).

The internet's global connectivity has currently made possible the replacement of humans' primary responsibilities by self-controlled devices. This digital interconnection has been named the Internet of Things (IoT). The irruption of these technologies on the industry implies the emergence of more efficient and adaptable factories, connected through autonomous systems, which can identify most favoring patterns and conditions[1]. This transition has been named the fourth industrial revolution (Industry 4.0)[2].

This new revolution carries the need to design and manufacture components and devices more adapted to the technological requirements, specifically transducers that can transform one form of energy into another. Among them, two main types could be distinguished: i) sensors, devices able to measure and responds to a signal, i.e., a stimulus produced by some energy (heat, light, motion, or chemical reaction); and ii) actuators, devices that convert energy into a measurable force under the specific stimulus, to make another device to act.

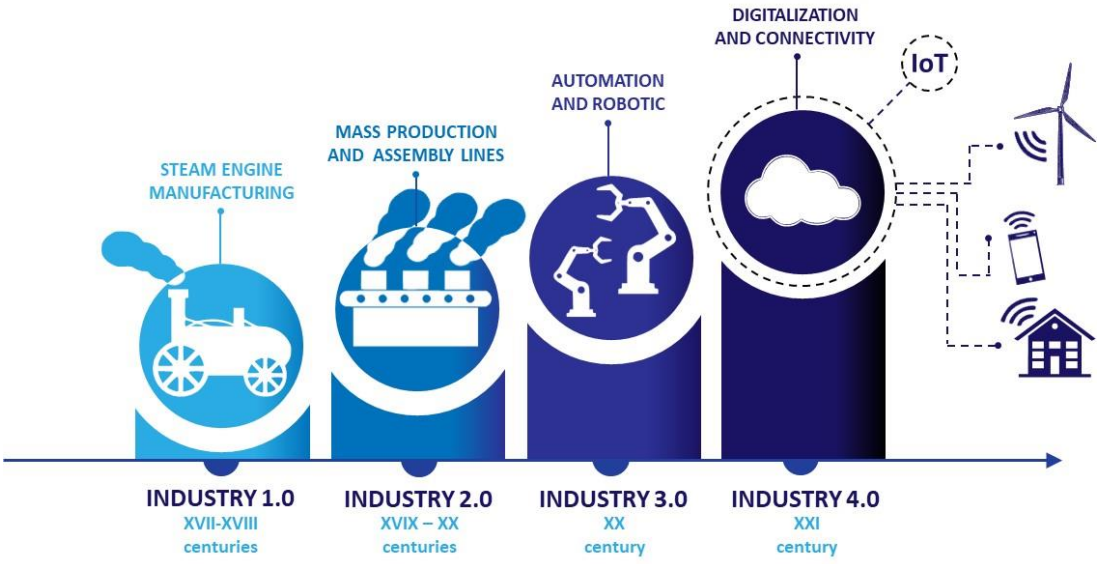

Figure 4. 1*. The four industrial revolutions*

Sensors and actuators are commonly found together because of their synergic behavior: sensors "read" the environmental conditions (an input) and convert it into a measurable signal, which can be translated into a human-readable display (output) or transmitted for further reading or processing. Actuators receive this signal and "respond" in a controlled way.

The integration of both components into a system makes possible its automation. Thus, both are one of the fundamental building blocks of modern data acquisition systems and automation. It is estimated that the global sensor market will grow by 12% from 2020 to 2025[3] (at a compound annual growth rate (CAGR)), while the actuators market is projected to reach an 8.6 % GAGR growth until 2024[4].

There are many sensor types. They strongly differ in function, output signal, composition, behavior, or even shape. Thus, the standard classification is based on the signal that they measure. Some of the most common ones are vision and imaging sensors, temperature sensors, radiation sensors, proximity sensors, humidity sensors, gas and chemical sensors, among others.

Regarding actuators, they can be classified according to their working principles: i) conventional actuators comprise a group founded on the phenomenon of electromagnetism; ii) Hydraulic actuators uses hydraulic energy by transferring the mechanical energy to a fluid; and iii) nonconventional actuators, which behavior is associated with the material's structure[5].

Among the different materials to develop sensors and actuators, those based on smart materials (with the self-ability to respond in a controllable way to external stimuli) are gaining special attention. This is mainly because their use reduces the device's complexity and derived features, e.g., processing steps, resources use, production costs, and waste, among others[6,7].

There are many types of smart materials, and the most common are: piezoelectric materials, shape-memory materials, chromo active materials, magnetorheological materials, and photoactive materials[7]. Some materials are naturally smart, e.g., piezoelectric quartz crystals[8] or shape memory of nickel-titanium alloys[9]. But usually, several materials are combined (not necessary smart materials) to obtain a hybrid smart material[10,11]. These materials are named smart composite materials, and due to their controllable combination, it is possible to adapt the final behavior of the material[12].

Among the different techniques for composite smart materials manufacture (see 3.2.3 apart), the addition of particles into a polymeric matrix represents one of the most promising routes, mainly because i) the wide range of available particles allows the addition of different properties[13–15], ii) the possibility to conserve the original self-properties while new ones are provided[16,17] and iii) the reproducibility of the production processes[18,19].

The main components of these polymeric composites are i) a polymer matrix, which can be considered the passive phase since it ensures the integrity of the whole material and gives structural stability, and ii) fillers or active phase, which give to the composite specific new properties. Filler's nature, shape, aspect ratio, or contents strongly affect the composite material's final behavior, so they must be carefully selected and controlled to adapt the composite material to the demanded requirements[20].

Currently, several smart polymeric materials are used for sensors and actuators development, e.g., zirconate titanate (PZT)– polyvinyl fluoride (PVDF) ferroelectric Sensors[21], Co(II)Fe(III) single bond O(OH)/P(VDF-TrFE) based magnetoelectric sensors [22] and carbon-based thermal actuator[23], among others. Unfortunately, most are based on synthetic materials matrix, which hinders the transition towards sustainability. In response to this, the use of bio-based materials represents a viable option, since i) their excellent properties and the increasing knowledge around them enables their practical use in specific requirements[1,2]; ii) the biodegradable matrix allows a more comfortable recovery of fillers after the component's useful life, iii) reduces the consumption of synthetic materials and the derived social, economic and environmental injuries and iv) allows the incorporation of new properties, into the new devices, unusual in synthetic polymers e.g. biocompatibility and natural accessibility.

The use of bio-based materials for sensors and actuators development has been explored. In general, flexible, stretchable, and durable support materials are selected, such as cellulose and chitin[24]. As fillers, carbonaceous materials (e.g., graphene and carbon black)[25,26], metallic particles (e.g., iron oxides, and cupper)[27,28] and conductive polymers (e.g., polyaniline)[29] are commonly used. However, bio-based materials are still slightly explored in this area.

Silk Fibroin (SF), in particular, has been very little used for sensors and actuators development, despite its promising intrinsic properties: i) it can be easily adapted to different requirements and scenarios, thanks to its versatile processability; ii) its unique properties,

especially its mechanical robustness, optical transparency and structural stability and iii) it can be processed through non-complex and less-pollutant procedures that avoid residual pollution and which facilitates industrial scaling.

In this work, the ability of Silk Fibroin as a matrix for sensors (piezoresistive sensors and object recognition) and actuators (magnetic and bending) development has been explored. For that, SF has been combined with different fillers such as carbon nanotubes, silver nanowires, cobalt ferrite, and ionic liquids to develop smart composite materials. The achieved new properties have been characterized, and the most promising materials used in functional devices are potentially applicable for IoT and Industry 4.0 revolution.

4.1. SILK FIBROIN / CARBON NANOTUBES BASED PIEZORESISTIVE FORCE SENSOR

BASED ON: A. Reizabal et al. Optimized silk fibroin piezoresistive nanocomposites for pressure sensing applications based on natural polymers, Nanoscale Adv., vol. 1, no. 6, pp. 2284—2292, 2019.

One of the IoT objectives is to monitor and respond in real-time to different environmental variables. To make it real, it is required to develop devices able to "read" the environmental changes and respond to specific conditions in a controlled way, e.g., light, heat, movement, humidity, pressure, or any other environmental phenomenon.

In function of the sensed physical stimulus, different sensors are distinguished. In specific, the force sensor measures the tension and compression forces and transforms them into a measurable electric signal, which changes in function on the sensed force. There exist several technologies for force sensor construction. Among them, those based on piezoresistive materials (able to change their bulk electrical resistance when they are subjected to a mechanical stimulus) represent one of the most promising options since they enable accurate measurement using simple devices. There exist a wide range of piezoresistive materials able to respond as force sensors. However, considering their flexibility, easy processability, and integrability, the most outstanding ones are piezoresistive polymer-based composites[30,31].

The most used fillers for this purpose are carbonaceous ones such as carbon black[32], carbon nanofibers (CNF)[33], carbon nanotubes (CNT)[34], and graphene [35]. In particular, CNT represents a highly attractive choice because it can be obtained from non-pollutant processes[36]. Also, their low mass density, high aspect ratio, extraordinary strength, and flexibility make them the ideal fillers for enhancing the mechanical, electrical, and thermal properties of composites[37].

The matrices for piezoresistive composites include from thermoplastics[38] to elastomers [39], but bio-based materials are scarce in the literature. Some works based on SF and CNT composites have been reported for i) SF fibers mechanical reinforcement[40], ii) SF crystal structure control[41], iii) biomedical applications [40,42], and iv) enzymatic biofuel cells development[43]. But there is a lack of studies around SF's potentiality as an electronic component for sensors development. Thus, to explore more in deep the SF functionality and contribute to industry 4.0, this work proposes developing piezoresistive force sensors based on SF nanocomposites doped with CNT. Variable fillers compositions have been explored to analyze the effect of the filler over the SF matrix. Morphological, thermal, mechanical,

and electrical properties of composites have been analyzed, and SF/CNT composites percolation threshold has been defined. Finally, the most outstanding sample has been applied in the construction of a force sensor device. (***Figure 4.1.1***)

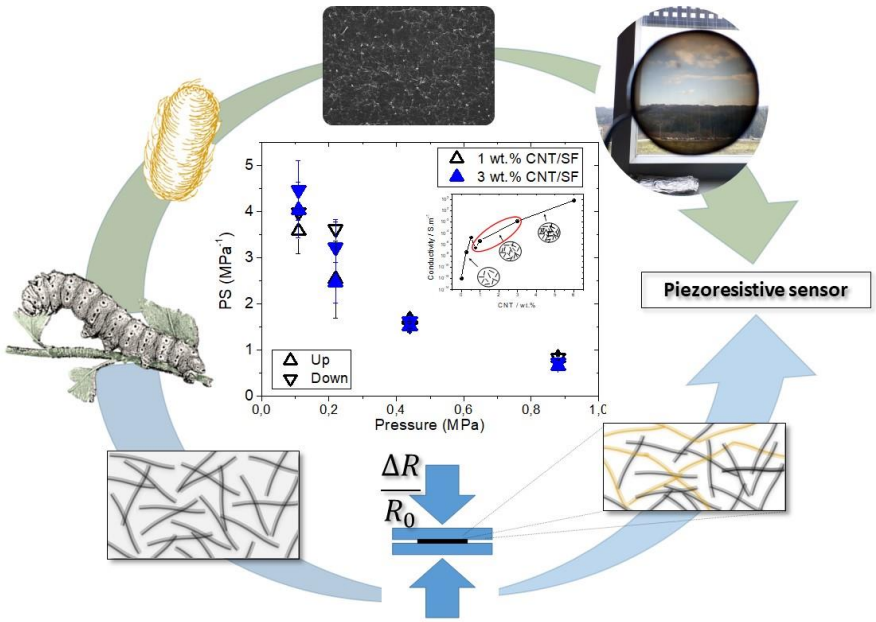

Figure 4.1. 1. *Graphical abstract of SF/CNT based piezoresistive sensor.*

4.1.1. MATERIALS AND EXPERIMENTAL METHODS

Materials

Bombyx mori cocoons were supplied by APPACDM from Castelo Branco (Portugal). Carbon nanotubes (CNTs) were provided by Nanocyl (reference NC7000, purity of 90%, 1.5 μm length and an outer mean diameter of 9.5 nm).

SF extraction

Bombyx mori cocoons were firstly degummed in 0.02M Na_2CO_3 solution for 30 minutes. For each 1 g of silk, 40 ml of aqueous Na_2CO_3 solution were used. Obtained neat SF fibres were then washed in a distilled water bath and completely dried before their posterior use.

To obtain an easily procurable solution, SF was dissolved in a formic acid/$CaCl_2$ 0.2M solution, with 10 ml FA per gram of SF. Non-solved residues were removed by centrifugation at 7500 rpm during 10 min. The silk solution was then placed in an airing chamber to allow fast evaporation of formic acid within 24 h. $CaCl_2$ salts retained on the film were removed by a water bath. Water was changed several times per day until reaching

a constant value of conductivity. Cleaned SF was finally dried at room temperature for 24 hours leading to brittle and whitish neat SF films.

Samples preparation

For SF/CNT composites manufacture, solutions were prepared in formic acid with different amounts of CNT (0.25, 0.5, 0.75, 1, 3, 6 wt. %, related to SF). Fillers were initially added to formic acid and mixed by ultra-sonication bath, during 3h, to ensure good dispersion and to prevent nanotubes agglomeration. Afterwards, SF (8% (wt. %)) was added to the dispersion and. Once proteins were completely dissolved by magnetic stirring, the solution was treated in a sonication needle during 5 minutes with 30 % of amplitude, 7 seconds of treatment and 3 seconds of landing, to ensure the correct dispersion of the fillers. The obtained SF/CNT mixture was cast overnight in polypropylene Petri dishes and dried to remove all the formic acid and promote β-sheets crystals formation. The processing steps and corresponding sequence are illustrated in ***Figure 4.1.2***.

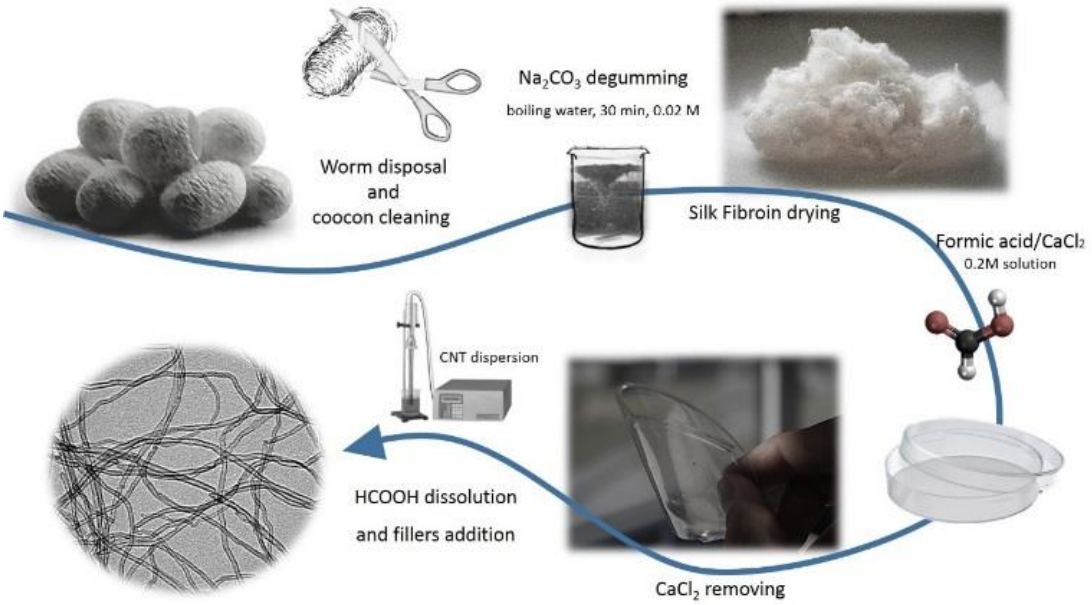

Figure 4.1. 2. *Main experimental steps for the processing of SF/CNT composites*

Characterization techniques

The morphology of the samples and the dispersion of CNT were examined with a scanning electron microscope (SEM, NanoSEM - FEI Nova 200 (FEG/SEM)) with an accelerating voltage of 15 kV. The films were previously deposited with a conductive gold layer by sputtering with a Polaron SC502 apparatus.

The structure of the silk fibroin films and possible interaction between the CNT and the polymer matrix were evaluated by Fourier Transformed Infrared Spectroscopy (FTIR) performed at room temperature with a Jasco FT/IR-4100 system. FTIR spectra were collected in the ATR mode from 4000 to 600 cm^{-1} after 64 scans with a resolution of 4 cm^{-1}.

During silk fibroin secondary structure formation, polypeptide chains interact one each other. These interactions are mainly based on H-bonds formed between amino (NH) and carbonyl (CO) groups[44]. As consequence, proteins secondary structure is directly related with the hydrogen bonds involved in the peptides carbonyl groups. FTIR Amide I region provides information about on the stretching vibrations of pure C=O bonds in the protein backbones. Thus, this region can be taken as a good indicator of the inter- and intramolecular interactions occurring in proteins chain backbone[45]. Thus the deconvolution of the amide I region FTIR patters allows obtaining the secondary structures formed during secondary folding[46].

To determine the relative content of the secondary structures present in each sample, the deconvolution of FTIR band in the spectral region corresponding to Amide I was carried out with the OriginPro 8.1 software (OriginLab, Northampton). Previous to deconvolution, the amide I region was set as display range and the baseline was subtracted making a straight line between the two extreme points. The approximate deconvolution peaks position of amide I region were placed using the minimum peaks from the second derivate, a cut of the frequency of 0.4 from FFT filter and 10% threshold height. The deconvolution of the peaks was finally performed by Gaussian line shape profile until peaks convergence.

The thermal behaviour of the samples was determined by Differential Scanning Calorimetry (DSC) and Thermo Gravimetric Analysis (TGA).

DSC was performed with a Mettler Toledo DSC 822e apparatus with sample robot between 25 and 350 ºC at 10 °C min^{-1} under nitrogen purge (50 $mL \cdot min^{-1}$) in 40 µL aluminium cans with perforated lids. Before DSC data recovering, thermal annealing from 25 to 170 ºC was performed to remove the water absorbed by the SF matrix. TGA was carried out using a TGA/SDTA 851e Metter Toledo apparatus under a flow rate of 50 $mL \cdot min^{-1}$ operating between 25 to 800 °C at 10 °C min^{-1}.

Dynamic mechanical analysis (DMA) was performed with a Metter Toledo DMA1 apparatus in the tensile mode. The storage modulus and loss tangent were measured as a function of

temperature at a frequency of 1 Hz from 0 ºC to 280 ºC and a heating rate of 3 ºC·min^{-1}. The measurements were performed in samples with typical dimensions of 10mm x 4mm x 50 µm.

Dielectric measurements were performed using a Quadtech 1920 LCR precision meter. The capacity and the dielectric losses (tan δ) were obtained at room temperature in the frequency range of 20 Hz to 1 MHz with an applied voltage of 0.5 V. Circular gold electrodes of 5 mm diameter were deposited on both sides of each sample with a Polaron SC502 sputter system. The error associated with the dielectric measurements is ~1 %, mainly due to the determination of the geometrical parameters with as Mitutoyo micrometre.

The real part of the dielectric function (ε′) and the a.c. electrical conductivity (σ′) were determined through the following equations:

$$\varepsilon' = \frac{C.d}{\varepsilon_0.A} \tag{4.1.1}$$

and

$$\sigma' = \varepsilon_0 \omega \varepsilon' tan\delta \tag{4.1.2}$$

Where C is the capacitance (F), ε_o is the permittivity of vacuum (8.85×10^{-12} F m^{-1}), A is the electrode area (m^2), d is the thickness of samples (m) and $\omega=2\pi\nu$ is the angular frequency.

The D.C. electrical conductivity of the samples was obtained by a 2-wire method with an applied voltage between ±10 V and measuring the current through a Keighley's 487 picoammeter/voltage source. Volume resistivity was measured at room temperature in samples with circular contacts of 5 mm diameter and the resistivity of the samples (ρ in S/m) was obtained from the slope of the I–V curves and calculated by:

$$\rho = \frac{R.A}{d} \tag{4.1.3}$$

where R is the resistance of the sample, d its thickness and A is the electrode area.

Electro-mechanical tests were performed by measuring the volume electrical resistance (Agilent 34401A multimeter) in real-time using the two-probe method while the samples were subjected to the cyclic compression load with a Shimadzu AG-IS with a load cell of 500 N (Instron 5544) at 2 mm·min^{-1}.

The electro-mechanical test was evaluated by the pressure sensitivity (PS) through the following equation [47]:

$$PS = \frac{\Delta R / R_0}{P} \tag{4.1.4}$$

where R_0 is the initial electrical resistance in the unloaded state, ΔR is the electrical resistance change and P is applied pressure.

For each experimental technique, at least three measurements were performed in each sample.

4.1.2. RESULTS AND DISCUSSION

Morphological and FTIR characterisation.

The morphology of the samples and the dispersion of the CNT were evaluated by SEM. ***Figure 4.1.3*** shows the SEM images of SF/CNT composites with 0, 0.75 and 6 wt.% CNT content, being these images representative for the rest of the concentrations.

It is shown that the compact morphology of neat SF (***Figure 4.1.3a***) is preserved in the composites (***Figure 4.1.3b-c***). A good dispersion of CNT (bright spots in ***Figure 4.1.3b-c***) is observed for all the composites, independently of the filler content. Larger agglomerates were observed for the SF/CNT composites, with CNT clusters of ~1–2 μm in size, well distributed throughout the sample.

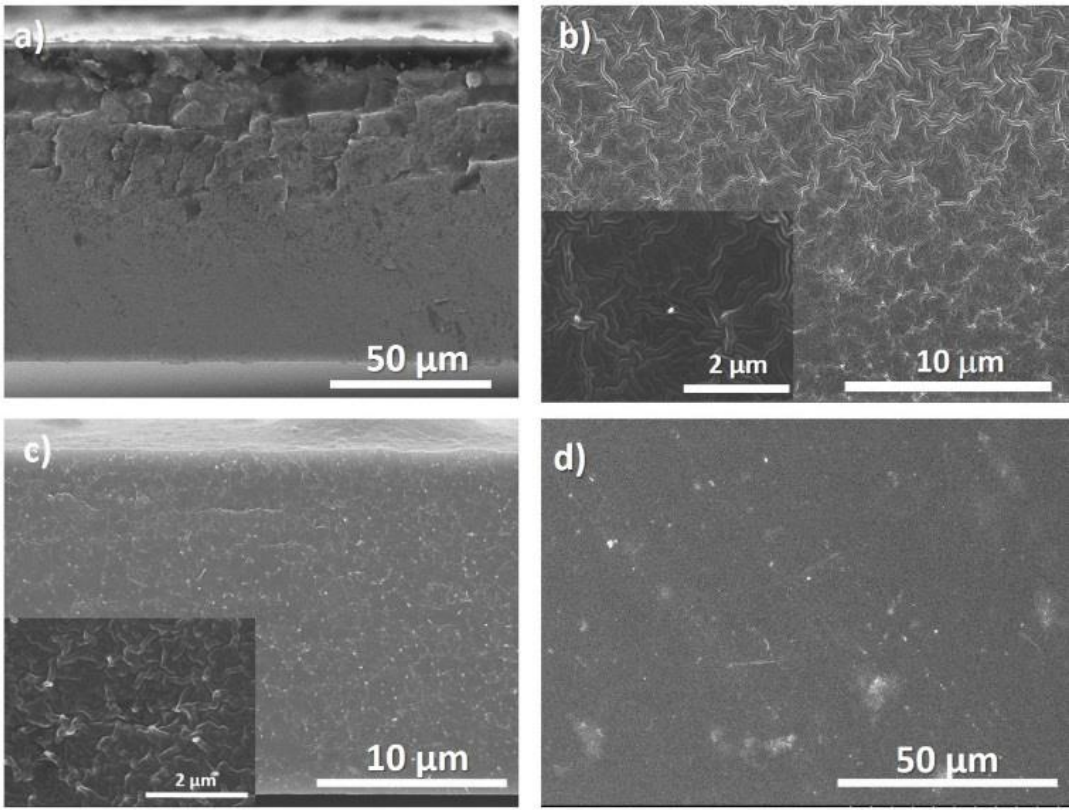

Figure 4.1. 3. SEM cross-section images of a) SF/CNT composites of neat SF, b) 0.75 wt.% CNT, c) 6 wt.% CNT and d) surface image of 6wt.% CNT.

Figure 4.1.3c-d (6 wt. % CNT composite) shows that the fillers are also uniformly distributed along the cross-section of the samples, allowing suitable mechanical and electrical macroscopic response (see later). The insert in ***Figure 4.1.3c*** also shows the proper wetting of the CNT by the polymer.

As it was observed by Zhou et al., SF films present globule-like nanostructure[48]. Films regenerated from formic acid solvent casting show globule-like size of around 100 nm [48] as a consequence of SF chains self-assembling during the solvent evaporation process. SF/CNT composites show a similar structure for the different CNT concentrations.

To gain insight into the secondary structural changes of SF chains with the addition of the fillers, the ATR-FTIR spectra of the composites are presented in ***Figure 4.1.4***. The full-range ATR-FTIR spectra in which the frequency from 1800 cm^{-1} to 1400 cm^{-1} contains the most important amide I and amide II regions, describing the metastable state between a partially ordered α-helix and the β-sheet structures, and antiparallel β-sheet structure, respectively[49].

The strong absorption at 3500–3000 cm^{-1} in ***Figure 4.1.4a*** represents the OH stretching vibration, H-bonded and NH stretching vibration[50].-

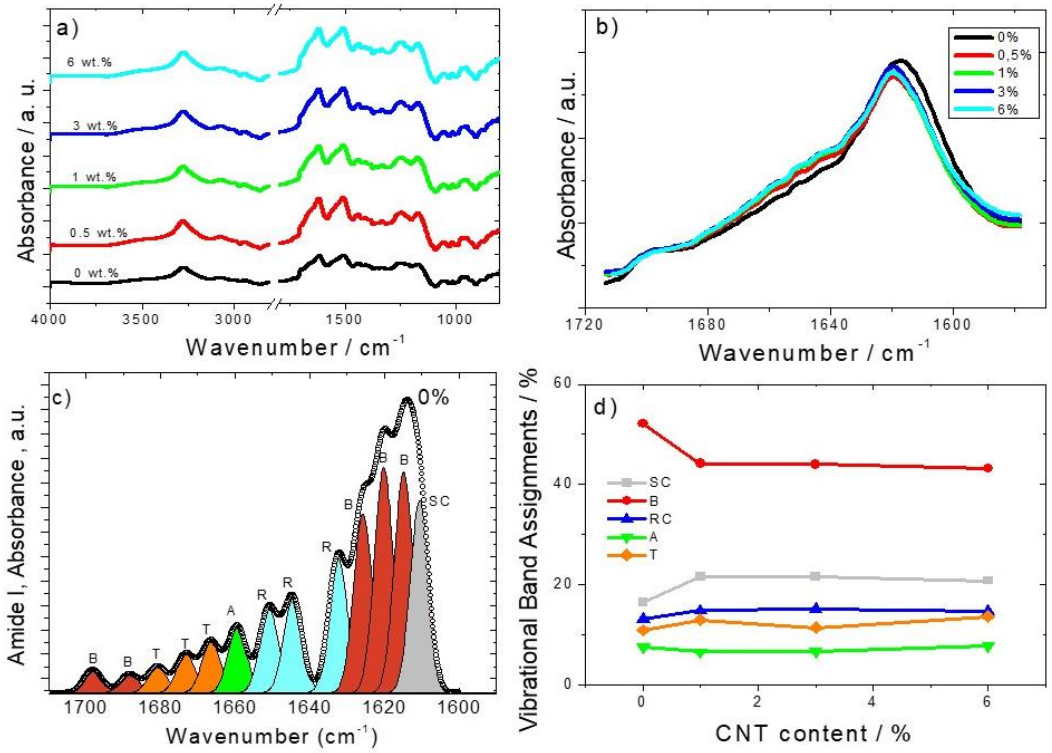

Figure 4.1. 4. *a) Full-range ATR-FTIR spectra for neat SF and the different composites. b) Amide I region of the ATR-FTIR spectra for all SF/CNT composites. c) Typical deconvolution spectrum of amide I for neat SF and d) Integral area fraction of the different spectral components resolved in this spectral region. The different contributions to the amide I envelope are marked as random coil (R, blue), β-sheets (B, red), α-helices (A, green), turns (T, orange), and side chains (SC, grey).*

The secondary structures of SF are usually determined after the amide I band between 1700 to 1600 cm^{-1} (***Figure 4.1.4b***) associated the C=O stretching vibration, NH in-plane bending, out of phase CN stretching vibration, and CCN deformation [51] (***Table 4.1.1***). ***Figure 4.1.4b*** shows that the inclusion of CNT affects the vibration bands of SF but that the effect is independent of CNT content.

The FTIR signals of secondary structures can be found in ***table 4.1.1***, which can be differentiated, as ***Figure 4.1.4c*** shows in a typical deconvolution indicating the corresponding area for each component for pure SF. The same procedure was performed for all SF/CNT composites and the results are summarized in ***Figure 4.1.4d***.

Table 4.1.1. *FTIR-ATR main absorption peaks of CFO/SF nanocomposites.*

Bands (cm-1)	*Assignments*	*Ref.*
3500-3000	*OH stretching vibration, H-bond and NH stretching vibration*	49,52
1600-1700	*Amide I (C=O stretching vibration, NH in-plane bending, out of plane CN stretching vibration, and C-CN deformation)*	
1517-1539	*Amide II (stretching of C–N and N–H in-plane bending)*	
1230	*Amide III*	
Assignments	*Amide I deconvolution peaks*	*Ref.*
1605–1615	*Side chains*	53,54
1619–1628/ 1697–1703	*β-sheet crystal conformation*	
1638–1655	*Random coil*	
1656–1662	*α-helix*	
1663–1696	*Turns*	

Figure 4.1.4d shows that the dominant conformation of SF is β-sheet with 52 %. This conformation is reduced to 44% for the SF/CNT composites independently of CNT content [51]. This can be ascribed to a reduction on the degree of crystallinity of the samples [51], which is mainly attributed to the defects induced by the nanofillers.

Figure 4.1.4d reveals that the proportion of the random coil and turns is practically the same (15 vs. 13 %, respectively) and the α-helix conformation is approximately 7 % for all SF/CNT composites. Thus, the presence of the fillers does not modify those SF conformations.

Thermal and mechanical characterisation

The thermal and mechanical characterization of SF/CNT composites was performed to evaluate their dependence on CNT content, due to the thermal conductive properties and mechanical reinforcement effect of CNT [55].

DSC thermograms of the SF/CNT composites shown in ***Figure 4.1.5a*** demonstrate that all samples exhibit a similar thermal behaviour characterized by an endothermic peak around 290 ºC associated with the degradation of SF molecular chains. Melting endotherm peaks were not observed in any samples because silk fibroin degrades at a temperature lower than the melting point. During the first annealing, an endothermic peak at 100 ºC attributable to evaporation of bonded and non-bonded water was observed (***Figure 4.1.5a***) [56]. Water lost signals show samples ability to absorb ambient water during the casting process.

During annealing, were not observed variations in the glass transition or random coil/α-helix to β sheet conformational changes [57]. This behaviour usually observed in high crystallized samples corroborates FTIR data. Thermal degradation endothermic peak was not influenced by fillers addition, thus CNT-SF interactions not influence chains packing and their degradation.

TGA thermograms are essential for the determination of the temperature range in which the samples will not undergo any weight loss process affecting the macroscopic response of the materials. Further, it will allow to evaluate water content in the samples since SF has the ability to contain water molecules as shown in ***Figure 4.1.5b*** [56].

Figure 4.1.5b shows the TGA thermogram for all SF and SF/CNT samples, demonstrating that the decomposition of the samples occurs in two main stages.

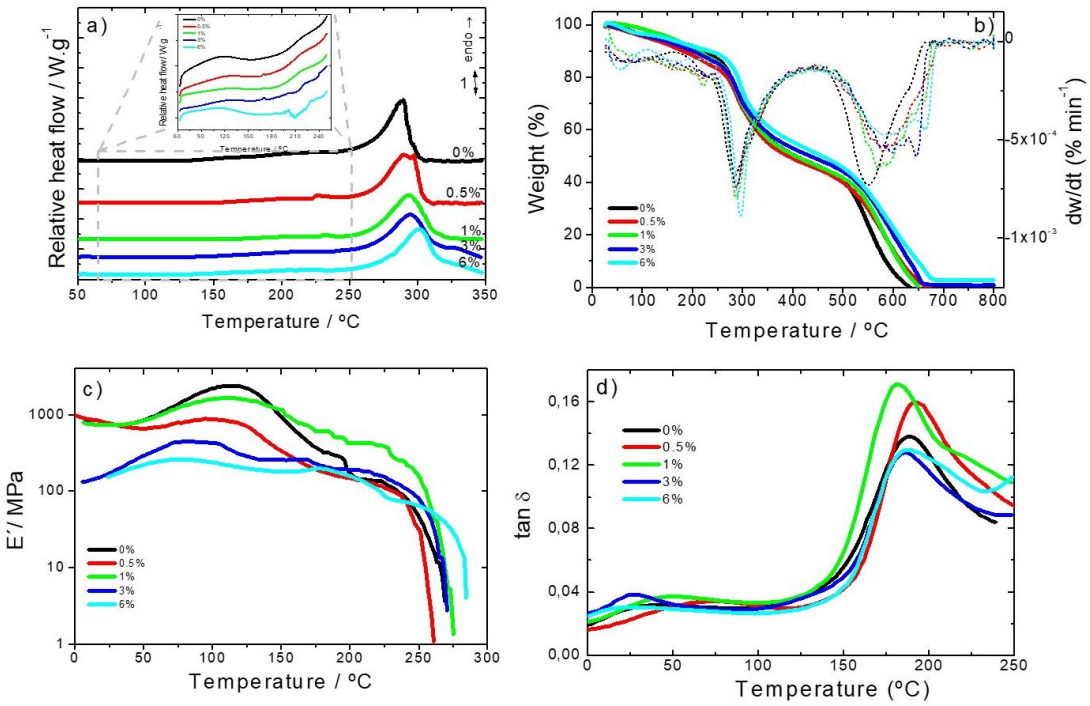

Figure 4.1. 5*. a) DSC curves at first annealing; b) TGA thermograms; c) viscoelastic modulus (E') and d) loss tangent (tan δ) for SF and the corresponding SF/CNT composites.*

An initial weight decrease is observed up to 150°C for all samples (***Figure 4.1.5b***) due to water removal (evaporation), corresponding with the first DTGA peak. The storage of water in silk films can be of two different types: free water molecules that can be easily removed and, therefore, being the first to evaporate under heating and bonded-water, bonded to

protein chains by the interactions between the amide groups of proteins and the OH groups of water [56].

The water content of the silk samples was determined by the weight decrease in the first step (***Figure 4.1.5b***) and show a similar water content of ~10 % in all the samples, since CNTs do not vary the ability of silk fibroin to stock water. The second degradation step ranges from 200 ºC to 270 ºC and corresponds to the degradation of the samples through the breakage of the primary chain of the silk molecules. This step is independent of the water content [56] and the inclusion of the CNT. Before the second degradation peak in the DTG curve (***Figure 4.1.5b***) a small peak at 235 ºC is observed corresponding to a degradation of the less stable crystal domains not observed in pure SF samples.

The mechanical properties of the films, i.e., the elastic modulus (E') and the loss tangent (tan δ), are shown as a function of temperature (0 - 280 ºC) at 1 Hz in ***Figures 4.1.5c***-d.For all SF and SF/CNT composites (***Figure 4.1.5c***) the elastic modulus remains constant until 50 ºC, sharply increases at about 100 ºC and then decreases abruptly at about 150 ºC. This behaviour predicts water molecules plasticising effect over SF and make sense to the storage modulus increase as consequence of evaporation. With increasing temperature above 150 ºC, the storage modulus decreases until reaching 280 ºC where modulus strongly drops as a consequence of the beginning of the polymeric structure degradation, as shown in the TGA thermograms (***Figure 4.1.5b***).

The loss tangent (***Figure 4.1.5d***) increases slowly up to about 150 ºC, increases sharply above this temperature, until it reaches a peak at about 180 ºC. The decrease in the elastic modulus (***Figure 4.1.5c***) at about 150 ºC and the peak of loss tangent (***Figure 4.1.5d***) at 200 ºC are explained in terms of the segmental motion of the main chains of the silk fibroin molecules in the amorphous film [58].

The storage modulus of the SF/CNT composites increases as the content of CNTs increases due to the stiffening effect of the carbon nanotubes, which is particularly significant in SF/CNT composites of 6 wt.% where the modulus increases by two orders of magnitude when compared to the lowest CNTs contents (0.75 wt.%) (***Figure 4.1.5c***).The CNTs content of 0.5 and 1 wt. % in SF/CNT composites is not enough to produce a significant mechanical variation and shows a similar behaviour to neat SF. In addition, the peak of tan δ (***Figure 4.1.5d***) moves to slightly lower temperatures with increasing carbon nanotube content, showing that the T_g of the SF/CNT composites decreases with the addition of nanotubes.

This fact is explained by the better transmission of the heat by carbon nanotubes which can promote the energy gain for a glass transition.

Electrical and electro-mechanical behaviour

For sensors applications, the electrical properties can be tuned by the inclusion of CNTs. The dielectric response (ε', tan δ and σ') calculated after ***equations 4.1.1 and 4.1.2*** for the different samples is shown in ***Figure 4.1.6***.

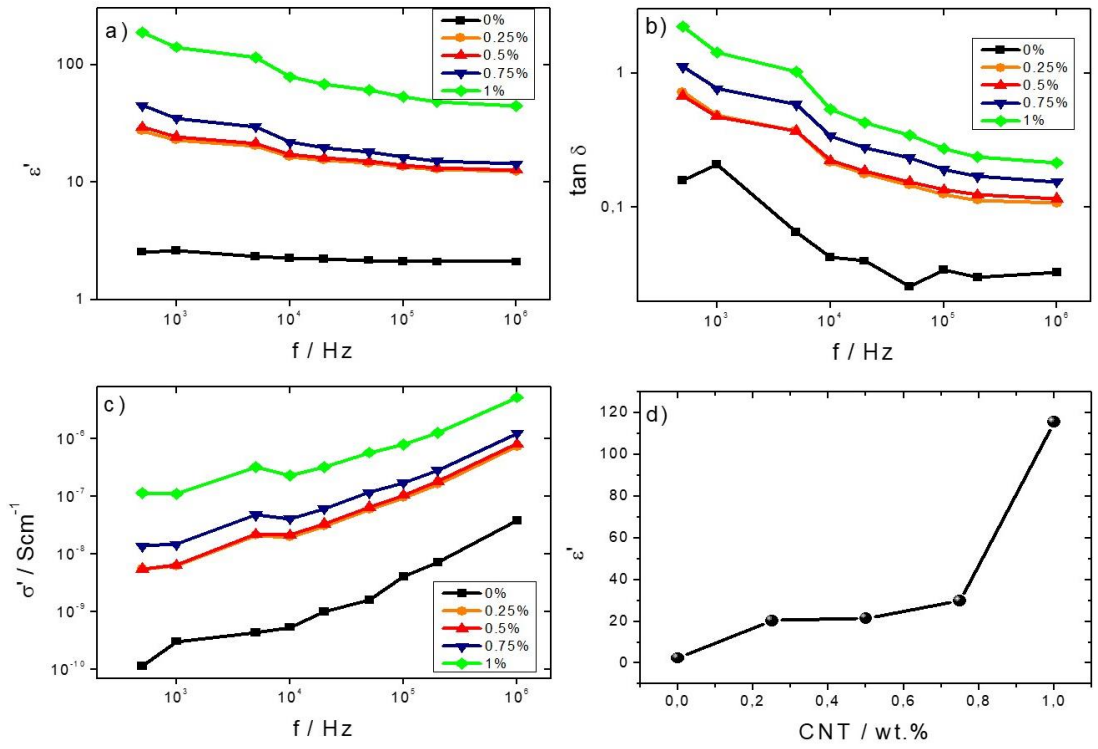

Figure 4.1. 6*. a) dielectric constant, ε', b) tan δ and c) a.c. conductivity for all SF/CNTs composites. d) Variation of the dielectric constant as a function of CNTs content at 5 kHz.*

Figures 4.1.6a and b show the dielectric constant and loss tangent, respectively, for SF and SF/CNTs composites, except for the composite with 6 wt. %, which is very conductive, as a function of the frequency at room temperature. For all samples, ***Figure 4.1.6a and b*** show that the dielectric constant and tan δ decreases as the frequency increases due to slow dipole mobility [59]. It is also detected that the dielectric constant increases with the addition of the CNTs, regardless of the frequency, due to increased charge carriers, with eventual contributions from the Maxwell-Wagner-Sillars (MWS) effect due to interfacial charge accumulation under an external electric field (***Figure 4.1.6a)***[60]. This is also confirmed by the increase of both tan δ and σ' and shown in ***Figures 4.1.6b and c***.

Figure 4.1.6c shows the σ' values for the different samples as a function of frequency. It is verified that the electrical conductivity increases with increasing frequency at room temperature, independently of the CNT content, indicating increased charge carrier mobility at localized states. The a.c conductivity increases with addition of CNTs due to both, the introduction of additional charge carriers and to the formation of a conductive network, until reaching a percolation, as shown in ***Figure 4.1.6*** for the d.c. conductivity[61].

Figure 4.1.7d shows the room temperature dielectric constant of the samples at 5 kHz as a function of CNT content. The dielectric constant increases with increasing CNTs content due to contributions of the localized charge movement and the formation of local micro capacitors, as explained the percolation theory [62].

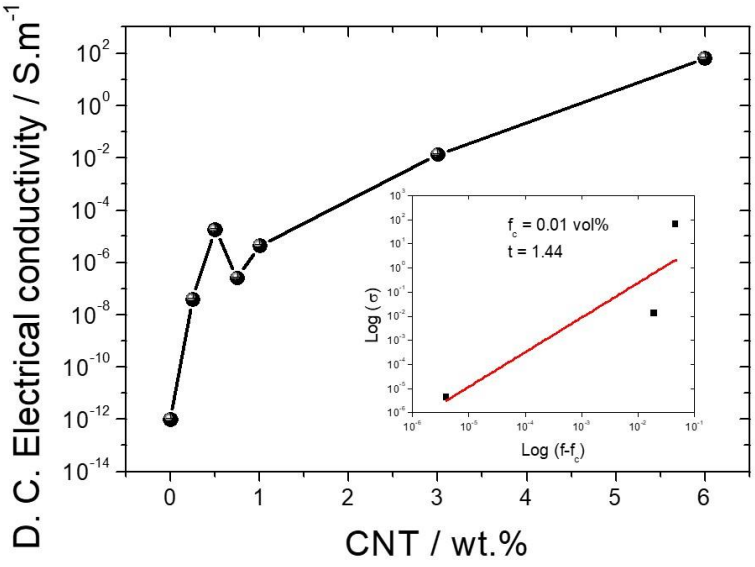

Figure 4.1. 7. *D.C. electrical conductivity of SF and the SF/CNT composites.*

In order to determine the percolation threshold, the dc electrical conductivity was evaluated and the results as a function of CNT content are shown in ***Figure 4.1.7***.The D.C. electrical conductivity increases by over 14 orders of magnitude when the filler content increased up to 6 wt.%, the percolation threshold being at approx. 3 wt.% of CNT.

The result of ***Figure 4.1.7*** show that the carbon nanotubes conductive networks is formed within the silk fibroin polymer. The electrical conductivity of SF/CNT composites can be theoretically predicted by the percolation model through the following equation [63]:

$$\sigma \approx (f - f_c)^t \text{ for } f > f_c$$

(4.1.5)

where f and f_c are the volume fraction of CNT and the percolation threshold of the SF/CNT composites, respectively, and t is the critical exponent in the conducting region.

It can be seen in the insert of ***Figure 1.4.7***, after the application of ***equation 4.1.5***, that the percolation volume is fc = 0.01 vol% (1 wt. %) and the critical exponent in the conducting region is t = 1.44. It is to notice that the critical exponent obtained for SF/CNT composites is 1.44, close to 1.1-1.3 for two-dimensional system [64].

Taking into account the electrical results of ***Figure 4.1.7***, the electromechanical performance was evaluated for SF/CNT composites with 1 and 3% wt. % of CNT, as shown in ***Figure 4.1.7***. It has been concluded that the piezoresistive response of carbonaceous composites is the largest around the percolation threshold due to larger variations of the conductive network under mechanical solicitation [34].

The electromechanical response was evaluated under compressive loading cycles with a maximum applied pressure of 400 N (equivalent to 0.88 MPa), as shown in ***Figure 4.1.8***.

The loading-unloading pressure cycles from 50 up to 400 N are presented in ***Figure 4.1.8a***, for 10 cycles in each measurement. ***Figure 4.1.8b*** shows the relative variation of resistance during cycle loading and pressure application variation at a strain rate of 1 mm·min^{-1} for SF/CNT composites with 1 wt. % of CNT. The behaviour is similar for the sample with 3 wt. % filler content.

It is observed that the piezoresistive behaviour presents an excellent real-time response without hysteresis effect (***Figure 4.1.8b and c***). The stability of the cyclic response is shown in ***Figure 4.1.8c*** by the resistance variation for 50 cycles. The minimum and maximum electrical resistance is constant with cycles (except for the initial 3-4 cycles), thus, we can conclude that the mechanical stability of these composites is good and can be used as sensor material.

It can be seen that SF/CNT composites present good reproducibility and signal stability and that the conductive network variations of carbon nanotubes into silk fibroin is stable, the resistance variations upon mechanical cycling being explained by variations of the tunnelling distance among fillers [65]. This fact is verified for both composites (1 and 3 wt. %).

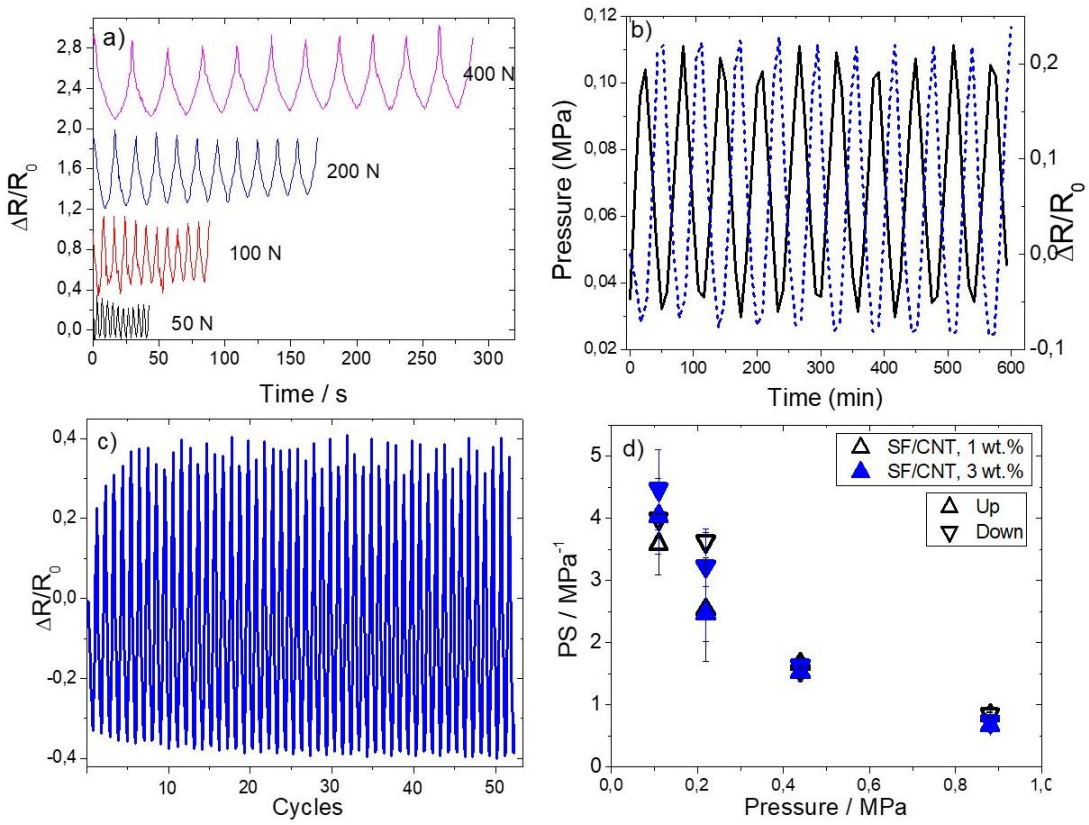

Figure 4.1. 8. *a) Mechanical behaviour of the SF/CNT composites for several applied forces (from 50 to 400 N). b) Piezoresistive response (up to 50 N or 0.11 MPa) for 1 wt.% of CNT and c) stability over repeated cycling (larger than 50 cycles) for the same sample. d) Piezoresistive performance in pressure sensibility (PS) up to pressures near 1 MPa for SF/CNT composites with 1 and 3 wt. % of CNT.*

By applying varying maximum pressures (***Figure 4.1.8d***) it is observed a decrease of the piezoresistive sensitivity (PS) upon increasing pressure: the application of increasing pressure leads to permanent reorientation and reconfiguration of the fillers and, eventually, conductive network breakage 31. It is observed that the PS value is independent of CNT amount and it is the lowest (0.72 MPa^{-1}) for 0.88 MPa, due to the aforementioned permanent deformation of the conductive network.

The piezoresistive sensor based on silk fibroin shows excellent piezoresistive sensitivity value and represents an advance in comparison with the ones shown in the state-of-art for conventional polymers (i.e., thermoplastic polyurethane (TPU) [66], polyester-based TPU [67], silicon rubber [68] and polydimethylsiloxane (PDMS) [69]) in terms of environmental friendliness.

Implementation of a pressure sensor prototype based on SF/CNT composites

As a proof of concept on sensor implementation based on the developed materials, a simple prototype was fabricated envisioning that it could be used as a touch/pressure sensor, for example, by being embedded inside the paper sheets of a hybrid book, allowing a digital interaction with the user, but without the negative environmental impact that plastic-based sensors usually carry on. Therefore, the developed silk-based material can be used as a touch/pressure sensor, either analogically or digitally.

To achieve that goal, two pairs of gold electrodes were deposited in the film using sputtering technique, two in the top layer and the other two in the bottom layer, so that each pair was overlapping, as presented in ***Figure 4.1.9a***. A SF/CNT film with 1 wt. % CNT content was used due to its s electrical resistivity: >> 200 MΩ between side electrodes, and 150 to 300 kΩ approximately between top and bottom pairs. Therefore, if multiple pressure points are being sensorized simultaneously, no interference will occur between pair of sensing elements within one film.

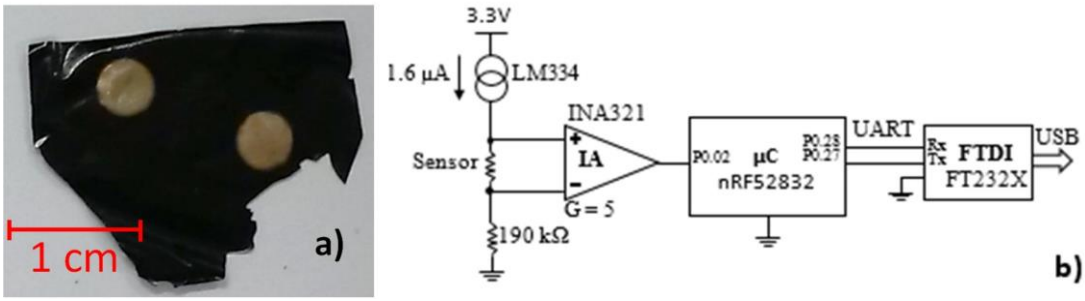

Figure 4.1. 9. *a) SF/CNT 1 wt.% CNT content film with 4 gold electrodes (2 on top and 2 on bottom); b) Schematic of the test circuit, consisting in a current source and an instrumentation amplifier (IA).*

Two terminals were connected per electrode to assure the good electrical connection between the terminals and the electrodes, which consisted in aluminium foil glued to the electrodes with z axis conductive adhesive tape (3M 9703). The maximum terminal-electrode-terminal resistance measured in the prototype was < 100 Ω, which warranted a good connection from the terminals to the electrodes.

The developed circuit to measure sensor response was based on a current source through the sensor, shown in ***Figure 4.1.9b***, which provides a linear voltage drop on the sensor versus its resistance that can be amplified by an instrumentation amplifier (IA), and then fed to the

analog-to-digital converter (ADC) of a microcontroller (µC). Finally, the data is sent to a computer via a Universal Serial Bus (USB) to universal asynchronous receiver-transmitter (UART) converter.

The selected components for the circuit were as follows: current source: Texas Instruments LM334; IA: Texas Instruments INA321; µC: Nordic Semiconductor nRF52832; USB to UART converter: FTDI Chip FT232X.

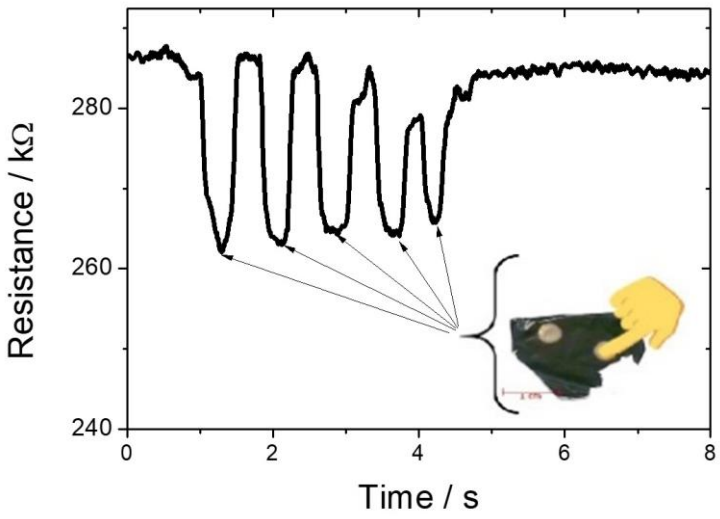

Figure 4.1. 10. *Resistance variation response when force was applied on the sensor by a fingertip touch.*

The IA is characterized by a gain (G) of 5, which amplifies the differential voltage in the sensor to 1.2 V to 2.4 V. The 190 kΩ resistance in the negative pin of the IA simply rises the voltage in this pin to 304 mV, above the minimum operating voltage of the IA. The reference voltage for the ADC comparison was 3.3 V. The sensor was read at a rate of 100 samples per second, using 8 bits, and the UART communication was configured with a baud rate of 1 Mbps.

Figure 4.1.10 shows that the resistance variation of SF/CNT composites when the pressure is applied by a fingertip touch. The resistance response is proportional to the deformation (***Figure 4.1.8 and Figure 4.1.10***) and recovers the initial values when the pressure is released.

Thus, considering environmental issues and the suitable electro-mechanical response of the developed SF/CNT composites, the present work demonstrates the applicability of these

natural polymer based composites for the development of the next generation of environmental friendlier pressure and deformation sensors.

4.1.3. CONCLUSIONS

Silk fibroin/carbon nanotube SF/CNT composites have been prepared for pressure sensor applications. The composites were prepared by simple solvent-casting method with different filler contents (0-6 wt. %). In all the samples, CNT fillers were homogeneously distributed in the silk fibroin matrix. Thermal and mechanical properties of these composites are independent of the CNT content, which shows that SF main properties have been well conserved.

The addition of CNT into the silk fibroin matrix, affects the β sheet content and as expected the electrical properties (dielectric constant and electrical conductivity). The content of the β sheet decreases and the electrical conductivity increases with increasing CNT content, the percolation threshold being around 3wt.% of CNT.

The piezoresistive behaviour of these composites shows a correspondence with the applied pressure without hysteresis. Electro-mechanical behaviour shows good reproducibility over cyclic loading and suitable pressure sensitivity of ~ 4 MPa^{-1} at small pressures of 0.11 MPa. The results were confirmed by the implementation of a touch/pressure sensor prototype with the corresponding readout electronics.

Thus, it is concluded that the SF/CNT composites show excellent overall performance to contribute to the development of high-performance pressure sensors based on natural polymers.

4.2. SILK FIBROIN / SILVER NANOWIRES BASED TRANSPARENT AND FLEXIBLE SENSOR

BASED ON: A. Reizabal et al. Optically Transparent Silk Fibroin/Silver Nanowire Composites for Piezoresistive Sensing and Object Recognitions. J. Mater. Chem. C, 2020 8, 13053.

The traditional electronic industry, which is based on semiconductor materials and transistors for data processing, has dramatically accelerated the development of technology. The scope, accessibility, and mobility of this technology are so great that electronic components have extended worldwide. In fact, according to the latest available estimations released by the united nations (UN's), electronic(e)-commerce sales represented $25.6 trillion globally in 2018, which was equivalent to 30% of global gross domestic product (GDP) of this year and suppose up to 8% grow from 2017[70].

Electronics components are mainly based on metal oxide semiconductor (CMOS) systems constructed by metals and semiconductors with high moduli and excellent electric properties. Unfortunately, the most extended commercial components are based on rigid structures, e.g., silicon, which reduces the area of application of electronics to laminar constructions, limiting the scope and the adaptability of the technology.

The IoT revolution advances towards a fully connected reality where all devices will be linked and working together. Nevertheless, it is necessary to ensure an accessible technology that enables the integration of electronic components everywhere. The rise of novel flexible and transparent electronic components has opened a new chance for this goal since it offers the same advances as conventional electronics, as the time that is adaptable, portable, wearable, and even implantable for biomedical purposes.

The use of active and multifunctional materials in this scope increases in interest due to their ability to respond to specific physical-chemical stimuli by varying their behaviour[71]. Active materials based on polymer nanocomposites are particularly interesting as they allow them to easily tailor their response[72]. Among commonly used polymer matrices, most are based on fossil fuels, which due to their large environmental impact, are not compatible with the present needs of sustainability and circular economy [73]. Thus, it becomes necessary to redirect the focus on an alternative generation of materials.

Due to its adequate properties that can be easily controlled, SF generates interest in flexible electronic devices development. However, to turn this technology, more adaptable, flexible,

and transparent electronic devices are required. To make this possible, SF must be combined with fillers able to conserve the intrinsic material properties (especially those related to mechanical resistance and optical transparency) while endow it with improved electrical conductivity. Silver nanofillers have recently attracted interest due to their biocompatibility, chemical stability, electric conductivity, and catalytic properties[74]. Among silver nanofillers, silver nanowires (SNW) deserve a particular interest due to their ability to reduce the electrical resistance of nanocomposites at lower filler contents that silver nanoparticles, as the time that preserve the visible light transmittance of the material, which allows the production of conductive and transparent materials and devices[75]. Further, silver nanowires can be used for electronic applications, including hybrid Nanogenerators for e-skins[76] and electronic textiles[77].

SF/SNW composites have already been used in the optoelectronic field, showing that the inclusion of SNW results in flexible and electrically conducting films suitable for biosensors and implantable thermoelectric wireless switching devices[78]. SF/SNW composites' resistance increases with temperature linearly, proving its potential as a transparent and conductive temperature sensor. Also, SNW can be synthesized through a non-pollutant water-based process, which follow the road to sustainability[79].

In this context, the present work focuses on developing bio-based composites with optical transparency and mechanical stability, obtained from SF, as the time that their conductive properties are controlled by SNWs inclusion. Following the idea of contributing to industry 4.0 and IoT, these new materials have been studied as a piezoresistive sensor for force deformations. Nanocomposites have been prepared by simple and scalable solution processing. To achieve a broader understanding of the electrical behavior and achieve more adaptable materials, SF has been combined in different amounts, with SNW of two different aspect ratios. Through a morphological, thermal, mechanical, optical, electrical, and electromechanical characterization, the effect of processing, fillers aspect ratio, and concentration has been analyzed.

Further, the SF/SNW nanocomposites dependence on filler aspect ratio and content has been evaluated[80]. Finally, taking advance from the processed nanocomposite's inherent ability to generate electricity[81], their practical implementation in an object recognition device has been demonstrated. (***Figure 4.2.1***)

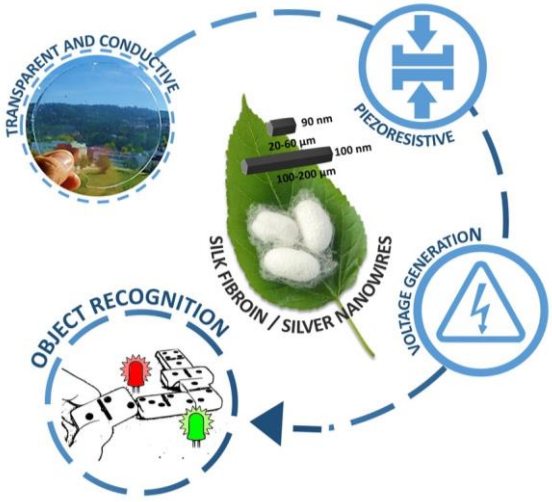

Figure 4.2. 1. *Graphical abstract of SF/SNW composites and devices based on them.*

4.2.1. MATERIALS AND EXPERIMENTAL METHODS

Materials

Silver Nanowires (SNW) with two different aspect ratios were purchased from ACS Material. In order to maintain a similar diameter and to study the effect of length variation on the electrical conductivity, SNW-100 and SNW-90 were selected. Both products present diameters between 90 and 100 nm and lengths of 100-200 and 20-60 µm for Long (L)-SNW and Short (S)-SNW, respectively. Along the paper SNW-100 will be designed as Long (L)-SNW and SNW-90 as short(S)-SNW, to be more explicit in the analysis of the data. The Bombyx mori cocoons were obtained from APPACDM from Castelo Branco (Portugal). Formic acid was provided by Sigma Aldrich with a 98.9% of purity.

Samples preparation

A schematic representation of the experimental procedure is presented in in ***Figure 4.2.2***. SF was extracted following the *SF extraction* procedure of 4.4.1 section. SF/L-SNW and SF/S-SNW composites with filler content of 0.25, 0.5, 0.75, 1, 3 and 6 wt. % were prepared by solvent casting. For that, SNW dispersed in ethanol were initially dried in an oven at 60 ºC for 12h and then re-dispersed in FA by 3h of low-energy ultrasonic bath to preserve the fillers aspect ratio. The previously obtained SF was then dissolved in the SNW/FA dispersion by 1h magnetic stirring. The final SF/SNW solution in formic acid was casted

over Low-density Polyethylene (LDPH) petri dishes to obtain SF/SNW films of 50 μm of thickness.

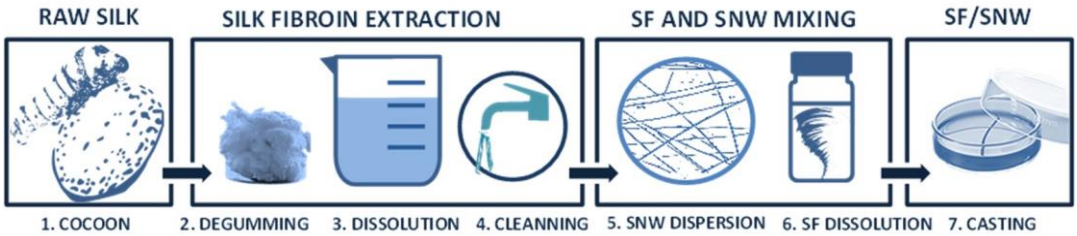

Figure 4.2. 2. *Schematic representation of the experimental procedure for the preparation of SF/SNW nanocomposites*

Characterization techniques

The silk fibroin structure and the possible chemical interactions between silk fibroin and SNW were studied by Fourier Transform Infrared Spectroscopy (FTIR) in ATR mode with a Jasco FT/IR-4100 system. All measurements were performed at room temperature in the range from 4000 to 600 cm^{-1}, with a resolution of 4 cm-1 and 64 scans. The relative content of secondary structure of silk fibroin samples was obtained by deconvolution of the Amide I, Co=O stretching band (1700-1600 cm^{-1}) with the OriginPro 8.1 software (OriginLab, Northampton), as described in "characterization techniques" apart of 4.1 section.

Thermogravimetric analysis (TGA) and Derivative Thermogravimetric (DTG) were used to evaluate the solvent content and the thermal weight loss of the samples. The measurements were performed with a TA/SDTA 851e Metter Toledo apparatus from 25 to 800 °C at 10 °C·min^{-1}, under an air flow of 50 mL·min^{-1}.

Differential scanning calorimetry (DSC) measurements were carried out with a Mettler Toledo DSC 822e equipment. In order to avoid solvent contribution into the measurements a first heating process from 25 to 170 ºC was carried out. After cooling down to room temperature, samples were heated again from 25 to 350 ºC. All the measurements were performed at 10ºC·min^{-1} under N2 flow.

The morphology of the samples and nanowires dispersion along the film was studied by scanning electron microscopy (SEM, NanoSEM – FEI Nova 200 (FEG/SEM)) with an accelerating voltage of 15 kV. The samples were previously coated with a 15 nm conductive gold layer with a Polaron SC502 apparatus.

The optical properties of the SF/SNW films optical were measured by light transmittance in the 200-900 nm range in a Shimadzu UV-2501 PC spectrophotometer. All the measurements were performed at room temperature with a resolution of 1 cm^{-1}.

Dielectric measurements were performed using a Quadtech 1920 LCR precision meter. The capacitance (C) and dielectric losses (tan δ) of the SF/SNW films were obtained and the real part (ε´) and imaginary part (ε´´) of the dielectric function were calculated using ***equations 4.2.1 and 4.2.2***:

$$\varepsilon' = \frac{C.d}{\varepsilon_0.A} \tag{4.2.1}$$

where d is the thickness of samples, ε0 is the permittivity of vacuum ($8.85x10^{-12}$ $F{\cdot}m^{-1}$) and A is the electrode area.

$$\varepsilon'' = tan\delta \cdot \varepsilon' \tag{4.2.2}$$

All measurements were performed at room temperature using the parallel plate capacitor configuration in the frequency range 103 Hz to 1Mz with an applied voltage of 0.5V. Previous to the measurements, two gold circular electrodes of 5 mm of diameter and 20 nm thickness were deposited with Polaron Coater SC502 onto both sides of each sample.

The a.c. electrical conductivity ($\sigma_{A.C.}$) of the samples was calculated after ***equation 4.2.3***:

$$\sigma_{A.C.} = \varepsilon_0 \cdot \omega \cdot \varepsilon'' \tag{4.2.3}$$

where ω is the angular frequency (ω=2πʃ).

The d.c. electrical conductivity ($\sigma_{D.C.}$) ($\sigma_{D.C.} = \rho^{-1}$) of the films was measured at room temperature, using the four-wire method with a Keighley's 287 picoammeter/voltage source with an applied voltage between ±10 V. The parallel plate configuration and gold contact of 5 mm of diameter were used for volume conductivity (σ) measurements, calculated by ***equation 4.2.4***:

$$\sigma_{DC} = \frac{1}{\rho} = \frac{d}{R.A}$$

(4.2.4)

where R is the sample resistance, calculated from the slope of the I-V curves, A is the electrode area and d is the sample thickness.

The performance of the composites as transparent conductors depends both on the light transmittance and sheet resistance. The ratio between samples DC conductivity and optical transmittance (σ_{DC}/σ_{Op}) was evaluated by the Figure of merit (FOM). Rs measurements and FOM were obtained from the ***equations 4.2.5 and 4.2.6*** respectively [82].

$$R_S = {}^{\rho}/_{d}$$

(4.2.5)

$$FOM = {}^{Z_0}/_{2 \cdot R_S \left(T^{-1/2} - 1\right)}$$

(4.2.6)

Where ρ was calculated from electrical conductivity measurements ($\sigma_{D.C} = \rho^{-1}$), Z_0 is the impedance of the free space (377 Ω) and T is the transmittance.

Electro-mechanical tests were carried out by measuring the volume resistivity variations (measured with an Agilent 34401A multimeter) under cyclic compression generated by a universal testing machine (Instron 5544) with a load cell of 500N at 1 $mm \cdot min^{-1}$. Measurements were performed in samples with thickness in the range 100 to 200 μm.

The electro-mechanical test were performed under compression and allowed to o evaluate pressure sensitivity (PS) using ***equation 4.2.7:***

$$\boldsymbol{PS = \frac{{}^{\Delta R}/_{R_0}}{P}}$$

(7)

where R_0 is the initial electrical resistance in the unloaded state, ΔR is the electrical resistance change and P is the applied pressure.

4.2.2. RESULTS AND DISCUSSION

Morphological and Optical Characterization

SF/SNW films morphology and fillers dispersion was evaluated by SEM images. Cross section images of neat SF and SF/L-SNW 3 wt. % are shown in ***Figure 4.2.3a*** and b respectively, being representative of the other composites. Cross section image of neat SF film presents a non-porous and compact morphology without specific features (***Figure 4.2.3a***). This compact morphology is conserved in all the composites even at the highest filler contents. As can be observed in ***Figure 4.2.3b***, SNW fillers are well dispersed along all the matrix, as corroborated by the amplification image where single wires can be observed without any agglomeration.

Further, the optical images presented in ***Figures 4.2.3c*** to 2f show that transparency of the SF/SNW composites decreases with increasing filler content, though they maintain suitable levels of transparency and flexibility even at high filler concentration.

The UV-Vis transmittance spectra for SF/S-SNW and SF/L-SNW composites is shown in ***Figure 4.2.3g and h***, respectively. The transmittance spectra of neat SF films show an optical transmittance close to 90% in the visible light range from 400 to 750 nm 31. Between 200 and 300 nm, SF films transmittance decays until a total absorbance of UV light is observed due to the UV absorption of aromatic amino acids such as Try, Phe, and Tyr molecules[83]. The addition of S-SNW and L-SNW (***Figure 4.2.3g and h***, respectively), corroborates the previous observations on samples transparency and show that the introduction of SNW lead to a decrease in transmittance. This decrease in optical transparency is attributed to the SNW absorption band of visible light. SF/L-SNW exhibits a small decrease in optical transparency showing transmittance values in the range of visible light above 25% at SNW concentrations of 3 wt.%. All the SF/SNW composites show a sharp decrease in transmittance at 360 and 380 nm, mainly derived from transverse and longitudinal surface plasmon resonance of SNW[84].

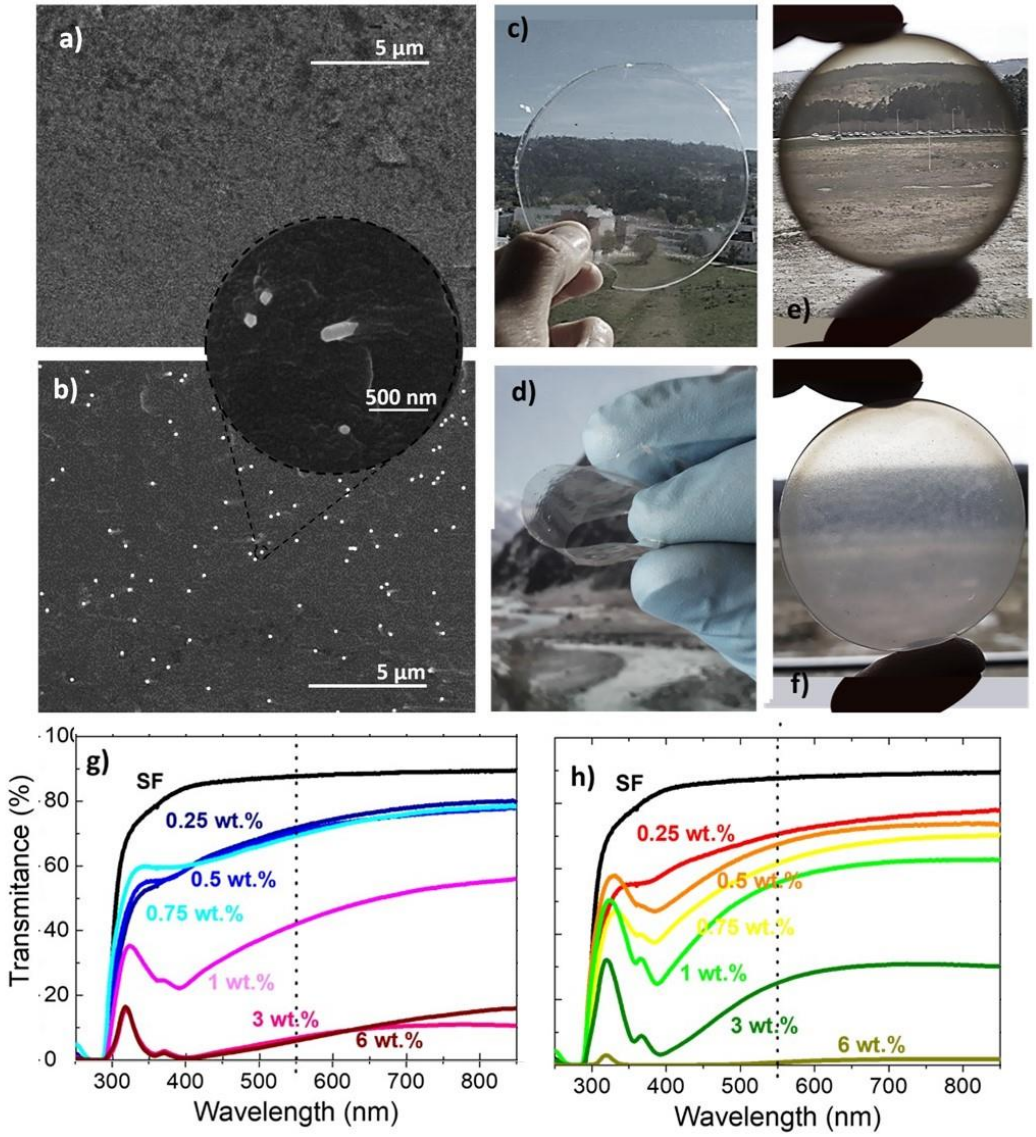

Figure 4.2. 3. *SEM images of a) SF cross section and b) SF/L-SNW 3 wt.% cross section. Optical images of c) neat SF, d) SF/L-SNW 0.5 wt.%, e) SF/S-SNW 3 wt.% and f) SF/L-SNW 3 wt.% (Note that darker zones surrounding SF/L-SNW 3 wt.% film, are due to an optical effect and not due to fillers agglomeration). UV-Vis spectra in transmittance mode of g) SF/S-SNW and h) SF/L-SNW.*

FTIR and thermal characterization

FTIR measurements were performed in order to study SF films composition after SNW addition. The obtained FTIR curves for neat SF and SF/S-SNW composites between 600 and 4000 cm^{-1} are presented in ***Figure 4.2.4a*** as representative for all the composites. It is observed that the main characteristic peaks amide I (1630 cm^{-1}), amide II (1530 cm^{-1}), amide III (1230 cm^{-1}) of neat SF [85] are present, independently of the SNW type and content.

The deconvolution of the amide I was performed for obtaining the secondary structure composition of side chains (SC), β-sheets (B), random coils (RC), α-helix (A) and turns (T)) [53]. Deconvolution results are presented in ***Figure 4.2.4b and c*** for the different SF/SNW composites. Independently to the SNW type and content, when small amounts of fillers (0.25 wt. %) are added to the SF matrix, the β-sheet content decreases from above 52% to values around 40% (***Figure 4.2.4b and c***). This fact is attributed to the defects induced by the SNW, regardless its size. The constant values of ordered β-sheets despite of SNW addition, also observed in SF/ CNT, can be explained due to homogenous fillers distribution along the matrix (observed in SEM images, ***Figure 4.2.4b***), which induce defects into polypeptide structure that hinder polymer chain arrangement independently of the concentration (***Figure 4.2.4b and c***).

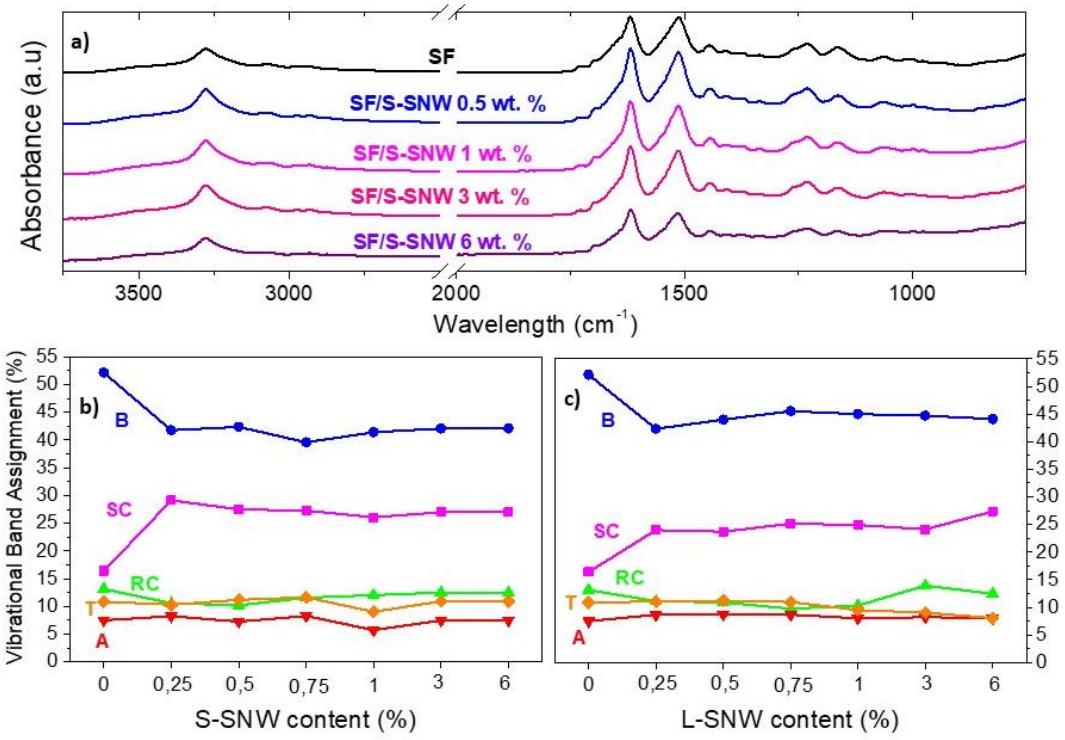

Figure 4.2. 4. *FTIR spectra of a) SF/S-SNW composites and vibrational band assignments of secondary structures of b) SF/S-SNW composites and c) SF/L-SNW composites. The secondary structures correspond to side chains (SC), β-sheets (B), random coils (RC), α-helix (A) and turns (T).*

Figure 4.2.5 presents the thermal behaviour of SF/SNW nanocomposites. As can be observed, SF presents a first weight loss step at 100 ºC, corresponding to the evaporation of

water molecules [86] (***Figure 4.2.5a***). Around 290 ºC a second weight loss step is observed, related with SF side chain group's breakdown as well as peptide bonds cleavage, followed by a final degradation step at 550 ºC ascribed to organic compounds combustion. The total degradation of SF is found at 650ºC.

SNW addition induces a slight variation of the thermal behaviour, which is especially visible in the 25 – 220 ºC range, where a reduction of the SF/SNW composites thermal stability can be observed with increasing filler content (***Figure 4.2.5a***). The same effect is also observed in the DTGA curves, as indicated by the black arrow. In order to observe the variation of the thermal stability, a reference temperature was placed in 180ºC, where neat SF side chain group's breakdown and peptide bonds cleavage begin. As can be observed, at this point SF only shows the weight loss due to water evaporation (~ 7 %), while SF/SNW composites show weight reductions of 12 % and 17 %, when 3 and 6 wt. % of fillers are added, respectively. This change of materials behaviour can be ascribed to SC increase (previously observed in FTIR results, ***Figure 4.2.4***) as well as metallic fillers thermal conductivity that favour the side chains and amino acid residues breakdown. As a consequence of SNW addition, it can be also observed a shift of organic compounds combustion to higher temperatures, attributed to the high thermal stability of the silver inorganic fillers. After 800 ºC annealing, a final residue can be observed for all the SF/SNW samples according to the corresponding filler feed. Further, it cannot be observed significant differences between both SNW types in the TGA measurements, being concluded that SF/SNW nanocomposites thermal stability is mainly dominated by fillers intrinsic properties, a not by their nano-morphology.

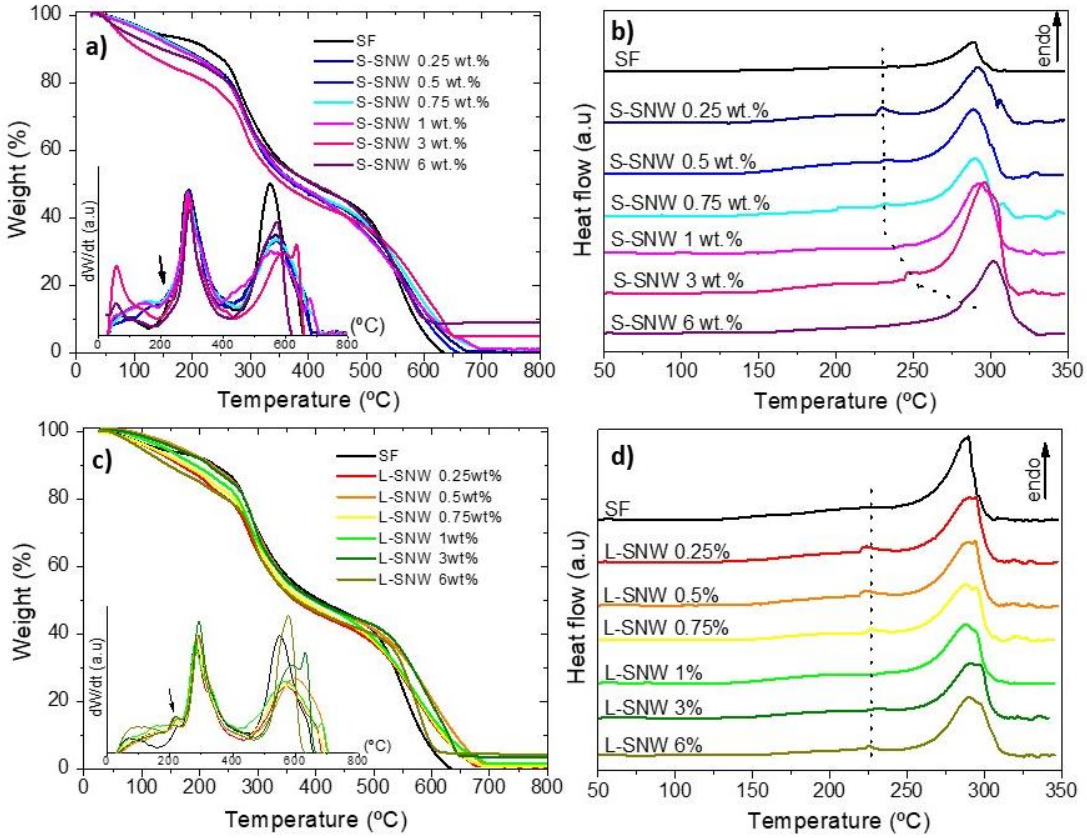

Figure 4.2. 5 *a) TGA and DTGA curves and b) DSC curves for SF/S-SNW nanocomposites. c) TGA and DTGA curves and d) DSC curves for SF/L-SNW nanocomposites.*

The DSC curves presented in ***Figures 4.2.5b*** show the thermal transitions of the SF/S-SNW composites as representative for all the SF/SNW samples. Data hide the first heating scan where bonded and non-bonded water has been removed by 170ºC isotherm. As can be observed, the resultant neat SF does not present any peak along heating scan, suggesting the lack of first order thermal transitions in the 25ºC-270ºC temperature range. The weak second order transition found between 150ºC and 200ºC can be related with the glass transition temperature (Tg) of SF, typically found around 170ºC. The endothermic peak observed around 220 ºC is related with SC group's breakdown and peptide bonds cleavage[58], previously observed in the TGA curves. After SNW addition, the DSC curves of the composites remain almost unchanged. The only difference can be found in the second order transition, which increases in intensity due to the increase of the amorphous domains (RC) (***Figure 4.2.4***).

Electrical and electro-mechanical characterization

The electrical properties of the insulating SF matrix have been modified by the addition of conductive SNW fillers, as presented in ***Figure 4.2.6***. As an insulating material, neat SF films are characterized by a low dielectric constant ε′ and low tan δ. The addition of conductive fillers leads to an increase of the dielectric response as observed in ***Figure 4.2.6a*** for SF/S-SNW and ***Figure 4.2.6b*** for SF/L-SNW. The introduction of the conductive fillers allow to increase the ε′ mainly as a result of the formation of a mini-capacitor network where SNW behave as conductive layers and SF matrix as insulator[87]. However, a decrease of ε′ can be observed in the composites for filler contents exceeding 0.25 wt. % and 0.75 wt. % of S-SNW and L-SNW, respectively. This behaviour is ascribed to the formation of a conductive network of SNWs, increasing the electrical conductivity and reducing the functional polarizable area. In all SF/SNW composites, ε′ decreases with increasing frequency due to the low dipolar dynamics, the high value of the ε′ at a lower frequency being ascribed to interface charges between the sample and electrodes, also with low dynamic response [60]. Tan δ for the SF/S-SNW and SF/L-SNW composites is shown in ***Figure 4.2.6c and d***, demonstrating an increase of Tan δ with SNW addition as a consequence of the constant increase of the electrical conductivity. This effect corroborated the previous affirmations of mini-capacitors effect loss as conductivity effect. Further, Tan δ values above 0.1 are observed for all the nanocomposites, suggesting the effectiveness of SF/SNW materials as capacitors. The observed decrease of tan δ with increasing frequency can be related with the slow dipolar and interfacial charge dynamics.

As is observed in ***Figures 4.2.6e and f,*** $\sigma_{A.C}$ increases close to two orders of magnitude with the addition of SNW fillers as a consequence of interface charge polarization and intrinsic electric dipole polarization that occurs in metal-polymer composites below the percolation threshold, resulting in the accumulation of the mobile charges at the interfaces, which forms charges in localized states and interfacial charges[62]. Increasing the frequency, $\sigma_{A.C}$ also increases, due to the increased charge carrier mobility at localized states and electron hopping mechanism in the co-ordination sites[62]. ***Figure 4.2.6*** also shows that the dielectric response of SF/S-SNW (left) and SF/L-SNW (right) is quite similar, demonstrating the small influence of SNW aspect ratio on the reported properties.

Figures 4.2.6g shows that the SF/SNW composites D.C. electrical conductivity ($\sigma_{D.C}$) increases with the addition of conductive fillers. Only 0.25 wt.% of SNW increases the $\sigma_{D.C}$

in one magnitude order, and then increases further with increasing filler content up to a maximum value of 6.6×10^{-6} $S\cdot m^{-1}$ with the maximum filler content of 6 wt.%. In fact, $\sigma_{D.C}$ will further increase with increasing filler concentration, but as the optical transparency of the samples is already strongly reduced for the sample with 6% SNW content, higher filler concentrations fall beyond the scope of the present work.

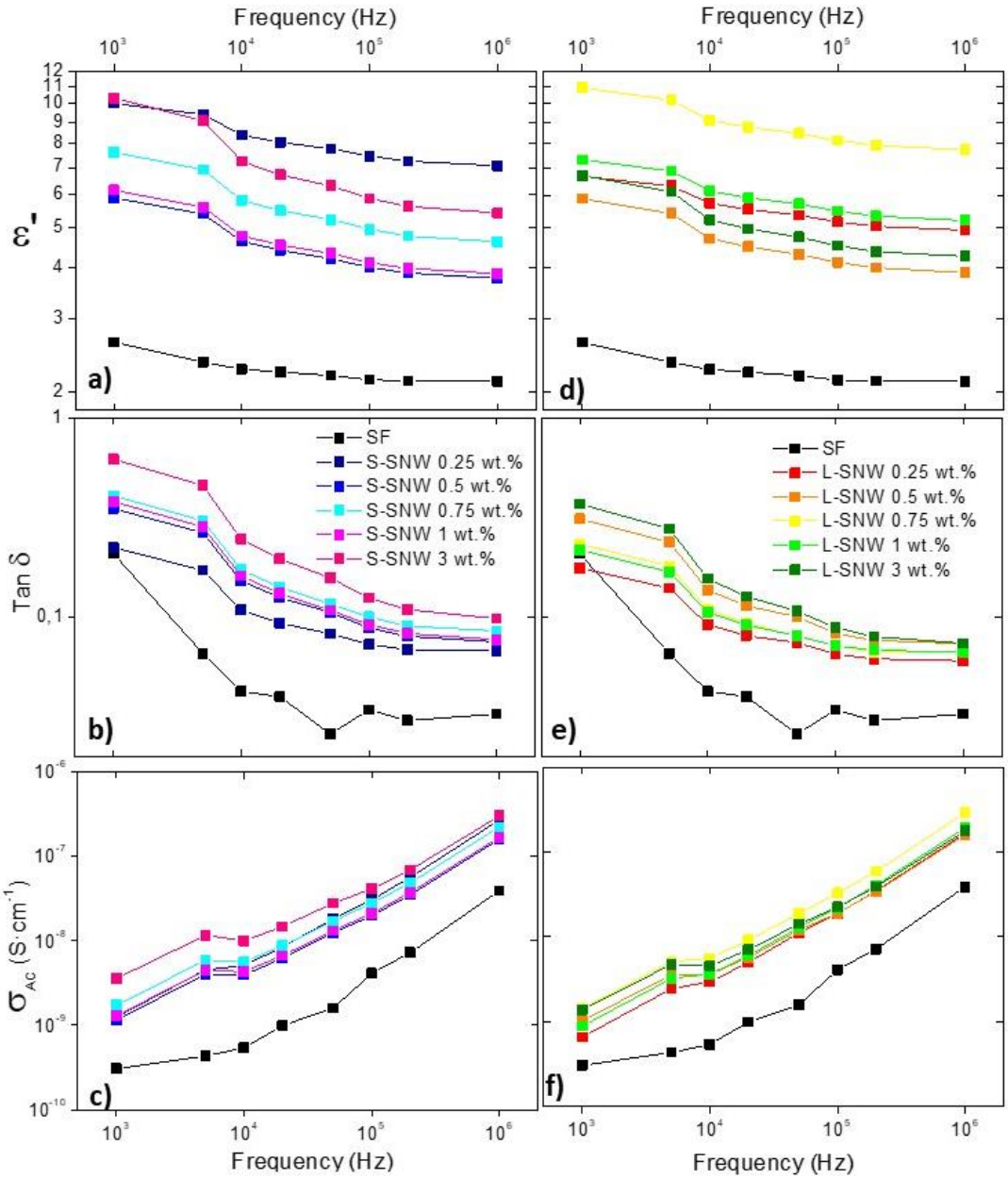

Figure 4.2. 6*. SF/S-SNW composites a) real part of dielectric constant (ε′), b) dielectric loss (tan δ) and c) A.C. conductivity (σA.C). SF/L-SNW composites d) ε′, e) tan δ and f) σA.C. SF/SNW composites g) D.C conductivity and h) Figure of merit (FOM). Measurements performed at room temperature.*

This $\sigma_{D.C}$ behaviour shows the formation of a conductive network even at low SNW concentrations, which can be ascribed to the contacts between fillers. The observed plateau between 0.5 wt. % and 1 wt. % SNW suggests that at these fillers contents the topology of the conductive network does not suffer significant variations and, therefore, the number of conductive paths and the electrical conductivity remain nearly similar.

Independently of the SNW aspect ratio, it is observed that the percolation threshold ramps up above 3 wt. %. Once again, the higher $\sigma_{D.C}$ values were found for L-SNW, due to its higher aspect ratio. Similar results have been observed previously, for SF composites with carbon nanotubes (CNTs) and ionic liquids (IL).

FOM relates the optical transmittance of the samples to the visible light with the $\sigma_{D.C}$ and can be thus used to evaluate the performance of transparent conductors. Derived from semi-constant transmittance value of SF/SNW composites in visible light, 550 nm has been

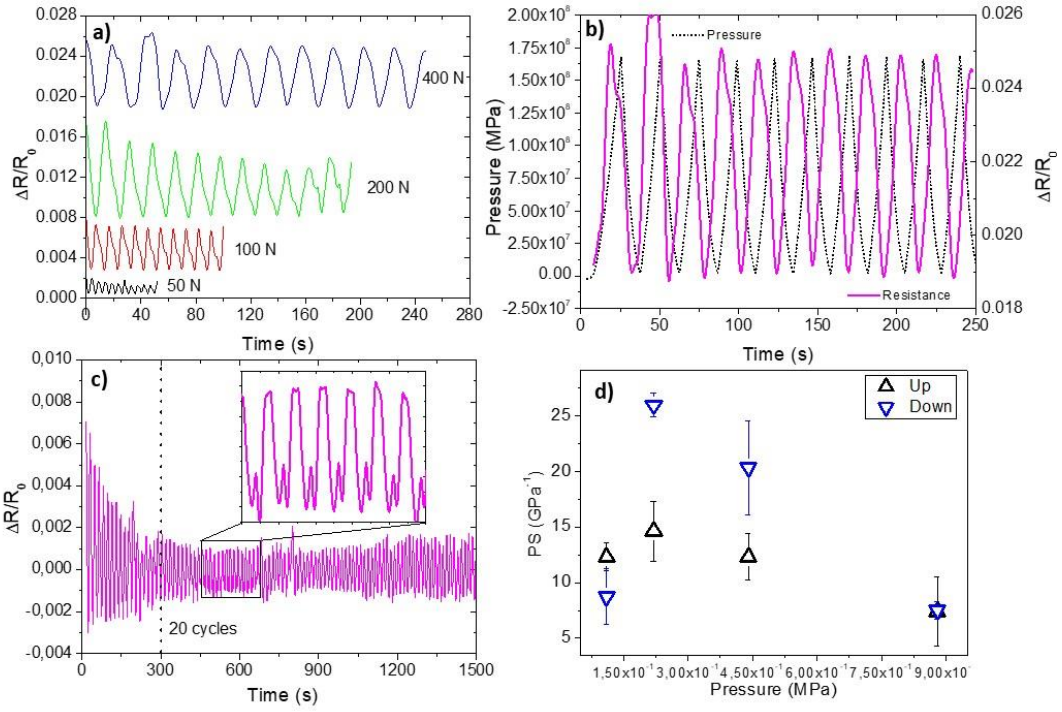

Figure 4.2. 7. *SF/S-SNW and SF/L-SNW samples a) mechanical behaviou with several applied forces (from 50 to 400N), b pressure and relative resistance variation as function of time for SF/S-SNW with 6 wt.% and 200N and c) Electromechanical test for 100 cycles for SF/L-SNW 6 wt.% nanocomposite and d) Piezoresistive performance in pressure sensibility (PS) up to pressures for SF/S-SNW with 6 wt.%.*

selected as reference value to estimate the nanocomposites FOM. ***Figure 4.2.6h*** shows that FOM values increases with SNW addition and is optimized at 0.5 wt.% for S.SNW and 0.75 wt.% for L-SNW[84]. The higher FOM values observed for SF/L-SNW composites are ascribed to the higher conductivity of the fillers given by their higher aspect ratio. The maximum FOM value is found in SF/L-SNW 0.75 wt. % and sets the maximum performance of SF/SNW based composites as transparent conductive materials. Taking into account the electrical results and the higher conductivity value obtained for SF/S-SNW with 6 wt. %, the electro-mechanical response was measured in this sample as shown in ***Figure 4.2.7***. The electromechanical response of the SF/SNW samples was obtained upon repetitive compressive loading cycles (see ***Figure 4.2.7b and c***).

By this measurement, the composites ability to vary their electrical resistance with the applied mechanical force was demonstrated, variation which is ascribed to the variations of the conductive fillers tunnelling average distance[88]. ***Figure 4.2.7a*** shows the resistance variations of the SF/S-SNW - 6 wt. % with variable compression forces up to 50, 100, 200 and 400 N. In all the applied forces constant variations of resistivity can be noted signalling the SF/SNW piezoresistive behaviour. The most notable variations were found at 200 N and 400 N of applied force, so 200 N was selected for piezoresistive behaviour measurements. ***Figure 4.2.7b*** shows the piezoresistive response during 10 repeated cycles of loading-unloading up to 200 N applied at a strain rate of 1 $mm \cdot min^{-1}$. As can be clearly observed, electrical resistance variation follows the mechanical strain applied to the composites, so increasing mechanical deformation leads to an increase of the electrical resistance of the samples. Equally, a decrease of the strain leads to an electrical conductivity increase. ***Figure 4.2.7c*** shows the hysteresis of sample during 100 times repeat cycling. Data shows a constant response of nanocomposite after 20 aging cycles. This behaviour typical of polymer based piezoresistive composites, can be related with irreversible configurations of the non-conductive network that stabilizes after aging cycles. The stable response observed after aging time show the SF/SNW composites potentiality to be applied as quantitative force and/or deformation sensors.

Figure 4.2.7d shows the piezoresistive sensitivity (PS) as a function of applied pressure. PS maximum values can be observed between 0.2 and 0.4 MPa pressure, which results in PS values between 12 and 26 GPa^{-1}. The observed PS decreasing at large pressure can be related

with the permanent reconfiguration of SNW which results on permanent conductive network breakage[47].

Thus, SF/SNW nanocomposites electrical and electro-mechanical properties mainly depend on fillers dispersion (***Figure 4.2.3b***), concentration and aspect ratio.

Samples voltage generation and object recognition

SF has the inherent ability to generate electricity due ionic and water mediated proton-hopping charge transfer[89], the inclusion of SNW fillers increasing the electric potential difference due to the electric charges at the interfaces as well as through the electrochemical properties that were used for object recognition applications. Also, silk fibroin has a high water vapour permeability in which the amorphous region plays a relevant role[90]. The protein in contact with water increases the mobility of the amorphous region through the disruption of intermolecular cohesive forces between the protein chains, improving charge transfer.

Each SF/SNW sample builds up an electric potential difference between 30 to 124 mV with short circuit current between 470 pA to 11 nA in which it increases with increasing SNW concentrations and regardless of the SNW aspect ratio but depends on its formulation, thickness, humidity and other physical characteristics. To collect the produced charge, two gold electrodes were deposited in the samples through magnetron sputtering, following the parallel plate capacitor configuration described in the experimental section, but with a diameter of 4 mm, as shown in ***Figure 4.2.8a***.

To validate the applicability of the developed materials, it was used a domino game as a demonstrator, to identify the correct or wrong orientation of the tiles in a slot. For the simplicity of this demo, the system was only prepared to identify two tiles. To prepare the tiles, a piece of SF/SNW with 6 wt. % composite was placed under each domino tile, as visible in ***Figure 4.2.8b***).

Two sheets of aluminium foil were glued on the base of the domino tile so that they could act as terminals. The connection between the terminals and the electrodes was assured by a z-axis conductive adhesive tape made of silver nanoparticles, purchased from 3M (reference 9703).

To place the domino tiles, it was printed a 3D slot in PLA (polylactic acid), as visible in ***Figure 4.2.8c***. Two stripes of adhesive copper tape connect to the aluminium terminals of

the domino tiles, forwarding the signals to a microcontroller (µC). In the upper part of the slot piece, four LEDs (light-emitting diodes) were also placed, two red and two green.

The designed electrical circuit for this application is presented in ***Figure 4.2.8d***.

It was used the microcontroller Microchip ATmega328P. The microcontroller was powered with a 5V supply, and, therefore, the reference voltage of the ADC (analog-to-digital converter) was also 5V. Additionally, a 3.3V supply was also used as reference for the dominoes slot. In this way, it was possible to detect the generated voltage by the tile placed on the slot, as well as its polarity. The four LEDs (two green, two red) were simply used to indicate the right or wrong states of two domino tiles (as easily understandable in the video from the supporting information). In addition, the microcontroller was also connected to a computer via UART (universal asynchronous receiver-transmitter), with a baud rate of 1Mbps, 8 bits. The ADC was acquiring samples at a rate of 8,300 samples per second, but they were being averaged by software at each 1,000 samples to limit noise, therefore only 8.3 samples per second were actually being sent to the computer. In the computer, the data was presented and stored by a Java application. To identify the different domino tiles, the sample of SF/SNW placed in each tile must have different electrical properties, namely different generated voltage. According to the circuit from ***Figure 4.2.8d***, the voltage read by the ADC will have a 3.3 V reference, added or subtracted by the voltage of the placed tile, according to its polarity (no to mention the capacitive coupling effect to ground).

It is important to notice the effect the series resistance of the SF/SNW samples (which is estimated over 100 MΩ), and the capacitive coupling to ground of this specific ADC, which constantly pulls down the ADC pin to 0 V. This results that, due to the high series resistance of the tile, the ADC input pin gets close to an “airwire” situation, and in fact, the read voltage by the ADC will actually be slightly lower than the arithmetic sum of the 3.3 V reference with the voltage of the tile. The same way, when no tile has been placed on the slot, the read voltage by the ADC is 0 V. ***Figure 4.2.8e*** makes a detailed explanation of this behaviour, where it is visible that, despite the 3.3 V reference, actually, no polarity can make the ADC pin rise above it.

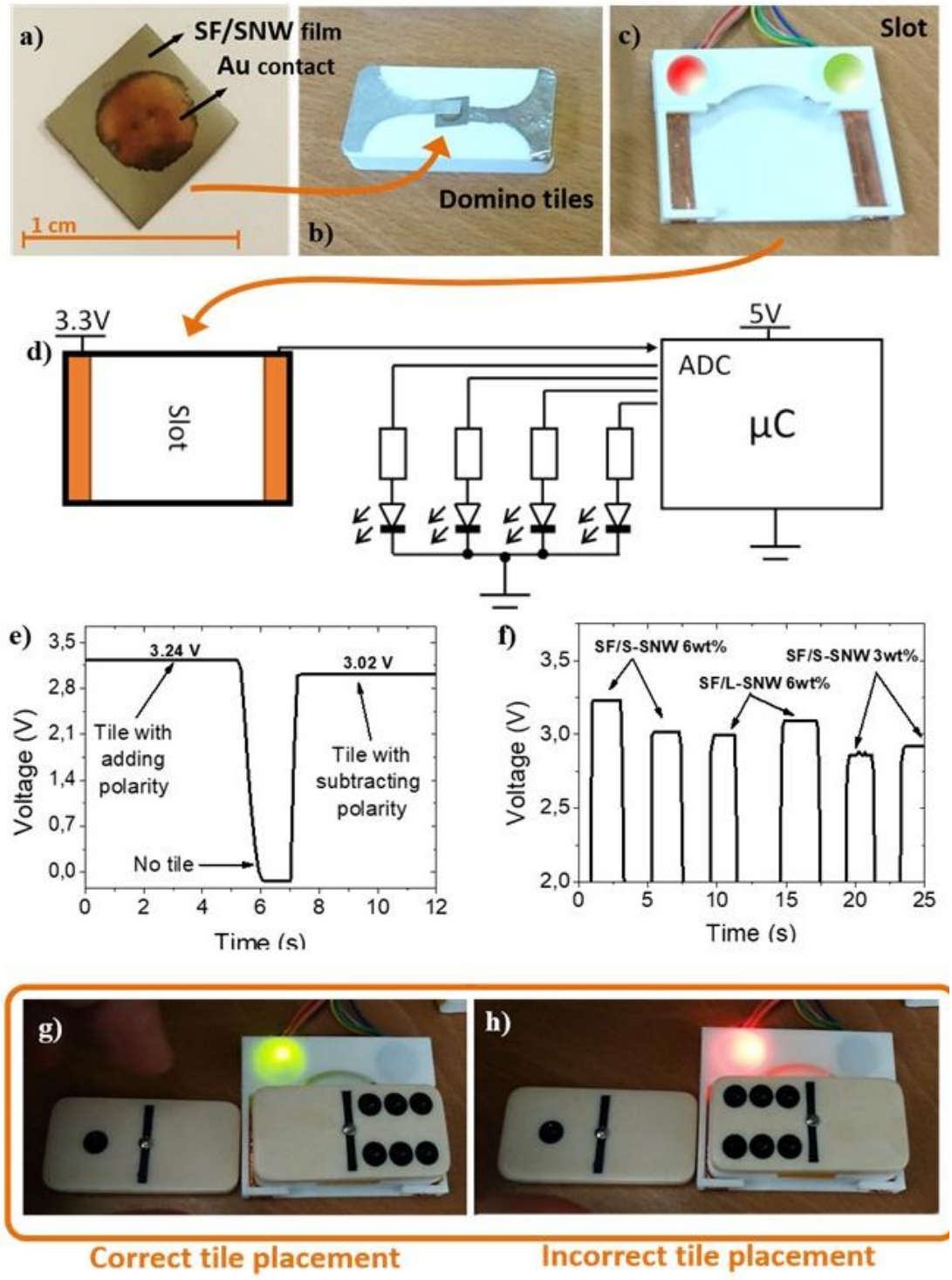

Figure 4.2. 8. *a) Gold spin-coated electrodes deposited in the SF/SNW film, b) Piece of SF/SNW film placed under an upside-down domino tile, c) 3D printed slot for the domino tile and d) Electrical circuit of the system. Measured voltage by the microcontroller between the terminals of the slot: e) adding and subtracting polarity situations (for the sample 6 wt% 20 30 nm), as well as the detection of no tile in the slot and f) difference of voltage levels for different samples and different polarities. System applied to a domino game, a) green light when tile is correctly placed and h) red light when tile is incorrectly placed.*

Figure 4.2.8f shows the read voltage by the ADC of the microcontroller when different tiles are placed in the slot, as well as when the polarity of those tiles is inverted. Likewise, neither of the SF/SNW used samples can make the ADC pin to rise above 3.3 V.

Figures 4.2.8g and h show the prototype in operation, and a short video of the functioning of the system is also available in supporting information. The green light at the top right corner indicates that the tile placed on the slot is the correct tile and that it is in the correct orientation. The tile to the right of the slot is merely illustrative and no electronic detection is made on it.

It is to notice that the simple production method of the SF/SNW composite films allows industrial implementation.

Thus, it is shown that natural polymers can represent an alternative to synthetic polymers also in electronic applications and that their electrical properties can be also properly tuned with specific fillers.

These SF/SNW composite films can be used next-generation polymer nanocomposite for transparent conductive materials, piezoresistive sensors and object recognition in wearable electronics and implantable devices.

4.2.3. CONCLUSIONS

SF/SNW nanocomposites ranging from 0 to 6 %wt. filler contents have been successfully developed by a simple and easily scalable solution casting. To analyse the effect on final behaviours, two types of SNW with different longitude (100-200 μm and 20-60 μm) and similar diameter (90-100 nm) have been evaluated.

Good dispersion of the SNW is obtained along the nanocomposites and optical transmittance in the visible range above 25% have been obtained for filler contents up to 3% wt. Conductive fillers presence into the non-conductive matrix, resulting in the formation of mini-capacitor along nanocomposite, which endows samples dielectric constant above 10 for samples with SNW 3 wt.% and more.

SNWs tunnelling effect combined with mechanical stimulus give to the SF/SNW nanocomposites piezoresistive response between 12 and 26 GPa^{-1} when pressure is between 0.2 and 0.4 MPa.

The combination of all the cited properties leads to samples with shelf ability for electrical voltage generation (above the 3.3V). This capacity has given rise to the application of SF/SNW nanocomposites in an electronic device with excellent results for object recognition. This work can be concluded to be a starting point for the development of transparent and flexible electronics based on bio-based materials.

4.3. SILK FIBROIN / COBALT FERRITE NANOPARTICLES BASED MAGNETIC ACTUATOR

BASED ON: A. Reizabal et al. *Silk Fibroin Based Magnetic Nanocomposites for Actuator Applications.* Adv. Eng. Mater., vol. 22, no. 6, p. 2000111, 2020.

Few studies have been reported on the use of SF in actuator devices. For instance, Silk actuators have been fabricated using SF and poly(pyrrole) (PPy) for tissue engineering[91]. The actuation of produced composites was reproducible and generated forces comparable with natural muscle (>0.1 MPa)[92]. Moreover, trilayer actuators based on two silk-PPy composite layers separated by an insulating silk film were also developed[93], showing a larger deflection angle per applied volt and maintaining a consistent current response over cycling[93]. Furthermore, the in situ incorporation of PPy into silk films during pyrrole polymerization allowed the development of electromechanical actuation with stable stress and strain during repeated bending cycles. The silk-PPy composite films show improved electrical properties, making them suitable as a biocompatible and biodegradable actuator for biologically relevant environments[91]. Another example of a silk-based actuator corresponds to SF hydrogel and conductive polycarbazole/silk fibroin hydrogel composites that can provide considerable deflection distance and a dielectrophoretic force of 8.00 mm and 9.19 mN, respectively, at electric field strength variations from 0 to 600 V/mm 12. However, all the achieved SF actuators are based on complex processing techniques, pollutant regiments, or multi-component devices that are not in line with the sustainability.

This work focuses on developing novel actuators based on a non-pollutant bio-based matrix using simple and low toxic techniques. The combination of SF with cobalt ferrite nanoparticles as magnetic actuators has been carried out to develop the first demonstrator actuators based on the magnetic behavior of SF based composites. Current work demonstrates the SF applicability as an actuator and explores the SF's physical-chemical behavior in combination with magnetic fillers.

Currently, SF based magnetic nanocomposites have been mainly used for biomedical applications: i) composites based on SF with cobalt ferrite ($CoFe_2O_4$ / CFO) or magnetite (Fe_3O_4) nanoparticles have been fabricated as scaffolds for tissue-engineering applications: ii) magnetic SF e-gel scaffolds prepared by the electro gelation have been explored for cell growth[94]; iii) electrospinning nanocomposite mats based on SF and superparamagnetic iron oxide nanoparticles (SPIONs) have been used for magnetically responsive cytocompatible

scaffold development[95], iv) magnetic nanoparticles have been added to silk-elastin-like protein polymers (SELPs) also for biomedical applications[95], and v) SF nanofibers have been used as template and coating to synthesize nanoparticles of core-shell (Fe_3O_4)/SF magnetite with controllable size[96]. Thus, the potentiality of these materials has been slightly explored for alternative applications.

In this work, cobalt ferrite nanoparticles have been selected as fillers to develop magnetic actuators. This is due to their high magnetization properties and magnetostrictive response, allowing active materials processing even by low magnetic nanoparticle addition. The effects of cobalt ferrite nanoparticles' concentration on the morphological, thermal, mechanical, electrical, and magnetic properties of SF composites have been analyzed. Also, SF/CFO magnetic composite has been integrated into an actuator to demonstrate its functionality. (***Figure 4.3.1***))

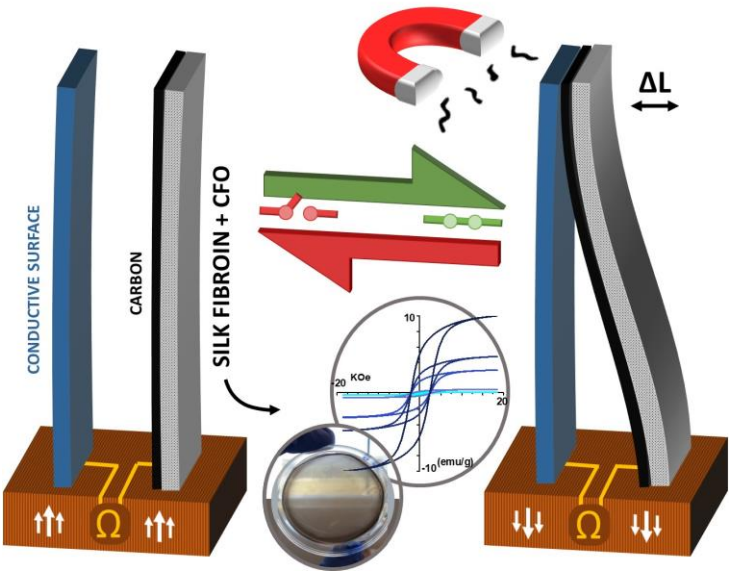

Figure 4.3. 1. *Graphical abstract of SF/CFO magnetic actuator*

4.3.1. MATERIALS AND EXPERIMENTAL METHODS

Materials

SF was extracted from B. mori cocoons supplied by APPACDM from Castelo Branco (Portugal). FA, sodium carbonate (Na_2CO_3), and calcium chloride (CaCl2) were purchased from Sigma-Aldrich. Cobalt ferrite nanoparticles with 35–55 nm size were brought from Nanoamor.

Samples preparation

SF was extracted following the *SF extraction* procedure of 4.4.1 section. CFO/SF nanocomposites of 0.5, 1, 5, 10, and 20 wt. % of CFO were prepared by a mixing and solvent casting process, as shown in ***Figure 4.3.2***. Before preparation of the nanocomposites, all the components were well dried in an oven at 40 °C for 24 h. After that, two different solutions were prepared; a first one based on SF dissolved in FA (liquid to silk ratio of 5:1 w/v) and a second one with CFO nanoparticles dispersed in FA by ultrasonication (3 h.). Both solutions were mixed in a vortex mixer MX-S during 5 min and casted over polyethylene petri dishes for 24 h. The obtained composites with a thickness of 40 μm were kept in dry atmosphere until their use. Neat SF films were prepared by the same method, without CFO nanoparticles incorporation.

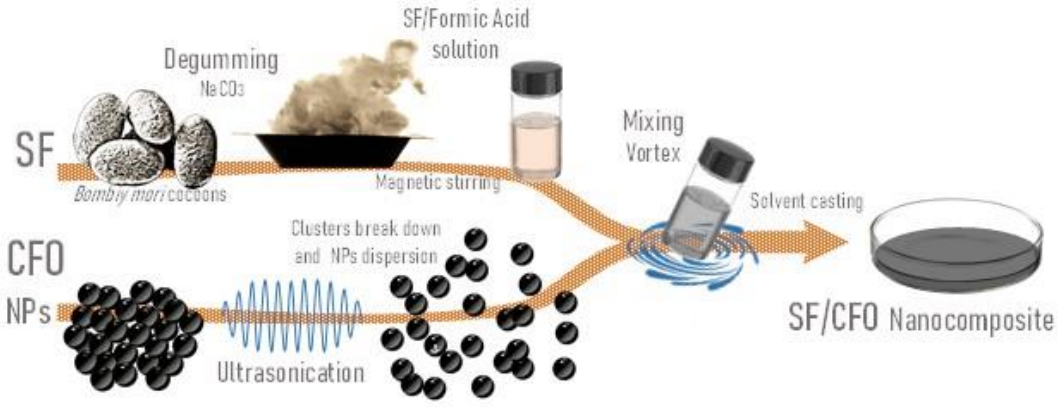

Figure 4.3. 2. *Schematic representation of CFO/SF films preparation*

Characterization techniques

SEM (SEM, NanoSEM – FEI Nova 200 (FEG/SEM)) and EDX (Hitachi Tabletop Microscope TM 3000) were used to study CFO/SF composites morphology, as well as nanoparticles dispersion and distribution within the films. Prior the measurements, CFO/SF films were coated with a conductive 20 nm gold layer by sputtering with a Polaron SC502 apparatus.

ATR/FTIR measurements were performed with a Jasco FT/IR-4100 system apparatus at room temperature from 4000 to 600 cm^{-1} using 64 scans at a resolution of 4 cm^{-1}. The assignment of the vibrational bands was performed by deconvolution of the Amide I region, as described in "characterization techniques" apart of 4.1 section.

Thermal analysis was performed with a thermal gravimetric analyzer (TGA) TGA/SDTA 851e Metter Toledo apparatus in the temperature range from 25 to 800 °C at a heating rate 10 °C·min^{-1} under air flow. DSC measurements were carried out with a Mettler Toledo DSC 822e equipment. To remove bonded water, nanocomposites were first heated from 25 to 170 ºC and then cooled to 25 ºC. Calorimetric scanning corresponds to the second heating process from 25 to 350 ºC. All heating and cooling ramps were performed at 10 ºC·min−1 under nitrogen purge (50 mL min^{-1}).

The mechanical response of the nanocomposites to thermal variations was analysed by DMA, with a Mettler Toledo DMA1 apparatus in tensile mode. Both storage modulus (E′) and loss tangent (tan δDMA) were measured as function of the temperature from 0 to 280 °C at 10 °C•min^{-1} at a frequency of 1 Hz.

To study samples dielectric response, the capacity (C) and dielectric losses (tan δ) of the CFO/SF composites was obtained using an automatic Quadteh 1929 Precision LCR meter at room temperature in the frequency range of 20 Hz to 1 MHz. Measurements were carried out in samples in which circular gold electrodes of 5 mm diameter were deposited on both sites of each sample by magnetron sputtering with a Polaron Coater SC502. The real (ε′) and imaginary (ε″) part of the dielectric function were calculated from ***equation 4.3.1 and 4.3.2***, respectively.

$$\varepsilon' = \frac{C.d}{\varepsilon_0.A} \tag{4.3.1}$$

and

$$\varepsilon'' = tan\delta \cdot \varepsilon' \tag{4.3.2}$$

where C is the sample capacity, ε0 is the permittivity of vacuum (8.85 × 10^{-12} F·m^{-1}), A is the electrode area and d is the films thickness.

Nanocomposites AC electrical conductivity (σAC) was calculated using ***equation 4.3.3***.

$$\sigma_{A.C.} = \varepsilon_0 \cdot \omega \cdot \varepsilon''$$

(4.3.3)

where ω is the angular frequency (ω = 2π∫).

Nanocomposites magnetic properties were obtained with a MicroSense EZ7 VSM from −1.8 to 1.8 T. The temperature dependent magnetic response of the CFO/SF 20% sample was studied at 50, 100, 150, and 175 °C.

4.3.2. RESULTS AND DISCUSSION

Nanocomposites morphology and filler dispersion

Homogeneous dispersion of the fillers along the polymer matrix will provide a homogeneous behaviour across the nanocomposites. Thus, an important issue in the development of nanocomposite materials is the promotion of a suitable dispersion of fillers within the polymer matrix. To analyze CFO nanoparticles dispersion, optical images, scanning electron microscopy (SEM), and energy dispersive X-ray spectroscopy (EDX) were used. Representative images from these three complementary techniques are shown in ***Figure 4.3.3***. Optical photographs (***Figure 4.3.3a***) reveal a macroscopic homogeneous dispersion of the CFO nanoparticles for filler concentrations below 5 wt. %. However, due to magnetic nanoparticles aggregation trend[97] CFO nanoparticles form macroscopic clusters for filler concentrations above 5 wt.%. Magnetic nanoparticles show a tendency to aggregate due long-range magnetic and van der Waals attractive forces[98].

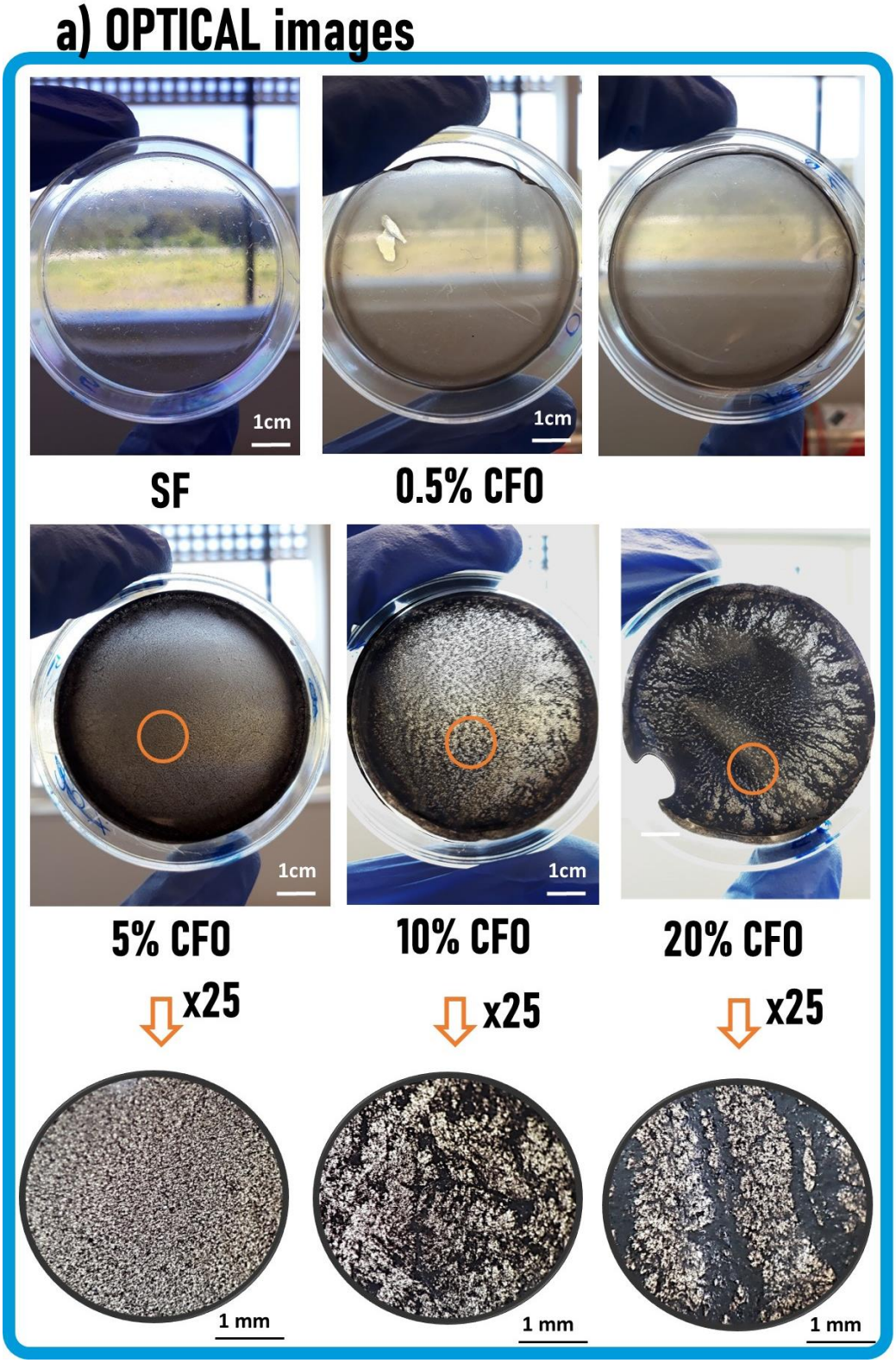
a) OPTICAL images
1cm
1cm
SF
0.5% CFO
1cm
1cm
5% CFO
10% CFO
20% CFO
x25
x25
x25
1 mm
1 mm
1 mm

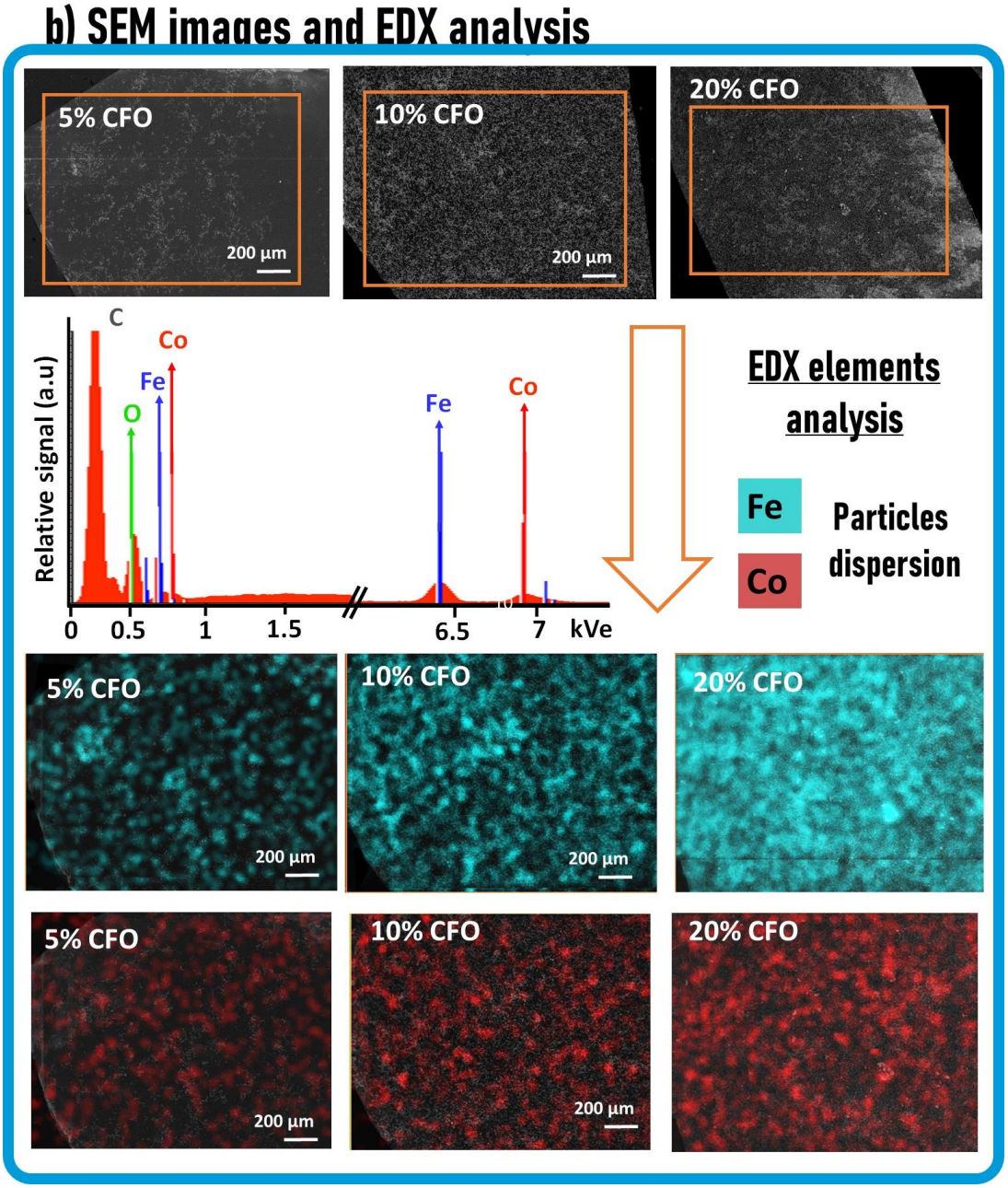

Figure 4.3. 3. *a) Optical images of CFO/SF films for 5, 10, and 20 wt% CFO, b) SEM (above) and EDX (below) images of Fe (blue) and Co (red) for 5, 10 and 20 wt% CFO samples.*

This aggregation process can be divided into two main steps: 1) Brownian motion leads the dispersed nanoparticles to come together in discrete µ-sized agglomerates; 2) Collision and consequent adhesion effects make the µ-sized agglomerates to join into higher clusters[97]. Amplifications of the optical images reveal that up to 5 wt. % of CFO content, nanoparticles are mainly affected by the first agglomeration regime, forming a well-dispersed micro sized clusters. Above 5 wt.% CFO concentration, the volume occupied by nanoparticles grow and

consequently, the collision and adhesion effects between micro sized clusters increase, resulting in the formation of macroscopic clusters.

SEM and EDX (for Fe and Co) images are shown in ***Figure 4.3.3b*** revealing the nanofiller dispersion along the nanocomposites surface. Both SEM and EDX images reveal that increasing filler content from 5 to 20 wt. % results in increasing nanoparticle clustering, especially at the outer side of the samples. In contrast, both SEM images and, in particular, EDX results (Fe and Co signal, represented as blue and red dots) show that the nanoparticles are homogenously dispersed along the nanocomposites thickness, showing that even when nanoparticles clustering is macroscopically observable on the nanocomposites surface, the CFO nanoparticles are overall properly dispersed through the nanocomposites.

Vibrational FTIR–ATR spectra

Figure 4.3.4 shows the Fourier Transform infrared (FTIR) spectra and the vibrational band assignments of the main molecular conformations for the CFO/SF nanocomposites. The full-range FTIR spectra of the samples in the frequency range from 4000 to 600 cm^{-1} are represented in ***Figure 4.3.4a***. It is observed that no peaks are formed or displaced after CFO nanoparticles addition, and all the samples show the main representative Amide I, II, OH stretching vibration, H-bond and NH stretching vibration peaks of SF30 at 1600–1700, 1517–1539, 3500–3000 cm^{-1}, respectively (***Table 4.1.1***). Thus, it is shown that magnetic nanoparticles addition does not induce any changes in the primary SF structure.

Physical–chemical properties of the SF films are highly influenced by the secondary structure of polypeptide chains, which was analyzed from the measured area under the deconvoluted peaks of amide I (***Figure 4.3.4b***). The observed main representative vibration peaks of the different secondary structures used for the Amide I deconvolution (side chains (SC), β-sheets (B), random coil (RC), α-helix (A), and turns (T)) are listed in Table 4.3.1. It is observed that the nanocomposites processing results in a highly crystalized SF, mainly dominated by β-sheet structures in all the cases. The incorporation of CFO nanoparticles progressively leads to a decrease in the β-sheet conformation content. Consequently, β-sheet portion ranges from 50% in neat SF to values around 40% in samples with 20 wt. % CFO. This fact confirms previous studies that suggest that the inclusion of CFO fillers hinder the formation of β-sheet crystals[99].

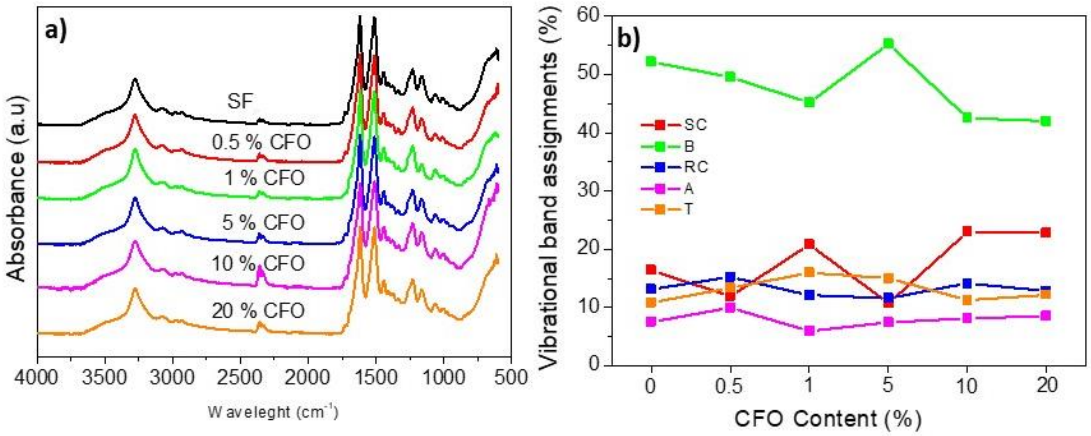

Figure 4.3. 4. *a) FTIR-ATR absorbance spectra and b) vibrational band assignment for SC, β-sheets (B), RC, α-helix (A), and turns (T) of CFO/SF nanocomposites.*

Thermal and dynamic mechanical analysis

Thermal degradation and thermal transitions define the thermal range in which materials can be applied, allowing also the understanding of the physicochemical properties of the composites. Thermogravimetric (TGA) curves and differential scanning calorimetry (DSC) were used (***Figure 4.3.5a, b***, respectively) for the thermal characterization of the samples. TGA and the corresponding derivate (DTGA) show (***Figure 4.3.5a***) that neat SF films present an initial weight loss of 6% at 100 °C, which corresponds with solvent loss (water + formic acid). A second weight loss, observed at 290 °C, is mainly ascribed to the breakdown of SF SC groups, amino acid residues, and the split of peptide bonds[100].The final weight loss at 650 °C matches with organic polypeptide chains combustion. With the inclusion of the CFO magnetic nanoparticles to the SF matrix, the solvent loss signal remains still visible at 100 °C. Similarly, no observable changes happen in the second degradation step. The final weight loss (signalled by a black arrow), on the contrary, switches to lower temperatures as CFO nanoparticles are added, effect which is attributed to the decrease in the β-sheets structures (observed in FTIR data, ***Figure 4.3.5b***), which are mainly responsible for SF thermal stability[101]. As a result, the final degradation temperature of the CFO/SF nanocomposites moves from 580 °C in the sample with 0.5 wt.% CFO content to 500 °C in the sample with 20 wt.% CFO content. The remaining residues after final organic phase combustion correspond with the nonorganic content of the CFO nanoparticles[102]. Thus, the

final residues increase with increasing filler content from 0.4% in the sample with 0.5 wt.% CFO content to 8% in the sample with 20 wt.% CFO content.

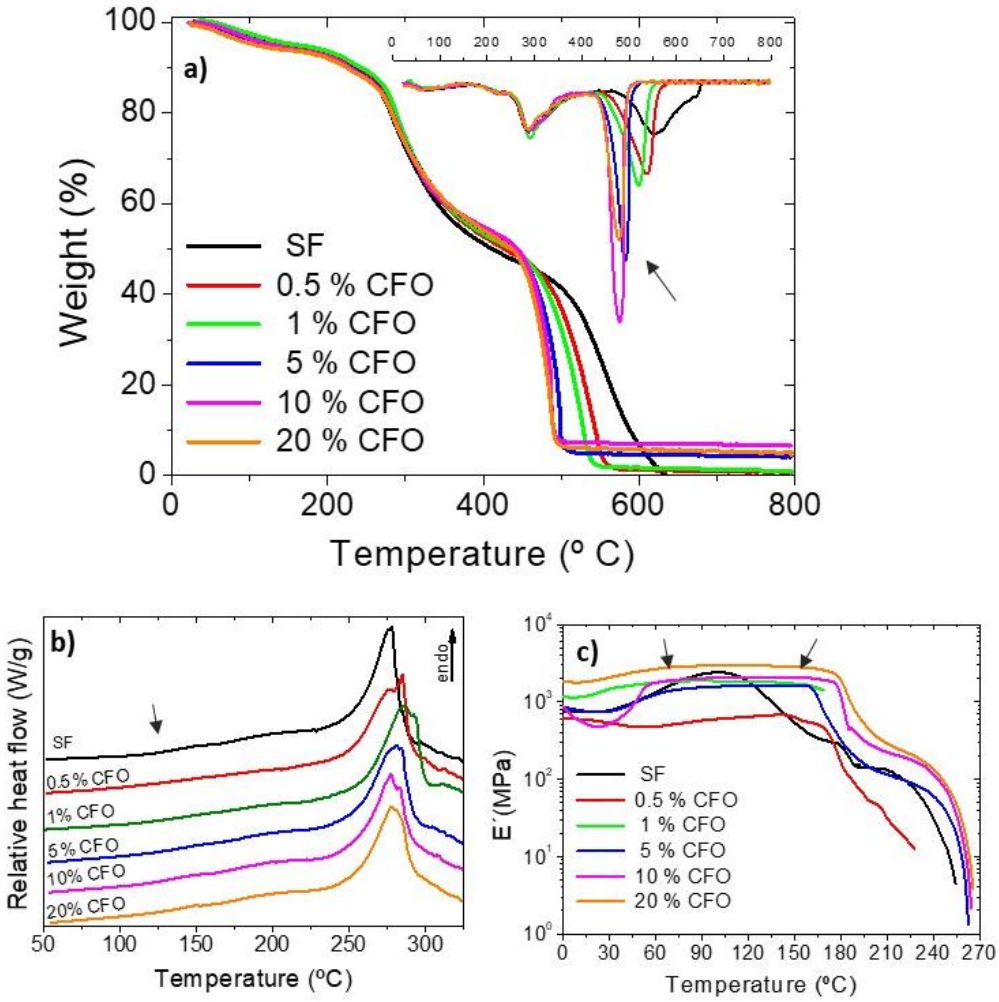

Figure 4.3. 5. *SF and CFO/SF nanocomposites: a) TGA and DTG TGA curves, b) DSC thermograms, and c) storage modulus (E') obtained after DMA measurements.*

SF and CFO/SF nanocomposites thermal transitions were studied by DSC. Bonded solvent evaporation may mask the SF thermal transitions and therefore, to remove them, all the samples were heated at 170 °C for 5 min before the DSC analysis. The DSC thermograms after this procedure are plotted in ***Figure 4.3.5b***.

SF and CFO/SF nanocomposites show a clear endothermic peak at 290 °C, corresponding to the breakdown of SC groups, amino acid residues, and the split of peptide bonds observed in TGA curves. At lower temperatures, it is also observed a heat flow variation commonly related with the glass-transition temperature (signalled by a black arrow)[101]. This effect has

been also reported in electrospun membranes with different CFO contents. However, no significant differences could be observed as a consequence of the incorporation of CFO fillers. Dynamic mechanical analysis (DMA) was conducted to further clarify SF and CFO/SF nanocomposites thermal transitions and to evaluate the viscoelastic properties of the materials. The storage modulus (E′) obtained from DMA is plotted in ***Figure 4.3.5c*** showing, for all samples, that the storage modulus shows a first increase in E′ related to solvents evaporation. Due to the plasticizer effect of solvents, after their evaporation, the polypeptide chain becomes stiffer and consequently E′ becomes three times larger. At higher temperatures, the behaviour of SF and CFO/SF nanocomposites become different. It can be observed for neat SF films that E′ starts decreasing shortly after reaching 125 °C (signalled by a right-facing black arrow) due to molecular chains flowing process (glass transition). Furthermore, E′ continues decreasing with increasing temperature until a strong fall of its value is observed due to SC group's breakdown and peptide bonds split. CFO/SF nanocomposites, on the contrary, maintain the glassy state stable until 160–175 °C where suddenly undergo the glass transition (signalled by a left-facing black arrow). After that, E′ also continues to decrease with increasing temperature until the rapid decrease is observed. Thus, CFO/SF nanocomposites behaviour shows that CFO nanoparticles are filling the free volume and consequently increase the needed energy for the glass transition to occur. This behaviour also explains the hindering effect of CFO fillers over β-sheet crystals formation observed in FTIR-ATR results.

Dielectric properties

CFO/SF nanocomposites dielectric behaviour was evaluated considering the ***equations 4.3.1, 4.3.2, and 4.3.3*** presented in the Experimental Section. From these equations, the real (ε′) and imaginary (ε″) components of the dielectric constant, as well as the AC electrical conductivity ($\sigma_{a.c}$), were obtained (***Figure 4.3.6***).

The dielectric behaviour of polymers is dependent on the contributions of dipolar moments, cations, and space charge polarizations[103]. Neat SF is mainly free of cations and space charge polarization and, as a consequence, it shows ε′ values around 2 (***Figure 4.3.6a***). The increase in polarising contributors derived from CFO nanoparticles addition, mostly dominated by interfacial and space charge polarization[104], induces the progressive increasing of ε′ in the CFO/SF nanocomposites as shown in ***Figure 4.3.6a,b***. In the different nanocomposites, increasing frequency leads to a decrease in ε′ as consequence to the dipole relaxation

process[105], due to the inability of the dipolar contributions to follow the increasing electric field variations[106]. Furthermore, for CFO/SF nanocomposites, the decrease in ε′ with increasing frequency is larger for the samples with the larger filler contents, indicating the slower dynamic of the interfacial contributions[103]. It is to notice that the increase in the dielectric response with increasing filler content is not linear (***Figure 4.3.6b***), being observed as a strong increase in the dielectric response for filler contents up to 1 wt.%, and a progressive slow increase for larger filler contents. This effect reveals the important contributions to the dielectric response of defective structures and interfacial contributions, which becomes less relevant with nanofiller aggregation and hindered mobility[107].

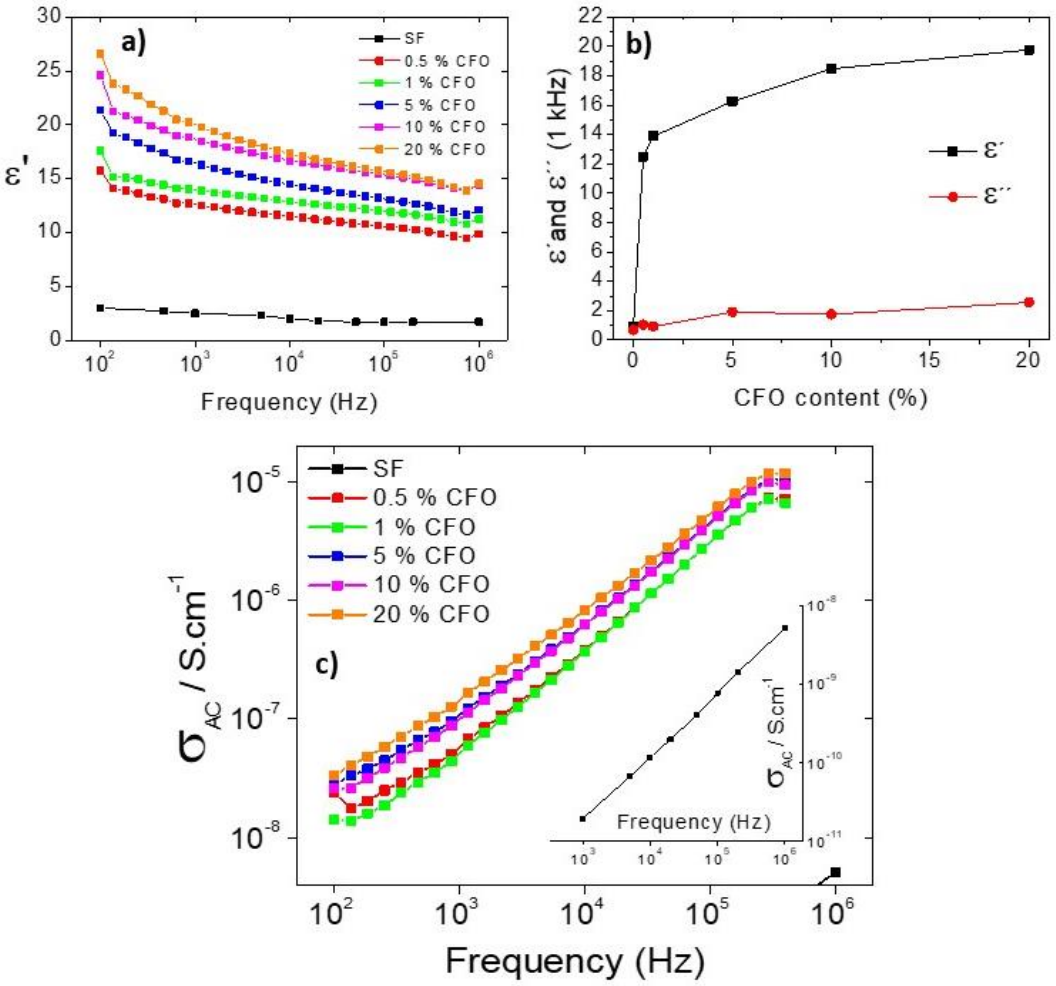

Figure 4.3. 6. *Dielectric constant, a) real (ε') part, b) variation of the dielectric and imaginary (ε") constant as a function of CFO content at 1 kHz, c) AC electrical conductivity of the different CFO/SF nanocomposites.*

In fact, as the main contributions to the dielectric response comes from interfacial and space charge contributions, this leads to an increase in the dielectric losses, ε″, (***Figure 4.3.6b***) and of the AC electrical conductivity (***Figure 4.3.6c***) with increasing filler content. It is to notice that the increase in the dielectric losses with increasing ferrite content (***Figure 4.3.6b***) is not linear due to particle agglomeration effects. As it is shown in ***Figure 4.3.6c***, the addition of CFO nanoparticles induces an increase on the AC which increases with increasing frequency, indicating the local contribution to the electrical conductivity.

Magnetic properties

To understand the magnetic behaviour of the CFO/SF nanocomposites, all samples were measured in a vibrating sample magnetometer (VSM) at room temperature in a temperature range from 20 to 175 °C (***Figure 4.3.7***). The used nanoparticles with a size distribution around 50 nm, are larger than the critical size of 27–28 nm for single domain particles[108], so the magnetic behaviour of the nanocomposites is expected to be dominated by a multi-domain magnetic behaviour. ***Figure 4.3.7a*** shows the hysteresis loops of neat CFO and CFO/SF nanocomposites, whereas ***Figure 4.3.7b*** shows the most important parameters obtained from the hysteresis loops.

Figure 4.3.7a shows that CFO nanoparticles present the typical hysteresis loop indicating the random orientation of magnetic domains. Under strong magnetic field (20 KOe), CFO nanoparticles reach the saturation (60 emu·g^{-1}) signalling that all magnetic domains have been oriented in the direction of the field. When magnetic field is removed most domain loses the orientation, but few remains invariable conserving certain magnetization (30 emu·g^{-1}), which is easily removed when a magnetic field of 1.97 kOe is applied in the opposite direction[109].

CFO/SF composites also reveal closed hysteresis loops showing that the magnetic particles preserve their original ferromagnetic behaviour once included in the SF matrix[110]. It is also observed that the magnetic behaviour of the nanocomposites is highly dependent on the CFO content. (***Figure 4.3.7b***). As expected, the magnetization saturation and magnetic field remanence increase with the addition of CFO particles. In nanocomposites, CFO nanoparticles are dispersed throughout the matrix and consequently their magnetic fields do not just add up, depending on different factors such as nanofiller agglomeration. The saturation and remanence magnetization decrease from 60 and 30 emu·g^{-1}, respectively, in neat CFO nanoparticles to 7 and 4 emu·g^{-1} in 20 wt. % CFO.

The coercive field of the CFO/SF nanocomposites increases with increasing fillers addition, until reaching a limit of 2.2 KOe at 10 wt. % CFO where it begins to decrease. This behaviour matches with previously reported data on CFO nanoparticles size-coercivity dependence[111]. It was concluded that CFO magnetic nanoparticles coercivity increases with increasing size until reaching a nanoparticle size of 100 nm, where coercivity start decreasing again. Thus, it can be concluded that the agglomeration effect observed in CFO/SF nanocomposites (as discussed in the morphological analysis), leads to a similar effect of having increasingly larger particles, matching the CFO nanoparticles size in 10 wt. % CFO with 100 nm.

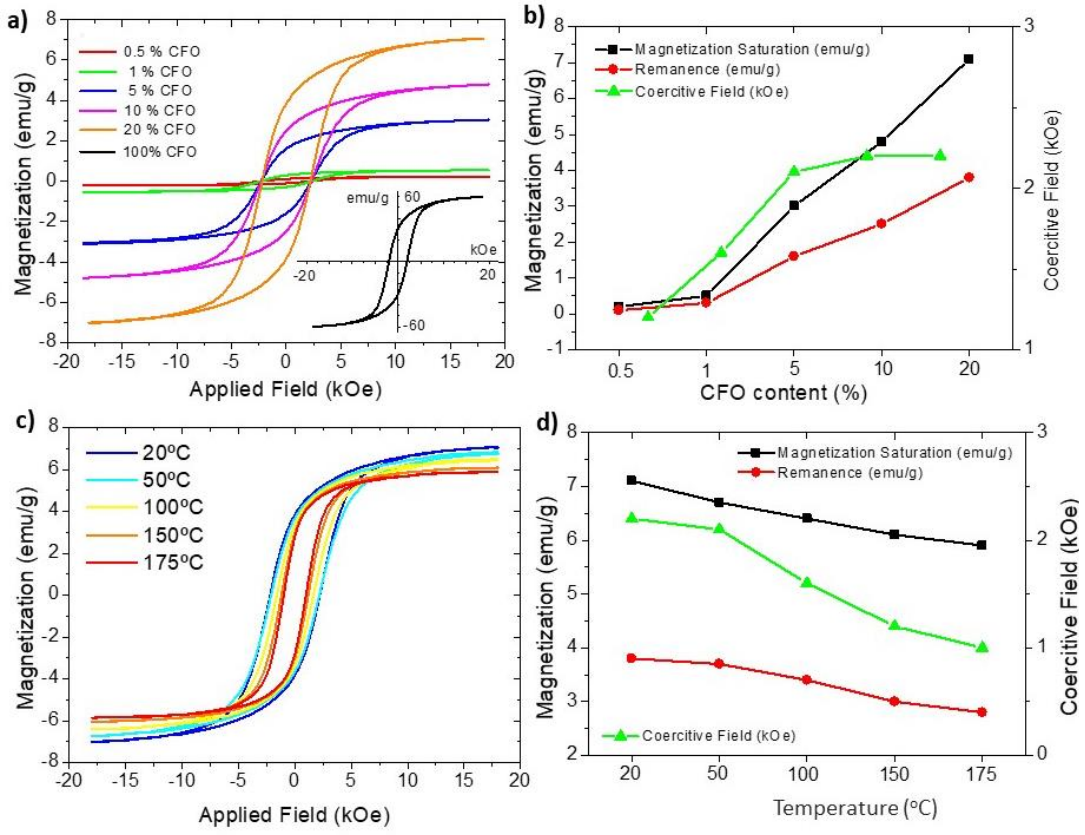

Figure 4.3. 7*. a) Room temperature hysteresis loops for neat CFO particles and CFO/SF nanocomposites, b) magnetic properties of CFO/SF nanocomposites obtained from Figure 5a, c) hysteresis loops measured at different temperatures for the 20 wt% CFO sample, and d) temperature dependence of the magnetic properties for the 20 wt% CFO content sample.*

The temperature dependence of the magnetic behaviour of the nanocomposites is shown in ***Figure 4.3.7c***. The 20 wt. % CFO composite data is plotted as representative for all composites. As the Curie temperature of the CFO particles is 500 °C[112], no changes in magnetic properties are observed in this sense in ***Figure 4.3.7c***. Furthermore, the applied maximum temperature (175 °C) is near the SF glass transition previously determined

between 160 and 175 °C, thus, the thermal measurements will report data on nanocomposites mainly in the glassy state (below 175 °C) and in the first rubbery points. Temperatures do not exceed T_g in any case, ensuring the SF mechanical stability.

Figure 4.3.7c shows that closed hysteresis loops are observed in all temperature range, confirming that CFO/SF nanocomposites still maintain the magnetic behaviour even at high temperatures. As temperature increases, maximum magnetization, coercivity, and remanence decrease (***Figure 4.3.7d***), as expected, due to the decrease in magnetocrystalline anisotropy[113]. Due to the temperature increase, nanoparticles internal energy increases, and the energy barrier that separates the energetically degenerated magnetic orientations decreases, thus a minor energy fluctuation lead to the switching of domains orientation. As a consequence of temperature increases, lower applied magnetic field is necessary to induce the maximum magnetization, lower amount of domains remains magnetized after magnetic field removal and consequently lower field is necessary to demagnetize the samples (***Figure 4.3.7d***)[111]. Thus, the addition of CFO nanoparticles provides the CFO/SF composites with a controllable magnetic response and opens a functional way to produce sensors and actuators with adjustable properties.

Magnetic actuator

Considering the magnetic properties of the CFO/SF nanocomposites, a device that acts as magnetic actuator switch in the proximity of a magnetic field was fabricated. For that, a resistive ink based on carbon nanotubes was deposited over the CFO/SF nanocomposite film to act as conductor and placed in front of another conductive surface separated with an air gap of 500 μm as shown in ***Figure 4.3.8a***). When no magnetic field is present, the conductive surfaces are mechanically separated from each other, being in open circuit. When a magnetic field is present the two conductive surfaces touch, and the resistance decreases as the circuit is closed, as it is shown in the schematic representation in ***Figure 4.3.8a***).

The magnetic actuator was fabricated by placing the 20 wt.% CFO composite (SF/CFO/Carbon) on a cantilever configuration with the carbon surface turn to the conductive structure fabricated by 3D printing with conductive PLA (CDP11720) from Proto-pasta using a PRUSA i3 MK3 as shown ***Figure 4.3.8a***) (see video in Supporting Information). The electronic circuit is based on a voltage divider and an ADC (analog to digital converter) of 10 bits present on the Arduino Nano converts the voltage variation

(resistance variation through ***Equation 4.3.4***), in the magnetic switch to a digital signal that then sends the data to the laptop via USB.

$$Rs = \frac{5 \times R1}{5 - V_{Rs}}$$

(4.3.4)

When a magnetic field is present by approaching a permanent magnet (BX0C8-N52 from K&J Magnetics, Inc) with a surface field of approximately 5336 Gauss, the film bends and touches the conductive plate that changes the resistance of the circuit. ***Figure 4.3.8b*** shows the resistance variation from open circuit to approximately 700 MΩ when the magnet is approximated.

It is observed that the resistance behaviour is reproductive when the magnet is approximate to the nanocomposites as a function of the time (***Figure 4.3.8b***). As expected, if the sample is closer to the magnet, the displacement increases and the resistance decreases

Considering the magnetic and dielectric response of the developed CFO/SF nanocomposites, this work demonstrates that it is possible to develop magnetically responsive actuators based on natural polymer such as SF to produce a new generation of environmental-friendly multifunctional materials.

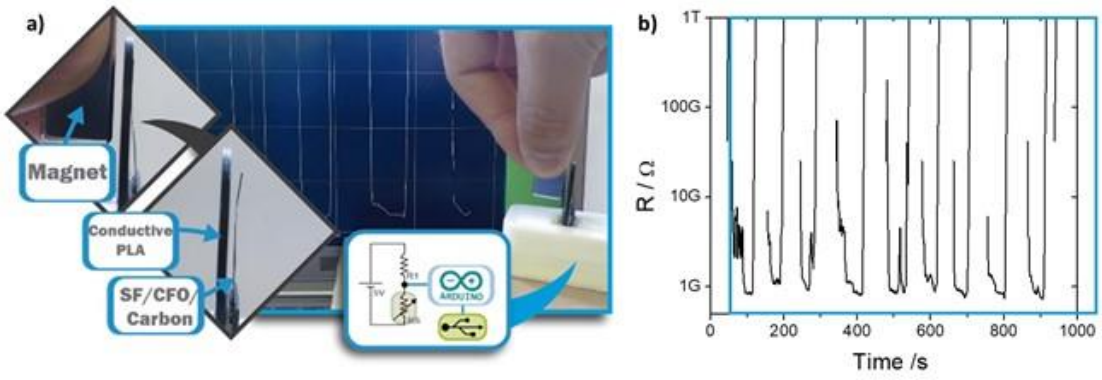

Figure 4.3. 8. . *a) Electronic circuit and representation of the actuation by the magnet and b) resistance variation as a function of time with the approximation of the magnet.*

4.3.3. CONCLUSIONS

CFO/SF nanocomposites were successfully processed by solvent casting. The selected SF solution in formic acid (FA) allowed the incorporation of CFO nanoparticles with different amount, ranging from 0.5 to 20 wt. %. Good dispersion of the CFO nanoparticles is achieved, as observed by SEM and confirmed by EDX analysis.

FA makes the polypeptide structure to fold into a highly ordered structure rich in β-sheets, an organization which provides to the samples with large thermal stability, being able to stand temperatures above 250 °C without thermal degradation.

The incorporation of the CFO nanoparticles in the SF matrix strongly affects nanocomposites behaviour given to the thermal and mechanical stability to the samples also above 160 °C. CFO nanoparticles incorporation leads to a significant increase in samples dielectric response, reaching values above 20 with when CFO contents of 20 wt. % is added to SF.

Successfully, the CFO nanoparticles incorporation to the SF matrix results in a magnetic composite characterized by strong magnetic response, even with low CFO nanoparticles addition, CFO/SF nanocomposites show magnetization values around 10 emu g^{-1} and coercive values of almost 4 kOe when 20 wt.% of CFO nanoparticles are added. This magnetic behaviour allowed the development of magnetic actuators based on natural polymers.

4.4. SILK FIBROIN / IONIC LIQUIDS BASED ELECTRICAL BENDING ACTUATOR

BASED ON: A. Reizabal et al. Silk Fibroin Bending Actuators as an Approach Towards Natural Polymer Based Active Materials. ACS Appl. Mater. Interfaces, vol. 11, p. 30197-30206, 2019.

There is a wide range of actuators, but most are composed of assembled multi-component devices made by toxic components or complex processing techniques. The current technological transition (IoT) requires sustainable actuators, in which the complexity and toxicity of the components and processes are reduced. With this aim, the development of actuators based on polymer composites and bio-based materials represents an accessible and suitable option.

The combination of ionic liquids (ILs) and highly polar polymers has emerged as an interesting new class of smart materials for developing ionic electroactive polymer (EAP) actuators[114]. The great attention that has been paid to ILs, defined as molten salts at room temperature composed of cations and anions, relies on properties such as low melting temperature, negligible vapor pressure, high chemical and thermal stability, and ionic conductivity[115]. Further, ILs present a broad electrochemical window making them suitable for the development of ionic EAP actuators[114]. The incorporation of ILs into a polymer matrix leads to the development of a new generation of materials combining the functional properties of ILs and polymers' characteristics, such as lightweight, low cost, fracture tolerance, and easily processing[116]. The main advantages associated with ionic EAP actuators are the large deformations achieved, in comparison with inorganic actuators, lightweight, flexibility, and low voltage actuation, among others.

Different polymers and ILs have been used to develop ionic EAP actuators, focusing on the effect of cation and anion type[114], IL concentration[116] and polymer-ion interactions[117]. Ionic EAP actuators have been mainly based on synthetic polymers such as polyvinylidene fluoride (PVDF) and its copolymers, which have been applied in biomedical applications. The development of biologically inspired actuators devices with tunable electromechanical responses has attracted increasing attention, particularly for the development of artificial muscles[118].

SF represents the right candidate for the development of actuators[119]. In the present study, SF composite films have been prepared by solvent casting. Different contents of two ILs: 2-hydroxy-ethyl-trimethylammonium (or cholium) dihydrogen phosphate ([Ch][DHP]) and 1-

n-Butyl-3-methylimidazoliumtricyanomethanide ([Bmim][C(CN_3)]) have been added. Both possess different properties in terms of viscosity, electrical conductivity, and polar surface area of anion and cation (see Table 4.4.1), which allows to evaluate the effect of those parameters on the physical-chemical properties of the composite and its bending response. Further, ([Ch] [DHP] IL was selected due to its biocompatibility and high melting point (190 ºC). About ([Bmim][C(CN3)]), it is the typical IL based on imidazolium and shows hydrophobic behaviour[120]. SF/IL actuator's performance and the physical-chemical and electrical characteristics have been evaluated (***Figure 4.4.1***).

Figure 4.4. 1. *Graphical abstract of SF/IL bending actuator*

4.4.1. MATERIALS AND EXPERIMENTAL METHODS

Materials

Formic acid was purchased from Sigma-Aldrich and used as received from the provider. Bombyx mori cocoons were supplied by APPACDM from Castelo Branco (Portugal). The ILs Choline dihydrogen phosphate ([Ch] [DHP]) (purity higher than 98% and electrical conductivity ≥0.04 $S \cdot m^{-1}$) and 1-Butil-3-methylimidazolium tricyanomethanide ([Bmim] [C(CN_3)] or [C4mim] [TCM]) (purity higher than 98% and electrical conductivity of 0.0883

$S \cdot m^{-1}$) (***Table 4.4.1***) were purchased from Iolitec. Their chemical structures are given in ***Table 4.4.1***.

Table 4.4. 1. [Ch][DHP] and [Bmim] [C (CN_3)] main physical-chemical properties (data obtained from the provider).

IL	*[Ch][DHP]*		*[Bmim][C(CN_3)]*	
Properties	***Viscosity (cP):***	*solid*	***Viscosity (cP):***	*25.7 (25 °C)*
	Conductivity ($mS \cdot m^{-1}$):	*<0.4 (25°C)*	***Conductivity ($mS \cdot m^{-1}$):***	*8.83 (30°C)*
Ion	***Cation***	***Anion***	***Cation***	***Anion***
	Choline	*Dihydrogen phosphate*	*1-Butil-3-methylimidazolium*	*Tricyanomethanide*
Structure	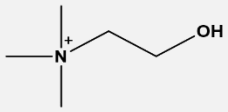	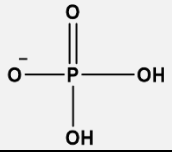	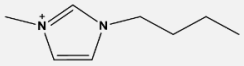	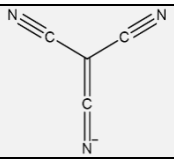
Molecular weight (g/mol)	*104.2*	*136.1*	*139.2*	*90.7*
Polar surface area ($Å^2$)	*20*	*81*	*9*	*48*

Samples preparation

SF was extracted following the *SF extraction* procedure of 4.4.1 section SF/IL film composites were prepared by solvent casting as schematically represented in ***Figure 4.4.2***. Different amounts of each IL (20, 40 and 60% wt.) were initially dispersed into 4 mL of formic acid under magnetic stirring at 400 rpm. Then, SF was dissolved into the IL/formic acid solutions and films with a thickness of 80 µm were obtained by casting the solution into Petri dishes at room temperature.

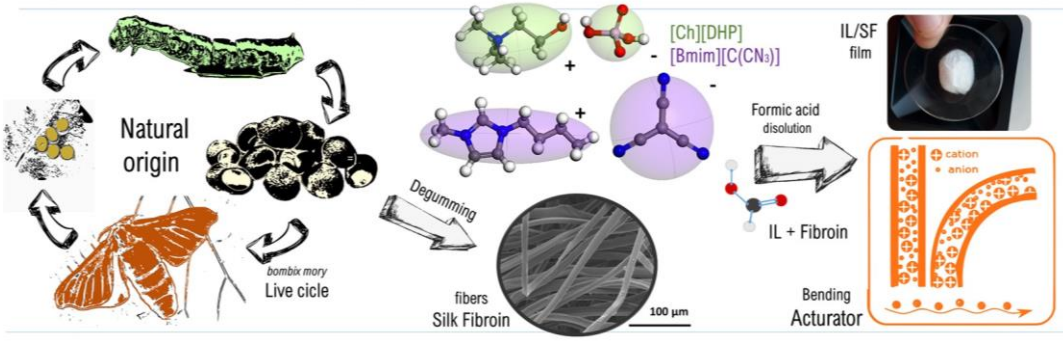

Figure 4.4. 2*. Schematic representation of the procedure for the preparation of the SF/IL*

Characterization techniques

The morphology of the SF/IL composites was evaluated by scanning electron microscopy (SEM, NanoSEM - FEI Nova 200 (FEG/SEM)) with an accelerating voltage of 15 kV. Prior to the analysis, the SF/IL samples were deposited with a conductive 20 nm gold layer by sputtering with a Polaron SC502 apparatus.

Attenuated Total Reflectance (ATR)/Fourier Transform infrared (FTIR) measurements were performed with a Jasco FT/IR-4100 system apparatus at room temperature from 4000 to 600 cm-1 using 64 scans at a resolution of 4 cm^{-1}. All the FTIR scans were normalised with the amide I region for proper quantification of the silk structure. The assignment of the vibrational bands was performed by deconvolution of the Amide I region, as described in "characterization techniques" apart of 4.1 section.

Thermal analysis was performed with a Thermal Gravimetric Analyser (TGA) TGA/SDTA 851e Metter Toledo apparatus between 25 to 800 °C at a heating rate of 10 °C·min^{-1} under airflow.

Differential scanning calorimetry (DSC) measurements were carried out with a Mettler Toledo DSC 822e equipment. In order to remove all the absorbed water, samples were initially heated from 25 ºC to a 170 ºC, cooled to 25 ºC and heated again until 350 ºC. All the heating and cooling DSC processes were performed at 10 ºC min-1 under nitrogen purge (50 mL min^{-1}).

Mechanical characteristics of the samples were evaluated by tensile testing using a Metrotech MTE-1 from Techlab systems. Stress-strain curves were obtained at 2 mm·min^{-1} in 5 mm wide, 15 mm long samples. Displayed results were obtained from the mean of 3 measurements. Young modulus was extracted from the slope between 0.5 – 1.5 % strain in the stress-strain plot.

For the dielectric measurements, circular gold electrodes of 5 mm diameter and 20 nm thickness were deposited by magnetron sputtering with a Polaron Coater SC502 onto both sides of each sample. Dielectric measurements were performed at room temperature using the parallel plate capacitor configuration using a Quadtech 1920 LCR precision meter.

The real (ε′) and imaginary (ε′′) part of the dielectric function were obtained from the measurements of the capacity (C) and the dielectric losses (tan δ) in the frequency range of

100 Hz to 1 MHz with an applied voltage of 0.5 V through the ***equations 4.4.1*** and 4.4.2 respectively[121]:

$$\varepsilon' = \frac{C \cdot d}{\varepsilon_0 \cdot A} \tag{4.4.1}$$

and

$$\varepsilon'' = tan\delta \cdot \varepsilon' \tag{4.4.2}$$

where C is the capacity, ε_o is the permittivity of vacuum (8.85×10^{-12} F m^{-1}), A is the electrode area and d is the thickness of samples.

The AC electrical conductivity (σ_{AC}) was calculated using ***equation 4.4.3***[60]:

$$\sigma_{A.C.} = \varepsilon_0 \cdot \omega \cdot \varepsilon'' \tag{4.4.3}$$

where ω (ω=2πʃ) is the angular frequency.

Bending response (ε) measurements were performed in samples with 12 mm × 2 mm x 80 µm with 20 nm gold electrodes deposited on both sides by magnetron sputtering (Polaron SC502). The needles of the sample-holder were connected to an Agilent 33220A function generator and an oscilloscope PicoScope 4227. A square wave signal with different peak voltages (3.0, 4.0, 5.0 and 10.0 V) at 100mHz were applied to evaluate the bending, ε, of the samples by applying ***equation 4.4.4***[116].

$$\varepsilon = \frac{2d\delta}{L^2+\delta^2} \tag{4.4.4}$$

where L is the sample free length, d the thickness and δ the displacement along the x axes.

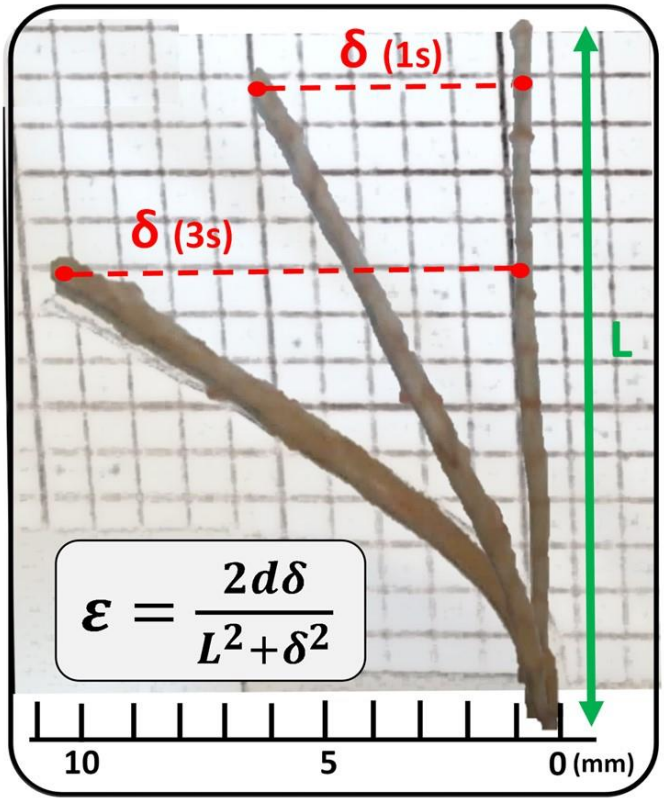

Figure 4.4. 3. *Representative image of SF/IL based actuators bending and identification of the main parameters used for the quantification of the bending response.*

4.4.2. RESULTS AND DISCUSSION

Morphology

Figure 4.4.4 shows the cross-section SEM images of the SF/IL samples showing that neat SF (***Figure 4.4.4a***) presents a dense and wrinkled surface with non-defined morphology. The absence of a smooth surface is attributed to the diffusion of the molecules from the solvent evaporation and the corresponding mass and heat transfer during film[122], as well as to the non-regular packing of SF macromolecular chains during the casting process[123].

Figure 4.4.4b, show that the incorporation of [Ch] [DHP] into the polymer matrix promotes internal micro-fractures in [Ch] [DHP]/SF films. Micro-fractures, appears throughout the material suggesting that the damages are caused by internal stresses from [Ch][DHP]/SF-solvent (formic acid + water) interactions during the casting process which affects the solvent evaporation and polymer crystallization kinetics[124]. The presence of solvent in [Ch] [DHP]/SF films is corroborated by TGA measurements (see later).

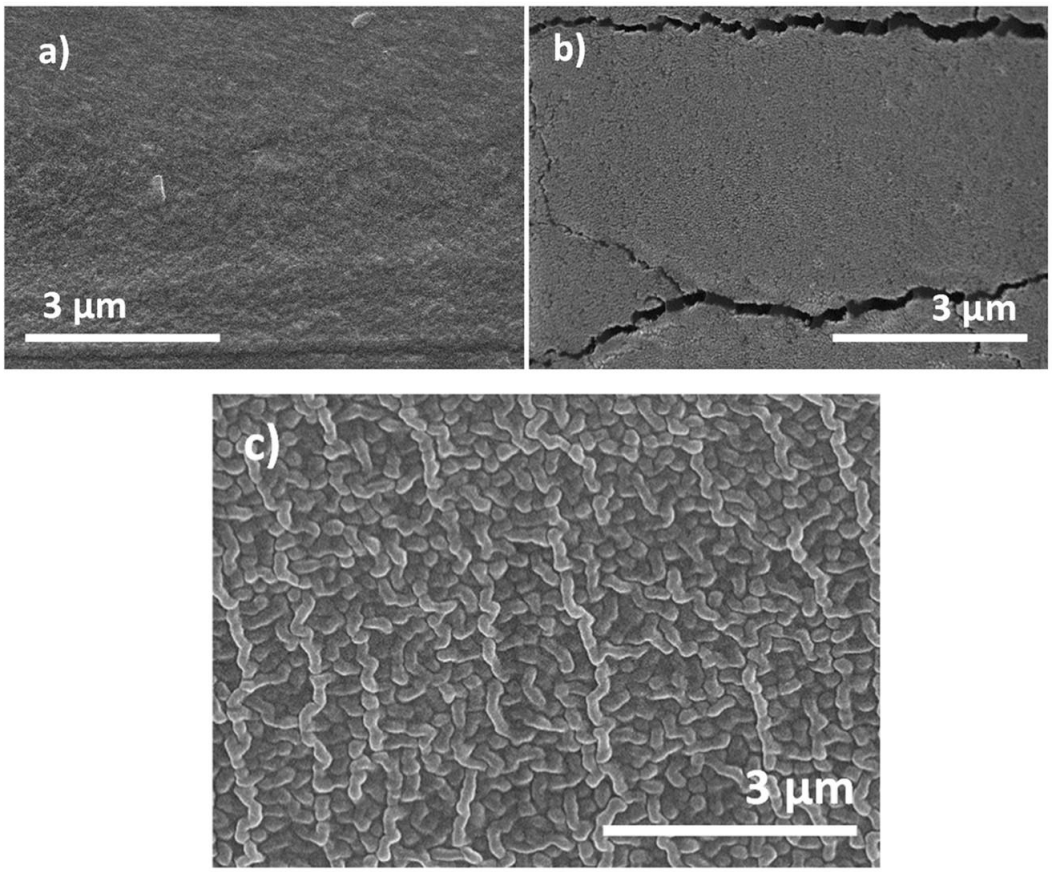

Figure 4.4. 4. *Cross-section morphology of (a) neat SF, (b) SF composite with 60% wt [Ch][DHP] and (c) SF composite with 60% wt [Bmim][C(CN$_3$)].*

As shown in ***Figure 4.4.4c***, the incorporation of [Bmim] [C (CN3)] entangled globule-like nanostructures. This morphology, previously observed in SF nanocomposites with carbon nanotubes, suggest that the organization of SF into globule-like nanostructures is related with specific filler-SF interactions. During [Bmim][C(CN$_3$)]/SF casting, IL dissociated ions can act as nucleating agents and, as a consequence, when SF secondary structure is formed, the polar side chains can orient towards ions side while the least bulky non-polar side chains oriented in the opposite direction. This configuration leads the polypeptide chain to curve in globular β-proteins[123].

Physical-chemical characterization

FTIR-ATR measurements, ***Figure 4.4.5***, were performed in order to study the molecular conformations of SF/IL composites.

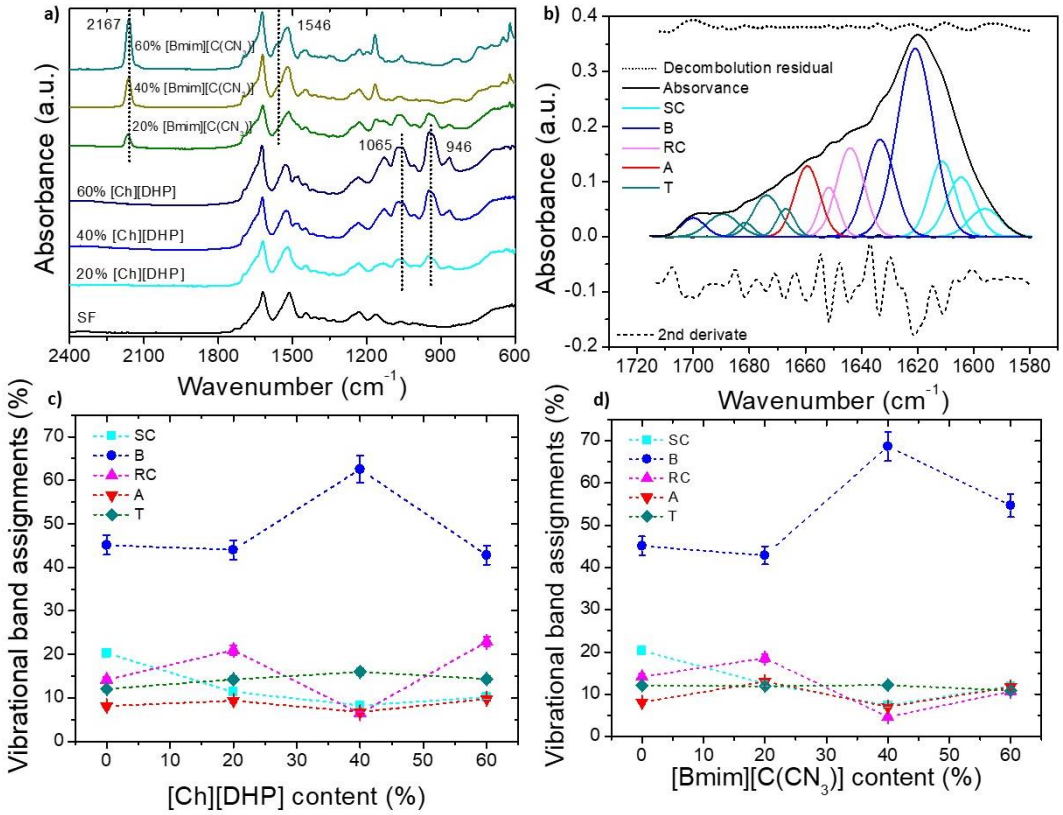

Figure 4.4. 5. *FTIR-ATR spectra for (a) [Ch][DHP]/SF and [Bmim][C(CN3)] /SF composites. b) Typical example of the deconvolution of amide I region and vibrational band assignments for side chains (SC), β-sheets (B), random coil (RC), α-helix (A) and turns (T) for SF, c) [Ch][DHP]/SF composites vibrational band assignments and d) [Bmim][C(CN3)] /SF composites vibrational band assignments.*

Figure 4.4.5 shows that, independently of the IL type, the main characteristic absorption bands of the SF can be observed for all composites (***Figure 4.4.5a***). The main FTIR absorption bands are listed in Table 4.4.2.

Table 4.4. 2. *FTIR main absorption peaks of the SF/IL samples.*

Bands (cm^{-1})	*Assignments*	*Ref*
1620	*Amide I (C=O stretching vibration, NH in plane bending, out of phase CN stretching vibration, and C-CN deformation)*	125
1517-1539	*Amide II (stretching of C–N and N–H in-plane bending)*	126
1230	*Amide III*	127
1250 and 800	*Primary structure of polypeptides*	99
1015	*-(gly-g1y)- sequence*	
1000 and 980	*-(gly-a1a)- sequence*	
946	*[Ch][DHP] phosphorous dioxide*	128
1065	*[Ch][DHP] hydrocarboxylic radical*	129
2167	*[Bmim][C(CN3)] cyan groups*	

SF presents highly crystalized conformation (β-sheet content of 45%) after the casting process (***Figure 4.4.5c and d***). This organization can be explained due to effect of formic acid over SF molecules. Due to the polar behaviour of formic acid and the strong interaction with SF, SF self-interactions are weakened and, consequently, SF secondary structure unpacks and becomes random coils. On the other hand, the removal of formic acid induces the crystallization into β-sheet conformation[130]. The incorporation of 20% wt. of [Ch][DHP] and [Bmim][C(CN3)] ILs does not affect the secondary structure of SF, but, when the IL content increases to 40% wt., the β-sheets SF/IL composites crystallization also increases (above 65%). Nevertheless, when IL contents reach to 60%, the crystallinity fall to initial values. This behaviour suggests also the double IL effect as promoting or hindering crystallinity, depending on the type and concentration and, therefore, the interactions with the SF chains[51]. This fact can be explained by the chaotropic and osmotrophic behaviour of ILs ions. [Ch][DHP] is composed of chaotropic cations and a osmotrophic anions[131], and [Bmim][C(CN3)], on the contrary is composed by osmotrophic cation and chaotropic anion[132]. Osmotrophic agents promote the water structure, while chaotropic agents destroy that structure[133]. As a consequence, osmotrophic agents stabilize proteins native structure while chaotropic agents destabilize as it disturbs the hydrogen bonding network that makes the crystal domains to form. This chaotropic effect makes the proteins to unfold irreversibly with high salt concentration[133]. Due to this chaotropic effect, [Ch][DHP] was found to be an effective solvent of natural proteins at high concentrations[131]. Further, [Ch][DHP] has been proven to have a large potential as refolding matrix for aggregated matrix[134].

Thus, it can be suggested that the osmotrophic effect of [DHP] anion and [Bmim] cation at 40% wt. of IL content, triggers SF refold and lead to an increase of β-sheets content. On the other hand, at 60% wt. ILs content, the chaotropic effect of ions increases, leading to the secondary structures to unfold.

Thermal properties

Thermogravimetric results (TGA) and the corresponding derivate (DTGA) are shown in ***Figures 4.4.6a and b***. For all composites, an initial weight loss is observed before reaching 100 ºC, which is attributed to the solvent (formic acid + water) evaporation. Due to the high hygroscopic characteristic of the ILs, the amount of bonded water to the polymer matrix increases as IL content increases. This effect is more noticeable for composites containing

[Ch] [DHP], where a weight loss from 5.6% (neat SF) to 18.5% ([Ch] [DHP] 60 % wt.) is observed. The mass loss up to 300 ºC in the composites containing [Ch][DHP] is attributed to the dehydration of the [DHP] anion[86].

A second degradation step starts to occur at approximately 260 ºC for neat SF and SF/IL composites. This degradation is attributed to the breakdown of side chain groups of amino acid residues as well as the cleavage of peptide bonds of SF[99]. ***Figure 4.4.6a and b*** and the corresponding DTG curves (inset) show that the thermal stability of SF is affected by the introduction of the [Ch] [DHP] and [Bmim] [C (CN_3)] ILs. The incorporation of [Ch] [DHP] leads to a decrease of the thermal stability, decreasing the initial degradation temperature (Tonset) with increasing IL content. On the contrary, the thermal stability of the SF slightly increases with increasing [Bmim] [C (CN_3)] content.

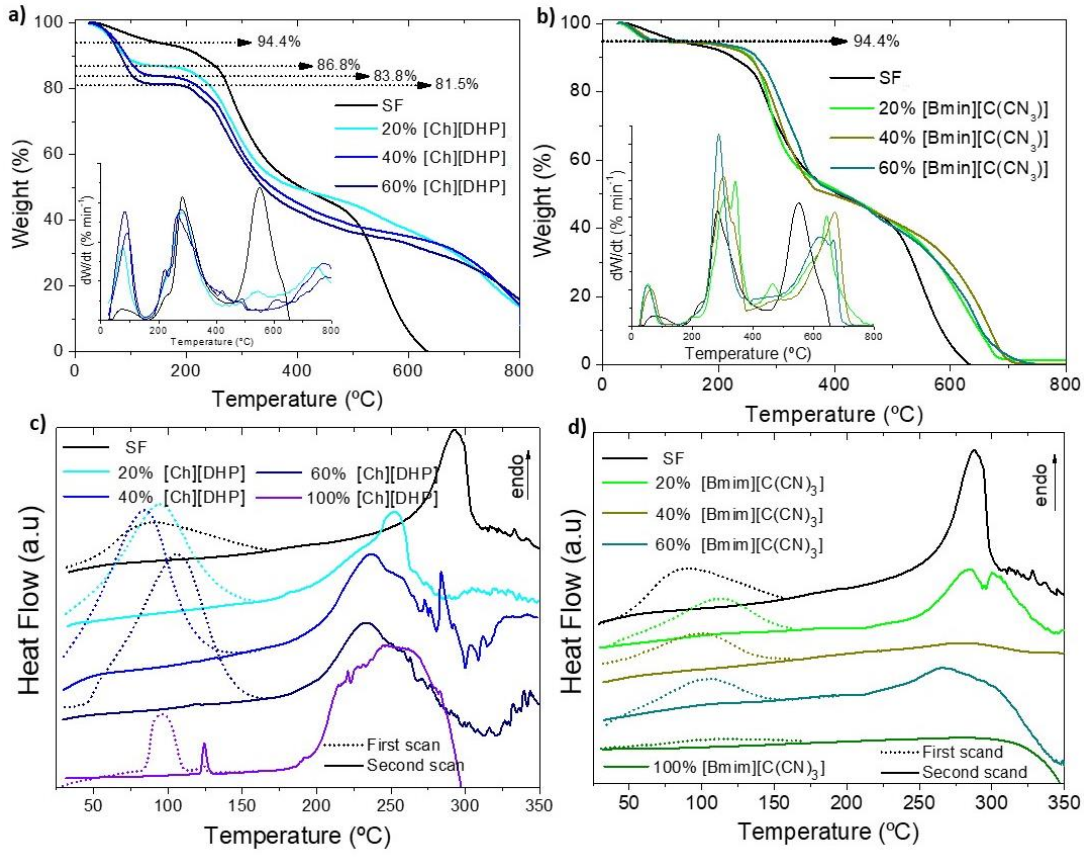

Figure 4.4. 6. *TGA and DTG thermogravimetric curves for a) [Ch][DHP]/IL composites and b) [Bmim][C(CN3)]/IL composites. DSC thermograms for c) [Ch][DHP]/IL composites and d) [Bmim][C(CN3)]/IL composites.*

A third weight loss is observed for neat SF at approximately 550 ºC, which is related to the combustion of the remaining organic compounds. When [Ch][DHP] and [Bmim][C(CN_3)] are incorporated into the polymer matrix, due to the interactions between IL and SF the final degradation peaks shift to 780 ºC and 660 ºC, respectively.

The DSC thermograms of SF and SF/IL composites with different IL contents are presented in ***Figure 4.4.6c and d***. Independently of the IL type and content, in the first annealing all samples show a single endothermic peak between 75 and 150 ºC, attributed to the solvent evaporation[58]. With increasing [Ch][DHP] content in the composites the solvent evaporation peak shifts to higher temperatures due to bonded water loss[58].

After solvent evaporation SF/IL samples do not show relevant transitions until the degradation temperature, shown as an endothermic peak. Matching with TGA thermogravimetric curves, [Bmim] [C (CN_3)]/IL DSC scans show slight endothermic peaks, showing the higher thermal stability of the [Bmim] [C (CN3)]/IL samples.

Mechanical response

SF/IL mechanical properties directly affects electromechanical actuators performance. Uniaxial tensile testing of [Ch] [DHP]/SF and [Bmim] [C (CN3)] /SF was performed and representative stress-strain curves, Young modulus (E) and elongation at break (ε_b) were plotted in ***Figures 4.4.7a and b***.

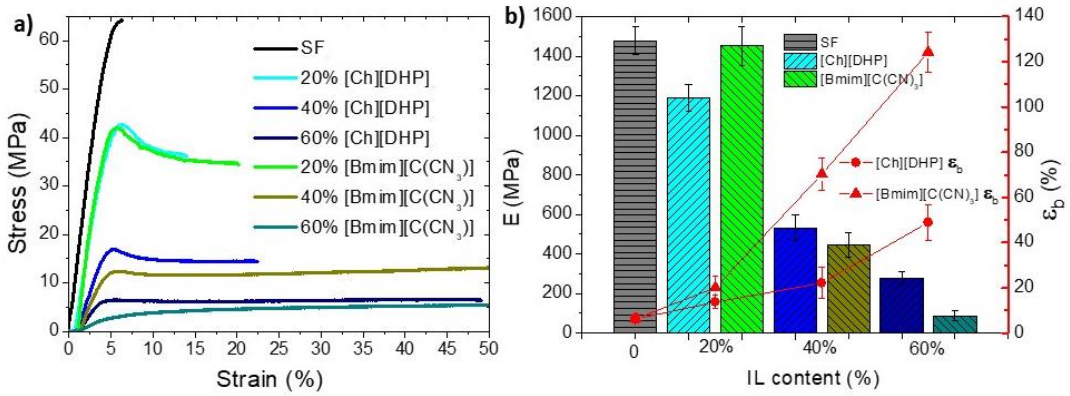

Figure 4.4. 7. *a) Stress-strain tensile curves for the SF/IL composites and the corresponding b) Young Modulus (E, bars) and strain at break (ε_b, dots) values.*

SF samples show stress at yield values above 64 MPa. Nevertheless, when elongation reaches 6.3%, it breaks denoting the fragility of highly crystallized SF films. IL incorporation leads to a large increase of elongation at break for all SF/IL samples (***Figure***

4.4.7a), related with ILs dissociation along SF, which triggers the formation of mobile ions that are inserted through the protein chains[135]. As a consequence, polypeptide chains gain mobility and samples plasticity increases, leading to a decrease of the Young modulus with the incorporation of the IL and with increasing IL content, independently of the IL type. [Ch][DHP]/SF composites show larger stress at yield due to the stronger interactions between IL and SF.

Electrical response

The real part of the dielectric constant (ε′), loss tangent (tan δ) AC conductivity (σ_{AC}) and imaginary part of the dielectric constant (ε′′) of SF/IL composites as function of frequency are shown in ***Figure 4.4.8a, b, c and d*** respectively. The electrical response of IL based composites depends on ions type, size and geometry[136]. The addition of ILs increases the dielectric constant in comparison to neat SF in all frequency range. This behaviour confirm the IL ions dissociation on the SF matrix which leads to an increase of the number of charge carriers into the polymer matrix[137]. For both composites, the incorporation of 20% wt. of each IL strongly increases the ε′ when compared with SF, effect which is further enhanced with IL content up to 60% wt., where the increase reaches 5 orders of magnitude. Thus, both for [Ch][DHP]/SF and [Bmim][C(CN3)]/IL samples the dielectric constant increases with increasing IL content, as a consequence of increasing charge carrier content, the increase being relatively smaller for increasing IL concentrations from 40 to 60 % wt., due to the larger IL content and therefore hindered mobility of the charge carriers within the polymer matrix. For all SF/IL composites, the dielectric constant decreases with increasing frequency due to ionic dynamic relaxation as observed in the dielectric losses, in particular for the higher IL contents[138]. The dielectric loss tangent of the SF/IL shows the increase of conductivity of the sample with increasing IL content as well as the dielectric ionic relaxation, with a maximum around 104 and 105 Hz for [Ch][DHP]/SF and [Bmim][C(CN3)]/IL respectively, the dielectric loss tangent peak shifting toward higher frequencies with increasing IL content.

Figure 4.4.8c shows the AC conductivity, calculated after ***equation 4.4.3***, as a function of frequency for the different samples, showing the increase of the electrical conductivity with increasing IL concentration, as previously mentioned. For the higher IL content, the AC conductivity slightly increases with frequency al lower frequencies becoming nearly frequency independent around 103 Hz, as a consequence of the ionic relaxation and the

limitations in responding to the fast varying electric field. It can be observed that the highest AC conductivity values are observed for the [Ch] [DHP]/SF. As it was aforementioned, the incorporation of [Ch][DHP] into the SF matrix leads to more water absorbance when compared with the [Bmim][C(CN3)] /SF samples, leading to a larger respond to the applied electric field, as a result of increased dissociation of charge carriers[139]. This fact is also demonstrated in the ***Figure 4.4.8d***.

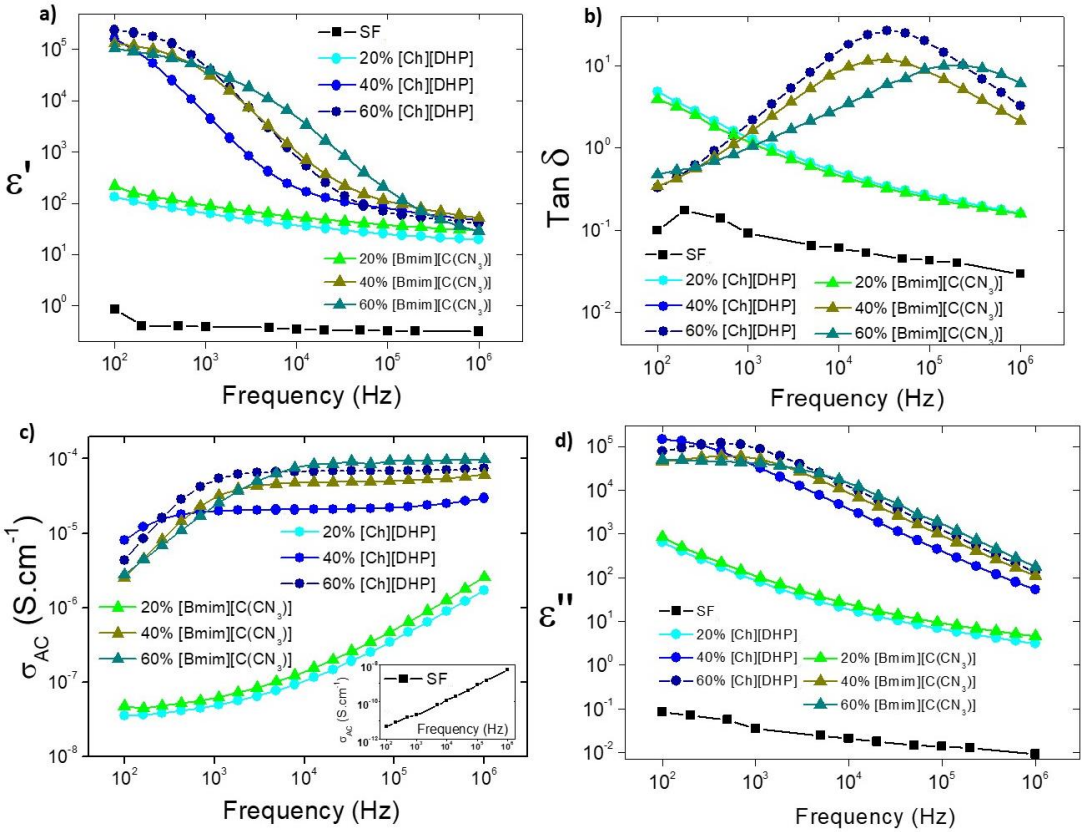

Figure 4.4. 8. *Electrical measurements for the SF/IL composites: a) real part of the dielectric constant, b) dielectric loss tangent, c) AC conductivity and d) imaginary part of the dielectric constant.*

Bending response

The influence of the IL type and content on the actuator bending response was evaluated for different applied voltages and a frequency of 100 mHz, applying ***equation 4.4.5***. The ILs incorporation into the SF matrix results in bending responsive films when subjected to an applied electric field as a result to the anions and cations diffusion displacement to the negative and positive electrode layers[140].

The displacement was measured from the distance of the actuator tip to the relaxed position during the bending. ***Figure 4.4.9a*** shows a representative time-displacement response curve for the [Ch] [DHP]/SF 40% wt. composite under an applied voltage of 100 mHz, showing displacements above 8 mm. A similar behaviour was observed for the other samples.

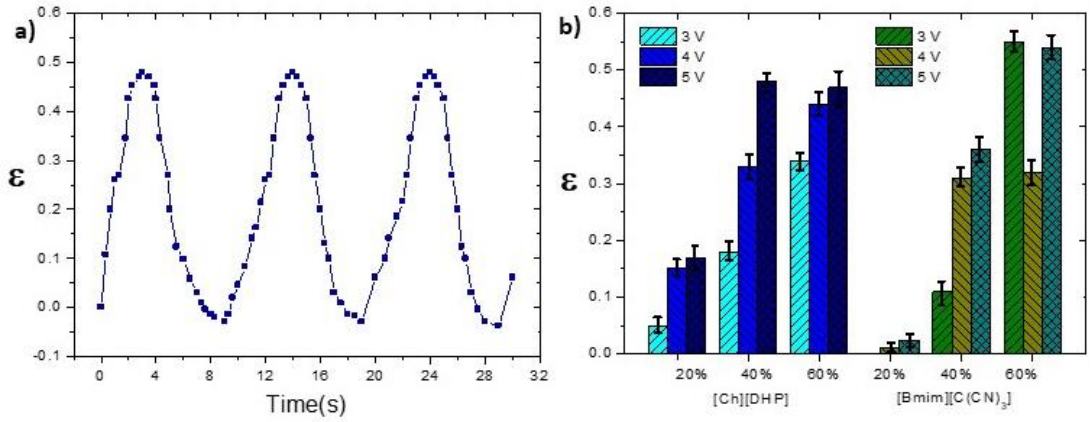

Figure 4.4. 9. *a) Displacement as a function of time for the [Ch][DHP]/SF 40t% wt. composite at 100 mHz frequency and 4 V, b) maximum bending response at different voltages for [Ch][DHP]/SF and [Bmim][C(CN3)]/SF films.*

It is observed that the bending response is not symmetric with respect to the initial position, indicative of the impossibility of ions to cross along the sample, due to strong electrostatic interactions and large size of anions and cations. Thus, cyclic bending actuation occurs from the relaxed position (no electric field applied) to the maximum displacement, either to one size or to the other, depending on the applied polarity to the samples, and back to the relaxed position (***Figure 4.4.9a***). The plasticizing effect of the IL on the SF, observed in mechanical tests, and the increased ionic mobility, decreases the energy needed for films bending and, as a consequence, low voltages are able to produce a relevant bending on the SF/IL composites.

Figure 4.4.9b shows the maximum bending response for all composite samples at different applied maximum voltages. Independently of the IL type, SF/IL films show a bending motion increasing with increasing IL content due to the increasing number of ions, the bending response increasing also with increasing applied voltage, correlated with the flowing current between the electrodes. Bending displacement is particularly relevant in [Bmim] [C (CN3)]/SF 60% wt., which lead with bending responses above 0.5. This observed bending, correlates with the IL with the highest conductivity and ions with smaller polar

area. At low IL content, [Ch] [DHP]/SF samples bending motion is higher than the one observed for [Bmim] [C (CN3)]/SF composites, probably due to the presence of residual solvent which enables ions diffusion. Contrary, at higher IL contents, the presence of solvent reduces its effect due to the larger ion content and [Ch] [DHP]/SF samples show lower bending response due to their minor conductivity and ions larger polar area. Thus, the obtained result confirms the possibility of obtaining high performance bending actuators based on natural polymer, as an example of a new generation of smart and multifunctional active materials based on natural resources.

4.4.3. CONCLUSIONS

SF/IL composites with different IL contents of [Ch] [DHP] and [Bmim] [C (CN3)] were successfully prepared by solvent casting for the development of bending actuators.

Increasing IL content affects the morphology of the composites, leading to micro-fractures into the SF surface upon the introduction of the [Ch] [DHP] and an entangled globule-like nanostructure in the [Bmim] [C (CN3)] composites. Independently of the IL type, the introduction of ILs into the polymer matrix induces an increase of the SF β-sheet conformation. The thermal properties are affected by the IL incorporation, decreasing the thermal stability with increasing [Ch] [DHP] content and increasing with [Bmim] [C (CN3)] incorporation into the SF matrix. The plasticising effect of the ILs increases samples strain at break and decreases the Young modulus.

Electrical measurements revealed that the AC electrical conductivity increases with increasing IL content due to the introduction of mobile charge carriers. A suitable bending response is obtained for all samples for applied voltages as low as 3 V. The highest bending responses around 0.5 are obtained for both [Ch] [DHP]/SF and [Bmim] [C (CN3)]/SF composites at voltages of 4 and 5 V, respectively and at a frequency of 100 MHz.

It is concluded that high-performance actuators can be prepared based on SF polymers, leading to the next generation of natural polymer-based smart and multifunctional active materials.

4.5. REFERENCES

1. Tan, L. & Wang, N. Future Internet: The Internet of Things. in *ICACTE 2010 - 2010 3rd International Conference on Advanced Computer Theory and Engineering, Proceedings* vol. 5 (2010).
2. Stock, T. & Seliger, G. Opportunities of Sustainable Manufacturing in Industry 4.0. in *Procedia CIRP* vol. 40 536–541 (Elsevier B.V., 2016).
3. *Global Sensor Market by Type, by End User, by Geography and the Impact of Covid-19 (2020-2025)*. https://www.researchandmarkets.com/reports/5135985/global-sensor-market-by-type-by-end-user-by?utm_source=GNOM&utm_medium=PressRelease&utm_code=4cxcv8&utm_campaign=1431942+-+Sensors+-+World+Market+to+Grow+at+a+CAGR+of+12%25+Between+2020+%26+2025&utm_exec= (2020) doi:5135985.
4. Actuators Market. *Actuators Market by Actuation (Electrical, Pneumatic, Hydraulic), Type (Linear, Rotary), Application (Industrial Automation, Robotics, Vehicles & Equipment), Vertical (Automotive, Electronics, Healthcare), and Region - Global Forecast to 2024*. https://www.marketsandmarkets.com/Market-Reports/global-actuators-market-59465451.html?gclid=Cj0KCQjwit_8BRCoARIsAIx3Rj4bIOGK3ucFlt_-GPJ3uLLRZpsakWFnT3BZQtlXHTsD2pf6s88mbJQaAlHMEALw_wcB (2019).
5. Cura, V. O. Del, Cunha, F. L., Aguiar, M. L. & Cliquet Jr., A. Study of the Different Types of Actuators and Mechanisms for Upper Limb Prostheses. *Artif. Organs* **27**, 507–516 (2003).
6. Ko, W. H. The future of sensor and actuator systems. *Sensors Actuators, A Phys.* **56**, 193–197 (1996).
7. Tzou, H. S., Lee, H. J. & Arnold, S. M. Smart materials, precision sensors/actuators, smart structures, and structronic systems. *Mech. Adv. Mater. Struct.* **11**, 367–393 (2004).
8. Bunde, R. L., Jarvi, E. J. & Rosentreter, J. J. Piezoelectric quartz crystal biosensors. *Talanta* vol. 46 1223–1236 (1998).
9. Zhang, Y. & Xu, X. Transformation Temperature Predictions Through Computational Intelligence for NiTi-Based Shape Memory Alloys. *Shape Mem. Superelasticity* 1–13 (2020) doi:10.1007/s40830-020-00303-0.
10. Liu, H. *et al.* Electrically conductive polymer composites for smart flexible strain sensors: a critical review. *Journal of Materials Chemistry C* vol. 6 12121–12141 (2018).
11. Basit, A., Lhostis, G. & Durand, B. Investigation of the shape memory and actuation properties of different asymmetric smart polymer composites. *Adv. Compos. Mater.* 1–16 (2020) doi:10.1080/09243046.2020.1836572.
12. Kelly, A., Davidson, R., Uchino, K., Shanmuga Priya, N. & Shanmugasundaram, M. Smart composite materials systems. in *Comprehensive Composite Materials II* 358–363 (Elsevier, 2017). doi:10.1016/B978-0-12-803581-8.10298-X.
13. Dixit, S., Goel, R., Dubey, A., Shivhare, P. R. & Bhalavi, T. Natural Fibre Reinforced Polymer Composite Materials - A Review. *Polym. from Renew. Resour.* **8**, 71–78 (2017).
14. Budhe, S., Banea, M. D., de Barros, S. & da Silva, L. F. M. An updated review of adhesively bonded joints in composite materials. *Int. J. Adhes. Adhes.* **72**, 30–42 (2017).
15. Borenstein, A. *et al.* Carbon-based composite materials for supercapacitor electrodes: A review. *Journal of Materials Chemistry A* vol. 5 12653–12672 (2017).
16. Omairey, S. L., Dunning, P. D. & Sriramula, S. Influence of micro-scale uncertainties on the reliability of fibre-matrix composites. *Compos. Struct.* **203**, 204–216 (2018).
17. Patterson, B. A. *et al.* Influence of temperature dependent matrix properties on the high-rate impact performance of thin glass fiber reinforced composites. *Compos. Part B Eng.* **192**, 108009 (2020).
18. Chen, L., Wu, X., Zhang, X. F. & Zhang, J. M. Enhanced Reproducibility of Positive Temperature Coefficient Effect of CB/HDPE/PVDF Composites with the Addition of Ionic Liquid. *Chinese J. Polym. Sci. (English Ed.* 1–9 (2020) doi:10.1007/s10118-020-2475-x.

19. Mitra, R. & Saha, A. Reduced Graphene Oxide Based 'turn-On' Fluorescence Sensor for Highly Reproducible and Sensitive Detection of Small Organic Pollutants. *ACS Sustain. Chem. Eng.* **5**, 604–615 (2017).

20. Cravanzola, S., Haznedar, G., Scarano, D., Zecchina, A. & Cesano, F. Carbon-based piezoresistive polymer composites: Structure and electrical properties. *Carbon N. Y.* **62**, 270–277 (2013).

21. *Polymer Sensors and Actuators*. *Polymer Sensors and Actuators* (Springer Berlin Heidelberg, 2000). doi:10.1007/978-3-662-04068-3.

22. Gonçalves, R. *et al.* Synthesis of highly magnetostrictive nanostructures and their application in a polymer-based magnetoelectric sensing device. *Eur. Polym. J.* **84**, 685–692 (2016).

23. Hiremath, S. & Kulkarni, S. M. Modeling and optimization of thermally excited carbon black and polymer composite actuator. in *Materials Today: Proceedings* vol. 24 798–805 (Elsevier Ltd, 2020).

24. Sun, Q. *et al.* Functional biomaterials towards flexible electronics and sensors. *Biosensors and Bioelectronics* vol. 119 237–251 (2018).

25. Sakthivel, R. *et al.* A robust nitrobenzene electrochemical sensor based on chitin hydrogel entrapped graphite composite. *J. Taiwan Inst. Chem. Eng.* **80**, 663–668 (2017).

26. Liu, Y., Wu, F., Zhao, X. & Liu, M. High-Performance Strain Sensors Based on Spirally Structured Composites with Carbon Black, Chitin Nanocrystals, and Natural Rubber. *ACS Sustain. Chem. Eng.* **6**, 10595–10605 (2018).

27. Sadasivuni, K. K. *et al.* Flexible NO2 sensors from renewable cellulose nanocrystals/iron oxide composites. *Sensors Actuators, B Chem.* **233**, 633–638 (2016).

28. Solairaj, D., Rameshthangam, P., Muthukumaran, P. & Wilson, J. Studies on electrochemical glucose sensing, antimicrobial activity and cytotoxicity of fabricated copper nanoparticle immobilized chitin nanostructure. *Int. J. Biol. Macromol.* **101**, 668–679 (2017).

29. Kotresh, S. *et al.* Humidity sensing performance of spin coated polyaniline–carboxymethyl cellulose composite at room temperature. *Cellulose* **23**, 3177–3186 (2016).

30. Stassi, S., Cauda, V., Canavese, G. & Pirri, C. Flexible Tactile Sensing Based on Piezoresistive Composites: A Review. *Sensors* **14**, 5296–5332 (2014).

31. Dharap, P., Li, Z., Nagarajaiah, S. & Barrera, E. V. Nanotube film based on single-wall carbon nanotubes for strain sensing. *Nanotechnology* **15**, 379–382 (2004).

32. Sau, K. P., Chaki, T. K. & Khastgir, D. The change in conductivity of a rubber-carbon black composite subjected to different modes of pre-strain. *Compos. Part A Appl. Sci. Manuf.* **29**, 363–370 (1998).

33. Ferreira, A. *et al.* Effect of filler dispersion on the electromechanical response of epoxy/vapor-grown carbon nanofiber composites. *Smart Mater. Struct.* **21**, 075008 (2012).

34. Ferreira, A. & Lanceros-Mendez, S. Piezoresistive response of spray-printed carbon nanotube/poly(vinylidene fluoride) composites. *Compos. Part B Eng.* **96**, 242–247 (2016).

35. Costa, P. *et al.* High-performance graphene-based carbon nanofiller/polymer composites for piezoresistive sensor applications. *Compos. Sci. Technol.* **153**, 241–252 (2017).

36. Wang, J.-G. *et al.* Green Synthesis of Hierarchically Porous Carbon Nanotubes as Advanced Materials for High-Efficient Energy Storage. *Small* **14**, 1703950 (2018).

37. Xu, J., Li, S., Li, Y. & Ta, X. Preparation, morphology and properties of natural rubber/carbon black/multi-walled carbon nanotubes conductive composites. *J. Mater. Sci. Mater. Electron.* **27**, 9531–9540 (2016).

38. Ferrreira, A. *et al.* Electromechanical performance of poly(vinylidene fluoride)/carbon nanotube composites for strain sensor applications. *Sensors Actuators, A Phys.* **178**, 10–16 (2012).

39. Costa, P., Ribeiro, S. & Lanceros-Mendez, S. Mechanical vs. electrical hysteresis of carbon nanotube/styrene-butadiene-styrene composites and their influence in the electromechanical response. *Compos. Sci. Technol.* **109**, 1–5 (2015).

40. Kang, M., Chen, P. & Jin, H. J. Preparation of multiwalled carbon nanotubes incorporated silk fibroin

nanofibers by electrospinning. *Curr. Appl. Phys.* **9**, S95–S97 (2009).

41. Kwon, S. M., Kim, H. S. & Jin, H. J. Fabrication of organic silk fibroin/multiwalled carbon nanotube composite cryogels by freeze-drying method. in *Advanced Materials Research* vols 47-50 PART 2 1105–1108 (Trans Tech Publications, 2008).

42. Dionigi, C. *et al.* A nanostructured conductive bio-composite of silk fibroin-single walled carbon nanotubes. *J. Mater. Chem. B* **2**, 1424–1431 (2014).

43. Tseng, P. *et al.* Silk Fibroin-Carbon Nanotube Composite Electrodes for Flexible Biocatalytic Fuel Cells. *Adv. Electron. Mater.* **2**, 1600190 (2016).

44. Asakura, T., Okushita, K. & Williamson, M. P. Analysis of the Structure of Bombyx mori Silk Fibroin by NMR. (2015) doi:10.1021/acs.macromol.5b00160.

45. Skrovanek, D. J., Painter, P. C. & Coleman, M. M. Hydrogen Bonding in Polymers. 2. Infrared Temperature Studies of Nylon 11. *Macromolecules* **19**, 699–705 (1986).

46. GOORMAGHTIGH, E., CABIAUX, V. & RUYSSCHAERT, J. -M. Secondary structure and dosage of soluble and membrane proteins by attenuated total reflection Fourier-transform infrared spectroscopy on hydrated films. *Eur. J. Biochem.* **193**, 409–420 (1990).

47. Zhao, H. & Bai, J. Highly sensitive piezo-resistive graphite nanoplatelet-carbon nanotube hybrids/polydimethylsilicone composites with improved conductive network construction. *ACS Appl. Mater. Interfaces* **7**, 9652–9659 (2015).

48. Zhou, J. *et al.* Regenerated silk fibroin films with controllable nanostructure size and secondary structure for drug delivery. *ACS Applied Materials and Interfaces* vol. 6 21813–21821 (2014).

49. Ling, S., Qi, Z., Knight, D. P., Shao, Z. & Chen, X. FTIR imaging, a useful method for studying the compatibility of silk fibroin-based polymer blends. *Polym. Chem.* **4**, 5401–5406 (2013).

50. Qiu, W., Teng, W., Cappello, J. & Wu, X. Wet-spinning of recombinant silk-elastin-like protein polymer fibers with high tensile strength and high deformability. *Biomacromolecules* **10**, 602–608 (2009).

51. Rabotyagova, O. S., Cebe, P. & Kaplan, D. L. Role of Polyalanine Domains in $\hat{I}^2$ -Sheet Formation in Spider Silk Block Copolymers. *Macromol. Biosci.* **10**, 49–59 (2010).

52. Tretinnikov, O. N. & Tamada, Y. Influence of casting temperature on the near-surface structure and wettability of cast silk fibroin films. *Langmuir* **17**, 7406–7413 (2001).

53. Hu, X. *et al.* Determining Beta Sheet Crystallinity in Fibrous Proteins by Thermal Analysis and Infrared Spectroscopy. *APS* J34.010 (2007).

54. Lawrence, B. D., Omenetto, F., Chui, K. & Kaplan, D. L. Processing methods to control silk fibroin film biomaterial features. *J. Mater. Sci.* **43**, 6967–6985 (2008).

55. Wang, Q., Wang, C., Zhang, M., Jian, M. & Zhang, Y. Feeding Single-Walled Carbon Nanotubes or Graphene to Silkworms for Reinforced Silk Fibers. *Nano Lett.* **16**, 6695–6700 (2016).

56. Andrews, R. & Weisenberger, M. C. Carbon nanotube polymer composites. *Curr. Opin. Solid State Mater. Sci.* **8**, 31–37 (2004).

57. Yazawa, K., Ishida, K., Masunaga, H., Hikima, T. & Numata, K. Influence of Water Content on the β-Sheet Formation, Thermal Stability, Water Removal, and Mechanical Properties of Silk Materials. *Biomacromolecules* **17**, 1057–1066 (2016).

58. Agarwal, N., Hoagland, D. A. & Farris, R. J. Effect of moisture absorption on the thermal properties of Bombyx mori silk fibroin films. *J. Appl. Polym. Sci.* **63**, 401–410 (1997).

59. Wideman, T. H., Zautra, A. J. & Edwards, R. R. Structural Origins of Silk Piezoelectricity. **154**, 2262–2265 (2014).

60. Schönhals, A. & Kremer, F. Broadband Dielectric Measurement Techniques (10-6 Hz to 1012 Hz). in *Broadband Dielectric Spectroscopy* 35–57 (Springer Berlin Heidelberg, 2003). doi:10.1007/978-3-642-56120-7_2.

61. Song, S. *et al.* A Facile Strategy to Enhance the Dielectric and Mechanical Properties of

MWCNTs/PVDF Composites with the Aid of MMA-co-GMA Copolymer. *Materials (Basel).* **11**, 347 (2018).

62. Liu, C. *et al.* Origin of increasing dielectric constant at lower percolation threshold through controlling spatial distribution of carbon nanotubes in epoxy resin with microwave-assisted thermal curing technique. *J. Phys. Chem. C* **120**, 28875–28885 (2016).

63. Nan, C.-W., Shen, Y. & Ma, J. Physical Properties of Composites Near Percolation. *Annu. Rev. Mater. Res.* **40**, 131–151 (2010).

64. He, F., Lau, S., Chan, H. L. & Fan, J. High dielectric permittivity and low percolation threshold in nanocomposites based on poly(vinylidene fluoride) and exfoliated graphite nanoplates. *Adv. Mater.* **21**, 710–715 (2009).

65. Gao, J. F., Li, Z. M., Meng, Q. jie & Yang, Q. CNTs/ UHMWPE composites with a two-dimensional conductive network. *Mater. Lett.* **62**, 3530–3532 (2008).

66. Hu, N., Karube, Y., Yan, C., Masuda, Z. & Fukunaga, H. Tunneling effect in a polymer/carbon nanotube nanocomposite strain sensor. *Acta Mater.* **56**, 2929–2936 (2008).

67. Liu, H. *et al.* Lightweight conductive graphene/thermoplastic polyurethane foams with ultrahigh compressibility for piezoresistive sensing. *J. Mater. Chem. C* **5**, 73–83 (2017).

68. Lin, L. *et al.* Modified resistivity-strain behavior through the incorporation of metallic particles in conductive polymer composite fibers containing carbon nanotubes. *Polym. Int.* **62**, 134–140 (2013).

69. Luheng, W., Tianhuai, D. & Peng, W. Influence of carbon black concentration on piezoresistivity for carbon-black-filled silicone rubber composite. *Carbon N. Y.* **47**, 3151–3157 (2009).

70. Nations, U. *UNCTAD ESTIMATES OF GLOBAL E-COMMERCE 2018*. https://unctad.org/en/PublicationsLibrary/tn_unctad_ict4d15_en.pdf (2018).

71. McDowell, D. L. *et al. Integrated Design of Multiscale, Multifunctional Materials and Products*. *Integrated Design of Multiscale, Multifunctional Materials and Products* (Elsevier Inc., 2010). doi:10.1016/C2009-0-20058-4.

72. Müller, K. *et al.* Review on the Processing and Properties of Polymer Nanocomposites and Nanocoatings and Their Applications in the Packaging, Automotive and Solar Energy Fields. *Nanomaterials* **7**, 74 (2017).

73. Kerr, R. A. & Service, R. F. What can replace cheap oil-and when. *Science* vol. 309 101 (2005).

74. Pinchuk, A. O. Size-dependent hamaker constant for silver nanoparticles. *J. Phys. Chem. C* **116**, 20099–20120 (2012).

75. Zhang, Z., Wang, H., Li, S., Li, L. & Li, D. Transparent and flexible cellulose nanofibers/silver nanowires/acrylic resin composite electrode. *Compos. Part A Appl. Sci. Manuf.* **76**, 309–315 (2015).

76. Sun, J. G., Yang, T. N., Wang, C. Y. & Chen, L. J. A flexible transparent one-structure tribo-piezo-pyroelectric hybrid energy generator based on bio-inspired silver nanowires network for biomechanical energy harvesting and physiological monitoring. *Nano Energy* **48**, 383–390 (2018).

77. Wu, C., Kim, T. W., Li, F. & Guo, T. Wearable Electricity Generators Fabricated Utilizing Transparent Electronic Textiles Based on Polyester/Ag Nanowires/Graphene Core-Shell Nanocomposites. *ACS Nano* **10**, 6449–6457 (2016).

78. Shivananda, C. S., Lakshmeesha Rao, B. & Sangappa. Structural, thermal and electrical properties of silk fibroin–silver nanoparticles composite films. *J. Mater. Sci. Mater. Electron.* **31**, 41–51 (2020).

79. Wang, K., Jin, Y., Qian, B., Wang, J. & Xiao, F. One-step aqueous fabrication of a silver nanowire composite transparent conductive film with high uniformity and stability. *J. Mater. Chem. C* **8**, 4372–4384 (2020).

80. Zhao, Z. *et al.* A Sandwich-Structured Piezoresistive Sensor with Electrospun Nanofiber Mats as Supporting, Sensing, and Packaging Layers. *Polymers (Basel).* **10**, 575 (2018).

81. Liu, C. *et al.* Toward large-scale fabrication of triboelectric nanogenerator (TENG) with silk-fibroin patches film via spray-coating process Chaoran. *Nano Energy* **41**, 359–366 (2017).

82. Meenakshi, P., Karthick, R., Selvaraj, M. & Ramu, S. Investigations on reduced graphene oxide film embedded with silver nanowire as a transparent conducting electrode. *Sol. Energy Mater. Sol. Cells* **128**, 264–269 (2014).

83. Sionkowska, A. & Planecka, A. The influence of UV radiation on silk fibroin. *Polym. Degrad. Stab.* **96**, 523–528 (2011).

84. Meenakshi, P., Karthick, R., Selvaraj, M. & Ramu, S. Investigations on reduced graphene oxide film embedded with silver nanowire as a transparent conducting electrode. *Sol. Energy Mater. Sol. Cells* **128**, 264–269 (2014).

85. Boulet-Audet, M., Vollrath, F. & Holland, C. Identification and classification of silks using infrared spectroscopy. *J. Exp. Biol.* **218**, 3138–3149 (2015).

86. Yazawa, K., Ishida, K., Masunaga, H., Hikima, T. & Numata, K. Influence of Water Content on the β-Sheet Formation, Thermal Stability, Water Removal, and Mechanical Properties of Silk Materials. *Biomacromolecules* **17**, 1057–1066 (2016).

87. Chen, Y. G. & Wang, S. J. High dielectric constant of silver nanowires–epoxy composites. in *Materials Science Forum* vol. 848 9–12 (Trans Tech Publications Ltd, 2016).

88. Zhang, S. *et al.* Ultrasensitive and Highly Compressible Piezoresistive Sensor Based on Polyurethane Sponge Coated with a Cracked Cellulose Nanofibril/Silver Nanowire Layer. *ACS Appl. Mater. Interfaces* **11**, 10922–10932 (2019).

89. Ide, S. *et al.* Nanoscale structural analyses on Turkey/Taiwan originated spider cocoons. *Acta Crystallogr. Sect. A Found. Adv.* **73**, C1355–C1355 (2017).

90. Minoura, N., Tsukada, M. & Nagura, M. Physico-chemical properties of silk fibroin membrane as a biomaterial. *Biomaterials* **11**, 430–434 (1990).

91. Larson, J. D. *et al.* Enhanced actuation performance of silk-polypyrrole composites. *Mater. Chem. Phys.* **186**, 67–74 (2017).

92. Xu, Z., Shi, L., Yang, M. & Zhu, L. Preparation and biomedical applications of silk fibroin-nanoparticles composites with enhanced properties - A review. *Mater. Sci. Eng. C* **95**, 302–311 (2019).

93. Fengel, C. V., Bradshaw, N. P., Severt, S. Y., Murphy, A. R. & Leger, J. M. Biocompatible silk-conducting polymer composite trilayer actuators. *Smart Mater. Struct.* **26**, 055004 (2017).

94. Karahaliloğlu, Z., Yalçın, E., Demirbilek, M. & Denkbaş, E. B. Magnetic silk fibroin e-gel scaffolds for bone tissue engineering applications. *J. Bioact. Compat. Polym.* **32**, 596–614 (2017).

95. Lalegül-Ülker, Ö., Vurat, M. T., Elçin, A. E. & Elçin, Y. M. Magnetic silk fibroin composite nanofibers for biomedical applications: Fabrication and evaluation of the chemical, thermal, mechanical, and *in vitro* biological properties. *J. Appl. Polym. Sci.* **136**, 48040 (2019).

96. Sheng, W. *et al.* One-step synthesis of biocompatible magnetite/silk fibroin core-shell nanoparticles. *J. Mater. Chem. B* **2**, 7394–7402 (2014).

97. Phenrat, T., Saleh, N., Sirk, K., Tilton, R. D. & Lowry, G. V. Aggregation and sedimentation of aqueous nanoscale zerovalent iron dispersions. *Environ. Sci. Technol.* **41**, 284–290 (2007).

98. Golas, P. L., Louie, S., Lowry, G. V., Matyjaszewski, K. & Tilton, R. D. Comparative study of polymeric stabilizers for magnetite nanoparticles using ATRP. *Langmuir* **26**, 16890–16900 (2010).

99. Brito-Pereira, R. *et al.* Silk fibroin-magnetic hybrid composite electrospun fibers for tissue engineering applications. *Compos. Part B Eng.* **141**, 70–75 (2018).

100. Um, I. C., Kweon, H. Y., Park, Y. H. & Hudson, S. Structural characteristics and properties of the regenerated silk fibroin prepared from formic acid. *Int. J. Biol. Macromol.* **29**, 91–97 (2001).

101. Kaplan, D. L. *et al.* Silk I and Silk II studied by fast scanning calorimetry. *Acta Biomater.* **55**, 323–332 (2017).

102. Salunkhe, A. B. *et al.* Polyvinyl alcohol functionalized cobalt ferrite nanoparticles for biomedical applications. *Appl. Surf. Sci.* **264**, 598–604 (2013).

103. Kambale, R. C., Shaikh, P. A., Bhosale, C. H., Rajpure, K. Y. & Kolekar, Y. D. The effect of Mn

substitution on the magnetic and dielectric properties of cobalt ferrite synthesized by an autocombustion route. *Smart Mater. Struct.* **18**, 115028 (2009).

104. Panda, R. K., Muduli, R., Kar, S. K. & Behera, D. Dielectric relaxation and conduction mechanism of cobalt ferrite nanoparticles. *J. Alloys Compd.* **615**, 899–905 (2014).

105. Kumar, P., Sharma, S. K., Knobel, M. & Singh, M. Effect of La3+ doping on the electric, dielectric and magnetic properties of cobalt ferrite processed by co-precipitation technique. *J. Alloys Compd.* **508**, 115–118 (2010).

106. Rahman, M. T., Vargas, M. & Ramana, C. V. Structural characteristics, electrical conduction and dielectric properties of gadolinium substituted cobalt ferrite. *J. Alloys Compd.* **617**, 547–562 (2014).

107. Luo, H. *et al.* Interface design for high energy density polymer nanocomposites. *Chemical Society Reviews* vol. 48 4424–4465 (2019).

108. Srinivasa Rao, K., Ranga Nayakulu, S. V., Chaitanya Varma, M., Choudary, G. S. V. R. K. & Rao, K. H. Controlled phase evolution and the occurrence of single domain CoFe2O4 nanoparticles synthesized by PVA assisted sol-gel method. *J. Magn. Magn. Mater.* **451**, 602–608 (2018).

109. Stingaciu, M., Andersen, H. L., Granados-Miralles, C., Mamakhel, A. & Christensen, M. Magnetism in CoFe2O4 nanoparticles produced at sub- and near-supercritical conditions of water. *CrystEngComm* **19**, 3986–3996 (2017).

110. Martins, P. *et al.* Optimizing piezoelectric and magnetoelectric responses on CoFe 2O4/P(VDF-TrFE) nanocomposites. *J. Phys. D. Appl. Phys.* **44**, 495303 (2011).

111. Chakraverty, S. & Bandyopadhyay, M. Coercivity of magnetic nanoparticles: A stochastic model. *J. Phys. Condens. Matter* **19**, 216201 (2007).

112. Selvi, M. M., Manimuthu, P., Kumar, K. S. & Venkateswaran, C. Magnetodielectric properties of CoFe2O4-BaTiO 3 core-shell nanocomposite. *J. Magn. Magn. Mater.* **369**, 155–161 (2014).

113. Pal, D. *et al.* Micelles induced high coercivity in single domain cobalt-ferrite nanoparticles. *J. Appl. Phys.* **108**, 124317 (2010).

114. Mejri, R. *et al.* Effect of anion type in the performance of ionic liquid/poly(vinylidene fluoride) electromechanical actuators. *J. Non. Cryst. Solids* **453**, 8–15 (2016).

115. Zhang, S. *et al.* Beyond solvents and electrolytes: Ionic liquids-based advanced functional materials. *Progress in Materials Science* vol. 77 80–124 (2016).

116. Dias, J. C. *et al.* Electromechanical actuators based on poly(vinylidene fluoride) with [N1 1 1 2(OH)][NTf2] and [C2mim] [C2SO4]. *J. Mater. Sci.* **51**, 9490–9503 (2016).

117. Dias, J. C. *et al.* Improved response of ionic liquid-based bending actuators by tailored interaction with the polar fluorinated polymer matrix. *Electrochim. Acta* **296**, 598–607 (2019).

118. Romero, I. S. *et al.* Biocompatible Electromechanical Actuators Composed of Silk-Conducting Polymer Composites. *Adv. Funct. Mater.* **24**, 3866–3873 (2014).

119. Brito-Pereira, R. *et al.* Silk fibroin-magnetic hybrid composite electrospun fibers for tissue engineering applications. *Compos. Part B Eng.* **141**, 70–75 (2018).

120. Freire, M. G., Santos, L. M. N. B. F., Fernandes, A. M., Coutinho, J. A. P. & Marrucho, I. M. An overview of the mutual solubilities of water-imidazolium-based ionic liquids systems. *Fluid Phase Equilib.* **261**, 449–454 (2007).

121. Barber, P. *et al.* Polymer Composite and Nanocomposite Dielectric Materials for Pulse Power Energy Storage. *Materials (Basel).* **2**, 1697–1733 (2009).

122. Kapoor, S. & Kundu, S. C. Silk protein-based hydrogels: Promising advanced materials for biomedical applications. *Acta Biomater.* **31**, 17–32 (2016).

123. Zhou, C. Z. *et al.* Silk fibroin: Structural implications of a remarkable amino acid sequence. *Proteins Struct. Funct. Genet.* **44**, 119–122 (2001).

124. Awaja, F., Zhang, S., Tripathi, M., Nikiforov, A. & Pugno, N. Cracks, microcracks and fracture in polymer structures: Formation, detection, autonomic repair. *Progress in Materials Science* vol. 83

536–573 (2016).

125. Zhang, H. *et al.* Preparation and characterization of silk fibroin as a biomaterial with potential for drug delivery. 1–9 (2012).

126. Kong, X. D., Cui, F. Z., Wang, X. M., Zhang, M. & Zhang, W. Silk fibroin regulated mineralization of hydroxyapatite nanocrystals. *J. Cryst. Growth* **270**, 197–202 (2004).

127. Yang, X. *et al.* Green electrospun Manuka honey/silk fibroin fibrous matrices as potential wound dressing. *Mater. Des.* **119**, 76–84 (2017).

128. Wang, Y. L., Zhai, H. J., Xu, L., Li, J. & Wang, L. S. Vibrational resolved photoelectron spectroscopy of di-gold carbonyl clusters au2(CO)n- (n = 1-3): Experiment and theory. *J. Phys. Chem. A* **114**, 1247–1254 (2010).

129. Zanathy, L., Bock, H., Lentz, D., Preugschat, D. & Botschwina, P. Generation, isolation and photoelectron spectrum1 of HC≡C-N≡C. *J. Chem. Soc. Chem. Commun.* **0**, 403–404 (1992).

130. Um, I. C., Kweon, H. Y., Lee, K. G. & Park, Y. H. The role of formic acid in solution stability and crystallization of silk protein polymer. *Int. J. Biol. Macromol.* **33**, 203–213 (2003).

131. Armand, M., Endres, F., Mac Farlane, D. R., Ohno, H. & Scrosati, B. Ionic-liquid materials for the electrochemical challenges of the future. in *Materials for Sustainable Energy: A Collection of Peer-Reviewed Research and Review Articles from Nature Publishing Group* 129–137 (World Scientific Publishing Co., 2010). doi:10.1142/9789814317665_0020.

132. Mester, P., Wagner, M. & Rossmanith, P. Antimicrobial effects of short chained imidazolium-based ionic liquids-Influence of anion chaotropicity. *Ecotoxicol. Environ. Saf.* **111**, 96–101 (2015).

133. Constantinescu, D., Weingärtner, H. & Herrmann, C. Protein denaturation by ionic liquids and the Hofmeister series: A case study of aqueous solutions of ribonuclease A. *Angew. Chemie - Int. Ed.* **46**, 8887–8889 (2007).

134. Fujita, K., Nakano, R., Nakaba, R., Nakamura, N. & Ohno, H. Hydrated ionic liquids enable both solubilisation and refolding of aggregated concanavalin A. *Chem. Commun.* **55**, 3578–3581 (2019).

135. Quintana, R. *et al.* Enhancement of cellulose acetate degradation under accelerated weathering by plasticization with eco-friendly plasticizers. *Polym. Degrad. Stab.* **98**, 1556–1562 (2013).

136. Correia, D. M. *et al.* Ionic Liquid Cation Size-Dependent Electromechanical Response of Ionic Liquid/Poly(vinylidene fluoride)-Based Soft Actuators. *J. Phys. Chem. C* **123**, 12744–12752 (2019).

137. Leones, R. *et al.* Development of solid polymer electrolytes based on poly(vinylidene fluoride-trifluoroethylene) and the [N1 1 1 2(OH)][NTf2] ionic liquid for energy storage applications. *Solid State Ionics* **253**, 143–150 (2013).

138. Rybinska-Fryca, A., Sosnowska, A. & Puzyn, T. Prediction of dielectric constant of ionic liquids. *J. Mol. Liq.* **260**, 57–64 (2018).

139. Fabiani, D. *et al.* Effect of water adsorption on the dielectric properties of polymer nanocomposites. in *Proceedings of the International Symposium on Electrical Insulating Materials* 510–513 (2008). doi:10.1109/ISEIM.2008.4664470.

140. Liu, X. *et al.* Tough nanocomposite ionogel-based actuator exhibits robust performance. *Sci. Rep.* **4**, 1–7 (2014).

As a second approach to explore the Silk Fibroin (SF) potential as functional material, this chapter focus on technological applications in the areas of biomedicine, energy and environment.

In order to enlarge the knowledge around SF, this section has explored the main effects of the processing of SF porous materials. For this, porous materials have been developed by electrospinning, salt leaching, gas foaming, gelation and freeze drying, and microstructural variations have been analyzed.

The most promising samples have been used to develop tissue engineering scaffolds, Li-ion batteries and adsorbents for pollutants.

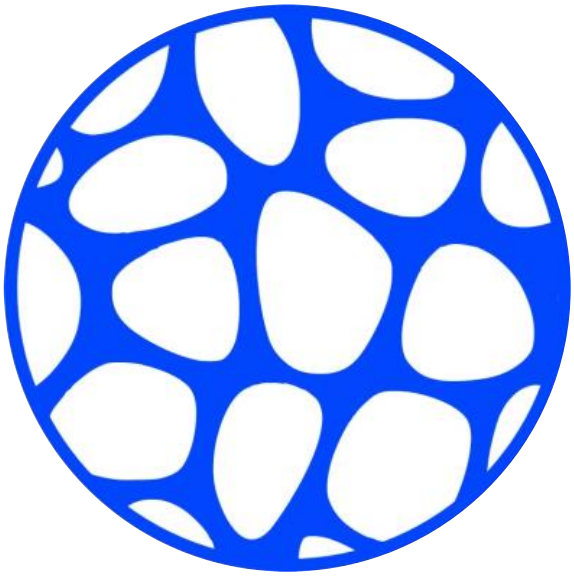

Chapter.5

TAILORING SILK POROUS STRUCTURES FOR ADVANCED APPLICATIONS

The most recent innovation strategic plan of the European Commission, (horizon 2021 - 2027) defines the main technological focus for the near future[1] on the following topics, i) technological interconnectivity: IoT and Industry 4.0, ii) living longer and better: biomedicine, iii) energetic neutrality: electrochemical energy storage, and iv) freshwaters: water remediation. (***Figure 5.1***).

In Chapter 4, the main required components for the first topic, the technological interconnectivity, have been tackled[2,3]. In the previous chapter, sustainable sensors and actuators have been developed using Silk Fibroin (SF) as the main component, as well as non-pollutant processing. To achieve the required behaviors (e.g., piezoresistivity, electrical conductivity, magnetic, and self-bending), SF has been combined with different fillers (CNT, SNW, CFO, and IL). Indeed, composites have proven to be a suitable choice for sustainable, functional materials design and smart devices development.

In this chapter (***Chapter 5***), two main goals have been defined: i) to progress in the SF morphological adaptation, processing techniques and their applicability in functional devices, and ii) to advance towards the most required technological innovations in different application fields, i.e., those proposed by the European Commission. One common demand can be highlighted for these innovations: the need of controllable porous structures for advanced technologies development.

Porous materials deserve special attention for i) biomedical purposes, particularly for drug delivery systems, wound healing[4], and tissue engineering, where scaffolds provide a framework for cell attachment, migration, differentiation, and tissues formation[5,6], ii) energy storage applications, including supercapacitors and batteries, because they can facilitate charge transfer through the electrode/electrolyte interface, reduce the ion diffusion pathway, and accommodate volume changes during cycling[7]. In this field, porous materials are mainly used as separator membranes in batteries and serve to isolate the two electrodes electrically while providing ionic conduction pathways through the liquid electrolyte that fills the pores[8]; and iii) gas and liquid absorption and adsorption, owing to their high permeability, homogeneous flow-through the porous structure, large surface areas, and abundant adsorption sites presence, which favor the loading and release of different substances[9] being especially useful for pollutants removal[10].

Porous structures have attracted considerable attention as functional materials in recent years owing to their diversity and performance. Generally, porous structures are highly porous materials, with high surface area, large accessible space, low density, variable chemical compositions, and interconnected hierarchical porosity at different length scales[11–13]. These behaviors are highly favorable for many applications, e.g., filtration and oil spill cleanup[14], catalytic processes[15], renewable energy systems[16], and heat transfer devices[17].

Among the main types of porous materials, three can be differentiated: i) meso- and microporous materials used for adsorption and catalytic process in where very high surface areas are required. Among them, the inorganic porous materials[18], such as zeolites and silica's and more most recent metal-organic frameworks (MOF), can be highlighted[11]; ii) Metal foams, highly useful in structural application because of their low body density, great specific strength, high stiffness, good thermal conductivity, energy absorption, and damping effect[19,20], and iii) polymeric foams[21] useful because of their facile processing, the control of their main behaviors and variable molecular composition, which together, bring the possibility of design custom devices[21].

Currently, for tissue engineering, electrochemical cells separators, and water remediation purposes, synthetic porous polymeric materials are mainly used because of there is a great knowledge on them and the consequent control of their properties[6] but just focused on the following compounds: i) The materials for tissue engineering mainly include hydrophobic compounds such as the α-hydroxy acids and polyanhydrides[22]; ii) electrochemical cells separators, are commonly made from uniaxially stretched polyethylene, polypropylene poly(acrylonitrile), poly(vinylidene fluoride) and its copolymers [23,24]; and finally iii) the most used porous polymers for water remediation are superhydrophilic polyacrylamide (PAM) mesh, polytetrafluoroethylene, polymethacrylic acid, poly(ethylhexylmethacrylate) and polyvinyl[25,26].

The search for sustainability, however, has directed the focus to alternative and fewer pollutant resources. This promotes the replacement of synthetic polymers by bio-based ones, which add some interesting and useful properties to the devices, e.g., biodegradability, non-toxicity, and low disposal costs. Among the main used bio-based materials for each purpose it can be highlighted: i) for tissue engineering: poly(hydroxy esters) (such as poly(-caprolactone) (PCL), poly(lactic acid) (PLA), poly(glycolic acid) (PGA)) for 3D printed devices[27] and collagen, gelatine, glycosaminoglycans, and derivatives for hydrogels

development[28], ii) for battery separators, natural fibers such as wool, cotton and chitin [29,30] and iii) for water remediation chitosan, alginate, and their derivate [31].

Despite its potential, silk has been slightly explored for these purposes. However, SF morphological adaptability, chemical composition, and control of its properties represent a highly interesting chance to tackle the proposed applications.

Two main types of porous SF structures can be defined, electrospinning non-woven mats and sponges (also named scaffolds or foams depending on the application area). Both structures are characterized by high porosity values (above 70%)[32], but their structures and properties highly differ.

Electrospinning mats are based on independent micro-metric fibers stacked into a single material. The gaps between micro-fibers (cavities) define pores size and porosity, while micro-fibers dimensions define the material surface area. Electrospinning mats always show, i) interconnected pores (because of the non-woven organization), ii) considerable flexibility (because of the dimensions of the fibers), and iii) narrow structures with large areas (in the order of m^2) [33,34].

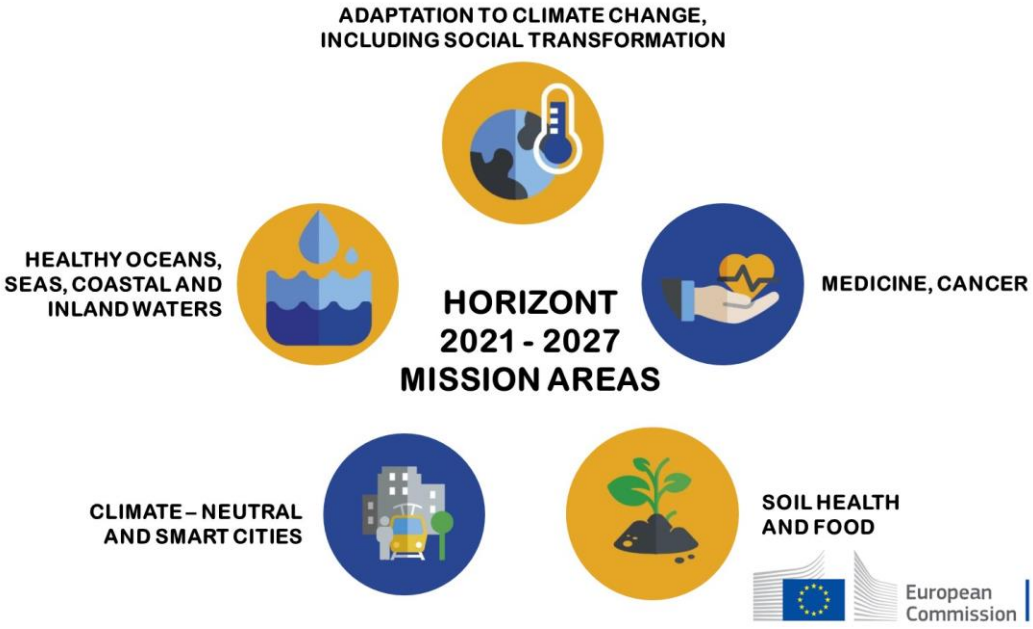

Figure 5. 1. European commission mission areas for horizon 2021 – 2027 innovation strategic plan.

In sponges, SF is distributed continuously, as a single structure, while pores are defined by the zones where material lacks. Several techniques are used to make SF porous materials [35–37]. The main processing ones are salt leaching, free drying, and gas foaming, and they highly differ in how they induce pores into SF compact structure. The porous materials pore shape, size, connectivity, and porosity values are variable and highly adaptable depending on the used processing method. This allows a more extensive control over SF porous structures and a consequent adaptation of the materials to the required application.

SF porous materials have been mainly explored for biomedical purposes. Specifically, electrospinning mats have been used as scaffolds for tissue engineering purposes. The fibers and pores distribution and shape provide the ideal place for molecular adhesion and growth[38]. While SF foams have been more used in drug delivery because of the provided reasonable control of materials uptake and release of different targets[39].

In general, SF has been mainly used as a part of a composite porous material, e.g., SF/chitosan copolymers and SF/hydroxyapatite composite [40,41]. But neat SF porous structures have been slightly explored. Consequently, there is a lack of studies exploring SF porous materials' potentiality and how to control their properties.

In the following, SF, as a functional material for tissue engineering, energy harvesting, and water remediation, has been studied. The results show the SF multifunctionality in differentiated fields and represent a good demonstrator of achieving different properties and applications by controlling material morphology and properties. This demonstration aims to be a good indicator of bio-based materials potentiality.

5.1. SILK/ COBALT FERRITE NANOPARTICLES BASED ELECTROSPINNING MAGNETOACTIVE MATS FOR TISSUE ENGINEERING

BASED ON: A. Reizabal et al. Silk fibroin magnetoactive nanocomposite films and membranes for dynamic bone tissue engineering strategies Materialia, vol. 12, p. 100709, 2020.

Bio-based materials have been positioned in the last times as the most required materials for biomedical purposes and tissue engineering. This is mostly because of their natural ability to target biomimetic approaches by mimicking human tissues' properties and improving cellular response outcome[42,43]. Porous structures deserve special attention in this field since they afford mechanical and structural support to cells, improving cell proliferation, and migration[44].

SF deserves particular interest in this field since it possesses unique properties to hold cellular growth, including biocompatibility, enhanced collagen biosynthesis, minimal immunogenicity, anti-inflammatory activity, and haemostatic activity[45]. Also, SF based structures hold specific biological cues recognized by cells for physiological processes, offering to the cells a recognizable environment for proliferation and tissue remodelling[43]. Indeed, silk is being reinvented as a biomaterial due to its unique mechanical properties[46], opportunities for genetically tailoring its structure and function[47], biocompatibility, and intrinsic piezoelectricity[48], an essential factor since bone itself is piezoelectric.

The porous structure, porosity, porous size, shape, interconnectivity, and distribution deserve special interest because they strongly influence the growing cellular dynamics. In this context, electrospun mats have gained considerable attention because of their morphology, pores interconnectivity, and samples large areas.

Electrospinning also allows the processing of materials with combined properties. One example is the development of nanocomposites comprising magnetic nanoparticles. These magnetic responsive materials have focused on tissue engineering[49], biosensors, or microfluidics, due to their controlled response and reproducibility[50]. In particular, cobalt ferrite nanoparticles are characterized by high magnetization properties and high magnetostrictive response. This has allowed their use for the formulation of silk-based non-cytotoxic magnetic biocomposites[51].

Without adding particles, SF shows an inherent piezoelectric response, able to mimic the piezoelectric mechanism of bone to promote a proper microenvironment for the efficient

growth and proliferation of tissues[52]. In fact, the interest and suitability of piezoelectric stimulation for tissue engineering have been investigated with synthetic polymers such as poly(vinylidene fluoride) (PVDF)[53]. The piezoelectric response of PVDF and PVDF nanocomposites incorporated with CFO fillers that respond to mechanical and magnetic stimuli, respectively, and its effective response for bone cell stimulation has been reported under static and dynamic mechanical stimuli[54].

Despite the promising results, synthetic polymer scaffolds show a poor cell attachment capability due to the lack of cell recognition sites compared to natural biopolymers[55].

Encouraged by the potential applications of SF magnetic composite scaffolds, the present study analyses the physical-chemical and magnetic properties of SF composites processed with different designs (films and fibers) and at varying concentrations of $CoFe_2O_4$ nanoparticles and evaluates the applicability of these nanocomposites for bone tissue engineering. (***Figure 5.1.1***)

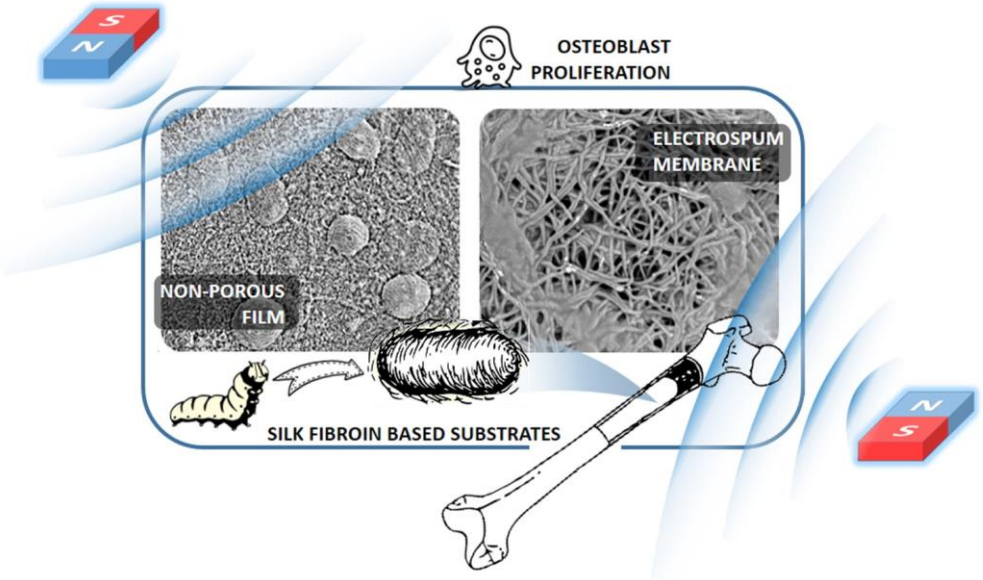

Figure 5.1. 1. *Graphical abstract of SF/CFO nanocomposites for tissue engineering*

5.1.1. MATERIALS AND EXPERIMENTAL METHODS

Materials

Bombyx mori silkworm cocoons were supplied by APPECDM from Castello Branco (Portugal). Na_2CO_3, formic acid and calcium chloride ($CaCl_2$) were obtained from Sigma-

Aldrich and were used as received. Cobalt ferrite - $CoFe_2O_4$ (CFO) round magnetic NPs with 35-55 nm diameter were purchased from Nanoamor.

Samples preparation

Samples were prepared following the main steps represented in ***Figure 5.1.2***. Firstly, SF was extracted following the *SF extraction* procedure of 4.4.1 section. In a second step, SF was dissolved in neat FA (5:1 v/w FA: SF) in order to obtain a SF/FA solution suitable for film and membranes preparation.

SF/CFO films with 5, 10 and 20% CFO content are named as SFF-5, SFF-10 and SFF-20 respectively. SF/CFO membranes of 5, 10 and 20% CFO content are named SFM-5, SFM-10, SFM-20. Films and membranes precursory solution was prepared by mixing two different solutions, the first one described ahead and a second one composed by CFO NPs dispersed in FA by 1.5 h of ultrasonication. In order to obtain a solution with the adequate viscosity, CFO NPs were dispersed in the same volume in which the SF was dissolved. Both solutions were then mixed in a vortex mixer MX-S during 5 min to obtain a SF/CFO solution (10:1 w: w). Due to the chemical stability of the CFO NPs, no variation occurs during the processing of the films and membranes[56].

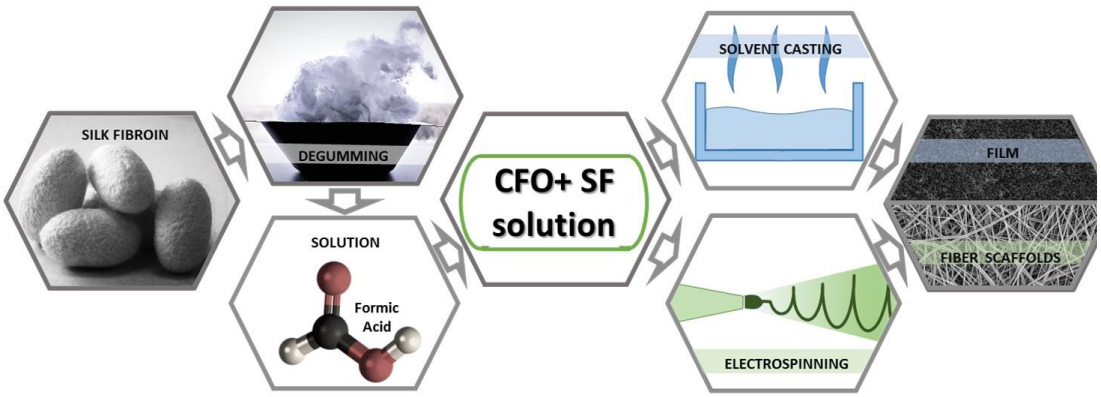

Figure 5.1. 2. *Schematic representation of SF/CFO based films and membranes processing procedure.*

SF/CFO films with a thickness of 40-60 μm were obtained by casting the final solution over polyethylene petri dishes for 24 h at room temperature. Neat SF films were prepared following the same steps without CFO NPs addition.

SF/CFO membranes were obtained by electrospinning technique. The SF/CFO solution was electrospun with a syringe connected to a HiTeh Power station Series 400. The syringe diameter was 0.8 mm, the distance to the collector was 20 cm, and power source parameters were 20 KV and 0.01 mA. Membranes with a thickness of 0.5 mm were prepared of both pristine SF and SF/CFO composites.

Characterization techniques

Atomic Force Microscopy (AFM) measurements were performed by CSInstruments in order to study the morphology of SF/CFO nanocomposites. Measurements were collected in 8 μm side squares at 0.25 lines per second and a resolution of 512 lines per side at room temperature. In order to avoid membranes damage and AFM tangling, non-contact resonant mode was used with frequency of 73 kHz and amplitude of 84º.

The morphology of the SF/CFO nanocomposites were examined using a scanning electron microscope (SEM, NanoSEM – FEI Nova 200 (FEG/SEM)) with an accelerating voltage of 15 kV.

Attenuated Total Reflectance (ATR) Fourier Transform infrared (FTIR) spectroscopy was used to study the secondary structure of SF nanocomposites with a Jasco FT/IR-4100 system. Data were collected at room temperature from 4000 to 600 cm^{-1} using 64 scans at a resolution of 4 cm^{-1}. The determination of beta-sheet content was performed by Amide I region deconvolution, by following the "characterization techniques" apart of 4.1 section.

Thermal Gravimetric Analyzer (TGA) - TGA/SDTA 851e Metter Toledo apparatus- was used to analyse the thermal degradation of the samples in the temperature range of 25 to 800 °C with a heating rate of 10 °C min^{-1} under constant air flow.

Differential scanning calorimetry (DSC) - Mettler Toledo DSC 822e equipment- was used to analyse the thermal transitions of the samples. Calorimetric scans were performed from 25 to 350 ºC at a heating rate of 10 ºC·min^{-1} under nitrogen purge (50 mL·min^{-1}). In order to remove the solvent lost endothermic peak, a first heating from 25 to 170 ºC was performed.

Mechanical characteristics were analysed by tensile testing using a Metrotech MTE-1 from Techlab system. Stress-strain tests were performed in specimens of 10 × 4 mm measured at 5 mm·min^{-1} at room temperature. Young modulus was obtained from the slope of the characteristic curves between 0.5 and 1.5% strain in the stress−strain plots. Results show the mean obtained from 3 measurements.

Vibrating sample magnetometry (VSM) -EZ7 from MicroSense apparatus- was used to study the magnetic behaviour of the SF/CFO nanocomposites between -1.8 and 1.8 T at room temperature.

Cell culture

MC3T3-E1 pre-osteoblast cells obtained from Riken Bank were used in all cell tests. The cells were maintained in Dulbecco's Modified Eagle's Medium (DMEM, Gibco) containing 1 $g \cdot L^{-1}$ glucose, 10% Fetal Bovine Serum (FBS, Biochrom) and 1% penicillin/streptomycin (P/S, Biochrom) at 37 ºC, in a humidified atmosphere with 5% CO_2, according to the recommendations of the manufacturer. The culture medium was replaced every 2 days. At pre-confluence, cells were harvested using trypsin-EDTA (Biochrom).

Preparation of the scaffolds: The different silk-based films and electrospun membranes were cut in circular samples with a diameter of 0.6 cm and sterilized using UV light for 1 h each side. The samples were then placed at the bottom of each well of a 48-well tissue culture polystyrene plate (Nunc).

Biocompatibility assays: The biocompatibility of the samples was determined by placing the pre-osteoblasts cells directly in contact with the surface of the material and by measuring the cell viability using 3-(4,5-dimethylthiazol-2-yl)-5-(3-carboxymethoxyphenyl)-2-(4-sulfophenyl)-2H-tetrazolium (MTS, Promega) assay at defined time-points of 24 h, 4 days and 7 days. To avoid cell seeding on the plate rather than on the material, 35 µL of DMEM containing 15 000 cells (cell density = 40 × 104 $cells \cdot mL^{-1}$) were first placed on the surface of the material for 30 min and then 250 µL DMEM was added to the well (drop method - ***Figure 5.1.3***). MTS assay was then performed to determine cell viability and consequently the biocompatibility of the scaffold. For this assay, after each time point, the samples were transferred to a new 48-well plate, MTS solution (in a 1:5 ratio) was added to each well and the plate was placed in a 5% CO_2 incubator at 37 ºC. After 2 h of incubation, 100 µL of each well were transferred to a 96-well plate (n = 3) and the optical density (OD) of each well was measured at 490 nm using a spectrophotometric plate reader (Biotech Synergy HT). The quantitative results were obtained from three independent experiments and analysed as the average of viability ± standard deviation (SD).

Cell culture assays in static and dynamic modes: Pre-osteoblast cells were seeded on the top of each sample using the above-mentioned drop method and two 48-well plates with the samples were prepared and incubated for 24 h. After this incubation time, one plate was

maintained at the same conditions (static culture – cell culture without any applied stimuli) and the other was transferred onto a home-made bioreactor system (dynamic culture – cell culture under magnetic stimulation, i.e. varying magnetic field) for up to 4 days with the following cycle: an active time of 16 h under magnetic stimulus (divided into 5 min of active time and 25 min of resting time) followed by a non-active time of 8 h (non-magnetic stimulation)[29]. These conditions were selected in order to mimic the human body mechanical stimulations (16 h of activity and 8 h resting time) (***Figure 5.1.3***)[57].

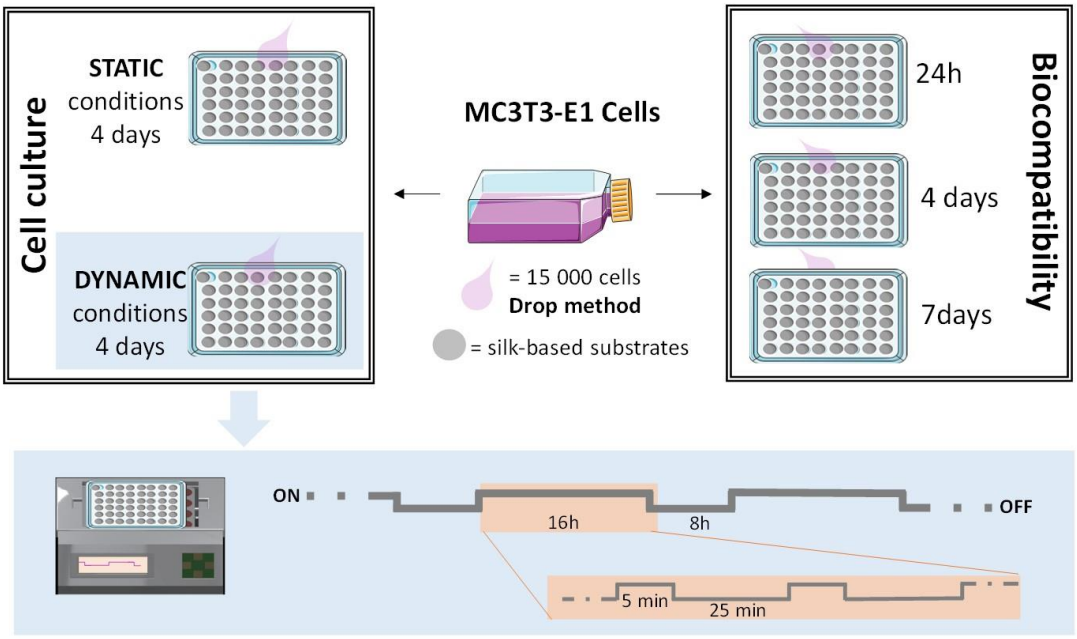

Figure 5.1. 3. *Schematic representation of the cell culture assays using either static or dynamic conditions (magnetic stimulation). Below: time dependence of the dynamic magnetic stimulation.*

The dynamic cell culture was performed under magnetic stimulation at a frequency of 0.3 Hz. The 15 mm displacement of the permanent magnets below the culture wells allowed the variation of the magnetic field from a maximum value of 230 Oe to 0 Oe within the culture wells, leading to magnetomechanical stimulation of the scaffolds due to the magnetrostriction of the magnetic nanoparticles[54] and to eventual local variations of the electrical potential based on the piezoelectricity of silk fibroin[48]. In each study, 5 replicates were used per studied conditions. The viability of cells growing on the top of the material was assessed using the MTS assay and the proliferation rate was calculated in relation to the cell grown over the material after 24 h using ***equation 5.1.1***.

$$Proliferation\ rate\ (\%) = \left[\left(\frac{Abs\ sample\ 4\ days_{490nm}}{Abs\ adhesion\ 24h_{490nm}}\right) x\ 100\right] - 100 \quad (5.1.1)$$

The morphology of the cells on the top of the materials was further analysed using a desktop Scanning Electron Microscope (SEM) (Phenom ProX, Netherlands), after fixing and dehydrating the sample. Briefly, the samples were collected and transferred for a new 48-well plate, washed twice with PBS 1x and the cells fixed with 4% formaldehyde (Panreac) for 10 min at 37 ºC in a 5% CO2 incubator. Following the fixation of the samples, they were dehydrated by immersing the samples to solutions with increasing ethanol content: 25%, 50%, 70%, 90%, 95%, and absolute ethanol for at least 10 min. The material was then sputter-coated with gold with a thickness of 20 Angstrom and the images acquired using the ProSuite software. The samples were added to aluminium pin stubs with electrically conductive carbon adhesive tape (PELCO Tabs™) on a Phenom Standard Sample Holder (SH).

The quantitative results obtained from each sample are presented as averages with the corresponding standard deviations. Results were analysed by Graph Pad Prism Version X for Windows (Graph Pad Software, San Diego, CA, U.S.A.). Statistical significance was determined by one-way ANOVA, followed by the unpaired two-tailed Student's t-test method.

5.1.2. RESULTS AND DISCUSSION

Morphological analysis

The morphology and roughness of the scaffolds is one of the most important parameters influencing cell activity[58] based on the mechanism of cell mechano-transduction phenomenon[59]. SF films and membranes morphology and roughness were analysed by Atomic Force Measurements (AFM), as presented in ***Figure 4.1.4a***. As the morphology of the films and membranes is influenced by the presence of the CFO NPs, the data from the SFF-20 and SFM-20 samples are used as representative for all samples.

The different processing techniques used to obtain films and membranes result in quite different morphologies. SF films show a smooth and compact surface with dispersed CFO NPs, no apparent fractures, and a small average roughness of 100 nm roughness (***Figure***

4.1.4b). This morphology is explained by the solvent evaporation rates in the preparation of the films. The casting process of SF films from a solution with high solvent content (silk solvent ratio of 1:20 w:v) and solvent evaporation at room temperatures ensures slow solvent evaporation, avoiding Marangoni instabilities, which are commonly responsible of large films roughness[60]. The resulting film roughness includes irregularities of 3 to 10 nm in depth and less than 100 nm in width. Along the surface of the SF films, it is observed the presence of CFO NPs that make increase the surface roughness as CFO NPs content is increased.

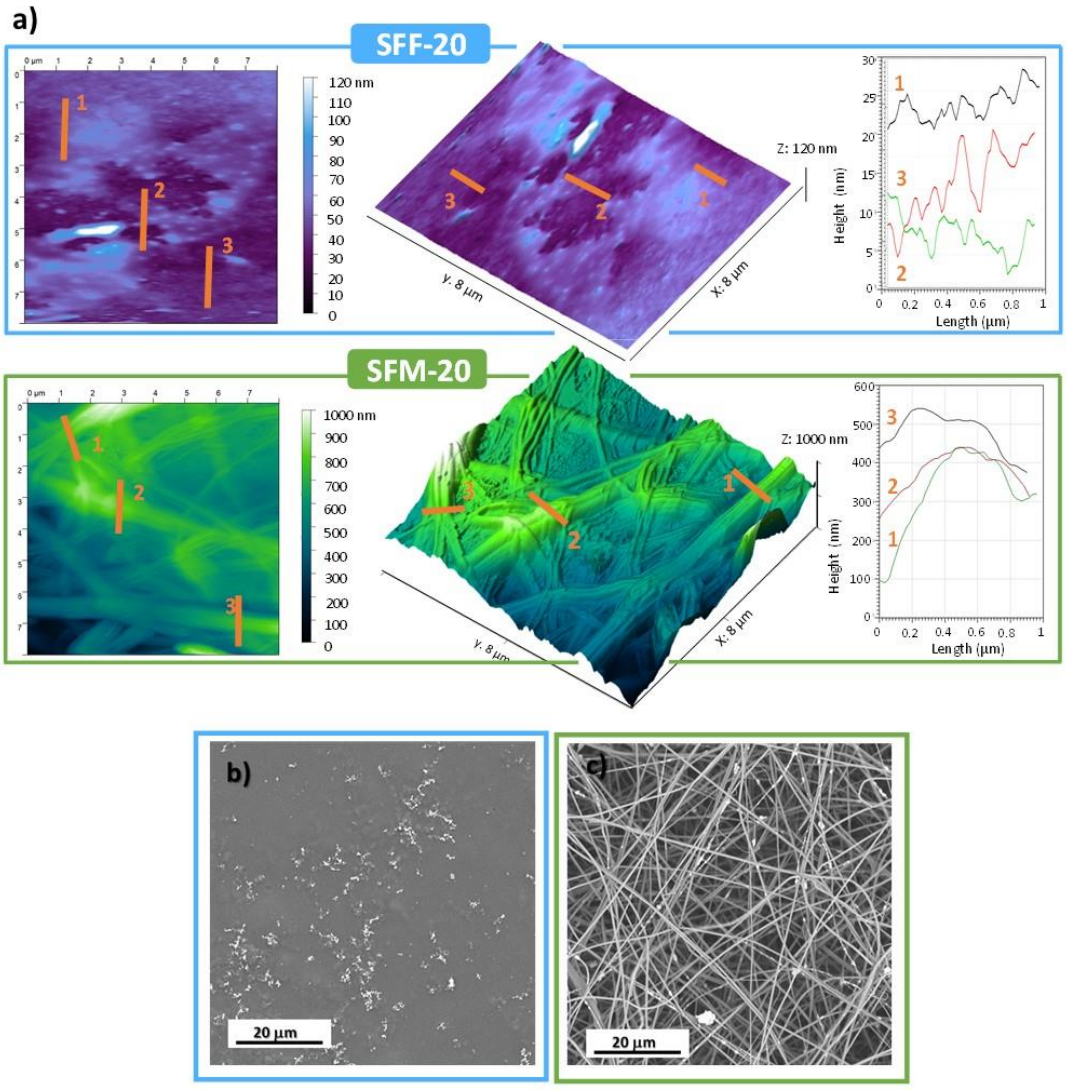

Figure 5.1. 4*. a) AFM images and surface topography measurements of SFF-20 (Up) and SFM-20 (Down) samples. The numbers 1, 2 and 3 represent three different scans for the determination of the average roughness of the samples. b-c) SEM images of SFF-20 and SFM-20 samples, respectively.*

In the electrospinning process, once the initial single jet is formed and elongated by the effect of electrical forces[61], physical instability processes related to Maxwell stresses and surface tensions, lead to the breakdown of the single jet static equilibrium, jet to undulation[62] and induced tensions along the jet. In those sections where tensions are accumulated, and once the surface solution tension is exceeded, continuous lateral branches are formed and elongated by electrostatic forces[63], leading to lateral fibres that join together packing in larger fibbers which are finally deposited in the collector, as observed in ***Figure 4.1.4.*** Fibres roughness show similar values as the ones observed for the films and it is also independent of the CFO NPs content.

Physical-chemical characterization

FTIR analysis allows to determine the effect at a molecular level of the different processing methods as well as that derived from CFO NPs addition. The FTIR data of SFF, SFF-20, SFM and SFM-20 are represented in ***Figure 4.1.5***. Amide I curves are thus shown in ***Figure 4.1.5a*** as the most relevant FTIR spectral range in order to analyse the secondary structure of SF. ***Figure 4.1.5b*** shows the vibrational band assignments for the main secondary structures of SF obtained from the deconvolution of the amide I region: side chains (SC), β-Sheets (β), random coil (RC), α-helix (A) and turns (T).

Regardless of the SF morphology and CFO addition and content, the main absorption bands of SF are clearly observed in all SF samples, suggesting that no relevant modifications of the primary structure of SF exists due to the selected processing methods due to the incorporation of the CFO NPs. In contrast, amide I data (***Figure 4.1.5a***), regardless of the CFO addition, show large variations depending on the morphology, this is indicative of a change in the secondary structure due to the processing method. The vibrational band assignments obtained from the amide I deconvolution were used in order to quantify the observed effect (***Figure 4.1.5b***). Slow solvent evaporation leads to improved polymer chain organization and therefore leading to a highly crystallized structure [42], therefore, the solvent casting process resulted in a highly ordered SF structure with β-sheet contents above 50% and low α-helix and random coil content. Although incorporation of CFO NPs in the SF film also leads to structures dominated by β-Sheets (>45%), a slight decrease in β-Sheets content could be observed. Diminished ordered structure content suggests the hindering effect of NPs on the SF crystallization processes[51]. CFO NPs interact with the amine groups

forming functional coatings[64], avoiding the free movement of the backbone and consequently, reducing the formation of ordered domains.

Neat SF membranes (***Figures 4.1.5 a and b***), on the contrary, show a secondary structure with low β-sheet (<25%) and high random coil and α-helix content. This result is related with the fast solvent evaporation rates during the spinning process, which leaves shorter times for the polypeptide repetitive sections to reorganize into β-sheet. Consequently, the non-ordered chains sections remain as random coils (amorphous phase). The increased amount of α-helix indicates that these structures are preferably formed when formic acid quickly leave the SF structure. SFM secondary structures are not significantly altered as a result of the addition of CFO NPs, suggesting that the hindering effect of NPs on the β-sheet is lower with respect to the effect of fast solvent evaporation.

The TGA results presented in ***Figure 4.1.5c***) show the thermal degradation processes of the different SF samples. Neat SF films are characterized by an initial weight loss at 100 ºC corresponding to a water loss process, a second degradation from 300 to 550 ºC mainly ascribed to the breakdown of SF side chain groups, the amino acid residues and the split of peptide bonds, and a final step related to the degradation of the main SF structure. After CFO NPs addition, the water lost remains equal, indicating allow effect of NPs in SF films water affinity. In contrast, the second degradation step is slightly retarded due to the addition of CFO NPs. The final degradation step, in contrast is highly affected by NPs shifting from 580 ºC in SFF to 500 ºC in SFF-20. The observed data are in good agreement with the FTIR data (***Figure 4.1.5a-b***). Improved thermal stability by the addition of NPs in the SF matrix has been reported due to the induced transition from amorphous to crystalline phases[65]. However, this effect does not correspond to here observed FTIR results, which show the reduction of β-Sheets due to CFO NPs addition. Indeed, the slight thermal enhancement observed is in line with the proposed trapping effect of NPs on SF polypeptide chains and the induced stability[66]. Consequently, side chain groups, amino acid residues and peptide bonds breakdown are slightly reduced, improving SF thermal stability. At the same time, lowβ-Sheets formation due to NPs incorporation reduces the content of stable thermal structures, favouring the degradation of the complete structure. Final thermal degradation is also improved by the catalyst effects given by the NPs[66].

SF membranes also show the three main thermal degradation steps. The weight loss due to water evaporation is equal to that observed in films, showing allow effect of SF morphology

on water affinity. However, the porous structure of the SF membranes seems to facilitate water evaporation, leading to more pronounced water loss curves. Compared with the films, no variation is observed in the first steps of second degradation. On the other hand, the side chains, amino acid residues and peptide bonds degradation and final degradation are highly affected in response to reduced β-Sheet content, which are the main responsible for the SF thermal stability[67]. The addition of CFO NPs in SF membranes does not affect the water loss process due to the low β-Sheet content of these samples, however, due to the catalytic effect of NPs, it greatly improves thermal degradation, leading to complete decomposition of SFM-20 at 300 ºC.

DSC thermograms show the thermal transitions of SF films and membranes during heating scan from 50 to 350 ºC (***Figure 4.1.5d***). The curves of SFF, SFF-20, SFM and SFM-20 are presented as representative for the rest of the samples. It can be seen that during the heating process neat SF films show the characteristic thermograms of highly crystalline SF structures (previously observed in SF composite films). The single endothermic peak near 300 ºC indicated the breakdown of SF side chains groups amino acid residues and the cleavage of peptide bonds as shown in previous TGA data (***Figure 4.1.5c***). The CFO NPs addition to the SF films has no significant effect on the secondary structure and therefore the DSC scans remain almost invariable. However, it could be observed by DSC a slight increase in the thermal stability with the NPs addition, as the endothermic peak shifts to higher temperatures, as a result of CFO-SF interactions that affect.

The polypeptide chains reorganization induced by the electrospinning technique results in SF membranes with new thermal transitions (***Figure 4.1.5d***). The increase in the number of non-ordered structures (RC) gives the peptide chains larger mobility and consequently a well-defined glass transition temperature (T_g) at 164 ºC. Further, crystallization (T_c) at 270 ºC appears and the peak corresponding to the degradation of peptide chains at 300 ºC remains invariable. The incorporation of CFO NPs into SF membranes leads to similar DSC thermograms, with clear T_g and T_c transitions and degradation peaks. However, the decreased mobility of the polymer chains related to the interaction between SF chains and CFO NPs reduces the intensity of thermal transition and leads to the loss of the endothermic peak.

With respect to the mechanical properties of SF films and membranes under tensile stress, ***Figure 4.1.5e*** shows the strong effect of the processing method and, therefore, sample

morphology. The stress-strain curves of SFF, SFF-20, SFM and SFM-20 were used as representative for all the samples. With stress at yield values above 64 MPa, SF films show the typical behaviour of non-ductile materials. Under stress, SFF shows an initial elastic region followed by a short plastic deformation until the final rupture. This behaviour can be understood by the ternary configuration of SF structures. SF mainly consists on a hydrogen-bonding network of β-structured crystallites (β-sheets), responsible for the strength and rigidity of the material, and non-ordered amorphous regions (random coils), more flexible and related to its elasticity[68]. During the first deformation steps, the amorphous domains maintain all the accumulated structural force, which causes the tangled chains to unfold, leading to the elastic behaviour of the film. Since the random coils are completely unwound, the deformation becomes supported by β-sheet nodes, which endure the force until their break. When CFO NPs are added, the secondary structure is slightly affected and consequently, low variation in stress-strain curves are observed (***Figure 4.1.5e***). Lower stress on yield in the presence of CFO NPs are related to the defects induced by the NPs.

The mechanical behaviour of SF electrospun membranes is characterized by fibre deformation followed by their reorientation on the direction of applied strain and finally[69], the effect on the secondary structure of the material inducing a long decrease in β-sheets formation and an increase in random structures. As a result, stress on yield values decrease to 23 MPa and elongation increases from 6% in SFF to 15% in SFM. In SFM-20 the defects induced by CFO NPs decrease both the elongation and stress at yield.

The magnetic response of the SF samples is shown in ***Figure 4.1.5f*** where the hysteresis loops of SFF-20 and SFM-20 are plotted. Under the effect of the magnetic field, both SFF-20 and SFM-20 show closed hysteresis loops, similar in shape to neat CFO (insert in ***Figure 4.1.5f***). This behaviour reveals that the magnetic particles preserve their original ferromagnetic behaviour when placed in the SF matrix, independently of the processing procedure and, therefore, of the morphology. The saturation magnetization decreases in comparison with neat CFO NPs (7 and 6 emu·g^{-1} for SFF and SFM respectively), which can be related with the matrix-filler interfacial interactions[70].The lower saturation magnetization values observed for SFM-20 are related to the precipitation of CFO NPs during electrospinning process. Equally to neat CFO NPs, SFF-20 and SFM-20 samples show strong remanence (3.8 and 3.3 emu·g^{-1} respectively) and coercivity values (both 2.2 kOe).

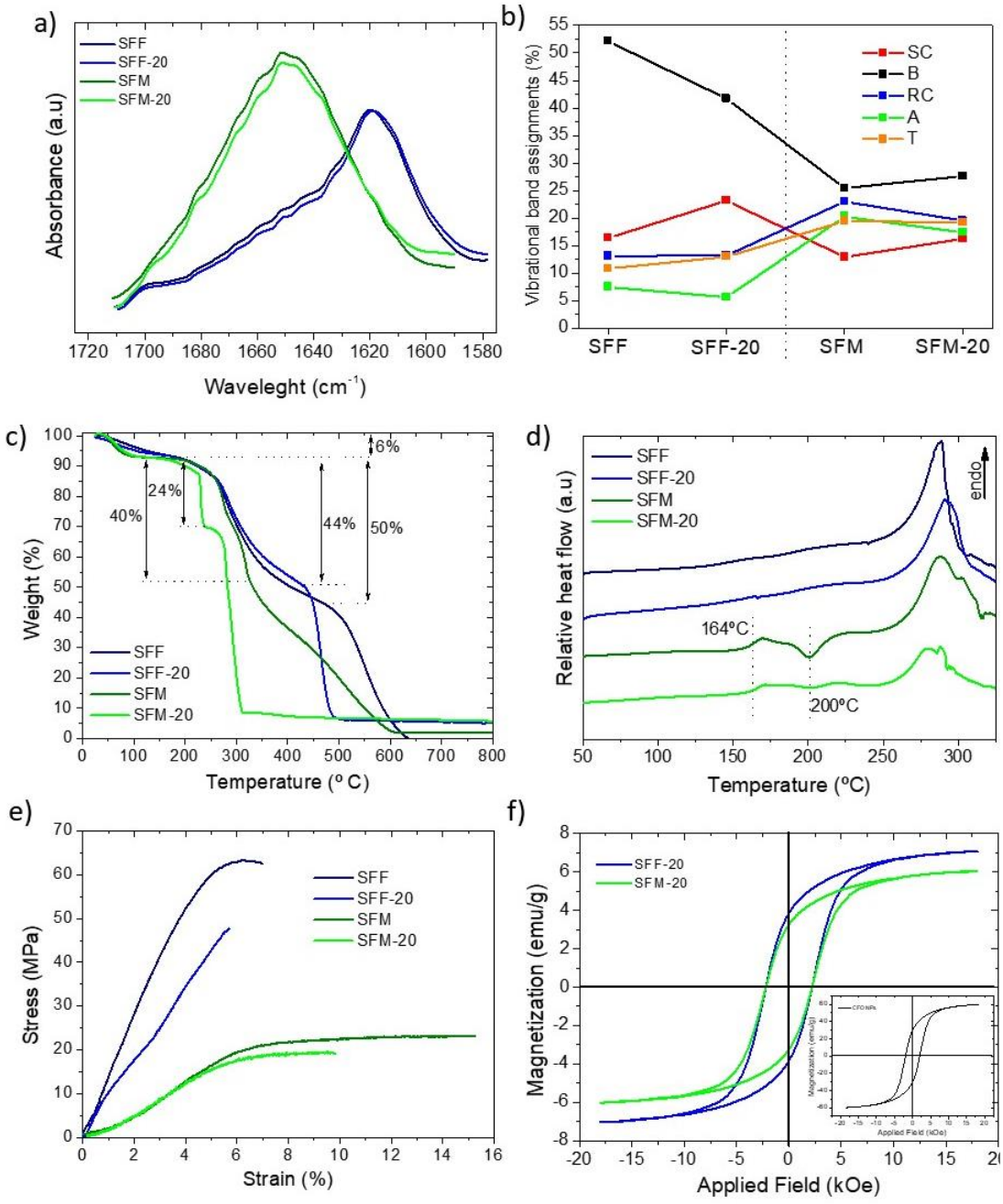

Figure 5.1. 5. *Neat SFF, SFF-20, neat SFM and SFM-20 scaffolds a) FTIR-ATR amide I spectra b) vibrational band assignments for side chains (SC), β-Sheets (B), random coil (RC), α-helix (A) and turns (T), c) TGA thermogravimetric curves, d) DSC thermograms, e) stress-strain curves and f) magnetic hysteresis loops.*

Bone tissue engineering applications

The SF films and membranes comprising different concentrations of CFO NPs, were further used as substrates that respond to magnetic stimuli for bone tissue engineering, and tested for their ability to act as an active support for cell adhesion and proliferation. Initially, the

biocompatibility of the substrates was measured by placing in contact the pre-osteoblasts cells with the surface of the material and by measuring their viability using MTS. The biocompatibility at different time-points were studied, namely at 24 h, 4 days and 7 days. An increased cell viability was observed increasing the time of culture in all scaffolds, indicating that the materials are biocompatible (***Figure 5.1.6***).

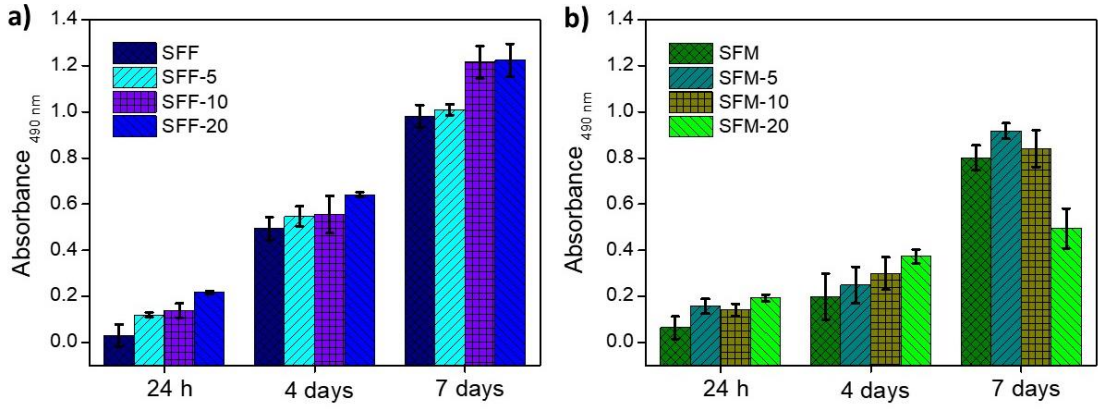

Figure 5.1. 6. *Biocompatibility MTS assay on pre-osteoblasts growing on the top of a) SF films and b) SF membranes increasing the CFO NPs content at three time points: 24 h, 4 days and 7 days.*

Figure 5.1.6 - Also, the higher the concentration of incorporated CFO NPs, the better is cell adhesion and proliferation, and this behaviour was observed for both films and membranes. The only exception was observed for SFM-20 that induced certain toxicity to the cells (***Figure 5a***), probably due to silk biodegradability. After 7 days is acceptable that silk fibres degrade in a more extent than the films[71]. This is in good agreement with previous studies that show that the degradation of silk may be established after 10 days in contact with DMEM[72]. Despite silk leachable are reported to induce no toxicity or immunogenic response to the cells, in this study the biodegradation profile of silk based structures may cause the release of CFO NPs which further induce toxicity to the cells[73].

It also should be noticed that cells grow better on the films (***Figure 5.1.6a***)) rather than on the electrospun membranes (***Figure 5.1.6b***)). In fact, between 24 h and 4 days, the cells growing on SF membranes do not experience a big increase on cell viability when compared with the cell growing over SF films. Higher cell viability in SF membranes is then observed after 7 days of culture but the results are rather low when compared to the viability levels observed on the films. In a first assessment, smooth surfaces seems to promote better adhesion to the cells.

SF substrates were then tested for their ability to induce proliferation of pre-osteoblasts with and without magnetic stimuli. Cells growing at the surface of the nanocomposites were subjected to a magnetic stimulus or left in static conditions for 4 days, a time-point which was earlier defined as non-toxic for the cells in both substrates (***Figure 5.1.6***). The cell behaviour was found to be different depending on the morphology of the scaffolds as previously suggested in ***Figure 5.1.6***.

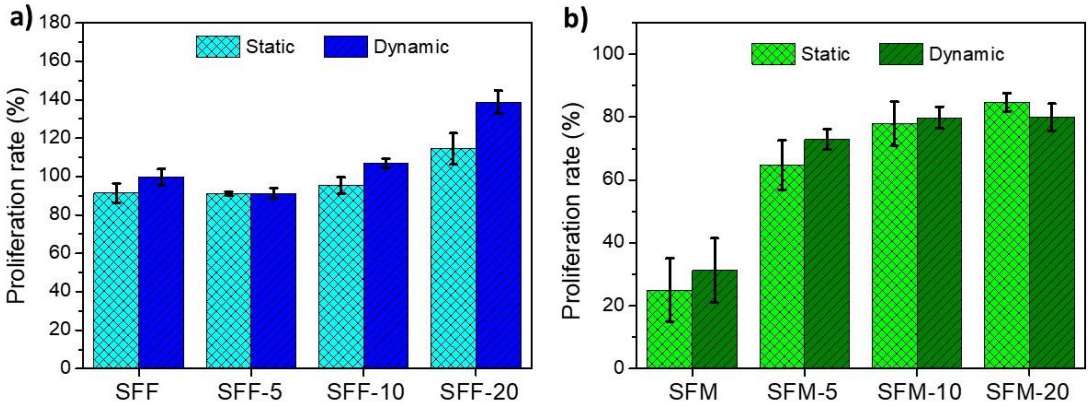

Figure 5.1. 7*. Proliferation rate of pre-osteoblasts seeded on the top of a) SF films and b) SF electrospun membranes after 4 days with and without magnetic stimuli. The proliferation rate was calculated regarding the cells growing on the material after 24 h adhesion, just before putting in contact with the bioreactor/magnetic stimuli (see Figure 2). The results are an average of three independent assays. *P < 0.01,**P < 0.1*

With the SF films, the effect of the stimuli was observed, since the proliferation rate was higher for the cells growing over the material with 10 % and 20 % CFO NPs subjected to the magnetic stimuli. The exception was found in the material with 5 % CFO NPs and the films without NPs, which has shown the same behaviour with and without stimuli, most probably due to the fact that 5 % incorporated CFO NPs into the SFF are not sufficient to apply significant enough magneto-mechanical stimuli to the cells, due to the low filler content.

Regarding the electrospun membranes, no significant differences were observed in the proliferation rate of cells growing on the material subjected to the stimuli and the ones maintained under static conditions. This may be indicative that these scaffolds do not induce the necessary mechanical/electrical effect on the cells (***Figure 5.1.7a***), as previously described in other magnetic responsive materials[54]. Nevertheless, as observed in ***Figure 5.1.6a***, it can be observed that a tendency for higher cellular proliferation on the scaffolds with higher concentration of NPs occurs, regardless the stimuli. This behaviour indicates

that the morphology of the scaffold plays an important role on the adhesion and proliferation of the cells, an effect that is, in the present case, more relevant than the magnetically induced stimuli.

To corroborate these results, the morphology of cells was visualized 4 days after cell seeding using SEM (***Figure 5.1.8***). In both samples, the surface of the scaffolds was observed prior to cell seeding in order to visualize the morphology and topography of the material (***Figure 5.1.4***).

In SF films, the cells seed on the surface of the material in a completely different way when compared to the membranes. While on the membranes a dense cell layer is observed, on the films the cells are round but well attached to the surface. While the rounding cells may be indicative that cells are not viable, in the herein tested films, the cells are well-attached as clearly shown by the well-established spider-like network around the cells and are indeed viable, as shown in ***Figure 5.1.6a and 5.1.7a***). The morphology observed may indicate that pre-osteoblast did not have time to differentiate into osteoblasts[74]. Under static conditions the cells seed at higher number with increased CFO NPs concentration (***Figure 5.1.8a***), as previously observed in ***Figure 5.1.7b***. Upon application of the stimuli, the cell density increases when compared to the static conditions, confirming the capability of the scaffolds to provide a proper magneto-mechanical or event local magneto-electric effect on the cells (***Figure 5.1.8a***).

When stimulated by a magnetic bioreactor, these scaffolds induce a mechanical[54] or electrical[74] cue on the cells due to the magnetostriction of CFO NPs and the piezoelectricity of silk within the nanocomposites. This type of stimuli has been reported to trigger the activation of intracellular signalling cascades in a cell[75]. More specifically, the application of an electrically active microenvironment has been a strategy increasingly explored in mammalian cells. It has been established that electroactive materials such as piezoelectric polymers and magnetoelectric composites develop voltage at the surface of the material when a mechanical stress[76] or a magnetic field[54], respectively, is applied, thus promoting the adhesion and proliferation of eukaryotic cells, such as osteoblasts.

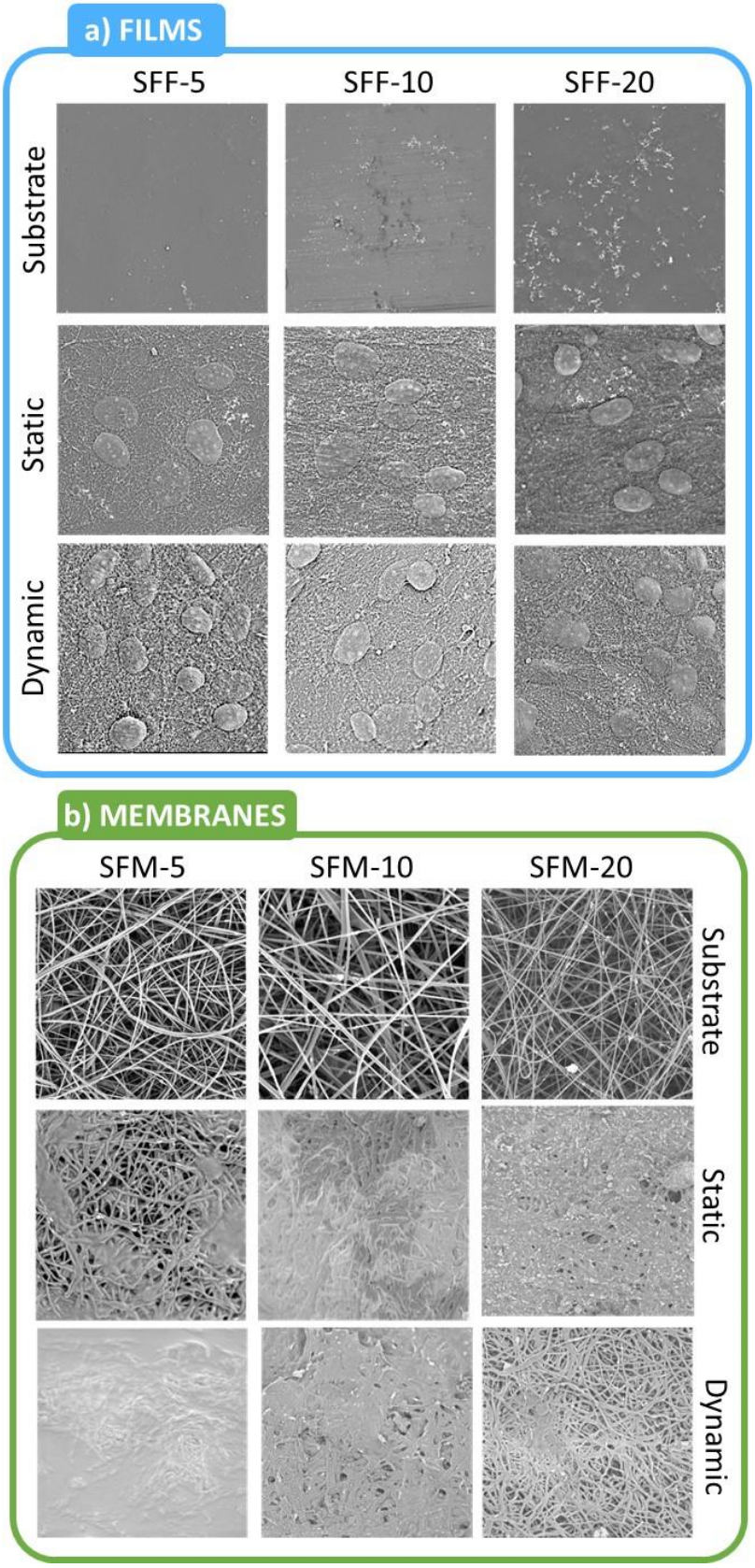

Figure 5.1. 8. *SEM images of the surface of SF a) film and b) membranes with 5, 10 and 20% of CFO NPs, after culture of pre-osteoblast cells for 4 days, with and without dynamic conditions.*

At static conditions, on the electrospun membranes the cells form a layer that is increasingly thicker with increasing concentration of CFO NPs (***Figure 5.1.8b***), as previously observed in ***Figure 5.1.7b***). This confirms that the morphology of the scaffold plays a key role on the proliferation of cells while the presence of CFO NPs may promote better adhesion due to the increased focal points they induce at the surface of the fibres. In fact, by observing the SEM images depicted in ***Figure 5.1.8***, before cell seeding, it can be observed that the CFO NPs are present at the surface of the fibres. Nevertheless, the cells growing on the membrane with 20% CFO NPs seem to be rounding up and detaching, indicating a previous state of cells death owed to the higher presence of CFO NPs.

After applying the magnetic stimuli, and despite the fact that MTS assay have shown little differences with and without the application of the stimuli, there is an increase on cell coverage over the material, mainly on the membranes with 5 % and 10 % CFO. The cells clearly penetrate the pores and a well-established cell layer is found on the surface of the material where the cells are intricated within the material. This effect is not so pronounced on the membrane with 20 % CFO NPs.

Thus, the developed magneto-active scaffolds have been shown beneficial to improve the proliferation of cells despite the piezoelectricity of silk being different from the commonly used PVDF, where the stimuli creates an electrically active microenvironment that improves cells adhesion and proliferation[52,54].

Silk fibroin, by itself, has been explored for tissue engineering purposes and proven to promote osteogenesis in vitro[77] and to have osteopromotive potential in critical sized defects in vivo[78]. Therefore, the morphology of the materials also play an important role on the proliferation of pre-osteoblasts. In fact, it has been suggested that cell survival and maintenance, as well as proliferation and differentiation, are regulated by their three-dimensional microenvironment, the so called niche[79]. This specific microenvironment regulates stem cell function through several mechanisms, related with the direct contact between cells and their adjacent niche cells. Their interactions are mediated either through adherence or gap junctions, which combined with the magnetic stimuli creates the appropriate microenvironment for cell proliferation.

5.1.3. CONCLUSIONS

Silk fibroin/cobalt ferrite nanoparticles ($CoFe_2O_4$, CFO) SF/CFO composites have been prepared with different fillers content (0 wt. % to 20 wt. %). To explore the influence of morphology on composite's behaviors, two composite shapes have been designed: films and electrospinning mats.

Despite the morphology, the CFO fillers show a good distribution within the biopolymer. The processing method affects the morphology and the subsequent roughness of the samples, as well as their β-sheet content. For electrospun membranes, multifibrillar fibers with a diameter of 850 ± 100 nm were obtained. The content of the β-sheet is independent of the filler content.

All composites show good thermal and mechanical properties affected by filler content and processing technique. The magnetic behavior of these composites shows a typical ferromagnetic behavior of the CFO nanoparticles in which the magnetic response is correlated with filler content.

The cell culture results show that dynamic stimulation enhanced cell viability and their morphology plays an important role in pre-osteoblast proliferation. Thus, it is demonstrated that the SF/CFO composites show excellent cell viability and can be suitable for tissue engineering applications.

5.2. POROUS SILK MEMBRANES AS LITHIUM-ION BATTERIES SEPARATOR

BASED ON: A. Reizabal et al. Tailoring silk fibroin separator membranes pore size for improving performance of lithium ion batteries. J. Memb. Sci., vol. 598, no. 117678, 2020

Renewable energy sources are essential for improving the sustainability of earth non-renewable resources[80]. Batteries are essential elements for storing the energy obtained from renewable systems. In particular, lithium-ion batteries play an important role based on their higher energy and power density compared with other battery systems, such as lead-acid and nickel-metal hydride batteries (NiMH)[81]. Further, lithium-ion batteries are increasingly used in many applications such as consumer electronics, medical applications, and electric vehicles, being the battery type most used in the world with high potential growth[82].

The main issues that should be improved concerning lithium-ion batteries are their energy density and power, materials availability, safety, and cost[83]. An especially relevant issue is the use of materials with benign environmental properties and low human health impacts. New materials should be developed to improve safety and produce more sustainable lithium-ion battery systems[84] for all components: electrodes and separator/electrolyte[85].

The electrodes correspond to the anode (negative electrode) that should show low potential to provide a high cell voltage and the cathode (positive electrode), which determines the battery capacity[82]. About the separator, it is localized between both electrodes (***Figure 5.2.1***). It serves as the medium for the transfer of lithium-ions during the charge and discharge processes[24]. The separator is typically constituted by a polymeric membrane soaked in the electrolyte solution, i.e., a liquid electrolyte where salts are dissolved in water or organic solvents[24]. Typically, the polymeric matrix is based on poly(ethylene) (PE), poly(propylene) (PP), poly(ethylene oxide) (PEO), poly(acrylonitrile) (PAN), poly (methyl methacrylate) (PMMA), and poly(vinylidene fluoride) (PVDF) and its copolymers poly(vinylidene fluoride-co-trifluoroethylene) (P(VDF-TrFE)), poly(vinylidene fluoride-co-hexafluoropropylene), (P(VDF-HFP)), and poly(vinylidene fluoride-co-chlorotrifluoroethylene), (P(VDF-CTFE)) [86]. Considering these synthetic polymers' environmental impact, conventional separators are substituted by natural polymers, such as cellulose[87], lignin[88], polyimide[89], and silk fibroin (SF)[90]. This contributes to the reduction of the environmental impact of lithium-ion batteries[91].

In particular, the main advantages for SF for battery applications are its non-toxicity, mechanical flexibility, excellent thermal properties, and suitable ionic conductivity[92]. SF also exhibits excellent cycling performance as a separator for lithium-ion batteries[90].

The correlation between SF β-sheet fraction and the ionic conductivity of SF membranes has been demonstrated[90], as well as its suitability for energy storage. Thus, SF is beginning to be used in the field of solid-state electrochemistry devices such as Mg–Air bioelectric batteries[93], lithium-sulfur batteries[94], magnesium primary batteries[95], lithium-oxygen batteries[96], and anode electrodes[97].

Figure 5.2. 1. *Graphical abstract of porous SF membranes for Li-ion batteries separator.*

It has also been shown that the degree of porosity affects the wettability process of the electrolyte solution and, consequently, the ionic conductivity. The pore structure of the separator is a critical design parameter that affects the true length of the ionic path (tortuosity). Thus, the goal of the present work is to prepare porous membranes based on SF through the solvent casting salt leaching method with the same degree of porosity but different pore size, allowing to optimize SF's performance as separator membranes. Further, the processing method is highly reproductive, scalable, and low cost. It allows obtaining three-dimensional separators with interconnected pores and sizes ranging from 22 to 250 μm, maintaining the necessary mechanical stability.

The morphology, polymer phase, thermal and mechanical properties, contact angle, and uptake value were analyzed for the different SF separators and the electrochemical properties. The results show a correlation between pore size, β-sheet conformation, and

discharge capacity value for the prepared SF separators, corroborating its applicability as a separator at lithium-ion battery systems.

5.2.1. MATERIALS AND EXPERIMENTAL METHODS

Materials

Bombyx mori cocoons were supplied by APPACDM from Castelo Branco (Portugal). Formic acid and sodium chloride (NaCl) were provided by Sigma Aldrich with a 98.9% of purity. Poly (vinylidene fluoride) (PVDF, Solef 5130, Mw = 1000–1300 kDa), C–LiFePO4 (LFP), and carbon black (Super P–C45) were acquired from Solvay, Phostech Lithium and Timcal Graphite & Carbon, respectively. The solvent N, N′-dimethylpropyleneurea (DMPU), the conventional electrolyte 1 M $LiPF_6$ in ethylene carbonate-dimethyl carbonate (EC-DMC, 1:1 vol) were purchased from LaborSpirit and Solvionic, respectively.

Samples preparation

Figure 5.2.2 shows the main processing steps for obtaining SF membranes with different pore size.SF was extracted following the *SF extraction* procedure of 4.4.1 section. Porous membranes were prepared by a salt leaching method. For that, the previously prepared pure SF was initially dissolved in FA by magnetic stirring (20 ml formic acid per gram of SF). After complete dissolution, well sifted NaCl particles in a proportion of 1:10 (w: w) SF: salt (always keeping constant the salt weight), were added to the solution. Sifted NaCl was divided into 3 different size ranges in order to produce membranes with variable porous sizes: 250-106 μm, 106-38 μm and 38-22 μm (***Figure 5.2.2***). Based on the sizes, the resulting membranes were named as SF 205–106, SF 106–38 and SF 38–22. After a few min of energetic stirring, a homogeneous mixture was obtained. The resulting solution containing dissolved SF and dispersed NaCl was poured over polyethylene petri dishes and dried until complete evaporation of the solvent.

The obtained SF/NaCl composites were finally washed by distilled water bath at room temperature to eliminate the non-desirable NaCl. After several water changes, the solution shows constant electrical conductivity values showing the completely removing of NaCl. The obtained porous membranes were placed in an airing chamber and dried for 24 h.

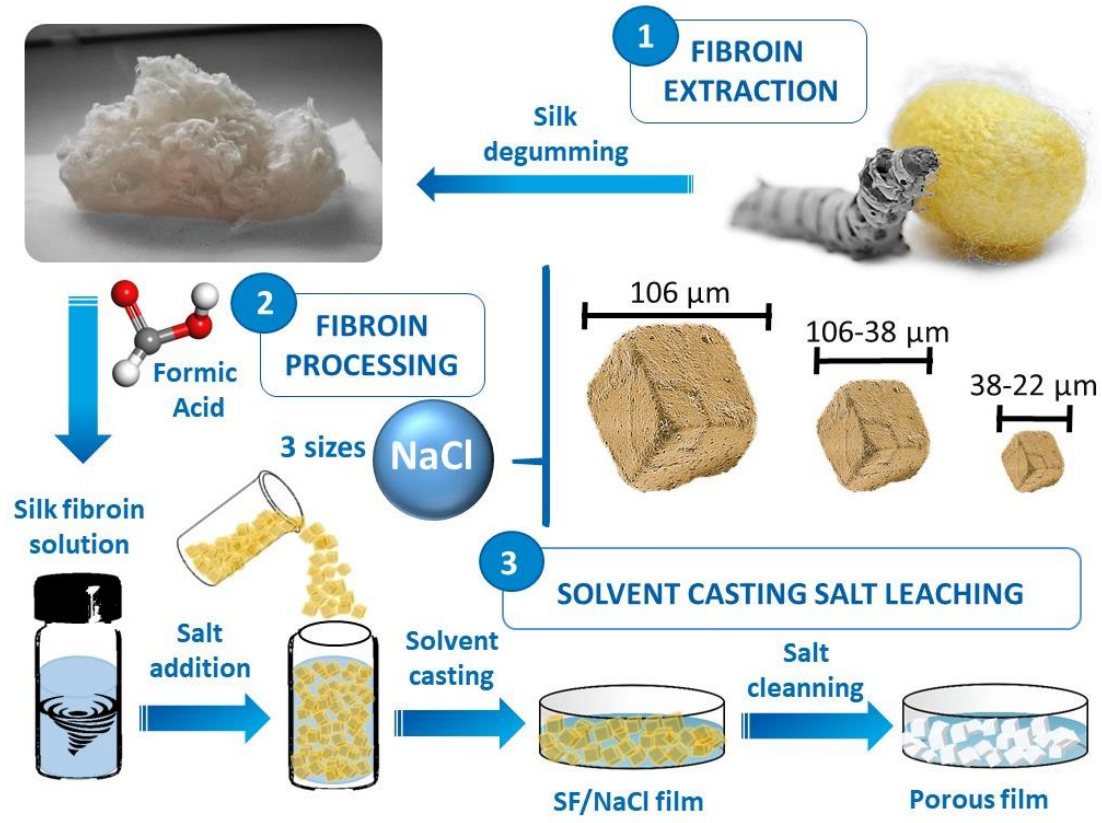

Figure 5.2. 2. Main processing steps for porous SF membranes preparation.

Characterization techniques

Morphological analysis: In order to analyse the microstructure of the samples, porous membranes were characterized by scanning electron microscope (SEM, NanoSem – FEI Nova 200 (FEG/SEM)) with an accelerating voltage of 15 kV. The membranes were previously coated by a conductive gold layer by sputtering with a Polaron SC502 apparatus. Cross section images were taken in cryogenically fractured samples.

Infrared spectroscopy: Samples secondary structure analysis was performed by Fourier Transformed Infrared Spectroscopy (FTIR) with a Jasco FT/IR-4100 system. FTIR spectra were collected in the ATR mode from 4000 to 600 cm^{-1} after 64 scans with a resolution of 4 cm^{-1}. In order to determine the vibrational band assignment of each sample, all the scans were normalized with Amide II. Then spectral region corresponding to Amide I was carried out, by following the methodology described in "characterization techniques" apart of 4.1 section.

Thermal and mechanical analysis: Thermal degradation and heating transitions were determined by Thermogravimetric Analysis (TGA) and Differential Scanning Calorimetry (DSC), respectively.

Samples thermal degradation was measured with a TA/SDTA 851e Metter Toledo apparatus under air flow of 50 mL·min^{-1} operating between 25 and 800 °C at 10 °C min^{-1}. DSC was performed with a Mettler Toledo DSC 822e under nitrogen flow of 20 mL·min^{-1} operating between 25 and 350 °C at 20 °C·min^{-1}. Before the measurements, samples were treated by dynamical heating from 25 to 168 °C for remaining solvent evaporation.

Samples tensile properties were analysed in 400 μm thick, 5 mm wide and 15 mm long samples with a Metrotech MTE-1 from Techlab systems at a stretching speed of 10 mm·min^{-1}. Specimens were stretched at room temperature until breaking. Young's modulus (E′) was determined from the slope between 1.5 and 2.5% strain in the stress-strain plot. Reported values represent mean average values and standard deviations (3 specimens were measured for each material).

Solvent affinity: The affinity between the electrolyte (1 M LiPF6 in EC: DMC, 1:1 vol) and the membranes was measured by contact angle and uptake.

Wettability of the SF porous membranes was measured by the formed contact angle between water and/or electrolyte solution and the membrane surface. 200 μl drops were deposited on a flat surface and the contact angle of the droplet with the surface was measured. No change in the contact angle during the measurement period was observed. 10 measurements per sample were performed at different points of the samples and the average value was calculated.

Samples ability to uptake electrolyte was obtained by immersing the membranes into the electrolyte solution (1 M LiPF6 in EC: DMC, 1:1 vol) over time, through the following equation:

$$uptake\ (\%) = \frac{m_i - m_0}{m_0} \times 100 \qquad (5.2.1)$$

where m_0 is the weight of the dry membrane and mi is the weight of the membrane after immersion in the electrolyte solution.

SF membranes characterization results were compared with neat SF films in order to give a close understanding of the physical-chemical changes occurring in SF as result of salt leaching process.

Porosimetry and surface area determination: Porosimetry and surface area determination were carried out by mercury intrusion porosimetry (MIP) in a Quantachrome Instruments Poremaster-60 GT operating in the pressure range from vacuum (10^{-4} MPa) to 414 MPa. Samples were degassed in situ at 120 °C during 12 h prior to measurement. A contact angle of 140° and a surface tension of 480 dyn·cm^{-1} for mercury and a pressure equilibration time of 11 s were used. Before the measurement of MIP the He gas density for all the samples were measured in a Quantachrome Instruments automatic Micro Ultrapycnometer.

Electrochemical characterization

Impedance spectroscopy measurements were carried out into SF membranes immersed of the conventional electrolyte 1 M LiPF6 in ethylene carbonate-dimethyl carbonate (EC-DMC, 1:1 vol) for 15 min. Measurements were performed in steel/membrane/steel symmetrical cells, at room temperature, in the frequency range between 10 mHz and 1 MHz with an amplitude of 10 mV with a Biologic VMP3 instrument. The ionic conductivity (σi) of the SF separators was calculated by the following equation:

$$\sigma_i = \frac{d}{R_b * A} \tag{5.2.2}$$

where Rb is the bulk resistance, d is the thickness and A is the area of the sample.

The Rb is obtained from the intercept of the imaginary impedance (minimum value of Z″) with the slanted line in the real impedance (Z′)[98].

Another relevant parameters such as tortuosity (τ) and MacMulin number (NM) of the SF membranes were calculated through the following equations:

$$\tau = \sqrt{\frac{\sigma_0 \varepsilon}{\sigma_i}}$$

(5.2.3)

$$N_M = \frac{\sigma_0}{\sigma_i}$$

(5.2.4)

where is the electrical conductivity of the pure electrolyte solution (10.07 $mS \cdot cm^{-1}$), is the conductivity of the membrane plus the electrolyte solution and ε is the degree of porosity of the SF membrane.

Cathode preparation

The cathode was prepared using 80 wt. % C–LiFePO4, 10 wt. % carbon black and 10 wt. % PVDF in 2.25 mL of DMPU for 1 g of solid material. More details on the electrode preparation are reported in Ref.[99]. The resulting slurry was then casted on aluminium foil by doctor-blade technique and dried at 80 °C for 2 h. The thickness and porosity of the cathode electrodes are 20 μm and 60%, respectively.

Lithium cell preparation and electrochemical performance

Swagelok type Li/C–$LiFePO_4$ half-cells were assembled in an argon-filled glove box where O_2 and H_2O levels were kept bellow 0.1 ppm and SF membranes were incorporated as separators (10 mm diameter) soaked in electrolyte solution as represented in ***Figure 5.2.3***.

Metallic lithium (8 mm diameter) was used as anode and the C–$LiFePO_4$ based electrode as cathode (8 mm diameter). Charge-discharge tests were obtained at room temperature in the voltage range from 2.5 to 4.2 V at current rates from C/5 to 2C (C = 170 $mAh \cdot g^{-1}$) using a Biologic VMP3 instrument.

The electrical properties of the Li/C–LiFePO4 half-cells were measured by electrochemical impedance spectroscopy (EIS) with a Biologic VMP3 instrument, in the frequency range from 10 mHz to 1 MHz, with an amplitude of 10 mV AC voltage signal.

Figure 5.2. 3. Schematic representation of the Swagelok cell type and its components.

5.2.2. RESULTS AND DISCUSSION

Membranes morphological parameters

Battery separators performance is strongly dependent on membranes morphological parameters such as pore size, thickness, porosity and pores interconnectivity[100]. SEM images allow a precise determination of membranes morphology and enable the determination of pores dimensions and membranes thickness. SF membranes cross section, up surface and down surface were evaluated and are summarized in ***Figure 5.2.4***.

As can be observed in cross section SEM images, in contrast with the flat and non-porous morphology of SF films obtained from solvent casting [39], those membranes obtained by salt leaching process result in structures with a well-defined porous morphology. In agreement with the used salt crystal sizes, the pores average dimensions decrease with salt size decrease, thus SF 250-106 μm membrane presents the biggest porous size, followed by SF 106-38 μm membrane and SF 38-22 μm membrane. The observed pores show a wide distribution of sizes and forms as the observed pores represent a single section of the irregular pores. The complete cross section images show the uniform pores distribution and the constant thickness of membranes, which confirms the effectiveness of the methodology to produce porous SF membranes. Even when the same amount of salt was used for the preparation of the membranes, a visible variation of thickness can be observed. Thus, SF 250-160 μm, SF 160-38 μm and SF 38-22 μm membranes present a thickness of 330, 390 and 445 μm. This effect is due to the increasing number of pores existing in the same matrix with decreasing salt average size. Each pore corresponds with a salt particle which is

completely surrounded by SF. Both surfaces (upper and lower) present a porous morphology, nevertheless due to the solvent evaporation method each surface are slightly different. The lower surface was in contact with the petri dishes, resulting in a flat and less porous surface compared with the upper face. However, the obtained pore sizes will provide enough space for the electrolyte adsorption ensuring the fast lithium-ion percolation through the separator while preventing short-circuit and self-discharge.

Mercury intrusion porosimetry (BET) was used in order to determine the total porosity and the surface area of the SF membranes. As expected, the results confirm that the total porosity is quite similar for all samples, unless the SF 250-106 μm that presents the highest total porosity and surface area, while for the SF 106-38 μm and SF 38-22 μm the values decrease (***Table 5.2.1***).

Table 5.2.1. Total porosity (%) and surface area (m2•g−1) of the SF 250-106 μm, SF 106-38 μm and SF 38-22 μm porous samples.

	Total Porosity (%)	*BET ($m^2 \cdot g^{-1}$)*
SF 38-22 μm	*80,67*	*54,50*
SF 106-38 μm	*82,55*	*66,40*
SF 250-106 μm	*86,03*	*69,74*

Membranes physical-chemical characterization

The SF chains arrangements can show different conformations depending on the processing method and conditions. To evaluate these conformations a FTIR-ATR spectra analysis was performed (***Figure 5.2.5a***). The main protein secondary polymorph crystalline structures of SF are silk I, II and III[101]. Each one of these crystalline structures represent: silk I – metastable state between α-helix and the β-sheet partially ordered structure; silk II – antiparallel β-sheet structure; silk III – formed at air-liquid interfaces. Silk II is the most stable structure and is typically present in pristine silk, typically leading to a random conformation in the SF regeneration[102].

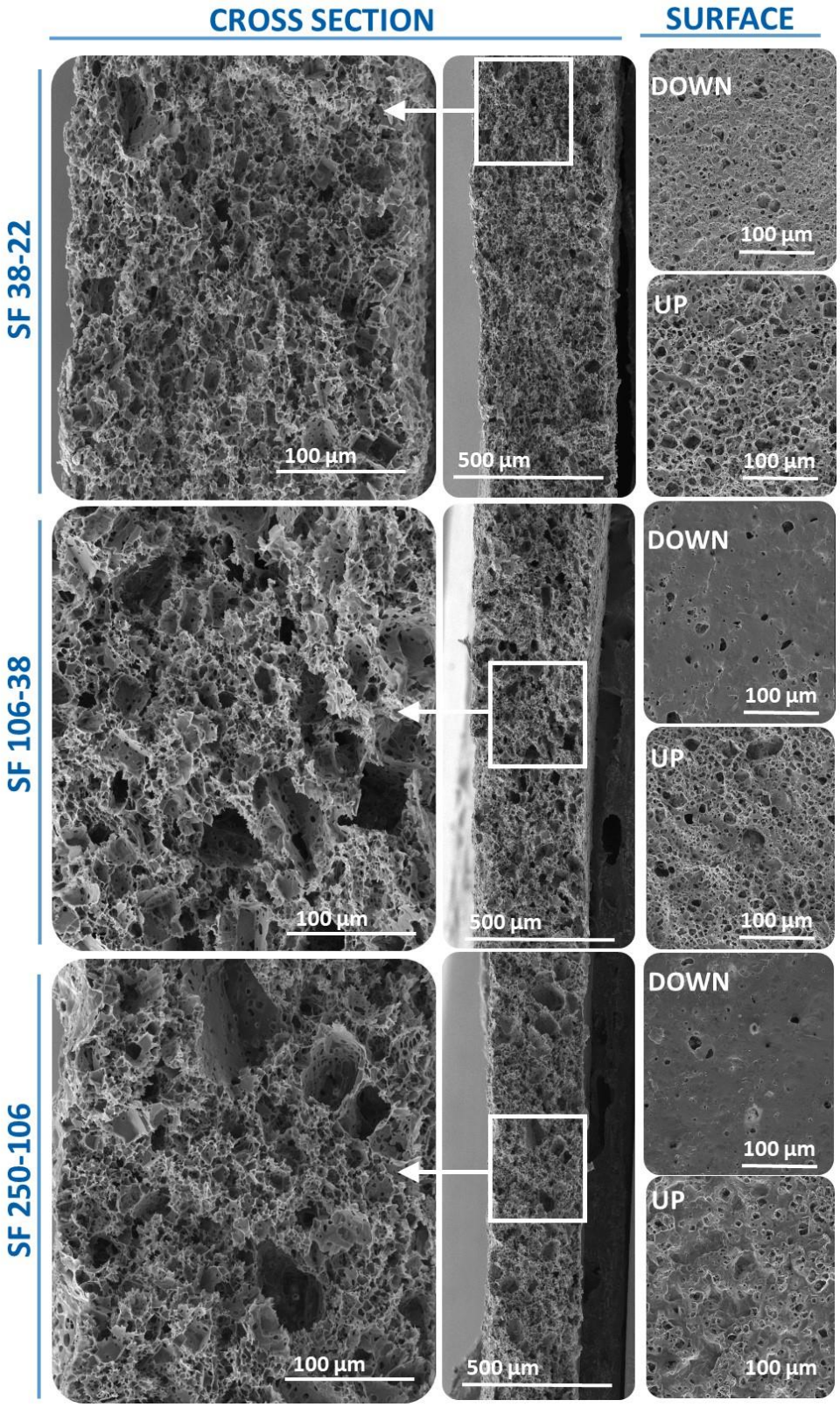

Figure 5.2. 4. *SEM micrographs cross section, up surface and down surface of a) SF 250-106 µm, b) SF 106-38 µm and c) SF 38-22 µm porous membranes.*

The amide I band is characteristic of the SF secondary structure, the stretching vibration of carbonyl group being very sensitive to the specificity and magnitude of the formed hydrogen bonds. According to this, the deconvolution of the amide I band (***Figure 5.2.5b***) was performed in all samples. Five conformations can be found in the amide I at different frequency ranges: turn (T, 1696-1663 cm^{-1}), α-helices (A, 1662-1656 cm^{-1}), random coil (RC, 1655-1638 cm^{-1}), β-sheet (B, 1637-1616 cm^{-1} and 1705-1695 cm^{-1}) and side chain (SC, 1615-1605 cm^{-1})[103]. According to the obtained results, the SF film presents 49.3% of β-sheet and with the inclusion of the salt (38-22 μm), the percentage keeps almost the same (48.0%). Increasing of the salt size, 106–38 and 250-106 μm, the β-sheet percentage increases to 65.1% and 65.9%, respectively. The results confirm that the pore size increase based on the inclusion of larger salt sizes leads to an increase in the β-sheet percentage with respect to SF films, fact which is attributed to the influence in the crystallization process based on surface interactions between the filler and the crystallizing SF. It is to notice that larger filler size also corresponds to a larger surface area (***Table 5.2.1***). It is also observed that the β-sheet percentage within the SF porous membranes is higher than the one obtained by those porous structures obtained from LiBr solutions[90]. The SF films display a profile of the amide I that contains 20.1% of SC, 9.8% of A, 10.3% of T and 10.5% of RC. With the addition of the salts 38-22 μm, the T (8.6%) and A (11.9%) content are maintained almost with the same percentage, but the RC increases to 19.0% and the SC decreases to 12.4%. Increasing the salt size to 106-38 μm, leads to a considerable decrease of the RC (7.0%), the T (11.9%), A (8.2%) and SC (7.7%) keeping almost with the same percentage. Finally, SF 250-106 leads to a situation in which all the conformations present almost the same values T (10.8%), A (8.2%), RC (6.5%) and SC (8.7%). Thus, it is concluded that the inclusion of the salt with different sizes and the corresponding modifications in the crystallization conditions based on the different surface area (***Table 5.2.1***), leads to variations in the SF conformations content present in each sample[104].

Thermal degradation and thermal transitions of SF porous membranes were studied by TGA and DSC techniques, respectively, and presented in ***Figure 5.2.5c and d***. Due to the identical thermal behaviour of the obtained SF membranes, SF 250–106 is presented as representative.

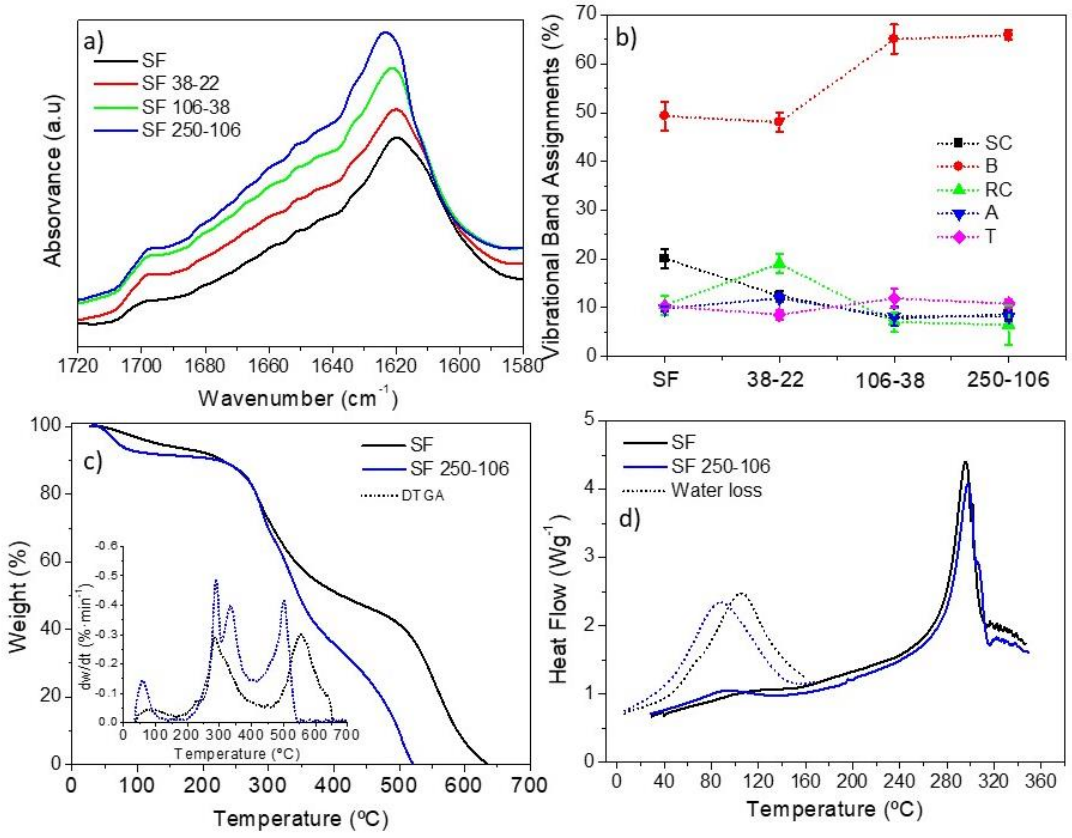

Figure 5.2. 5. *SF film and SF membranes a) FTIR spectra, b) vibrational assignment of the different conformations of the silk amide I band, c) TGA (insert figure represent the DTGA) and d) DSC thermographs.*

The thermal degradation of neat SF occurs in three main stages (***Figure 5.2.5c***). The first stage until 150 °C is related to solvent removal (water + solvent), the second degradation stage ranges from 200 °C to 270 °C and corresponds to the breakdown of side chain groups of amino acid residues as well as the cleavage of peptide bonds. The final degradation step, observed above 550 °C, is related with the combustion of the remaining organic compounds. The induced porosity by salt leaching triggers slight changes in SF thermal degradation process. As it can be observed, the first degradation peak, related with the removal of the solvent match in temperature with the one observed in the films. However, the intensity of the degradation increases, showing the enhanced ability of the porous membranes to hold back solvents or to absorb humidity from the ambient. The starting point of the second degradation stage of SF membranes also remains constant at 200 °C with respect to the one of the films, being also in the same temperature range of separator membranes with excellent thermal stability and well above commonly used separators based on polyolefin[105].

Around 300 °C SF membranes degradation process starts to accelerate. This effect remains during whole degradation process. This expected effect is attributed to the chaotropic effect of salt over the SF structure[106]. During the salt leaching process, salt crystals experience a slight dissociation process, which liberate free ions to de solution. Before solvent evaporation, these charged ions are able to interact with the still dissolved SF chains and produce small breaks into molecular chain. As a consequence, the more accessible side chain groups of amino acid residues as well as peptide bonds degrade more easily[107].

DSC curves (***Figure 5.2.5d***) reveal that, as observed in the thermal degradation process, the induced porosity into the SF membranes slightly affects the thermal transitions of the membranes. During the first thermal annealing, and in agreement with the thermal degradation results, neat SF shows an endothermic peak between 75 and 150 °C attributable to solvent evaporation. During the second annealing process, the obtained peaks suggest the almost total solvents elimination[108]. No thermal transitions are observable until 260 °C, which is related to the thermal degradation. The existence of the pores in the SF membranes just affects the endothermic peak observed during the first annealing, which is due to the increased surface area, as previously indicated. Thermal results confirm that no changes will occur during battery performance during the work temperatures range and even under uncontrolled heating.

Mechanical properties of the different samples were evaluated in order to verify the influence of the porosity in the mechanical properties of SF. From the stress-strain curves (***Figure 5.2.6a***), ultimate tensile strength, elongation at break (ε_B) and Young's modulus (E) were calculated (***Figure 5.2.6b***).

Figure 5.2.6. SF is composed by crystalized β-sheet nodes linked by amorphous domains and during the first elongation stages, amorphous domains unravel, storing the loaded force and giving to the structure elastic properties[46]. When linkers are completely stretched, the force happens to be supported by nodes, which no elongate[109]. H-bond that bonds β-sheets ordered structures are much weaker than the covalent forces that maintain the peptide chain connected. As a consequence, when loaded strength overpass the supported force by β-sheets the structure breaks. Nevertheless, the interconnected structure gives to the SF additional mechanical strength. After the individual β-sheets break, the loaded force is transmitted to the surrounding nodes along the cross-section.

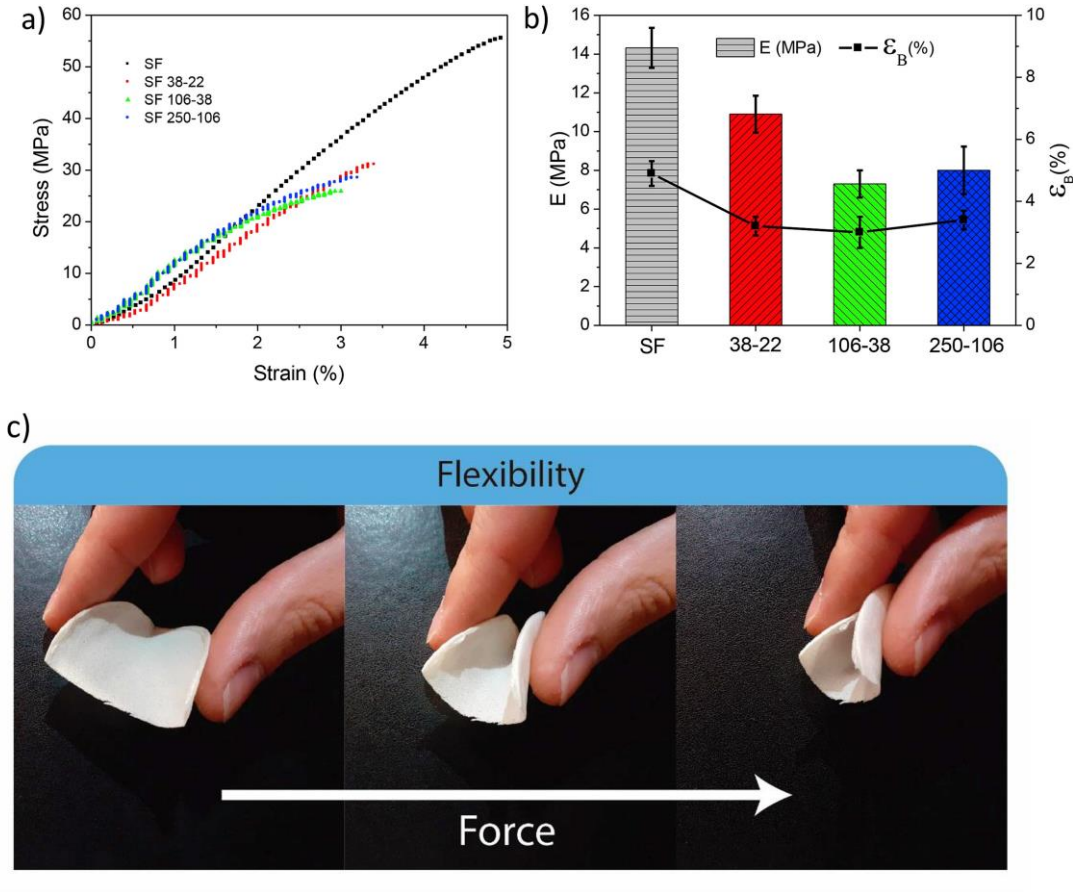

Figure 5.2. 6. *a) Representative stress-strain plots, b) Young's modulus and elongation at break (εB), for the SF film and the SF samples with different porosities and c) Bending flexibility of a SF membrane with 106–38 μm of pore size under compressive force.*

As consequence, mayor amorphous composition gives to the SF mayor elastic properties and mayor crystalline structure gives higher loading strength abilities. Thus, and related with the FTIR results (***Figure 5.2.5b***), the highly ordered structure of SF leads to fully reversible linear viscoelastic behaviour at low loading forces due to linkers elongation followed by brittle break due to the β-sheet nodes breaking process (***Figure 5.2.6a***). This advantageous secondary organization leads to loading stress up to 55 MPa and high elastic modulus. The same mechanical behaviour is observed for SF membranes even their break becomes at lower loaded forces due to the decreased SF content by section. The effect of the porosity in the mechanical properties is higher than the effect of the variations in the secondary structure. As a consequence, the existence of the pores reduces SF loading stress and elongation at break equally in all the porous membranes, independently of the average pore size. Despite of this reduction, the forces involved in battery assembly[110] (1 MPa) are lower

than the elongation at break results, showing that these samples can be applied as separators in batteries systems. It is also to notice that the sample show the required mechanical flexibility, as shown in ***Figure 5.2.6c*** for the SF membrane with 106–38 μm pore size.

Contact angle, uptake, ionic conductivity value and impedance behaviour

The contact angle was measured in order to evaluate the wettability of the membranes not only with water but also with the electrolyte solution. These measurements are essential to understand the surface characteristic of the samples. The contact angle between water and the prepared samples is illustrated in ***Figure 5.2.7a***. The results show that the water contact angle between with the SF film surface is variable over time. In the first moments after water drop, the contact angle between SF and water is near 90° (85 ± 4). This behaviour reveals a competition between the tendency of water to stick to itself[111] and to the SF surface as a result of the dual composition of SF based on hydrophobic domains of repetitive Gly-Ala-Gly-Ala-Gly-X (where X can be Ser or Tyr) hexapeptide sequence and non-repetitive hydrophilic domains[32]. Salt leaching process increases the amount of ordered hydrophobic domains in SF (see FTIR results, ***Figure 5.2.5b***). As a consequence, the trend of water to stick to the SF is reduced, increasing the formed contact angle between SF and water. Hydrophobic behaviour is also promoted by the increased surface roughness of SF membranes compared with SF films[111]. As time increases, the contact angle between water and the different samples reduces to 0° due to the water absorption induced by the polar peptides of SF. This behaviour is more noticeable in the measurements of the contact angle between electrolyte and SF. The results show that due to the mayor interactions between SF and the electrolyte solvents (ethylene carbonate and dimethyl carbonate) the samples are instantly fully wetted giving a contact angle of 0°. Comparing with other membranes as Celgard 2325, PP and PE with 52.0, 54.0 and 49.8° of EC/DMC LiPF6 electrolyte contact angles[112], respectively, the prepared SF membranes show outstanding electrolyte wettability. The good electrolyte wettability with the membrane results in an increase of the lithium ion mobility and diffusion through the membrane, by the pathways created inside the membrane[113].

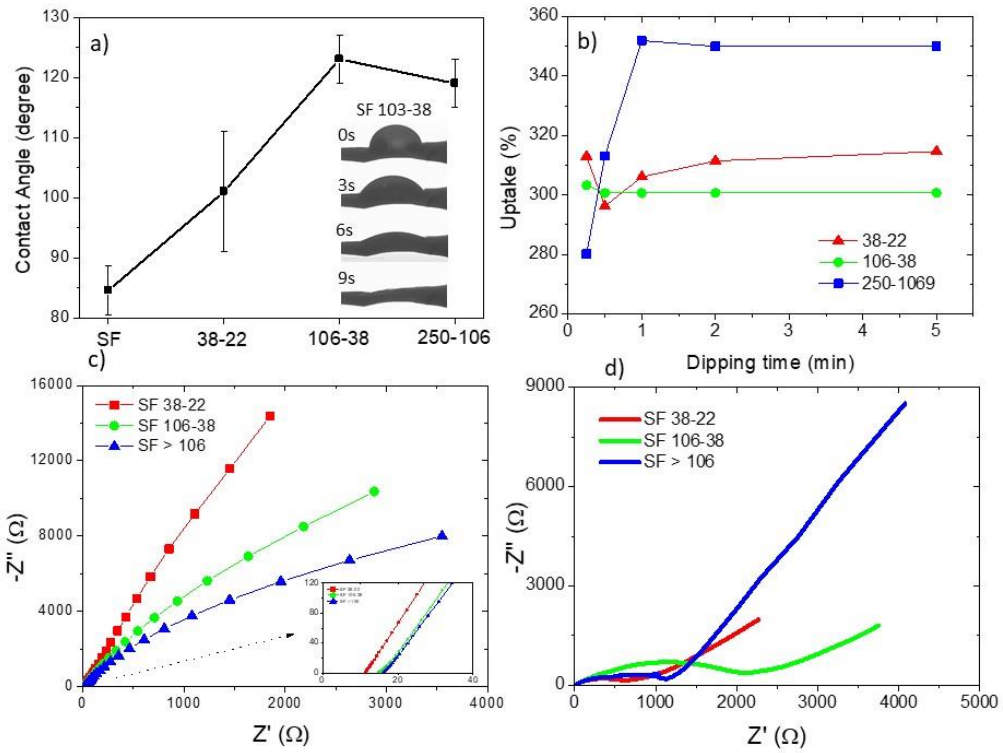

Figure 5.2. 7. *a) Water contact angle, b) electrolyte uptake value as a function of time and c) Nyquist plot for the different membrane separators. d) Electrochemical impedance spectroscopy of the half-cell batteries with the different separators before cycling.*

Figure 5.2.7b shows the electrolyte uptake measurements for the samples with porous structure (calculated from ***equation 5.2.1***). The porosity is an essential factor in the performance of the battery separators since it allows the lithium ion mobility between the cathode and the anode. Comparing the three SF porous samples results it is possible to conclude that the samples with higher salt size (SF 250-106 μm) leads to a higher electrolyte uptake (350%, after 5 min) than the other samples. The SF 38-22 μm and the SF 106-38 μm samples present almost the same uptake percentage after 5 min, 315 and 301%, respectively. The high electrolyte uptake percentage of these samples compared with the conventional separator Celgard 2500 (125%)[114], allows higher lithium ion transport pathways guaranteeing better electrochemical performance of the battery.

Electrochemical impedance spectroscopy (EIS) was performed for membranes previously soaked in the electrolyte and the corresponding results are presented in ***Figure 5.2.7c***. The results show the presence of the typical behaviour of electrolyte/electrode double layer capacitance due to the observed characteristic straight line. The interception of the high

frequency value of the Nyquist plot with the Z′ gives the bulk resistance of the membranes and by ***equation 5.2.2*** the ionic conductivity (σi) can be obtained. Tortuosity (τ) and MacMullin number (NM) of each sample were calculated by applying ***equations 5.2.3 and 5.2.4***, respectively. The obtained data of ionic conductivity, tortuosity and MacMullin number were summarized in ***Table 5.2.2***. The results show that the ionic conductivity is almost the same for all samples being the SF 38-22 μm the sample with highest ionic conductivity (2.5 $mS \cdot cm^{-1}$). The ionic conductivity is higher than that reported in previous works[90] where SF membranes present ionic conductivity of 1 $mS \cdot cm^{-1}$, demonstrating that the microstructure and β-sheet percentage of SF membranes which can be controlled by salt leaching solvent casting method directly affect the ionic conductivity. The ionic conductivity value obtained in this work demonstrates being suitable for lithium ion battery systems that require a minimum of 10^{-1} $mS \cdot cm^{-1}$ [115]. The tortuosity and the MacMullin number also show values compatible with separator membranes leading to good battery performance[116].

Table 5.2.2. Ion conductivity, tortuosity and MacMullin number calculated for the SF porous membranes.

Samples	$\sigma_i \pm 0.3$ $mS \cdot cm^{-1}$	$\tau \pm 0.2$	$N_M \pm 5\%$
SF 38-22 μm	*2.5*	*3.3*	*4.0*
SF 106-38 μm	*1.9*	*4.4*	*5.3*
SF 250-106 μm	*2.2*	*4.0*	*4.6*

Impedance measurements of the SF membranes in half-cells, before cycling (***Figure 5.2.7d***), were performed to study the interfacial properties between the separator and the cathode. The Nyquist plot exhibit a semicircle in the high-medium frequency region and a linear at a low frequency region. The semicircle corresponds to the overall resistance, which is due to the ohmic, contact film and charge-transfer reaction resistances. The linear region designates the lithium ion diffusion in the cathode active material. The different SF membranes present overall resistances of 604, 2037 and 1134 Ω for SF 38-22 μm, SF 106-38 μm and SF 250-106 μm, respectively, the results indicating the formation and stabilization of the solid electrolyte interface (SEI) layer.

Battery performance

In order to evaluate the membranes performance as separator in lithium ion batteries, half-cells with the SF porous membranes were fabricated and the results are shown in ***Figure 5.2.8***. Charge-discharge studies at different C rates (C/8, C/5, C/2, C and 2C) and charge-

discharge cycles (55 cycles) at the same C rate were carried out at room temperature from 2.5 to 4.2 V. ***Figure 5.2.8a*** presents the fifth charge/discharge curve profiles at the studied C rates for the SF 38-22 μm membrane sample (all the samples present the same type of curve profile). The curves profiles are characterized by two voltages, one for the charge and other for the discharge. The charge is originated from the lithium removal and the discharge from the lithium insertion, phenomenon that occurs due to redox reactions Fe^{2+}/Fe^{3+} in the C–LiFePO4 spinel, for all C rates[117]. It is observed a new plateau in the discharge curves at high scan rate above C that is explained by the volume change of the grain induced by the phase transformation between $LiFePO_4$ and $FePO_4$ [118]. Also, it is possible to verify that the cycling profile decreases with the increase of the C rate, excluding at C/8 that is slight lower than the C/5. This difference in capacity at the C/8 rate is explained by the ohmic polarization effect and by the formation of SEI at the first cycles. The discharge capacity values for the SF 38-22 μm membrane were 61.5, 94.9, 109.5, 122.0 and 119.9 $mAh \cdot g^{-1}$ at 2C, C, C/2, C/5 and C/8 rates, respectively. The obtained results present excellent electrochemical values at C rates above C/2. ***Figure 5.2.8b*** presents the fifth charge/discharge curve at 2C and C/8 rates for all the three samples. The obtained voltage profile is very similar for all the samples. It was verified a small over potential in the SF 250-106 μm sample (the charge capacity is higher than the discharge capacity). At both 2C and C/8 rates the sample with the highest charge/discharge capacity is the SF 250-106 μm (discharge capacities of 89.3 and 131.3 $mAh \cdot g^{-1}$, for 2C and C/8 respectively). At 2C rate the SF 106-38 μm sample shows higher charge/discharge capacity value than SF 38–22 (discharge capacities of 64.1 and 61.6 $mAh \cdot g^{-1}$, for SF 106–38 and SF 38–22 respectively). Otherwise, at C/8 rate, the SF 38-22 μm sample shows higher charge/discharge capacity value than SF 106–38. In this rate, the discharge capacity value is 111.3 and 119.9 $mAh \cdot g^{-1}$, for SF 106-38 μm and SF 38-22 μm, respectively. Also, the discharge rate performance of the samples at the different rates from C/8 to 2C were evaluated (***Figure 5.2.8c***). It is observed that the SF 250-106 μm sample shows the highest discharge capacity value verified for all C-rates followed by the SF 38-22 μm and SF 106-38 μm (excepting at 2C that SF 106-38 μm is higher than SF 38-22 μm). The membranes porosity, the uptake percentage and the β-sheet percentage characteristics of the samples are the main responsible for the charge/discharge capacity modification of the prepared batteries. The high porosity 250-106 μm, the uptake percentage of 350% and the β-sheet percentage of 65.9% lead to an enhancement of the electrochemical results. The high porosity and uptake percentage in the membrane leads to a higher number of pathways for

the lithium ion transport, decreasing also the resistance[119]. Also, the high β-sheet percentage is correlated with the good electrochemical performance through the electroactive properties and polarity of this silk conformation[120]. ***Figure 5.2.8d*** shows the capacity retention of the discharge process of the batteries with the SF membranes, normalized to the C/8 rate, for the studied C-rates. The decrease of the capacity retention with the C-rate is observed and is attributed to the lithium diffusion phenomenon between the cathode and the separator[121]. At 2C, the SF 250-106 sample increases its capacity retention percentage with respect to the remainder samples, due to its high porosity that allows higher lithium diffusion[122].

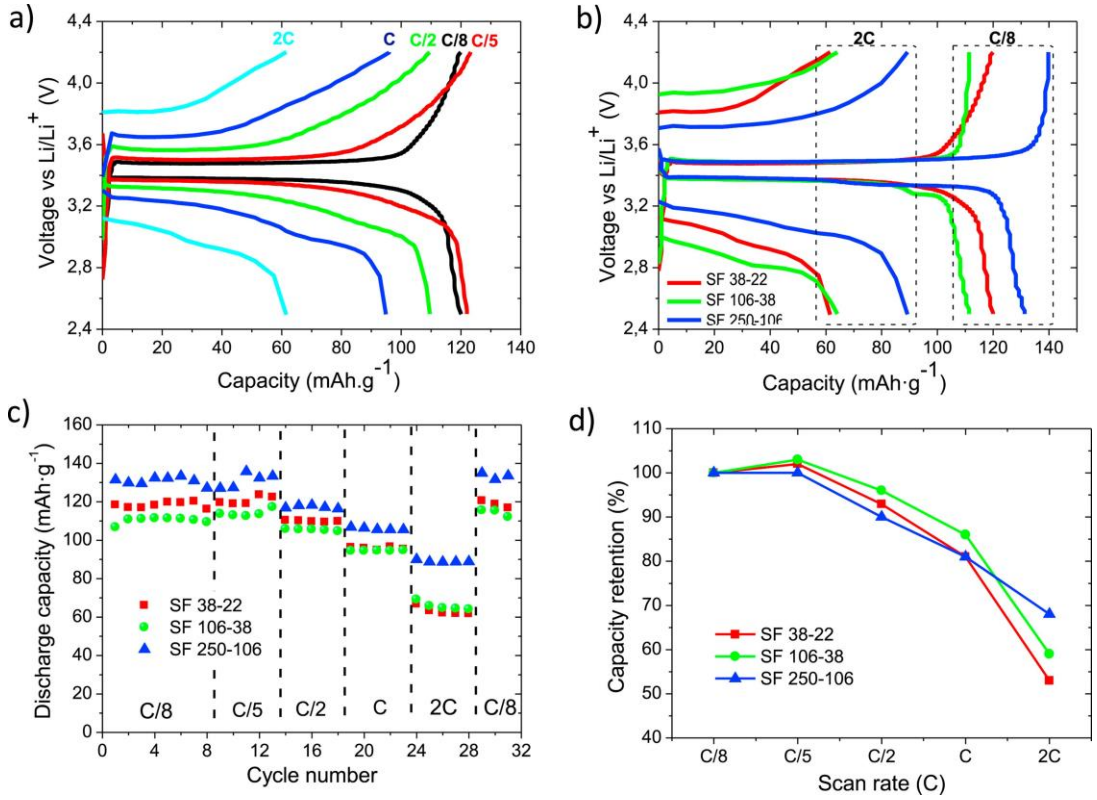

Figure 5.2. 8. *a) Charge/discharge C-rates profiles for the SF 38-22 μm membrane battery. b) fifth charge/discharge curve 2C and C/8 rate, c) rate performance as a function of the cycle number and d) capacity retention for all the membranes in half-cell batteries.*

Figure 5.2.9. The cycle performance and the coulombic efficiency percentage of the half-cell batteries prepared with the different membranes as separator were studied and the results are shown in ***Figure 5.2.9a***. In this analysis, fifty-five cycles at C and 2C were performed and the discharge capacity obtained. After the 55 cycles, the discharge capacity at C was 89.2, 84.7 and 78.5 $mAh \cdot g^{-1}$ and at 2C was 56.9, 38.0 and 22.4 $mAh \cdot g^{-1}$, for the SF 250-106 μm, SF 38-22 μm and SF 106-28 μm membranes in the half-cells, respectively. The capacity

retention obtained from the cycle performance were 86, 92 and 91% at C rate and 85, 79 and 84% at 2C rate, for the SF 250-106 μm, SF 38-22 μm and SF 106-28 μm membranes in the half-cells, respectively. The good cycling stability and capacity retention of the membranes is attributed to the higher uptake percentage value that correspond to a good swelling property of the membranes and the high ionic conductivity. Also, all the membranes present a coulombic efficiency percentage around 100%, demonstrating to the good active species reversibility of the process during the charge and discharge. ***Figure 5.2.9b*** shows the impedance measurements of the half-cells with the SF membranes after cycling. The obtained overall resistances for SF 38-22 μm, SF 106-38 μm and SF 250-106 μm were 937.1, 2200.0 and 452.4 Ω, respectively. Comparing the previously obtained overall resistances before cycling (***Figure 5.2.7b***) and the after cycling, it is verified that the resistance increases in the half-cells after cycling, excepting in the SF 250-106 μm membrane where a stable SEI layer facilitates the lithium ion transport through the interface between the cathode and the separator. This result explains the better performance of the SF 250-106 μm, comparing with the other samples. In the other two samples, with lower surface area, the SEI layer reduce the lithium-ion diffusion after the cycling process, resulting a lower battery performance.

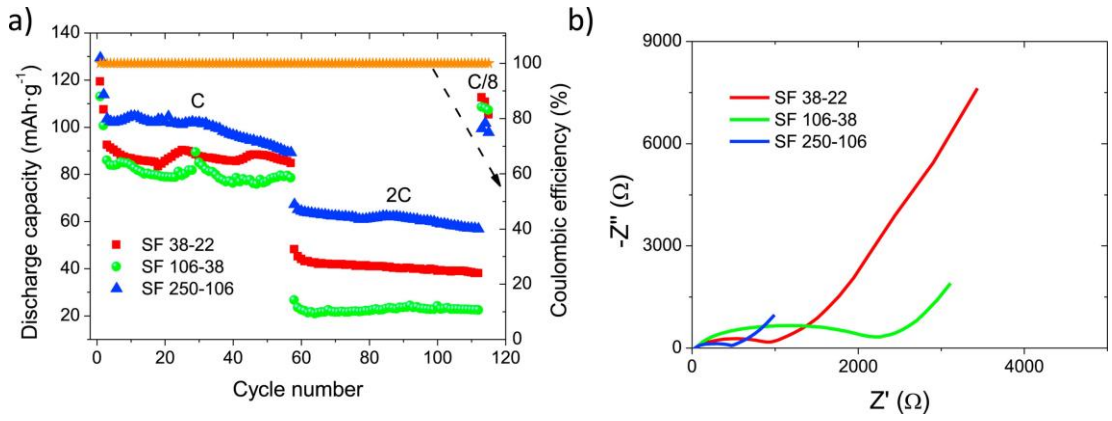

Figure 5.2. 9. *a) Capacity and coulombic efficiency at C and 2C rates and b) electrochemical impedance spectroscopy after cycling, of the half-cell batteries prepared with the different separator membranes*

The obtained results can be compared with the ones obtained for different natural materials used as separators in lithium-ion batteries, as shown in ***Table 5.2.3***.

The importance of the use of natural materials in the area of energy storage in general and in lithium-ion batteries in particular is not just promising but also needed in the scope of developing sustainable technologies with reduced environmental impact. Materials such as

cellulose (from different fonts), eggshell, chitin, lignin and silk have been used as lithium-ion separator membranes as shown in ***Table 5.2.3***. The present work demonstrates that SF is a promising natural material, competitive with the aforementioned ones, to be used as separator due to their availability, electrochemical performance, ionic conductivity, chemical and thermal stability and easy porous control that allows to tune separator characteristics for improving battery performance.

Table 5.2.3. Representative magnitudes of separator membranes from different natural polymers used in lithium-ion batteries.

Polymer	*Electrolyte Uptake / %*	*Porosity and Pore size / % and μm*	*σi / $mS.cm^{-1}$*	*Discharge capacity at 0.2C / $mAh.g^{-1}$*	*Ref*
Cellulose nanofibre paper-derived - CNP (95/5 - IPA/water)	-	-, <0.1	0.75	$LiCoO_2$ ≈ 138	123
Cross-linked cellulose membranes	542	-, -	6.34	NCM523 – 145	124
Cellulose pulp	275	70, -	108	$LiCoO_2$ – ≈ 130	125
Cellulose fibers from bleached softwood pulp (4 sheets)	425	73, -	1.5	Full battery $LiFePO_4$ ≈ 120	126
Cellulose-based composite nonwoven	270	70, 0.1-0.2	2	$LiCoO_2$ ≈ 129	127
Flexible egg shell membranes (ESM)	81	60, 1-5	0.1	$LiFePO_4$ - ≈ 75	128
Chitin nanofibres	242	40, 0.010-0.150	0.064	$LiFePO_4$ – 157 at 0.5C	129
Lignin	230	- , -	3.73	$LiFePO_4$ – 165	129
Rice paper	-	-, -	3 × celgard	$LiFePO_4$ ≈ 140 $LiCoO_2$ ≈ 130 $LiMn_2O_4$ ≈ 110	130
Bombyx mori Silkworm Cocoon	400	85, -	0.3	$LiFePO_4$ ≈ 131	131
Silk Fibroin prepared by lyophilization	1111	60, 150	1	$LiFePO_4$ ≈ 107	90
This work (SF 250-106)	350	90, 250-106	2.2	$LiFePO_4$ – 133.3	-

5.2.3. CONCLUSIONS

The simple and environmental friendlier approach is presented to prepare silk fibroin (SF) based separator membranes with tailored pore size for lithium-ion batteries, an increasingly relevant research field for improving suitability and decrease the environmental impact of

energy storage systems. Different NaCl size salts (38–22, 38–106, and 250-106 μm) were used to obtain SF membranes by solvent evaporation with different average pore sizes. It is shown that the processing method does not change significantly the thermal and mechanical behavior of the membranes concerning the SF films. On the other hand, the electrolyte uptake percentage is the highest for the SF 250-106 μm membranes (350%, after 5 min) due to their higher pore size, leading to an ionic conductivity of 2.2 ± 0.3 $mS \cdot cm^{-1}$, suitable for battery applications. The relationship between the β-sheet conformation percentage existing in the membrane and the pore size is evident, the β-sheet conformation content increasing with the average pore size. For battery performance, the discharge capacity of half-cells prepared with SF 250-106 μm separators is 89.3 and 131.3 $mAh \cdot g^{-1}$, for 2C and C/8, respectively, good performance when compared both with conventional and other natural materials-based separators. Further, the higher average pore size membranes, SF 250-106 μm, show the lowest overall resistance after cycling, a stable SEI layer facilitating the lithium-ion transport through the interface between the cathode and the separator that decreases the overall resistance. Thus, it is concluded that SF separator membranes with high porosity and tailored average pore size are suitable materials for lithium-ion battery separator membranes based on natural polymers, contributing to the green transition in the energy storage area.

5.3. SILK POROUS STRUCTURES FOR HEAVY METALS ADSORPTION

BASED ON: A. Reizabal et al. Processing Strategies to Obtain Highly Porous Silk Fibroin Structures with Tailored Microstructure and Molecular Characteristics and Their Applicability in Water Remediation J. Hazard. Mater., vol. 403, no. 123675, 2021.

The SF characteristics are defined by the convergence of multiple factors, such as the presence and ratio between crystalline and amorphous domains, their relation into the cross-slinked structure, the crystalline domains organization, and non-folded chains amphiphilic behavior. Accordingly, the controlled modification of the abovementioned characteristics represents an interesting tool to endow SF based materials of specific applicability.

Based on this idea, the present work focuses on establishing different processing strategies to tailor SF microstructure and properties. For that, two dissolving techniques ($CaCl_2/H_2O/EtOH$ ternary and $LiBr/H_2O$ binary solutions), three different processing methods (gelation, lyophilization, and gas foaming)[107] and one post-processing (EtOH treatment) have been used to produce SF based porous structures and tailor their properties. The above described SF processing approaches correspond to a green strategy where water-based solvents with low environmental impact have been used. It is worthy to note that the developed techniques are characterized by low complexity and high availability[132], a strategy that could facilitate their implementation and replication in future investigations. In parallel, the selected processing methods allowed controlling the SF molecular recombination time (i.e., gelation > lyophilization > gas foaming) before their freeze-drying, while the use of EtOH as β-sheets promoter[133], allows even further control of the SF final structure and properties.

To prove the relevance of shaping SF's porous and molecular structures, the processed biomaterials have been tested over the adsorption of highly hazardous arsenic and chromium model pollutants. Heavy metal water pollution is a severe environmental issue since many places worldwide show a natural concentration of these inorganic ions above the legal limits. Indeed, arsenic and chromium exhibit acute toxicity in aqueous environments (e.g., genotoxic, mutagenic, teratogenic, and carcinogenic), are non-biodegradable and long-term persistent, even when present at very low concentrations[134]. Also, their varied chemistry, and their high solubility and mobility, make current technologies inefficient to lower their concentration below the legal limits.

In this regard, one of the most promising technologies to achieve efficient water pollutant removal are composite materials[135], which are based on an active phase on which the pollutant is adsorbed and a non-active structure providing support and mechanical stability. Thus, commonly, the adsorption capacity of a composite system is mainly defined by the active phase's adsorption capacity and the accessibility given by the holding phase, the latter mainly depending on its porosity[136]. Whereas most efforts in this area have been devoted to improving the active phase's efficiency, few investigations have been directed to improve the self-absorption properties of the porous polymer structures. In this context and promoted by the control achieved on SF porous and molecular structures, a proof of concept study centered on bio-based materials applied for adsorption purposes has been carried out. It is to notice that the obtained materials can be further complemented with an active/selective phase to improve its characteristics for polluted waters remediation further.

The central hypothesis of our work is that the adsorption capabilities of SF over metal ions can be tuned just by modifying porous and molecular structure through simple and accessible techniques. This approach does not exclude the possibility to complement the capabilities of the SF materials with other active phases that can endow them with additional pollutant adsorption capacity and affinity. It is worth mentioning that some metal industrial processes, such as the chromium plating industry, led to metal, specifically to Zn, Cd, or Cr high concentrated solutions, with ppm values even higher than those studied in this work[137]. Therefore, the relevance of the SF materials could go beyond solely the water de-pollution purposes. Indeed, their application in industrial output waters could be another interesting application of the developed bio-materials. (***Figure 5.3.1***)

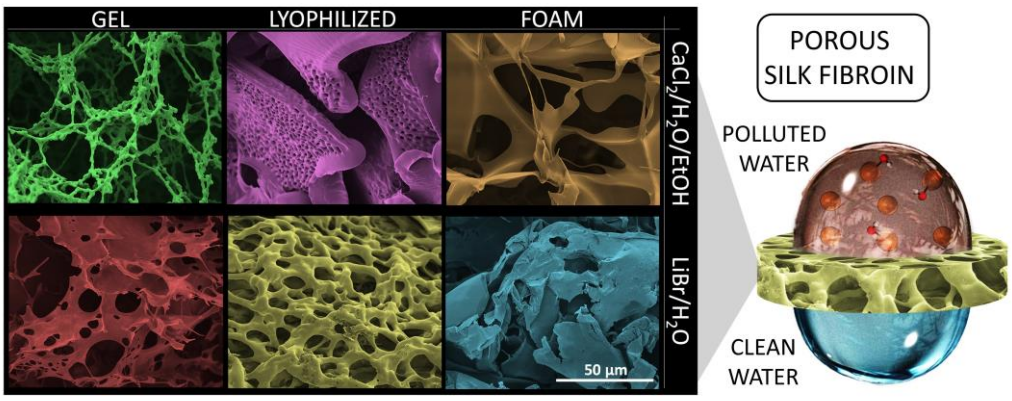

Figure 5.3. 1. *Graphical abstract of SF porous structures and their application for water remediation.*

5.3.1. MATERIALS AND EXPERIMENTAL METHODS

Materials

Silk Fibroin (SF) was extracted from Bombyx mori cocoons, supplied by APPACDM from Castelo Branco (Portugal). Sodium carbonate (Na_2CO_3), calcium chloride ($CaCl_2$) and lithium bromide were purchased from Sigma-Aldrich. Dialysis tubes with a diameter of 3 cm and molecular weight cut-of 3500 Daltons were obtained from Spectrum.

Precursor solution preparation

Porous structures were prepared from aqueous solutions of SF. The first step was the extraction of SF from the *Bombyx mori* Silk cocoons. For this, the cocoons were dry-cleaned and cut into small pieces of about 0.5 cm^2. The pieces were then degummed twice in 3.7 mM Na_2CO_3 aqueous solutions at 80-85 ºC during 10 min in a silk-to-liquid ratio of 1:40 (wt:v). Between first and second degumming the fibres where manually opened to facilitate the process. The resulting SF was immersed three times in consecutive distilled water baths and then rinsed thoroughly. The well-cleaned fibres were finally dried in an oven at 40 ºC for 24 h and then kept in dry until be used.

Afterwards, SF was dissolved by following two different procedures, as a result, two types of aqueous SF solutions will be obtained. The main difference between both procedures was the used solving agent: i) a $CaCl_2$/H2O/EtOH ternary solution 1/8/2 molar in a silk-to-liquid ratio of 1:10 wt.: v and ii) 9.3 M LiBr/H_2O binary solution in a silk-to-liquid ratio of 1:20 wt.: v. In both cases, SF was dissolved for 2 h at 60 ºC under magnetic stirring. The obtained solutions were dialyzed against distilled water in a 3500 Da cut-off cellulose cassette, with 3 water changes per day and until constant dialyzed water conductivity was achieved. The resultant SF aqueous solution with a concentration around 0.1 g/ml was used directly for the next steps. The SF aqueous solutions concentration was measured by drying a controlled solution volume and weighing the residues.

Samples preparation

As schematically represented in ***Figure 5.3.2***, SF porous structures were prepared by lyophilisation, but aqueous solutions were differently treated before this final step.

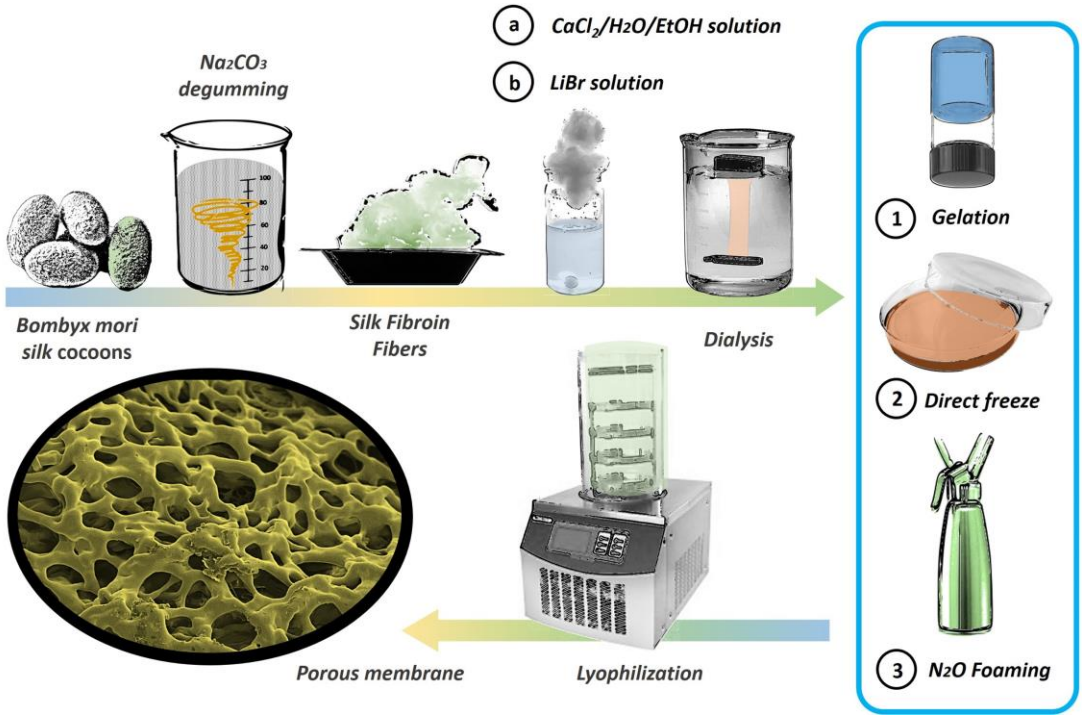

Figure 5.3. 2. *Schematic representation of the preparation procedures of the SF structures.*

The methods involve: i) the gelation of aqueous solution, placing it statically at 25 ºC for 24 h; ii) the use of the aqueous solution directly and iii) foaming aqueous solution by using a whip siphon, nitrous oxide (N_2O) as pressure gas and a nozzle of 6 cm long and 1 cm diameter. Gelled and direct samples were frozen at -20 oC during 12h, while foam samples were fast freeze by liquid nitrogen. ***Table 5.3.1*** shows the identification data of the samples, indicating also the dissolving agent, the processing method and the time elapsed since the samples are prepared until they completely freeze.

In order to induce the secondary structures conversion to highly stable β-crystals, all of SF structures were treated with EtOH [32]. For this, samples were immersed for 5 s in EtOH and dried for 12 h at room temperature. Samples treated with EtOH will be identified with the EtOH code at the end of the names presented in ***Table 5.3.1***.

Table 5.3.1.*SF porous structures identification and main processing parameters*

Sample	*Dissolving Agent*	*Processing*	*Time (h)*
CaCl-Gel	*$CaCl_2/H_2O/EtOH$*	*gelation + freezing (-20°C) lyophilisation*	*27-28*
CaCl-Lio	*$CaCl_2H_2O/EtOH$*	*freezing (-20°C) + lyophilisation*	*3-4*
CaCl-Foam	*$CaCl_2/H_2O/EtOH$*	*NO_3 foaming + N_2 freezing + lyophilisation*	*0*
LiBr-Gel	*$LiBr/H_2O$*	*gelation + freezing (-20°C) lyophilisation*	*27-28*
LiBr-Lio	*$LiBr/H_2O$*	*freezing (-20°C) + lyophilisation*	*3-4*
LiBr-Foam	*$LiBr/H_2O$*	*NO_3 foaming + N_2 freezing + lyophilisation*	*0*
CaCl-Gel-EtOH	*$CaCl_2/H_2O/EtOH$*	*gelation + freezing (-20°C) lyophilisation + EtOH*	*27-28*
CaCl-Lio-EtOH	*$CaCl_2H_2O/EtOH$*	*freezing (-20°C) + lyophilisation + EtOH*	*3-4*
CaCl-Foam-EtOH	*$CaCl_2/H_2O/EtOH$*	*NO_3 foaming + N_2 freezing + lyophilisation + EtOH*	*0*
LiBr-Gel-EtOH	*$LiBr/H_2O$*	*gelation + freezing (-20°C) lyophilisation + EtOH*	*27-28*
LiBr-Lio-EtOH	*$LiBr/H_2O$*	*freezing (-20°C) + lyophilisation + EtOH*	*3-4*
LiBr-Foam-EtOH	*$LiBr/H_2O$*	*NO_3 foaming + N_2 freezing + lyophilisation + EtOH*	*0*

Characterization techniques

The morphology of the structures was evaluated by scanning electron microscopy (SEM) with a NanoSEM - FEI Nova 200 (FEG/SEM). Prior evaluation, all the samples were coated by a 20 nm gold layer by magnetron sputtering with a Polaron SC502 apparatus.

The SF materials have been fully characterized by mercury porosimetry, FTIR, XRD and DSC. Experimental details are provided in as supplementary information.

The porosity was determined by mercury intrusion porosimetry (MIP) with a Quantachrome Instruments Poremaster-60 GT operating in the pressure range from 10^{-4} MPa to 414 MPa. Samples were degassed in situ at 110 ºC for 12 h prior to the measurements. A contact angle of 140º and a surface tension of 480 dyn•cm-1 for mercury and a pressure equilibration time of 11 s were used. The helium density measurements were performed in a Quantachrome Instruments automatic Micro Ultrapycnometer.

Molecular insights on the different samples were studied by Attenuated Total Reflectance (ATR)/Fourier Transform infrared (FTIR) spectroscopy with a Jasco FT/IR-4100 system from 4000 to 600 cm^{-1} using 64 scans at a resolution of 4 cm^{-1}. The secondary structure was analysed from ATR/FTIR data by following the methodology described in "characterization techniques" apart of 4.1 section. The results were analysed using one way, non-paired ANOVA (analysis of variance) with Tukey test and 5 % of tolerance.

The crystallinity of the SF structures was obtained from X-Ray diffraction measurements using a Philips X'Pert PRO diffractometer with CuKα radiation (λ=1.5406Å) in the range of $5 < 2\theta < 70^{o}$ with a step size of 0.05^{o} and an exposure of 10 s per step.

Thermal stability was measured by a Thermal Gravimetric Analyzer (TGA) TGA/SDTA 851e Metter Toledo apparatus at a heating rate of 10 $°C \cdot min^{-1}$ in the temperature range from 25 to 800 ^{o}C under air flow.

Thermal transitions were analysed with a differential scanning calorimetry (DSC) Mettler Toledo DSC 822e equipment at 10 $°C \cdot min^{-1}$ from 25 to 350 ^{o}C under nitrogen purge (50 $mL \cdot min^{-1}$). In order to remove bonded water, samples were first heated at 140 ^{o}C during 20 min.

Both water uptake and water stability were measured by the same experiment. For that, the weight of SF porous structures immersed in water was measured during consecutive 5 days. Water uptake (U %) was obtained from the relation between absorbed water and initial mass, following the ***equation 5.3.1***.

$$U\ (\%) = \frac{M_s - M_d}{M_d} \times 100 \qquad (5.3.1)$$

where U is the samples water uptake ability (%), Ms is the weight of the swollen sample in equilibrium (g) and M_d is the weight of dried sample (g). The total water uptake was obtained once samples stop absorbing water and show constant mass.

Water stability was measured by following the weight measurements over time, with the maximum water load as reference. Samples degradation was considered when weight loss is observed, while constant weight measurement signalled samples water stability.

Adsorption test

In order to carry out the pollutants adsorption experiments, 20 ppm solutions of metalloids (As^{5+}, As^{3+}) and heavy metals (Cr^{6+} and Cr^{3+}) were prepared, from the following precursor salts: As^{5+} - Na_2HAsO_4 (≥ 98 %), As^{3+} - $NaAsO_2$ (90 %), Cr^{6+} - $K2Cr_2O_7$ (99.8 %) and Cr3+ - $KCrSO_4 \cdot 12H_2$. The solutions pH was adjusted to 4 by adding HCl and NaOH diluted solution. For all the experiments the sample/solution ratio was fixed to 2 $g \cdot L^{-1}$. Thus, 10 mg of silk were added to 5 mL of solution, and mechanically stirred at room temperature for 18 h. Afterwards, silk structures were manually separated from the solution, and the final concentrations of chromium and arsenic were determined by slightly modified diphenylcarbazide[138,139] and heptamolybdate[140] colorimetric methodologies, respectively. Absorbance of the solutions was measured by a Spectronic 20 Genesys UV-Vis spectrophotometer. Triplicate punctual adsorption measurements were performed for all the samples.

5.3.2.. RESULTS

Morphological characterization

SEM images were used to analyse the morphology and pore microstructure of the developed SF structures. Representative images of the six different samples, CaCl-Gel, CaCl-Lio, CaCl-Foam, LiBr-Gel, LiBr-Lio and LiBr-Foam, are presented in ***Figure 5.3.3***. As can be observed, all the samples are characterized by a well-defined porous structure. In addition, the shape of the pores within the structures clearly differs from one another sample, demonstrating the strong effect of the solving agent and the regeneration procedure on the final morphology and structure of SF.

Figures 5.3.3a and h shows the morphology of CaCl2-Gel sample, which is dominated by a highly branched network of fibrils. Each SF-based fibril is formed by elongated structures of 1-2 µm in thickness connected to globular structures of 2-3 µm of diameter. The set forms a bean-like structure with interconnected and continuous pores ranging from 20 µm to 40 µm of diameter.

Both Gel samples were equally processed but with varying the solvent. This change leads to the formation of a completely different microstructure (***Figure 5.3.3d and k***). LiBr-Gels are composed by two-dimensional non-compact sheets, packed in a leaf-like macrostructure with an interconnected continuous pore system. The planar sheets of LiBr-Gel are

characterized by a thickness between 200 - 400 nm with interspersed pores in the 2 µm to 20 µm diameter range, leading to a pore system with two pores levels.

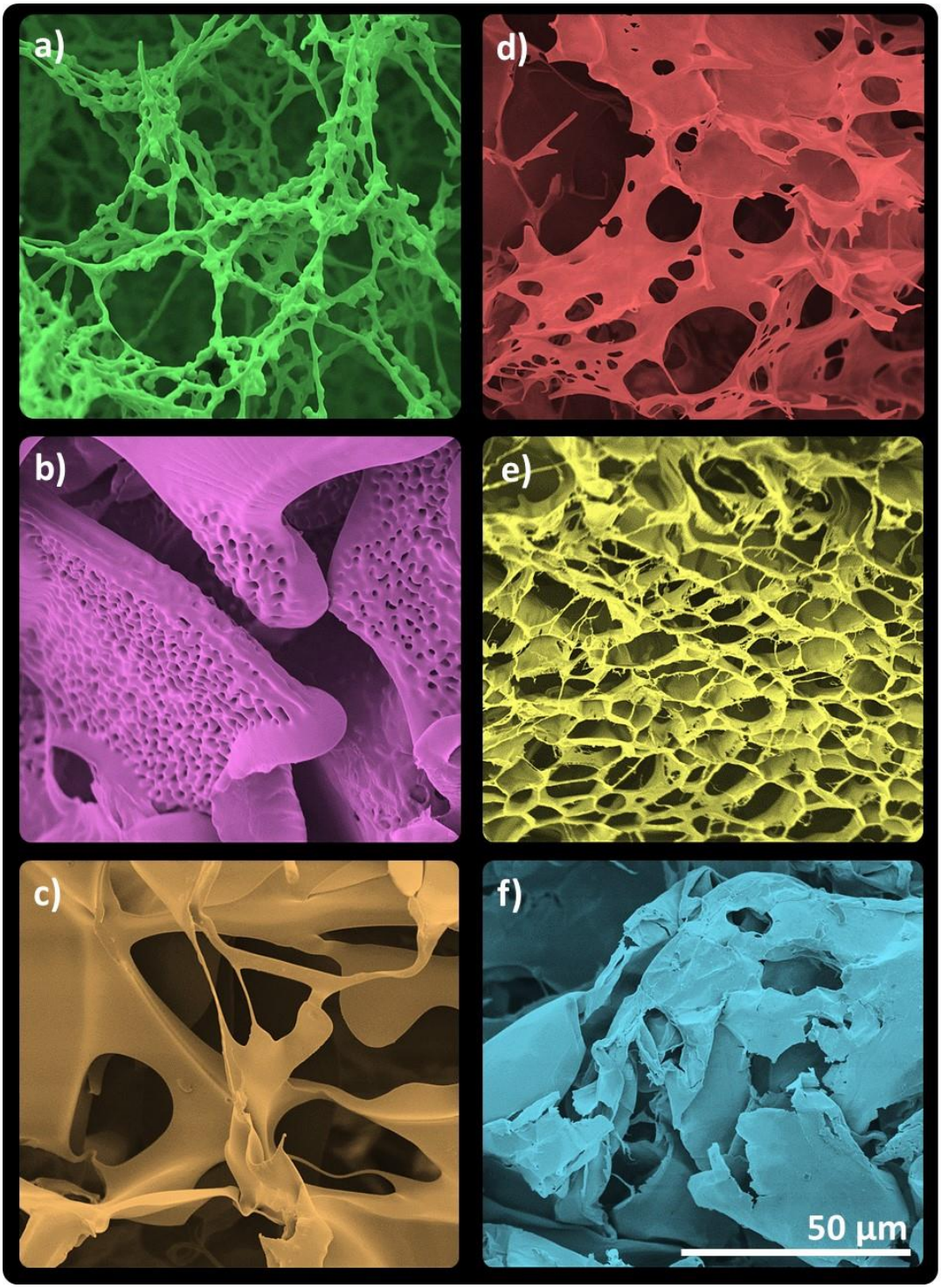

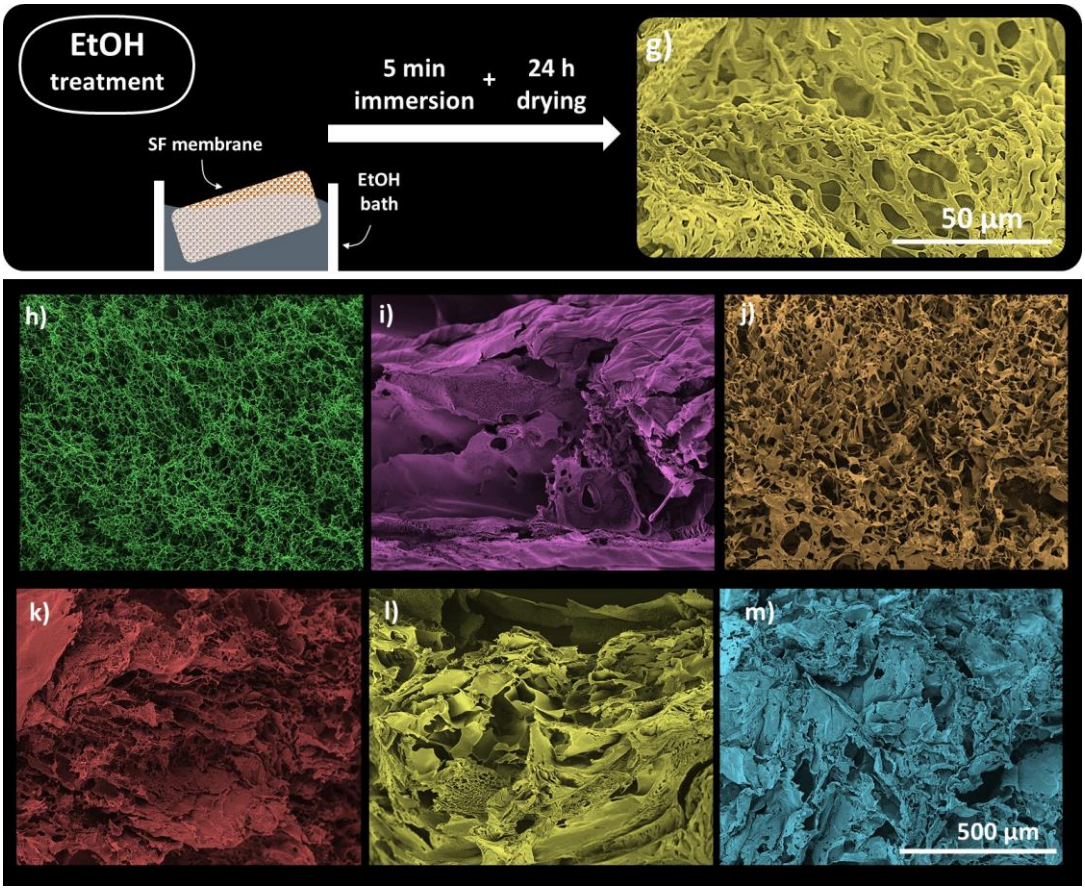

Figure 5.3. 3. *Representative SEM images of the SF porous structures: a·h) CaCl2-Gel b·i) CaCl2-Lio c·j) CaCl2-Foam d·k) LiBr-Gel e·l) LiBr-Lio and f·m) LiBr-Foam. g) LiBr-Lio sample after EtOH treatment. The scale is valid for all images. The colours were added digitally.*

Figures 5.3.3b, I, e and l show the morphology of $CaCl_2$-Lio and LiBr-Lio samples, respectively, both characterized by a leaf-like macrostructure, but different microstructure. The morphology of the CaCl2-Lio sample is formed by wide two-dimensional planar structures of 7-8 µm thickness, interspersed by small and homogeneously distributed pores of 1-2 µm diameter (***Figures 5.3.3b and i***). LiBr-Lio sample on the contrary, is composed by narrow planar structures with a thickness of 1-3 µm that fold in specific locations to form a sponge like/ honeycomb regions with irregular pores of 4-15 µm diameter (***Figures 5.3.3e and l***). In both cases, the existence of two-porosity levels leads to an overall porous structure with highly interconnected cavities.

Regarding the structures obtained by the N_2O foaming method, the morphology of the $CaCl_2$-Foam and LiBr-Foam samples (***Figures 5.3.3c, j, f and m***) also shows a leaf-like

shape macrostructure. The main difference between the two samples is found in the thickness of the flat sheets, varying between 2 μm and 7 μm for CaCl2-Foam and between 300-600 nm for the LiBr-Foam. Contrary to Gel and Lio samples, Foam samples do not show interspersed pores.

The effect of EtOH treatment on the porous SF structures can be observed in ***Figures 5.3.3g*** for the LiBr-Lio structure, being representative for the rest of the structures. After the treatment with EtOH, samples retain their porous structure, but with slight variations in the planar sheets conformation and a certain increase of the pore size.

Further insights on the structural characteristics of the samples were studied after mercury intrusion porosimetry, allowing to obtaining density, surface area and total porosity, as presented in ***Table 5.3.2***.

Table 5.3.2. *Degree of porosity, density and surface area of the different SF-based structures ("-" indicates the lack of measurable data).*

Sample	*Pore size (μm)*	*Total porosity (%)*	*He density (g/cm^3)*	*Surface area (m^2/g)*	*Specific surface area (10^7 m^2/m^3)*
$CaCl_2$-Gel	*20-40*	*94.0*	*1.34*	*71.1*	*4.47*
$CaCl_2$-Lio	*1-2*	*97.8*	*1.31*	*108.8*	*8.31*
$CaCl_2$-Foam	*-*	*94.9*	*1.42*	*45.5*	*3.20*
LiBr-Gel	*2-20*	*94.3*	*1.46*	*86.1*	*5.90*
LiBr-Lio	*4-15*	*93.7*	*1.64*	*59.6*	*3.63*
LiBr-Foam	*-*	*95.9*	*1.44*	*122.8*	*8.53*

Regardless of the preparation procedure, the degree of porosity varies between 94% and 98%, which is significantly higher than the reported porosity values of comparable porous structures based on SF, which generally range between 70% and 90%[141].

The specific surface areas range from 3.2×107 $m^2 \cdot m^{-3}$ to 8.53×107 $m^2 \cdot m^{-3}$, which are also higher than the values obtained for SF non-woven mats, commonly used for the preparation of membranes for environmental remediation[141].

Mercury (Hg) intrusion curves as a function of pore diameter for the different structures were collected in ***Figure 5.3.4***, showing that the intrusion values range between 1 and 300 μm, that indicates that all SF samples can be classified as macro-porous.

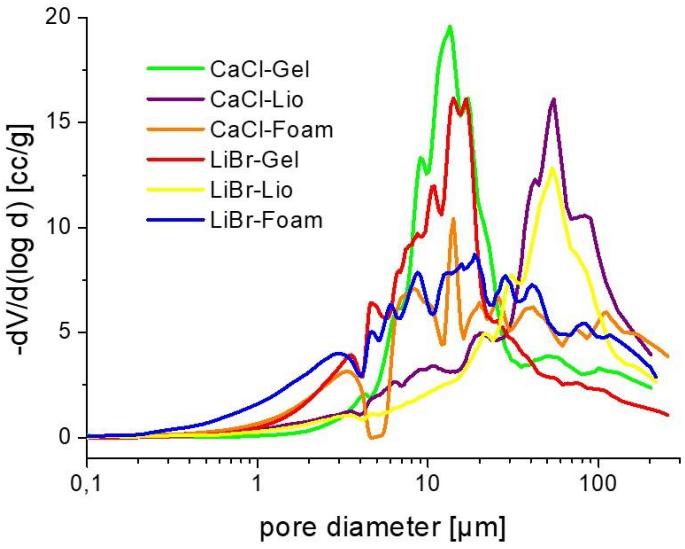

Figure 5.3. 4. *Hg intrusion values as a function of pore size for the different SF porous*

The main contributions to the final porosity differ between the different samples (***Figure 5.3.4***). CaCl2-Gel and LiBr-Gel samples show a pore distribution mainly centred at 13 µm pore diameter. But, CaCl2-Gel shows intrusion signals at 30 µm, while LiBr-Gel shows them in the region above 1 µm. These data suggest that even when the two gel samples are highly dominated by 13 µm diameter pores, there are also relevant contributions of larger pores in the case of CaCl2-Gel and smaller pores in LiBr-Gel, in good agreement with the microstructure observed at the corresponding SEM images (***Figure 5.3.3***).

CaCl2-Lio and LiBr-Lio samples show peaks with a maximum at 54 µm, being also contributions of even larger pores (around 200 µm) in both cases. Thus, the Lio process leads to average larger pore sizes. The slight signal in the region of smaller pore diameters on CaCl2-Lio sample can be related to the secondary pores observed in the SEM images (***Figure 5.3.3b***).

Finally, the intrusion results from CaCl2-Foam and LiBr-Foam samples show a wide and oscillatory signal ranging between 0.8 to 200 µm. This porosity distribution indicates that, in contrast to Gel and Lio samples, with pores size defined at 13 and 200 µm, respectively, the pores of Foam samples are not in a well-defined diameter range.

Molecular and structural conformations

FTIR measurements were performed to evaluate the molecular conformations of SF in the different samples (***Figure 5.3.5***). As can be observed in ***Figure 5.3.5a***, regardless of the solvent agent and processing method, the main absorption bands characteristic of SF, amide I - 1620 cm^{-1}, amide II - 1517 cm^{-1} and amide III - 1235 cm^{-1} remain unaltered. Comparing the FTIR spectra, the unique difference relies on the appearance of new absorption bands located at 2850 cm^{-1} (marked by black arrow), found for $CaCl_2$-Gel and LiBr-Gel samples.

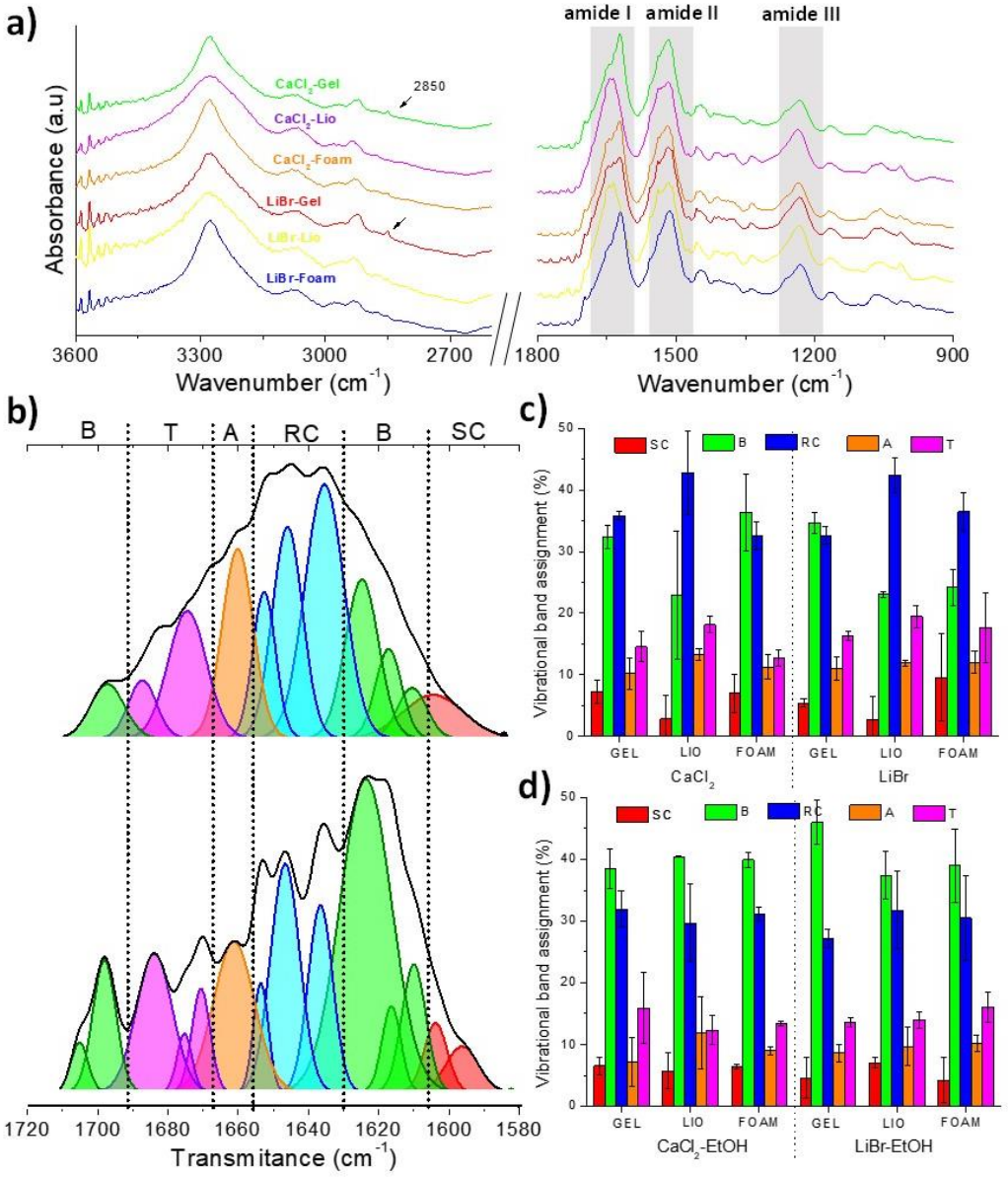

Figure 5.3. 5. For the different SF structures: a) FTIR absorbance curves, b) amide I deconvolution of the amorphous structure (above) and crystalline structure (below), c) band assignment and d) band assignment of *SF-EtOH treated samples.*

Figure 5.3.5b shows the deconvolution of the FTIR spectra in the amide I region, providing information on the secondary organization of SF. The possible secondary conformations are α-helix (A), β-sheets (B) and β-turns (T) belonging to crystalline domains and random coils (RC), and non-bonded side chains (SC), belonging to amorphous region. Each one, can be classified inside Amide I region according to its maximum wavenumber, in the following way: T (1696-1663 cm^{-1}), A (1662-1656 cm^{-1}), RC (1655-1638 cm^{-1}), B (1637-1616 cm^{-1} and 1705-1695 cm^{-1}) and SC (1615-1605 cm^{-1})[103]. The presence of each conformation was estimated by the area under the IR curve for all the peaks corresponding to the same conformation.

Figure 5.3.5b shows two examples of the FTIR amide I deconvolution. In the upper part, a typical example of amorphous SF is presented where the maximum is located in the RC region. The lower part of ***Figure 5.3.5*** shows an example of a highly crystalline SF structure, with maximum value in the B region, corresponding to β-sheet conformation.

Figures 5.3.5c shows the secondary conformation of SF structures. Differences are observed among them, showing the influence of the processing conditions on the SF secondary structure and therefore, on the final properties of materials. In order to analyse those differences, statistical analysis of variance (ANOVA) under 5% of tolerance has been applied. Due to their influence on SF properties, β-sheets (B) content and the relation between B and random coil (RC) structures have been considered as the most important parameters to analyse by this method. Regarding to the ability of the different processing methods to promote the presence of β-sheets into SF structure, it is only observed a significant difference ($p < 0.05$) in Gelled samples, where followed processing seems to have major ability to induce B structures (between 32 and 34%). Regarding to the relation between B and RC, it is observed a significant difference in lyophilized samples, which are clearly dominated by RC (~45%). In any case, no significant difference ($p>0.05$) between solving agents was observed.

The effect of EtOH treatment over SF porous structures is presented in ***Figure 5.3.5d***. Following with ANOVA statistical analysis, it can be observed that there exists a significant increase of B structures (reaching to values around 40-45 %.), when SF samples are treated with EtOH. The achieved similar values for β-structures in all the samples suggest the homogenous effect of EtOH over SF.

To analyse crystalline structures condition, X-ray data was used. It is important to consider that SF is formed by macromolecular chains, and therefore, it is unable to adopt a perfect crystalline structure with well-defined order. In contrast, SF crystallization is associated with the partial alignment of the molecular chains. This pseudo-packing leads to low crystalline diffraction patterns, accompanied by superimposed broad peaks ascribed to the not ordered regions. Further, the plasticization level of crystalline structures, represents a certain variability of crystalline spacing and consequently it is common to observe a slight displacement of diffraction peaks among samples[142]. ***Figure 5.3.6*** shows the X-ray diffraction patterns of the different samples. SF porous structures seem to reveal five different diffraction maxima at 12.4º, 14.5º, 20.1º, 24.9 º and 28.5º, which do not necessarily appear in all samples. Peaks 12º-13º, 14º-15º and >28º are commonly related with silk I structures[143], while the presence of peaks at 20-21º and 24-25 º is ascribed to highly packed silk II conformations[143]. The apparent lack of silk III representative maxima suggests that the used processing methods do not promote these structures, mainly ascribed to water-air interfaces.

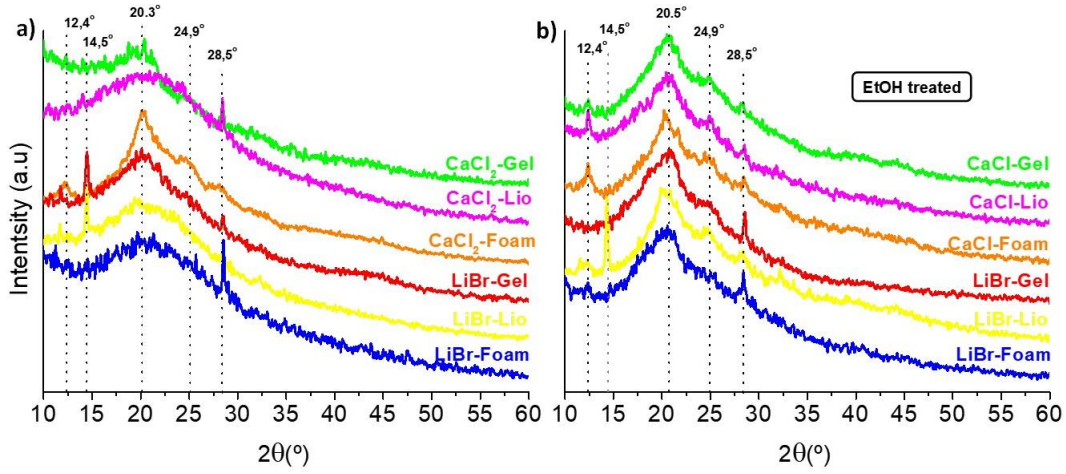

Figure 5.3. 6. *X-ray diffraction patterns of a) SF porous samples and b) EtOH treated SF porous samples.*

X-ray data suggest that i) processing methodology induces different ordering on crystalline structures, ii) Lio samples show the higher disorder degree, as revealed the broader diffraction peaks and iii) LiBr samples exhibit more non-stabilized Silk I structures, as revealed by the well-defined diffraction maxima observed around 12.4, 14.5 and 28.5º in 2θ (***Figure 5.3.6a***).

From the crystallographic structural point of view, the EtOH post-treatment of the samples has two side effects. Firstly, it modifies the crystals patterns of all the samples situating their maximum at 20-21º in 2θ, ascribed to Silk II structure. Secondly the broad diffraction signals ascribed to amorphous disorder domains is reduced.

Thermal behaviour

The thermal behaviour of the SF structures was studied by TGA and DSC (***Figure 5.3.7***). The TGA results (***Figures 5.3.7a and b***) show a similar weight loss profile as a function of temperature for all samples. Before 100 ºC, porous SF undergo a first weight loss due to water evaporation. Then, the weight of the samples remains constant until 290 ºC, temperature at which SF starts to degrade due to the side chains breakdown and peptide bonds cleavage[144]. Finally, around 330 ºC the combustion of the organic compounds starts, and it is completed at around 600 ºC. The main difference between samples is found during water evaporation step (<100 ºC), in where $CaCl_2$ processed samples show a weight loss around 10% and LiBr samples around 5%.

The treatment with EtOH, on the contrary, promotes larger variations in the thermal degradation profiles (***Figure 5.3.7a and b***). On one side, EtOH treated samples show a minor weight decrease during the water loss step. On the other side, it can be observed that the following degradation steps shift to higher temperatures (from 290 ºC to 300 ºC), including complete combustion process, which ends at 615 ºC[145].

The thermal transitions of SF could be hidden by the endothermic peak related to the water evaporation. Thus, previous to the DSC measurements, water was removed from the samples by 20 min isothermal heating at 140 ºC. The DSC scans performed after that procedure are shown in ***Figure 5.3.7c*** and 5d. The main characteristic transitions of SF are a glass transition temperature (T_g) around 185 ºC , ascribed to amorphous domains motion, a recrystallization temperature (T_c) found as a exothermic peak between 210 - 235 ºC, attributed to the amorphous domains folding into β-sheet crystalline regions and the degradation peak above 250 ºC, related to the beginning of the side chains and peptide bonds thermal decomposition. The slight endothermic peak that can be observed in some samples before glass transition is related to the evaporation of remaining bounded water molecules[146].

As observed, Lio samples showed a well-defined T_g and T_c, while the same transitions are slightly or non-visible in the other samples (***Figure 5.3.7a and b***).

After EtOH treatment, the thermal behaviour becomes homogenous for all samples (dashed line in ***Figures 5.3.7c and d***) and all thermal transitions of the porous structures disappeared which is directly related to the crystallization of amorphous domains (***Figure 5.3.5***).

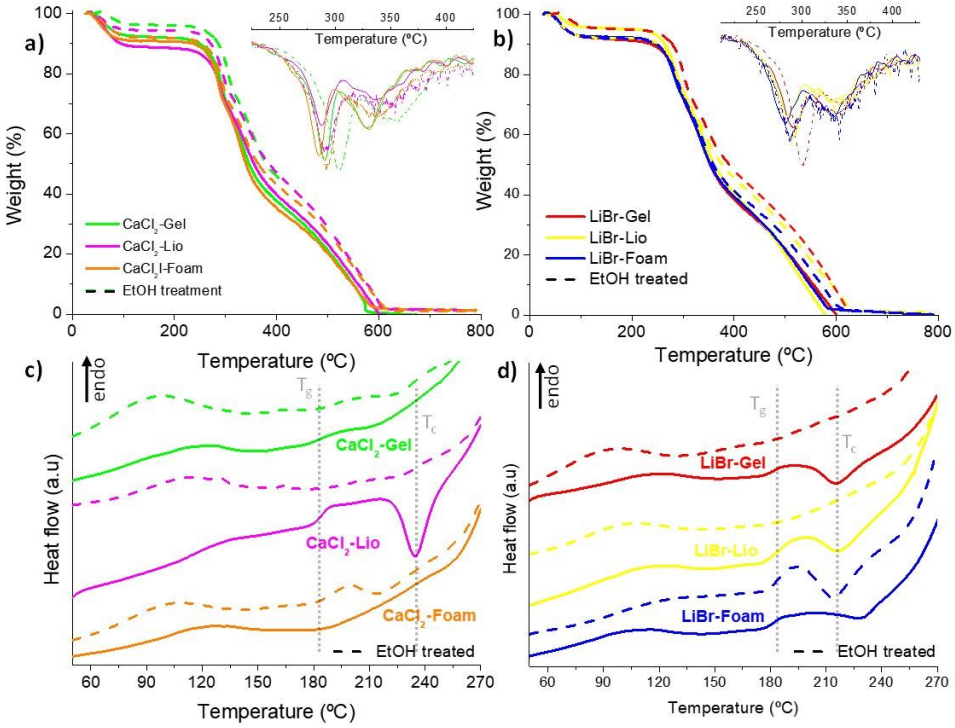

Figure 5.3. 7*. TGA and DSC thermograms for CaCl2-Gel, CaCl2-Lio and CaCl2-Foam samples (a and c) and LiBr-Gel, LiBr-Lio and LiBr-Foam samples (b and d), both pristine and treated with EtOH.*

<u>Water uptake and stability</u>

In order to apply SF-based porous materials for water pollution remediation purposes, it is highly desirable to fully understand samples behaviour in wet environments. Henceforth, water uptake and the water stability were measured.

Water uptake was monitored during the first 180 min of immersion (***Figure 5.3.8a***). Samples water saturation point is shown in ***Figure 5.3.8c***. As can be observed all the porous structures, reach a water uptake saturation after 20 min of immersion. Data point out the major adsorption of CaCl-Gel samples, with 24g·ml^{-1} adsorption.

EtOH treated samples water uptake data is collected in ***Figure 5.3.8c and d***. As can be observed, after EtOH treatment, water uptake appears to be reduced in all the cases, while water absorption speed and retention ability remains constant.

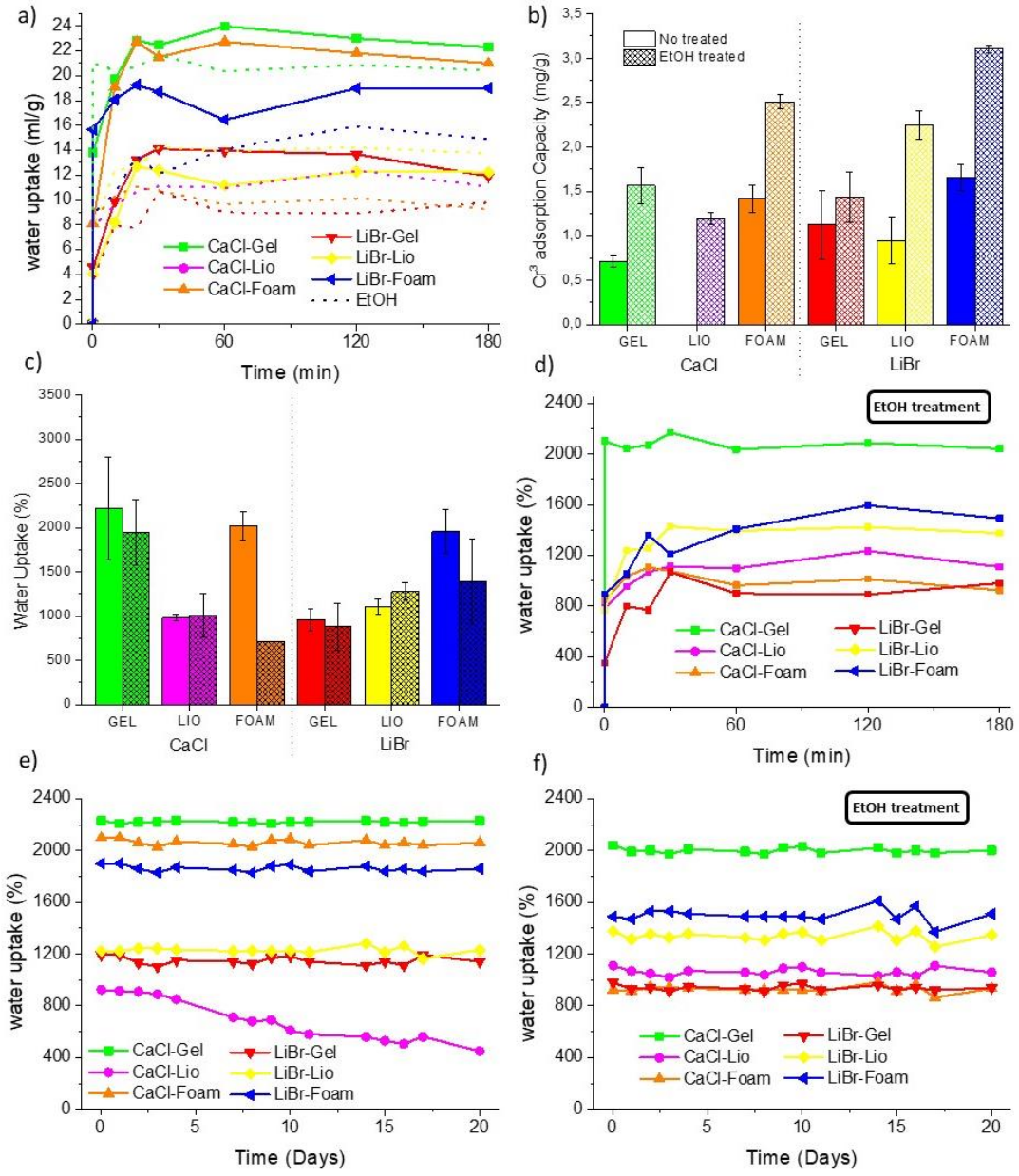

Figure 5.3. 8. *SF porous samples: a) water uptake, b) Cr3+ adsorption, c) Water uptake saturation of SF membranes before and after EtOH treatment, d) water uptake as a function of time for the EtOH treated SF membranes for the initial 180 min. Water uptake stability of the e) non treated and f) EtOH treated samples for a period of 20 days*

Water stability of SF structures was analysed by measuring the weight of the porous membranes after reached the maximum water uptake (***Figure 5.3.8e***). Data were collected for 3 consecutive weeks. After water immersion, practically all the samples show no significant weight loss, showing an excellent good stability. The $CaCl_2$-Lio sample was the only exception, resulting in a partial weight loss of nearly 50% of the total mass.

After treatment with EtOH, the porous structures conserve their water stability, even for the $CaCl_2$-Lio sample which becomes water stable. Results confirming the EtOH ability to stabilize SF structures (***Figure 5.3.8f***).

Heavy metals adsorption

The ability of the different porous SF structures to remove heavy metals from water was measured by water adsorption. SF samples were initially analysed versus different metalloids and heavy metal species: As^{3+}, As^{5+}, Cr^{6+} and Cr^{3+}. ***Figure 5.3.9***, collects the LiBr-Foam sample adsorption capacities as representative for all the samples. The initial results indicate that significant pollutant reduction is attained just in the case of Cr^{3+}. To understand the effect of the morphology and the physical-chemical properties of porous SF structures in the Cr^{3+} adsorption ability, the adsorption capacity of each sample before and after EtOH treatment was analysed. The obtained adsorption results are represented in ***Figure 5.3.8b***.

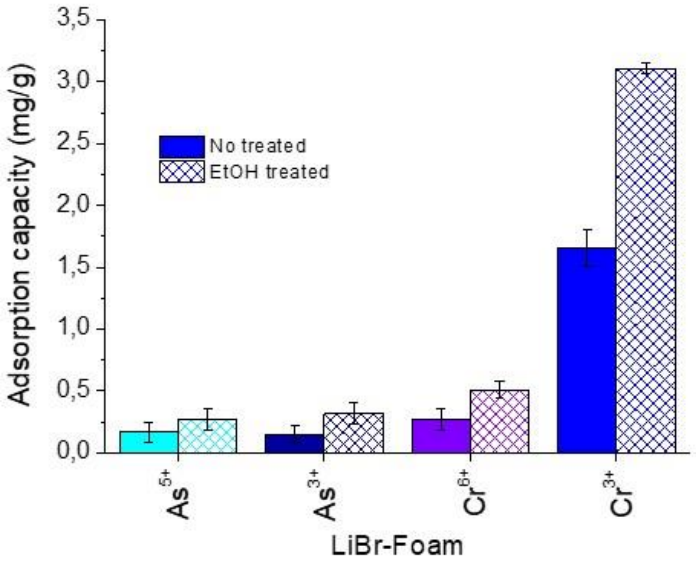

Figure 5.3. 9. *LiBr-Foam sample metalloids and heavy metals adsorption capacity*

Figure 5.3.8b shows that all samples allow significant adsorption of Cr^{3+}, between 0.7 and 1.65 mg of Cr^{3+} per g of SF, indicating the suitable characteristics of the developed SF structures for water pollution remediation[147]. The maximum retention values, slightly below 20% of the total concentration, were observed for the samples processes as foams ($CaCl_2$-Foam and LiBr-Foam).

Further, the Cr3+ adsorption nearly doubles for all samples after the EtOH treatment, (1.2 and 3.1 mg/g). Once again, the maximum adsorption values are observed in the Foam samples, with adsorption capacities above 30% of the initial concentration.

5.3.3. DISCUSSION

Silk fibroin porous structures have been processed following diverse procedures, including different solving agents, processing and post-processing. In the following, i) the origin of each morphology, ii) the effects of the processing and obtained microstructure on the physical-chemical properties of the material and iii) the potentials of the SF porous structures on water remediation will be discussed.

SF porous structures formation

During the solving, Ca^{2+} and Li^{+} cations from $CaCl_2$ and LiBr respectively, form chelates with SF carbonyl and hydroxyl groups, disrupting the intra- and intermolecular forces that keep the SF structure packed (***Figure 5.3.10a1***)[148]. Taking advance from the disruption, water molecules flow inside SF structure and form new H-bonds, leading to completely amorphous and opened SF conformation (***Figure 5.3.10a2***). In this point, SF molecules are free to interact with water generated polar environment[149] (***Figure 5.3.10b1***) and due to the SF amphiphilic behaviour, the polypeptide chains adopt micelles-like structures, in where hydrophilic domains occupy the shell and hydrophobic blocks the core (***Figure 5.3.10b2***)[150]. As H. Cho et al.[151] describe, during SF solution, strong ionic force of CaCl2, promotes the polypeptide chains scission into smaller chains. As a consequence, when SF micelles are formed, the small polypeptide sections aggregate, leading to molecules with high hydrodynamic radius (ranging from 100 to 300 nm). On the contrary, this effect is not observable for LiBr solutions, in where SF molecules self-assemble to form micelles with smaller hydrodynamic radius (10 to 30nm) (***Figure 5.3.10b2***) [151]. During micelles folding, water molecules could get trapped inside, hindering the hydrophobic interactions and delaying structures complete packing.

When SF solution is freeze, due to SF/water solution eutectic point, the formed pure water ice crystals exclude the SF micelles, grouping them into ice crystal walls (***Figure 5.3.10b3***). The increasing SF concentration , favours the protein-protein interactions, giving place to a continuous phase formation, as observed in sheet-like structures of SEM images (***Figure***

5.3.3)[152]. The definitive porous structure is formed once ice crystals are removed by lyophilization, leaving the planar structures without further changes[152] (***Figure 5.3.10b4***).

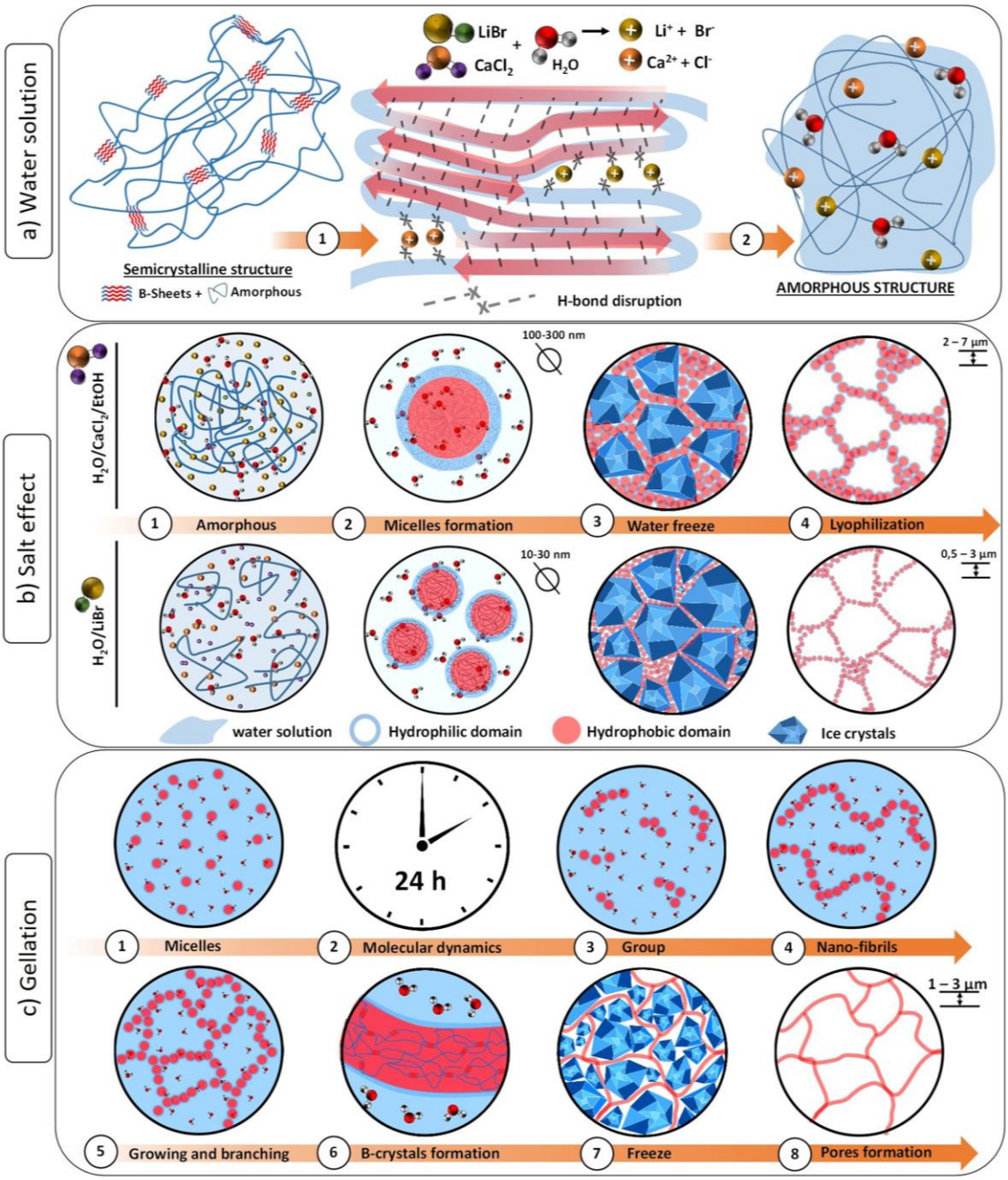

Figure 5.3. 10. *Graphical representation of Silk Fibroin (SF) a) aqueous solution (β-sheets disruption), b) CaCl2 and LiBr salts effect during solution and c) gelation process.*

As a result of the $CaCl_2$ micelles larger size, when they are accumulated into the ice crystals walls, thicker structures than those formed from LiBr smaller micelles are promoted (***Figure 7b4***). This effect explains the difference on sheet-like structures thickness observed between samples processed by $CaCl_2$ and LiBr solutions (***Figure 5.3.3***).

The nature of secondary order micro-pores, is related to the growth of secondary ice crystals embedded in highly concentrated SF regions[152]. Their size and shape respond to the dimensions of planar structures in where they are formed. The thicker structures formed in $CaCl_2$ samples represent a higher resistance to ice crystals growth than the narrower structures formed by LiBr processing. Thus, the formed secondary crystals from $CaCl_2$ ternary solution, adopt smaller and more regular shapes while secondary ice crystals of LiBr processed samples, with less resistance, facilitate the formation of bigger and more irregular pores. The lack of secondary pores on Foam planar structures, reveals that the faster freezing process of liquid nitrogen bath, does not provide enough time to form secondary ice crystals. The irregularity of foam samples pores sizes, could be related to N_2O gas molecules induced non-controlled cavities (***Figure 5.3.4***)[37].

The bean-like structure observed in $CaCl_2$-Gel samples is the one exception with respect to the microstructure (SEM images ***Figure 5.3.3***). Taking into consideration the given additional time for gelation (***table 5.3.1***), the observed bean-like structures must be related with molecular reorganization processes (***Figure 3.3.10c***). SF micelles have a tendency to group based on the formation of inter- and intramolecular interactions along the protein chains, including hydrophobic interactions and hydrogen bonds[153] (***Figure 3.3.10c3***). As described Z. Chen et al.[154] eventually, when SF micelles have enough time to interact one each other, they start growing in the form of elongated structures of repetitive micelles (***Figure 3.3.10c4***). These structures are named nano-fibrils and due to additional micelles junctions, nano-fibrils continue growing and branching until the formation of interconnected network (***Figure 3.3.10c5***)[154]. While fibrils remain still in solution, the water molecules trapped inside the micelles hinder the formation of crystalline structures[155]. However, when sufficient time for molecular interactions is given (as happened in Gel samples), the hydrophobic interactions finally happen, promoting the ordered domains packing into B ordered domains, which stabilize the structure and avoid its resolubilization[156] (***Figure 3.3.10c6***). During freeze, the formed fibrils will be slightly compacted by ice crystals grow (***Figure 3.3.10c7***), but due to the achieved stability, the network still remains unalterable

(***Figure 3.3.10c8***). The larger micelles from CaCl2 ternary solution seem to be the responsible of inducing more contacts between micelles, favouring larger hydrophobic interactions between them and supporting the fibrils network formation process in $CaCl_2$-Gel samples[156].

Processing effect on SF properties.

As it is shown in FTIR and XRD data, the secondary structure and crystallinity highly differ between samples. In Gel samples, the given longer molecular recombination time, promotes the formation of crystalline structures rich in β-sheets. These results also agree with the observed low intensity FTIR peaks at 2850 cm^{-1} in Gel samples (CaCl-Gel and LiBr-Gel), attributed to hydrogen bonding increase due to chains packing[153]. The shorter time for molecular recombination of Lio samples, results in slightly ordered structures with high RC amount (amorphous conformation). These data confirm the strong effect of molecular recombination time for SF structure formation.

Foam samples present differentiated secondary structure and crystallinity (***Figures 3.3.5 and 3.3.6***), even though both samples have equally processed. As described by D. Maniglio et al. [30] the SF foam is formed at the time that aqueous solution is extruded through the nozzle. Also, foam was immediately freeze by liquid nitrogen bath. This leaves the SF molecules without time for molecular recombination (***Table 5.3.1***). Thus, it can be suggested that during foaming process, the higher micelles from $CaCl_2$ ternary solution, promote more protein-protein interactions than LiBr solution. Consequently, in $CaCl_2$-Foam the hydrophobic interactions are promoted and more crystalline domains are formed.

Processing methods induced molecular organization, as is described by TGA data, seems to slightly affect samples thermal stability. However, a difference is observed between solvents induced water retention, having the samples from $CaCl_2$ ternary solution greater water amount (***Figure 5.3.7a and b***). Data suggest that bigger micelles formed in $CaCl_2$ ternary solution, retain a higher amount of water molecules inside, plasticising the resulting samples.

DSC data shows a clear effect of processing on thermal transitions. As can be observed, amorphous samples show the more pronounced transitions (both T_g and T_c), while crystalline samples practically lack them. Both T_g and T_c, are transitions related to free domains mobility. Chains packing and consequent B structures presence, suppose the formation of a cross-linked network in where the chains mobility is reduced by physical nodes. As a

consequence, greater B structures presence implies a minor mobility and therefore, less pronounced thermal transitions.

No experimental evidence was found to relate the water uptake with the secondary structure of SF. This suggests that the influence of microstructure prevails over the secondary structure for water absorbance and retention, being the bean-like structure of CaCl2-Gel sample the configuration with major water retention ability.

The good stability of SF porous samples in water, confirm the potentiality of samples for wet applications. $CaCl_2$-Lio sample is the only one not water stable, even when it has a similar secondary conformation and crystalline organization than LiBr-Lio samples. The main parameter which differs among both Lio samples is found on micelles formation and the plasticisation level of the samples, being the $CaCl_2$-Lio the most plasticised one. Data reveal once again the importance of the solvent contribution over samples properties and predict a water stability decrease with an increase on plasticisation.

Regarding to the effect of EtOH treatment, it is revealed a homogenous influence over almost all the parameters. It is known that EtOH highly interacts with water molecules, even more than SF (***Figure 5.3.11a1***). As consequence, during EtOH bath the H_2O molecules can link to EtOH. During the drying process and due to this interaction, bonded water and EtOH molecules are evaporated together, leaving the SF free of water. This SF dehydration, derives in more hydrophobic interactions, chains packing and crystalline domains increase (***Figure 5.3.11a2***)[133]. This effect, could be noted i) in SEM images where due to EtOH treatment, porous structures are contracted; ii) in FTIR and XRD, where the treated samples become highly crystalline Silk II (***Figures 3.3.5 and 3.3.6***); iii) in TGA where, thermal degradation was slightly delayed (***Figure 5.3.11***); iv) in DSC where highly stable and low mobile crystal domains lead to thermal transitions almost total loss (***Figures 3.3.6***) and v) in water behaviour where all the structures gain water stability (***Figure 5.3.8***) .

The only characteristic not homogeneously influenced by EtOH treatment was the water uptake ability. This heterogeneity can be ascribed to the higher influence of the microstructure on water absorption. The observed water uptake decreasing with respect to EtOH untreated samples, (***Figure 5.3.8***), is related to the structure contraction due to the dehydration (***Figure 5.3.3g***).

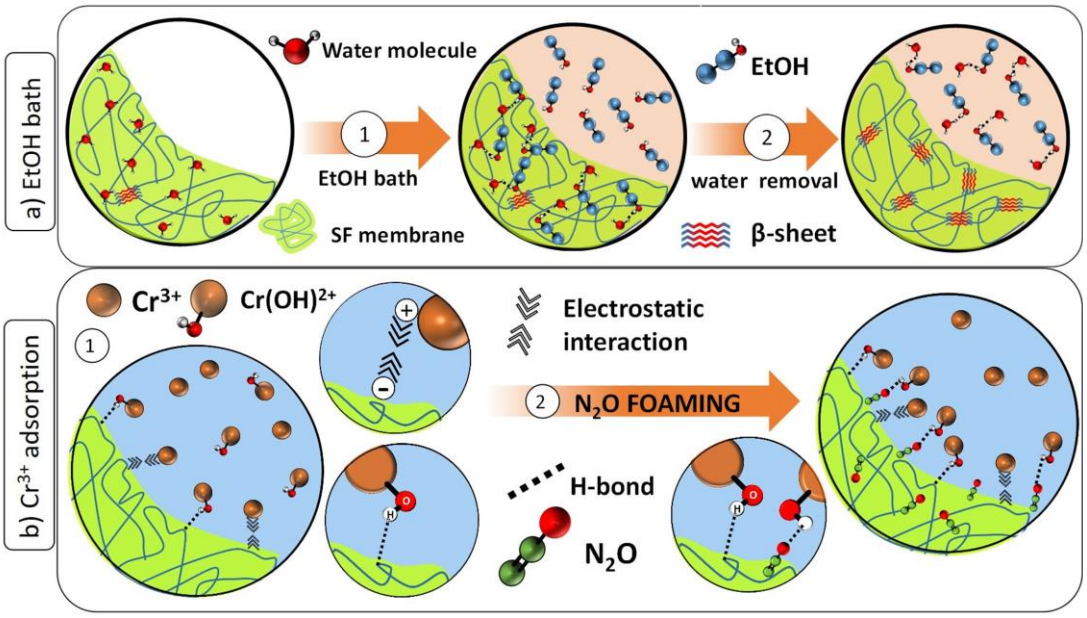

Figure 5.3. 11. *a) EtOH bath effect b) metals adsorption improvement by N2O addition.*

SF porous structures for water remediation.

Finally, SF adsorption ability for different heavy metal and metalloid ions, including As^{5+}, As^{3+}, Cr^{6+} and Cr^{3+} was studied. The selection of these ions is based on their varied chemistry and high toxicity in aqueous environments. In waters with pH 4, As^{5+} and Cr^{6+} are usually stabilized as negatively charged oxyanions like arsenate, chromate or dichromate[157]. On the contrary, $Cr^{3+}$is a hard cation that is stabilized as aquo-oxo species ($Cr(OH)^{2+}$ and Cr^{3+}) with neat positive charges [60]. Finally, As^{3+} is stabilized as neutral species. In general, the ions adsorption is driven by: i) electrostatic interaction with charged groups within the porous structure; ii) by anionic or cationic exchange processes where mobile ions within the SF structure could be replaced and iii) or direct interaction with reactive species. As adsorption data reveal (***Figure 5.3.8***), SF is affine to cationic species ($Cr(OH)^{2+}$ and Cr^{3+}), while practically does not show affinity for negative or neutral species. This behaviour suggests an electrostatic interaction between SF and cationic species ($Cr(OH)^{2+}$ and Cr^{3+}), mainly ascribed to the negative charge of SF surface, result of isoelectric point differences between hydrophilic and terminal domains[141,158] (***Figure 5.3.11a1***). Additionally, it can be predicted that SF and $Cr(OH)^{2+}$ will form direct interactions between reactive –OH group of $Cr(OH)^{2+}$ and accessible amine groups of SF polypeptide chain, increasing the porous structures adsorption capacity[134].

With respect to the effects of SF secondary structure and morphological characteristics in heavy metals adsorption, it can be stated that: i) Foam samples show larger adsorption values and ii) SF porous structures adsorption practically doubles after EtOH treatment.

The higher adsorption ability of the Foam samples must be related to the processing conditions. During the foaming, SF is mixed with N_2O in order to generate pores by decompression. The gas molecules get trapped within the SF polypeptide chains forming interactions with chelate and hydroxyl groups[159] (***Figure 11b2***). Thus, it can be hypothesized that, these new SF-N_2O complexes may generate more accessible points in where Cr $(OH)^{2+}$ could link , increasing the SF adsorption capacity (***Figure 11b2***).

Regarding to Cr^{3+} adsorption after EtOH treatment, it seems that all the samples undergo an increase of their capacity. To explain this change, three considerations have been taking into consideration after EtOH treatment: i) all the samples do not reach a homogenous behaviour, suggesting the effect of microstructure as additional factor; ii) the Cr^{3+} adsorption capacity increases despite of the decrease of samples water uptake (note that CaCl2-Gel sample in spite of having the major water uptake does not have the major Cr^{3+} adsorption capacity) and; iii) SF negative charges did not increase during chains packing, discarding the electrostatic interactions as the single reason for this effect[160]. Thus, we hypothesize that the dehydration caused by EtOH bath, generates new accessible polar bonding points (where H_2O molecules were attached) in where more Cr $(OH)^{2+}$ could be attached.

In this context, it can be concluded that, in SF porous structures, Cr^{3+} adsorption is mainly driven by direct interactions. However, while H_2O molecules remain bonded to the polypeptide structure (before EtOH treatment), the adsorption is driven by the combination of electrostatic and direct interactions.

The obtained adsorption results can be compared with the ones from different natural materials presented in ***Table 5.3.3***. Actually, few works focusing on As and Cr absorption can be found in the literature. As can be observed, most of the efforts have focused on the use of chitosan, cellulose, plants or minerals. The present work demonstrates that SF is a promising material, competitive with the aforementioned ones, to be used as adsorption material for pollutants removal. In addition, the given routes for SF based porous structures control, allowing also the possibility of developing composite materials, gives the chance for further tailoring the structures for specific applications.

Table 5.3.3. *Representative data of different natural materials used for heavy metals adsorption.*

Adsorbent	*Morphology*	*Pollutant / concentration (mg/L)*	*Charge (g/L)*	*Adsorption (mg/g)*	*ref*
modified chitosan	*crosslinked*	*Methylated Ar / 125*	*0.5*	*7.1 – 15.5*	161
Cocoa shells	*fibres*	*Cu / 45.5*	*40*	*2.6*	162
Aluminosilicate geopolymer	*powder*	*Pb, Ni, Hg Cu / 3000*	*5*	*200 - 600*	163
wood	*sawdust*	*Zn, Fe, Cu / 10*	*10*	*0.6 - 1*	164
wool keratose /silk fibroin	*Electrospinning mats*	*Cu^{2+} / 3.49*		*2.88*	165
SF	*Electrospinning mats*	*Cu^{2+} / 3.49*		*1.65*	165
Malic acid/ chitosan	*hydrogel beads*	*Cr(VI) / 100*	*1*	*383.2*	166
waste cotton	*cross-linked hydrogel*	*Pb / 7.6*	*1*	*7.5*	167
This work	*Porous*	*Cr^{3+} / 20*	*2*	*3.1*	-

5.3.4. CONCLUSIONS

To expand the applicability of the bio-based materials, the effect of different processing methods on Silk Fibroin (SF) porous structures properties has been addressed. For this purpose, six different SF structures with highly differentiated microstructure and porosity values above 94% were obtained from two dissolving agents, $CaCl_2$ and LiBr, and three different regeneration procedures, including gelation, freezing, and N_2O foaming.

It has been observed that $CaCl_2$/EtOH/H_2O ternary solution promotes SF molecules aggregation, increases the sample plasticization, and induces the formation of wider leaf-like structures. On the contrary, LiBr aqueous solution favors the formation of thinner leaf-like structures with bigger interspersed pores.

SF gelation promotes molecular recombination, enables the polypeptide chains folding into highly crystallized structures, and in combination with $CaCl_2$/EtOH/H_2O ternary solution, results in a bean-like microstructure. Directly lyophilized samples, contrary, promote amorphous structures and combined with LiBr solution, enable the formation of water-soluble structures.

SF shows an affinity for cationic species, which could be favored by N_2O gas foaming. EtOH treatment leads to an increase of SF crystalline configuration that slightly slows down

thermal degradation, increases sample water stability, and promotes the ability for Cr^{3+} adsorption.

This demonstrated SF's ability for heavy metals removal, as well as the capacity for controlling SF properties through processing, open a novel and promising investigation approach for the applicability of natural-based materials and highlight SF porous materials aptitude for water remediation purposes.

5.4. REFERENCES

1. European Commission. *Horizon Europe 2021-2027*. https://ec.europa.eu/info/horizon-europe_en.
2. Tan, L. & Wang, N. Future Internet: The Internet of Things. in *ICACTE 2010 - 2010 3rd International Conference on Advanced Computer Theory and Engineering, Proceedings* vol. 5 (2010).
3. Stock, T. & Seliger, G. Opportunities of Sustainable Manufacturing in Industry 4.0. in *Procedia CIRP* vol. 40 536–541 (Elsevier B.V., 2016).
4. Yadav, P., Yadav, H., Shah, V. G., Shah, G. & Dhaka, G. Biomedical biopolymers, their origin and evolution in biomedical sciences: A systematic review. *Journal of Clinical and Diagnostic Research* vol. 9 21–25 (2015).
5. Bose, S., Roy, M. & Bandyopadhyay, A. Recent advances in bone tissue engineering scaffolds. *Trends in Biotechnology* vol. 30 546–554 (2012).
6. Udenni Gunathilake, T., Ching, Y., Ching, K., Chuah, C. & Abdullah, L. Biomedical and Microbiological Applications of Bio-Based Porous Materials: A Review. *Polymers (Basel).* **9**, 160 (2017).
7. Sun, M. H. *et al.* Applications of hierarchically structured porous materials from energy storage and conversion, catalysis, photocatalysis, adsorption, separation, and sensing to biomedicine. *Chem. Soc. Rev.* **45**, 3479–3563 (2016).
8. Arora, P. & Zhang, Z. Battery separators. *Chem. Rev.* **104**, 4419–4462 (2004).
9. Inayat, A., Reinhardt, B., Uhlig, H., Einicke, W. D. & Enke, D. Silica monoliths with hierarchical porosity obtained from porous glasses. *Chem. Soc. Rev.* **42**, 3753–3764 (2013).
10. Martin Calvo, A. Porous Materials for Environmental Applications. (2015).
11. Rowsell, J. L. C. & Yaghi, O. M. Metal-organic frameworks: A new class of porous materials. *Microporous and Mesoporous Materials* vol. 73 3–14 (2004).
12. Yang, X. Y. *et al.* Hierarchically porous materials: Synthesis strategies and structure design. *Chemical Society Reviews* vol. 46 481–558 (2017).
13. Studart, R. *et al.* Silk fibroin scaffolds with inverse opal structure for bone tissue engineering. 2074–2084 (2016) doi:10.1002/jbm.b.33737.
14. Adebajo, M. O., Frost, R. L., Kloprogge, J. T., Carmody, O. & Kokot, S. Porous Materials for Oil Spill Cleanup: A Review of Synthesis and Absorbing Properties. *Journal of Porous Materials* vol. 10 159–170 (2003).
15. Kloprogge, J. T., Duong, L. V. & Frost, R. L. A review of the synthesis and characterisation of pillared clays and related porous materials for cracking of vegetable oils to produce biofuels. *Environmental Geology* vol. 47 967–981 (2005).
16. Rashidi, S., Esfahani, J. A. & Rashidi, A. A review on the applications of porous materials in solar energy systems. *Renewable and Sustainable Energy Reviews* vol. 73 1198–1210 (2017).
17. Rehman, T. ur, Ali, H. M., Janjua, M. M., Sajjad, U. & Yan, W. M. A critical review on heat transfer augmentation of phase change materials embedded with porous materials/foams. *International Journal of Heat and Mass Transfer* vol. 135 649–673 (2019).
18. Peisheng Liu & Guo-Feng Chen. *Porous Materials: Processing and Applications*. (2014).
19. Zhao, X. Porous materials for direct and indirect evaporative cooling in buildings. in *Materials for Energy Efficiency and Thermal Comfort in Buildings* 399–426 (Elsevier Inc., 2010). doi:10.1533/9781845699277.2.399.
20. Liu, P. S. & Chen, G. F. Application of Porous Metals. in *Porous Materials* 113–188 (Elsevier, 2014). doi:10.1016/b978-0-12-407788-1.00003-4.
21. Cheung, H. Y., Lau, K. T., Lu, T. P. & Hui, D. A critical review on polymer-based bio-engineered materials for scaffold development. *Compos. Part B Eng.* **38**, 291–300 (2007).

22. Kohane, D. S. & Langer, R. Polymeric biomaterials in tissue engineering. *Pediatric Research* vol. 63 487–491 (2008).

23. Lopez, J., Mackanic, D. G., Cui, Y. & Bao, Z. Designing polymers for advanced battery chemistries. *Nature Reviews Materials* vol. 4 312–330 (2019).

24. Costa, C. M., Silva, M. M. & Lanceros-Méndez, S. Battery separators based on vinylidene fluoride (VDF) polymers and copolymers for lithium ion battery applications. *RSC Advances* vol. 3 11404–11417 (2013).

25. Guan, Y., Cheng, F. & Pan, Z. Superwetting polymeric three dimensional (3D) porous materials for Oil/Water separation: A review. *Polymers* vol. 11 (2019).

26. Sun, Q., Aguila, B., Song, Y. & Ma, S. Tailored Porous Organic Polymers for Task-Specific Water Purification. *Cite This Acc. Chem. Res* **53**, 821 (2020).

27. Li, X. *et al.* 3D-printed biopolymers for tissue engineering application. *International Journal of Polymer Science* vol. 2014 (2014).

28. Van Vlierberghe, S., Dubruel, P. & Schacht, E. Biopolymer-Based Hydrogels As Scaffolds for Tissue Engineering Applications: A Review. *Biomacromolecules* **12**, 1387–1408 (2011).

29. Zhang, T. W., Tian, T., Shen, B., Song, Y. H. & Yao, H. Bin. Recent advances on biopolymer fiber based membranes for lithium-ion battery separators. *Composites Communications* vol. 14 7–14 (2019).

30. Lizundia, E. & Kundu, D. Advances in Natural Biopolymer-Based Electrolytes and Separators for Battery Applications. *Adv. Funct. Mater.* 2005646 (2020) doi:10.1002/adfm.202005646.

31. Agostini de Moraes, M., Cocenza, D. S., da Cruz Vasconcellos, F., Fraceto, L. F. & Beppu, M. M. Chitosan and alginate biopolymer membranes for remediation of contaminated water with herbicides. *J. Environ. Manage.* **131**, 222–227 (2013).

32. Qi, Y. *et al.* A review of structure construction of silk fibroin biomaterials from single structures to multi-level structures. *Int. J. Mol. Sci.* **18**, (2017).

33. Jin, H. J., Chen, J., Karageorgiou, V., Altman, G. H. & Kaplan, D. L. Human bone marrow stromal cell responses on electrospun silk fibroin mats. *Biomaterials* **25**, 1039–1047 (2004).

34. Khajavi, R. & Abbasipour, M. Electrospinning as a versatile method for fabricating coreshell, hollow and porous nanofibers. *Sci. Iran.* **19**, 2029–2034 (2012).

35. Makaya, K., Terada, S., Ohgo, K. & Asakura, T. Comparative study of silk fibroin porous scaffolds derived from salt / water and sucrose / hexafluoroisopropanol in cartilage formation. *JBIOSC* **108**, 68–75 (2009).

36. Zeng, C. *et al.* Silk fibroin porous scaffolds for nucleus pulposus tissue engineering. *Mater. Sci. Eng. C* **37**, 232–240 (2014).

37. Maniglio, D., Bonani, W., Migliaresi, C. & Motta, A. Silk fibroin porous scaffolds by N2O foaming. *J. Biomater. Sci. Polym. Ed.* **29**, 491–506 (2018).

38. Alessandrino, A. *et al.* Electrospun Silk Fibroin Mats for Tissue Engineering. *Eng. Life Sci.* **8**, 219–225 (2008).

39. Chen, Y. *et al.* Sustained Release SDF-1α/TGF-β1-Loaded Silk Fibroin-Porous Gelatin Scaffold Promotes Cartilage Repair. *ACS Appl. Mater. Interfaces* **11**, 14608–14618 (2019).

40. Farokhi, M. *et al.* Silk fibroin/hydroxyapatite composites for bone tissue engineering. *Biotechnology Advances* vol. 36 68–91 (2018).

41. Bhardwaj, N. & Kundu, S. C. Silk fibroin protein and chitosan polyelectrolyte complex porous scaffolds for tissue engineering applications. *Carbohydr. Polym.* **85**, 325–333 (2011).

42. Maji, K. Biomaterials for bone tissue engineering: Recent advances and challenges. in *Orthopedic Biomaterials: Progress in Biology, Manufacturing, and Industry Perspectives* 429–452 (Springer International Publishing, 2018). doi:10.1007/978-3-319-89542-0_17.

43. Sell, S. A. *et al.* The Use of Natural Polymers in Tissue Engineering: A Focus on Electrospun Extracellular Matrix Analogues. *Polymers (Basel).* **2**, 522–553 (2010).

44. Khorshidi, S. *et al.* A review of key challenges of electrospun scaffolds for tissue-engineering applications. *Journal of Tissue Engineering and Regenerative Medicine* vol. 10 715–738 (2016).

45. Min, B. M. *et al.* Electrospinning of silk fibroin nanofibers and its effect on the adhesion and spreading of normal human keratinocytes and fibroblasts in vitro. *Biomaterials* **25**, 1289–1297 (2004).

46. Koh, L. D. *et al.* Structures, mechanical properties and applications of silk fibroin materials. *Prog. Polym. Sci.* **46**, 86–110 (2015).

47. Fernandes, M. M. *et al.* Multifunctional magnetically responsive biocomposites based on genetically engineered silk-elastin-like protein. *Compos. Part B Eng.* **153**, 413–419 (2018).

48. Yucel, T., Cebe, P. & Kaplan, D. L. Structural Origins of Silk Piezoelectricity. *Adv. Funct. Mater.* **21**, 779–785 (2011).

49. Díaz, E., Valle, M., Ribeiro, S., Lanceros-Mendez, S. & Barandiarán, J. Development of Magnetically Active Scaffolds for Bone Regeneration. *Nanomaterials* **8**, 678 (2018).

50. Cardoso, V. F. *et al.* Advances in Magnetic Nanoparticles for Biomedical Applications. *Advanced Healthcare Materials* vol. 7 (2018).

51. Brito-Pereira, R. *et al.* Silk fibroin-magnetic hybrid composite electrospun fibers for tissue engineering applications. *Compos. Part B Eng.* **141**, 70–75 (2018).

52. Ribeiro, C., Sencadas, V., Correia, D. M. & Lanceros-Méndez, S. Piezoelectric polymers as biomaterials for tissue engineering applications. *Colloids and Surfaces B: Biointerfaces* vol. 136 46–55 (2015).

53. Martins, P. M. *et al.* Effect of poling state and morphology of piezoelectric poly(vinylidene fluoride) membranes for skeletal muscle tissue engineering. *RSC Adv.* **3**, 17938–17944 (2013).

54. Ribeiro, C., Correia, V., Martins, P., Gama, F. M. & Lanceros-Mendez, S. Proving the suitability of magnetoelectric stimuli for tissue engineering applications. *Colloids Surfaces B Biointerfaces* **140**, 430–436 (2016).

55. Kijeńska, E., Zhang, S., Prabhakaran, M. P., Ramakrishna, S. & Swieszkowski, W. Nanoengineered biocomposite tricomponent polymer based matrices for bone tissue engineering. *Int. J. Polym. Mater. Polym. Biomater.* **65**, 807–815 (2016).

56. Kooti, M. & Afshari, M. Magnetic cobalt ferrite nanoparticles as an efficient catalyst for oxidation of alkenes. *Sci. Iran.* **19**, 1991–1995 (2012).

57. Yuan, X., Arkonac, D. E., Chao, P. H. G. & Vunjak-Novakovic, G. Electrical stimulation enhances cell migration and integrative repair in the meniscus. *Sci. Rep.* **4**, 1–12 (2015).

58. Zhu, X., Chen, J., Scheideler, L., Reichl, R. & Geis-Gerstorfer, J. Effects of topography and composition of titanium surface oxides on osteoblast responses. *Biomaterials* **25**, 4087–4103 (2004).

59. Rosales-Leal, J. I. *et al.* Effect of roughness, wettability and morphology of engineered titanium surfaces on osteoblast-like cell adhesion. *Colloids Surfaces A Physicochem. Eng. Asp.* **365**, 222–229 (2010).

60. Strawhecker, K. E., Kumar, S. K., Douglas, J. F. & Karim, A. The critical role of solvent evaporation on the roughness of spin-cast polymer films [1]. *Macromolecules* vol. 34 4669–4672 (2001).

61. Abdel-Hady, F., Alzahrany, A. & Hamed, M. Experimental Validation of Upward Electrospinning Process. *ISRN Nanotechnol.* **2011**, 1–14 (2011).

62. Yarin, A. L., Koombhongse, S. & Reneker, D. H. Bending instability in electrospinning of nanofibers. *J. Appl. Phys.* **89**, 3018–3026 (2001).

63. Yarin, A. L., Kataphinan, W. & Reneker, D. H. Branching in electrospinning of nanofibers. *J. Appl. Phys.* **98**, 064501 (2005).

64. Mohapatra, S., Rout, S. R., Maiti, S., Maiti, T. K. & Panda, A. B. Monodisperse mesoporous cobalt ferrite nanoparticles: Synthesis and application in targeted delivery of antitumor drugs. *J. Mater. Chem.* **21**, 9185–9193 (2011).

65. Feng, X. X. *et al.* Preparation and characterization of novel nanocomposite films formed from silk

fibroin and nano-TiO2. *Int. J. Biol. Macromol.* **40**, 105–111 (2007).

66. Chrissafis, K. & Bikiaris, D. Can nanoparticles really enhance thermal stability of polymers? Part I: An overview on thermal decomposition of addition polymers. *Thermochimica Acta* vol. 523 1–24 (2011).

67. Yazawa, K., Ishida, K., Masunaga, H., Hikima, T. & Numata, K. Influence of Water Content on the β-Sheet Formation, Thermal Stability, Water Removal, and Mechanical Properties of Silk Materials. *Biomacromolecules* **17**, 1057–1066 (2016).

68. He, Y. X. *et al.* N-terminal domain of Bombyx mori fibroin mediates the assembly of silk in response to pH decrease. *J. Mol. Biol.* **418**, 197–207 (2012).

69. Maciel, M. M. *et al.* Relation between fiber orientation and mechanical properties of nano-engineered poly(vinylidene fluoride) electrospun composite fiber mats. *Compos. Part B Eng.* **139**, 146–154 (2018).

70. Guo, Z. *et al.* Magnetic and electromagnetic evaluation of the magnetic nanoparticle filled polyurethane nanocomposites. in *Journal of Applied Physics* vol. 101 09M511 (American Institute of PhysicsAIP, 2007).

71. Cao, Y. & Wang, B. Biodegradation of silk biomaterials. *Int. J. Mol. Sci.* **10**, 1514–1524 (2009).

72. Lee, O. J. *et al.* Biodegradation behavior of silk fibroin membranes in repairing tympanic membrane perforations. *J. Biomed. Mater. Res. Part A* **100A**, 2018–2026 (2012).

73. Ahmad, F., Liu, X., Zhou, Y. & Yao, H. An in vivo evaluation of acute toxicity of cobalt ferrite (CoFe2O4) nanoparticles in larval-embryo Zebrafish (Danio rerio). *Aquat. Toxicol.* **166**, 21–28 (2015).

74. Franz-Odendaal, T. A., Hall, B. K. & Witten, P. E. Buried alive: How osteoblasts become osteocytes. *Developmental Dynamics* vol. 235 176–190 (2006).

75. AIZAWA, M. *et al.* Electrically Stimulated Modulation of Cellular Function in Proliferation, Differentiation, and Gene Expression. *Electrochemistry* **67**, 118–125 (1999).

76. Ribeiro, C. *et al.* Piezoelectric poly(vinylidene fluoride) microstructure and poling state in active tissue engineering. *Eng. Life Sci.* **15**, 351–356 (2015).

77. Kim, H. J. *et al.* Bone regeneration on macroporous aqueous-derived silk 3-D scaffolds. *Macromol. Biosci.* **7**, 643–655 (2007).

78. Meinel, L. *et al.* Silk based biomaterials to heal critical sized femur defects. *Bone* **39**, 922–931 (2006).

79. Votteler, M., Kluger, P. J., Walles, H. & Schenke-Layland, K. Stem Cell Microenvironments - Unveiling the Secret of How Stem Cell Fate is Defined. *Macromol. Biosci.* **10**, 1302–1315 (2010).

80. Can Şener, Ş. E., Sharp, J. L. & Anctil, A. Factors impacting diverging paths of renewable energy: A review. *Renewable and Sustainable Energy Reviews* vol. 81 2335–2342 (2018).

81. Diouf, B. & Pode, R. Potential of lithium-ion batteries in renewable energy. *Renewable Energy* vol. 76 375–380 (2015).

82. Goodenough, J. B. & Park, K. S. The Li-ion rechargeable battery: A perspective. *J. Am. Chem. Soc.* **135**, 1167–1176 (2013).

83. Scrosati, B. & Garche, J. Lithium batteries: Status, prospects and future. *Journal of Power Sources* vol. 195 2419–2430 (2010).

84. Kang, D. H. P., Chen, M. & Ogunseitan, O. A. Potential environmental and human health impacts of rechargeable lithium batteries in electronic waste. *Environ. Sci. Technol.* **47**, 5495–5503 (2013).

85. Nitta, N., Wu, F., Lee, J. T. & Yushin, G. Li-ion battery materials: Present and future. *Materials Today* vol. 18 252–264 (2015).

86. Wu, Y. Lithium-ion batteries: Fundamentals and Applications. (2015).

87. Sheng, J., Tong, S., He, Z. & Yang, R. Recent developments of cellulose materials for lithium-ion battery separators. *Cellulose* vol. 24 4103–4122 (2017).

88. Gong, S. D. *et al.* A green and environment-friendly gel polymer electrolyte with higher performances

based on the natural matrix of lignin. *J. Power Sources* **307**, 624–633 (2016).

89. Park, S. *et al.* Multicore-shell nanofiber architecture of polyimide/polyvinylidene fluoride blend for thermal and long-term stability of lithium ion battery separator. *Sci. Rep.* **6**, 1–8 (2016).

90. Pereira, R. F. P. *et al.* Silk Fibroin Separators: A Step Toward Lithium-Ion Batteries with Enhanced Sustainability. *ACS Appl. Mater. Interfaces* **10**, 5385–5394 (2018).

91. Gaines, L. The future of automotive lithium-ion battery recycling: Charting a sustainable course. *Sustain. Mater. Technol.* **1**, 2–7 (2014).

92. Zhang, H., Magoshi, J., Becker, M., Chen, J. Y. & Matsunaga, R. Thermal properties of Bombyx mori silk fibers. *J. Appl. Polym. Sci.* **86**, 1817–1820 (2002).

93. Jia, X., Wang, C., Zhao, C., Ge, Y. & Wallace, G. G. Toward Biodegradable Mg-Air Bioelectric Batteries Composed of Silk Fibroin-Polypyrrole Film. *Adv. Funct. Mater.* **26**, 1454–1462 (2016).

94. Zhang, J., Cai, Y., Zhong, Q., Lai, D. & Yao, J. Porous nitrogen-doped carbon derived from silk fibroin protein encapsulating sulfur as a superior cathode material for high-performance lithium-sulfur batteries. *Nanoscale* **7**, 17791–17797 (2015).

95. Jia, X. *et al.* A Biodegradable Thin-Film Magnesium Primary Battery Using Silk Fibroin-Ionic Liquid Polymer Electrolyte. *ACS Energy Lett.* **2**, 831–836 (2017).

96. Kim, T. S. *et al.* Carbon-decorated iron oxide hollow granules formed using a silk fibrous template: Lithium-oxygen battery and wastewater treatment applications. *NPG Asia Mater.* **9**, 1–9 (2017).

97. Hou, J., Cao, C., Idrees, F. & Ma, X. Hierarchical porous nitrogen-doped carbon nanosheets derived from silk for ultrahigh-capacity battery anodes and supercapacitors. *ACS Nano* **9**, 2556–2564 (2015).

98. Maceiras, A. *et al.* Effect of cyano dipolar groups on the performance of lithium-ion battery electrospun polyimide gel electrolyte membranes. *J. Electroanal. Chem.* **778**, 57–65 (2016).

99. Gören, A. *et al.* High performance screen-printed electrodes prepared by a green solvent approach for lithium-ion batteries. *J. Power Sources* **334**, 65–77 (2016).

100. Lin-Gibson, S., Cooper, J. A., Landis, F. A. & Cicerone, M. T. Systematic investigation of porogen size and content on scaffold morphometric parameters and properties. *Biomacromolecules* **8**, 1511–1518 (2007).

101. Ling, S., Qi, Z., Knight, D. P., Shao, Z. & Chen, X. FTIR imaging, a useful method for studying the compatibility of silk fibroin-based polymer blends. *Polym. Chem.* **4**, 5401–5406 (2013).

102. Qiu, W. *et al.* Complete recombinant silk-elastinlike protein-based tissue scaffold. *Biomacromolecules* **11**, 3219–3227 (2010).

103. Hu, X., Kaplan, D. & Cebe, P. Determining beta-sheet crystallinity in fibrous proteins by thermal analysis and infrared spectroscopy. *Macromolecules* **39**, 6161–6170 (2006).

104. Magoshi, J. *et al.* Crystallization of silk fibroin from solution. *Thermochim. Acta* **352**, 165–169 (2000).

105. Woo, J. J., Zhang, Z., Dietz Rago, N. L., Lu, W. & Amine, K. A high performance separator with improved thermal stability for Li-ion batteries. *J. Mater. Chem. A* **1**, 8538–8540 (2013).

106. Zhong, J. *et al.* Self-assembly of regenerated silk fibroin from random coil nanostructures to antiparallel β-sheet nanostructures. *Biopolymers* **101**, 1181–1192 (2014).

107. Structure and solubility of natural silk fibroin. *Russ. J. Appl. Chem.* **79**, 869–876 (2006).

108. Agarwal, N., Hoagland, D. A. & Farris, R. J. Effect of moisture absorption on the thermal properties of Bombyx mori silk fibroin films. *J. Appl. Polym. Sci.* **63**, 401–410 (1997).

109. Xu, G., Toh, G. W., Du, N. & Liu, X. Y. Spider silk: The toughest natural polymer. *RSC Green Chem.* **1**, 275–304 (2012).

110. Cannarella, J. *et al.* Mechanical Properties of a Battery Separator under Compression and Tension. *J. Electrochem. Soc.* **161**, F3117–F3122 (2014).

111. Simpson, J. T., Hunter, S. R. & Aytug, T. Superhydrophobic materials and coatings: A review. *Reports Prog. Phys.* **78**, (2015).

112. Dahbi, M. *et al.* Interfacial properties of LiTFSI and LiPF 6-based electrolytes in binary and ternary mixtures of alkylcarbonates on graphite electrodes and Celgard separator. *Ind. Eng. Chem. Res.* **51**, 5240–5245 (2012).

113. Choi, J. A., Kim, S. H. & Kim, D. W. Enhancement of thermal stability and cycling performance in lithium-ion cells through the use of ceramic-coated separators. *J. Power Sources* **195**, 6192–6196 (2010).

114. Xie, Y. *et al.* Enhancement on the wettability of lithium battery separator toward nonaqueous electrolytes. *J. Memb. Sci.* **503**, 25–30 (2016).

115. Hassoun, J., Lee, D. J., Sun, Y. K. & Scrosati, B. A lithium ion battery using nanostructured Sn-C anode, LiFePO4 cathode and polyethylene oxide-based electrolyte. *Solid State Ionics* **202**, 36–39 (2011).

116. Costa, C. M., Lee, Y. H., Kim, J. H., Lee, S. Y. & Lanceros-Méndez, S. Recent advances on separator membranes for lithium-ion battery applications: From porous membranes to solid electrolytes. *Energy Storage Materials* vol. 22 346–375 (2019).

117. Fongy, C., Gaillot, A.-C., Jouanneau, S., Guyomard, D. & Lestriez, B. Ionic vs Electronic Power Limitations and Analysis of the Fraction of Wired Grains in LiFePO[sub 4] Composite Electrodes. *J. Electrochem. Soc.* **157**, A885 (2010).

118. Wu, G., Liu, X. & Hu, J. A Reexamination of Cultural-Based Effects on Judgment: The Impacts of Consumer Involvement and Product Involvement. in 223–223 (Springer, Cham, 2016). doi:10.1007/978-3-319-26647-3_44.

119. Saito, Y., Morimura, W., Kuratani, R. & Nishikawa, S. Ion transport in separator membranes of lithium secondary batteries. *J. Phys. Chem. C* **119**, 4702–4708 (2015).

120. Wang, Z. Modeling and Simulation of Piezoelectrically Driven Self-Charging Lithium Ion Batteries. *ACS Appl. Mater. Interfaces* **9**, 15893–15897 (2017).

121. Costa, C. M., Gomez Ribelles, J. L., Lanceros-Méndez, S., Appetecchi, G. B. & Scrosati, B. Poly(vinylidene fluoride)-based, co-polymer separator electrolyte membranes for lithium-ion battery systems. *J. Power Sources* **245**, 779–786 (2014).

122. Singh, M. *Comparison of Multi-Fractal Antenna with Star Shaped Fractal Antenna for Wireless Applications*. *International Journal of Computer Applications* vol. 133 www.ijcaonline.org (2016).

123. Chun, S. J. *et al.* Eco-friendly cellulose nanofiber paper-derived separator membranes featuring tunable nanoporous network channels for lithium-ion batteries. *J. Mater. Chem.* **22**, 16618–16626 (2012).

124. Du, Z. *et al.* A mechanically robust, biodegradable and high performance cellulose gel membrane as gel polymer electrolyte of lithium-ion battery. *Electrochim. Acta* **299**, 19–26 (2019).

125. Xu, Q. *et al.* Polydopamine-coated cellulose microfibrillated membrane as high performance lithium-ion battery separator. *RSC Adv.* **4**, 7845–7850 (2014).

126. Zolin, L. *et al.* Aqueous processing of paper separators by filtration dewatering: towards Li-ion paper batteries. *J. Mater. Chem. A* **3**, 14894–14901 (2015).

127. Zhang, J. *et al.* Sustainable, heat-resistant and flame-retardant cellulose-based composite separator for high-performance lithium ion battery. *Sci. Rep.* **4**, 1–8 (2014).

128. Raja, M. & Stephan, A. M. Natural, biodegradable and flexible egg shell membranes as separators for lithium-ion batteries. *RSC Adv.* **4**, 58546–58552 (2014).

129. Zhang, T. W. *et al.* Prawn shell derived chitin nanofiber membranes as advanced sustainable separators for Li/Na-Ion Batteries. *Nano Lett.* **17**, 4894–4901 (2017).

130. Zhang, L. C., Sun, X., Hu, Z., Yuan, C. C. & Chen, C. H. Rice paper as a separator membrane in lithium-ion batteries. *J. Power Sources* **204**, 149–154 (2012).

131. Pereira, R. F. P. *et al. Bombyx mori* Silkworm Cocoon Separators for Lithium-Ion Batteries with Superior Safety and Sustainability. *Adv. Sustain. Syst.* **2**, 1800098 (2018).

132. Chankow, S., Luemunkong, S. & Kanokpanont, S. Conformational transitions of Thai silk fibroin secondary structures. in *BMEiCON 2016 - 9th Biomedical Engineering International Conference*

(Institute of Electrical and Electronics Engineers Inc., 2017). doi:10.1109/BMEiCON.2016.7859597.

133. Li, M., Tao, W., Kuga, S. & Nishiyama, Y. Controlling molecular conformation of regenerated wild silk fibroin by aqueous ethanol treatment. *Polym. Adv. Technol.* **14**, 694–698 (2003).

134. Saiz, A. P. G. *et al.* Chromium speciation in Zr-based Metal-Organic Frameworks for environmental remediation. *Chem. - A Eur. J.* (2020) doi:10.1002/chem.202001435.

135. Hoslett, J. *et al.* Surface water filtration using granular media and membranes: A review. *Science of the Total Environment* vol. 639 1268–1282 (2018).

136. Loh, Q. L. & Choong, C. Three-dimensional scaffolds for tissue engineering applications: Role of porosity and pore size. *Tissue Eng. - Part B Rev.* **19**, 485–502 (2013).

137. Pizarro, J., Vergara, P. M., Rodríguez, J. A. & Valenzuela, A. M. Heavy metals in northern Chilean rivers: Spatial variation and temporal trends. *J. Hazard. Mater.* **181**, 747–754 (2010).

138. Sereshti, H., Vasheghani Farahani, M. & Baghdadi, M. Trace determination of chromium(VI) in environmental water samples using innovative thermally reduced graphene (TRG) modified SiO2 adsorbent for solid phase extraction and UV-vis spectrophotometry. *Talanta* **146**, 662–669 (2016).

139. Rai, D., Sass, B. M. & Moore, D. A. Chromium(III) Hydrolysis Constants and Solubility of Chromium(III) Hydroxide. *Inorg. Chem.* **26**, 345–349 (1987).

140. Das, J. & Sarkar, P. A new dipstick colorimetric sensor for detection of arsenate in drinking water. *Environ. Sci. Water Res. Technol.* **2**, 693–704 (2016).

141. Zhou, W. *et al.* Removal of copper ions from aqueous solution by adsorption onto novel polyelectrolyte film-coated nanofibrous silk fibroin non-wovens. *Appl. Surf. Sci.* **345**, 169–174 (2015).

142. Zhang, H. *et al.* Preparation and characterization of silk fibroin as a biomaterial with potential for drug delivery. 1–9 (2012).

143. Fan, Z., Xiao, L., Lu, G., Ding, Z. & Lu, Q. Water-insoluble amorphous silk fibroin scaffolds from aqueous solutions. *J. Biomed. Mater. Res. Part B Appl. Biomater.* **108**, 798–808 (2020).

144. Porter, D., Vollrath, F., Tian, K., Chen, X. & Shao, Z. A kinetic model for thermal degradation in polymers with specific application to proteins. *Polymer (Guildf).* **50**, 1814–1818 (2009).

145. Hu, X., Kaplan, D. & Cebe, P. Effect of water on the thermal properties of silk fibroin. *Thermochim. Acta* **461**, 137–144 (2007).

146. Cebe, P. *et al.* Fast scanning calorimetry of silk fibroin protein: Sample mass and specific heat capacity determination. in *Fast Scanning Calorimetry* 187–203 (Springer International Publishing, 2016). doi:10.1007/978-3-319-31329-0_5.

147. Leghouchi, E., Laib, E. & Guerbet, M. Evaluation of chromium contamination in water, sediment and vegetation caused by the tannery of Jijel (Algeria): A case study. *Environ. Monit. Assess.* **153**, 111–117 (2009).

148. Shen, T. *et al.* Dissolution behavior of silk fibroin in a low concentration CaCl2-methanol solvent: From morphology to nanostructure. *Int. J. Biol. Macromol.* **113**, 458–463 (2018).

149. Kasoju, N., Hawkins, N., Pop-Georgievski, O., Kubies, D. & Vollrath, F. Silk fibroin gelation via non-solvent induced phase separation. *Biomater. Sci.* **4**, 460–473 (2016).

150. Jin, H. J. & Kaplan, D. L. Mechanism of silk processing in insects and spiders. *Nature* **424**, 1057–1061 (2003).

151. Cho, H. J., Ki, C. S., Oh, H., Lee, K. H. & Um, I. C. Molecular weight distribution and solution properties of silk fibroins with different dissolution conditions. *Int. J. Biol. Macromol.* **51**, 336–341 (2012).

152. Byette, F. *et al.* Cell-culture compatible silk fibroin scaffolds concomitantly patterned by freezing conditions and salt concentration. *Polym. Bull.* **67**, 159–175 (2011).

153. Kim, U. J. *et al.* Structure and properties of silk hydrogels. *Biomacromolecules* **5**, 786–792 (2004).

154. Chen, Z. *et al.* Programing Performance of Silk Fibroin Materials by Controlled Nucleation. *Adv. Funct. Mater.* **26**, 8978–8990 (2016).

155. Um, I. C., Kweon, H. Y., Lee, K. G. & Park, Y. H. The role of formic acid in solution stability and crystallization of silk protein polymer. *Int. J. Biol. Macromol.* **33**, 203–213 (2003).

156. Matsumoto, A. *et al.* Mechanisms of silk fibroin sol-gel transitions. *J. Phys. Chem. B* **110**, 21630–21638 (2006).

157. Gayle Newcombe, D. D. *Interface Science in Drinking Water Treatment: Theory and Applications - Gayle Newcombe, David Dixon - Google Libros*. vol. 10 (2016).

158. Dubey, P. *et al.* Silk Fibroin-Sophorolipid Gelation: Deciphering the Underlying Mechanism. *Biomacromolecules* **17**, 3318–3327 (2016).

159. Einarsdottir, O. & Caughey, W. S. Interactions of the anesthetic nitrous oxide with bovine heart cytochrome c oxidase. Effects on protein structure, oxidase activity, and other properties. *J. Biol. Chem.* **263**, 9199–9205 (1988).

160. Lammel, A. S., Hu, X., Park, S. H., Kaplan, D. L. & Scheibel, T. R. Controlling silk fibroin particle features for drug delivery. *Biomaterials* **31**, 4583–4591 (2010).

161. Wei, Y. T., Zheng, Y. M. & Chen, J. P. Uptake of methylated arsenic by a polymeric adsorbent: Process performance and adsorption chemistry. *Water Res.* **45**, 2290–2296 (2011).

162. Meunier, N., Blais, J. F. & Tyagi, R. D. Selection of a natural sorbent to remove toxic metals from acidic leachate produced during soil decontamination. *Hydrometallurgy* **67**, 19–30 (2002).

163. Maleki, A., Hajizadeh, Z., Sharifi, V. & Emdadi, Z. A green, porous and eco-friendly magnetic geopolymer adsorbent for heavy metals removal from aqueous solutions. *J. Clean. Prod.* **215**, 1233–1245 (2019).

164. Balintova, M. & Demcak, S. *A study of sorption heavy metals by natural organic sorbents*. https://www.researchgate.net/publication/305259568 (2016).

165. Ki, C. S., Gang, E. H., Um, I. C. & Park, Y. H. Nanofibrous membrane of wool keratose/silk fibroin blend for heavy metal ion adsorption. *J. Memb. Sci.* **302**, 20–26 (2007).

166. Zhang, Y., Lin, S., Qiao, J., Ko, D. & Ju, Y. Malic acid-enhanced chitosan hydrogel beads (mCHBs) for the removal of Cr (VI) and Cu (II) from aqueous solution. **353**, 225–236 (2018).

167. Ma, J., Liu, Y., Ali, O., Wei, Y. & Zhang, S. Fast adsorption of heavy metal ions by waste cotton fabrics based double network hydrogel and influencing factors insight. *J. Hazard. Mater.* **344**, 1034–1042 (2018).

The potential of composites based on Silk Fibroin (SF) and active fillers has been demonstrated as well as, the role of the morphological adaptations and control of the material properties for new application areas, including biomedicine, energy and environmental remediation.

The following section aims to summarize the main conclusions extracted from this work, in particular, focusing on the applicability of SF based devices for the incoming technological transition.

Finally, the future trends of SF as well as bio-based materials will be compiled, based on the extracted conclusion and social, industrial and economic dynamics.

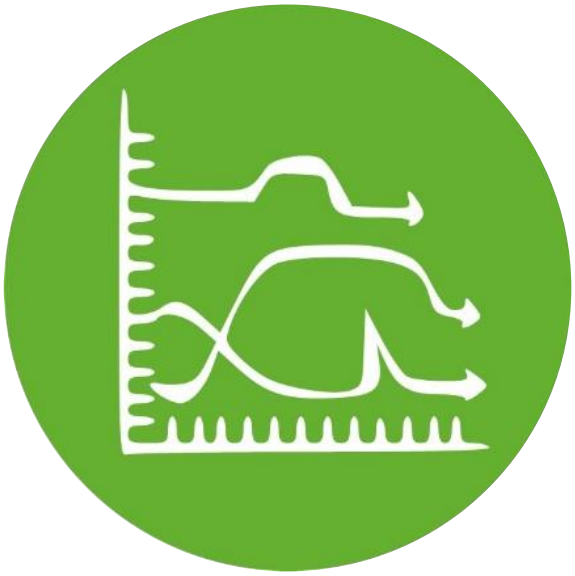

Chapter.6

CONCLUSIONS AND SILK FUTURE TRENDS

6.1. CONCLUSIONS

The work has demonstrated the multifunctionality of Silk Fibroin (SF) and the potential of functional bio-based materials for the technological transition. Two application areas have been selected: i) active composites for electronics (sensors and actuators) and ii) porous structures for biomedicine, energy, and environment. For sensor development, SF has been combined with carbon nanotubes (CNT) and silver nanowires (SNW). For actuators development, SF has been combined with cobalt ferrite nanoparticles (CFO) and two types of ionic liquids (IL) (Choline dihydrogen phosphate ([Ch] [DHP]) and 1-Butil-3-methylimidazolium tricyanomethanide ([Bmim] [C (CN3)] or [C4mim] [TCM])). For the development of porous structures, SF has been processed by i) electrospinning to obtain non-woven mats (also combined with CFO to obtain magnetic responsive mats); ii) salt leaching; iii) gas foaming, iv) gelation, and v) freeze-drying. (***Figure 6.1***).

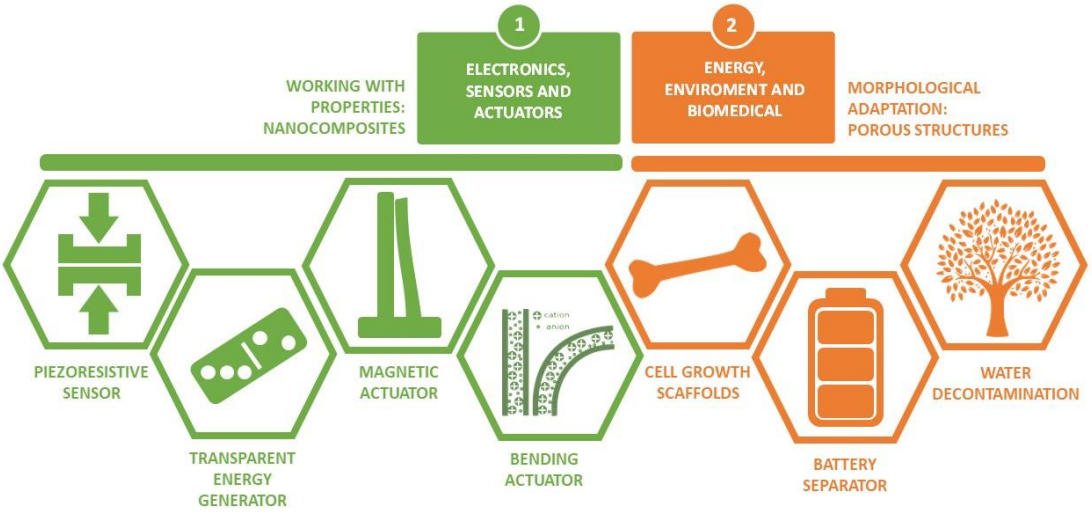

Figure 6. 1. *SF based devices for 1) electronics and actuators and 2) energy, environment and biomedicine*

All the processed materials and devices have been successfully processed through simple and low pollutant methods that reduce the pollution derived from materials developments and facilitate the eventual scale-up of the materials to industrial processes.

The obtained materials have been characterized according to their physical-chemical properties and functional characteristics, i.e., piezoresistive response, dielectric response, magnetic response, bending response, cellular proliferation, electrochemical response, and adsorption coefficients.

As general conclusions:

i) SF show an excellent performance as a matrix to hold fillers with different composition, shape, and properties.

ii) The SF based composites show excellent processability, high fillers loading ratios (reaching values up to 20%) while preserving the SF properties, i.e., mechanical resistance, flexibility, thermal and chemical stability.

iii) The morphological control through processing is a suitable method for SF properties regulation and even improvement.

The main conclusions regarding SF composites:

i) The addition of CNT makes it possible to progressively increase the SF electrical properties, particularly the electrical conductivity, being the percolation threshold around, at CNT 3 wt. %. The samples show a piezoresistive behavior with sensitivity values of approximately 4 MPa^{-1} at low pressures of 0.11 MPa. Thanks to this, the SF / CNT compound has been used to develop a pressure sensor prototype.

ii) The addition of SNW enables to increase the conductivity of the SF. Also, fillers' combined with the non-conductive matrix, results in micro-capacitors' formation throughout the compound, which provides samples with a dielectric constant up to 10 for SNW values of 3 wt. %. Furthermore, due to SNWs low light absorption, the obtained materials are transparent in the visible light range (25% of transparency for filler contents of up to 3 wt.%). The SNWs tunneling effect, combined with the mechanical stimulus, give the samples a piezoresistive response of between 12 and 26 GPa^{-1} when the pressure is between 0.2 and 0.4 MPa. Finally, the combination of all the mentioned properties leads to samples with the ability to store electrical charges and generate an electrical voltage above 3.3 V. This ability has led to the SF / SNW nanocomposite application in a prototype for object recognition.

iii) The incorporation of CFO nanoparticles leads to two significant effects: i) an increase in the dielectric response, reaching values above 20, and ii) the formation of a magnetic compound with a magnetization of ~10 $emu \cdot g^{-1}$ and a coercivity of almost 4 kOe, at CFO contents of 20 wt. %. % CFO. The SF / CFO nanocomposite's magnetic behavior allowed the development of magnetic actuators.

iv) The addition of IL ([Ch] [DHP] and [Bmim] [C (CN3)])) into SF, i) increases the electrical conductivity, and ii) due to the plasticization, increases the maximum deformation

of the samples and decreases Young's modulus. The provided ionic mobility by the ILs allowed the development of a bending actuator, with a great response at low applied voltages (3 V). The highest bending responses, ~ 0.5, are obtained at voltages of 4 and 5 V and at a frequency of 100 mHz, for [Ch] [DHP] / SF and [Bmim] [C (CN_3)] / SF, respectively.

Thus, it is concluded that it is possible to obtain homogenous and highly reproducible SF samples with novel and advanced properties by adding relatively low fillers content. The SF molecular structure and functional groups diversity ease the compatibility between SF and a wide range of fillers, which reduces the impractical interphases and the possibility of operational failures. After fillers addition, SF preserves its original properties and shape, adding at the same time the new properties of the fillers. The chance to add different fillers content supply highly controllable materials and provide devices with advantageous properties. Due to materials' active behavior, they can sense or respond to environmental inputs and reduce additional components for devices ensemble.

The main conclusions regarding SF porous samples have been:

i) Electrospinning is a viable technology to obtain porous scaffolds based on neat SF and even SF/CFO composites. In this way, it has been possible not only to study the capacity of SF tissues to host and promote bone tissue cells but also to analyze the effect of dynamic magnetic stimulation on tissue engineering. Cell culture results show that dynamic stimulation is the main factor in improving cell viability, while morphology has a more significant effect on pre-osteoblastic proliferation.

ii) Salt leaching is a viable technology to develop separators for lithium-ion batteries. The pores' size and shape and the samples' porosity have been used to study these changes' effect on a battery's operation. The obtained results indicate that the SF separator facilitates lithium ions' transport through the cathode and the separator interface. The reached best discharge capacity was 89.3 and 131.3 $\cdot g^{-1}$ for 2C and C / 8, respectively, with a pore size of between 250 and 106 µm.

iii) Gelation, N_2O foaming, and Freeze-drying are viable technologies to generate SF samples with porosity values up to 97%. The combination of different regeneration techniques with two dissolving techniques ($CaCl_2$ and LiBr aqueous dissolutions) and EtOH post-processing enables the control of SF properties and makes it possible to increase the affinity of Fibroin to different pollutants such as chromium and arsenic. The obtained results

show that the SF structures are capable of adsorbing Cr from an aqueous environment up to 3 mg/mg.

It is concluded that processing is a complementary and useful route for modifying SF properties and even the development of new materials and devices. Simple processing techniques allow the control of SF properties, which can be adapted depending on the application.

The devices developed along the work have provided a proof of concept about the interesting role of controlling materials properties and morphology. The whole work can be considered a demonstrator of SF potential, which can eventually be extrapolated to other bio-based materials. SF multifunctionality and the ability of bio-based materials to be part of different devices have been demonstrated. Although there is still much work to make SF and bio-based materials truly valuable and even competitive materials, this work has already confirmed their promising future.

6.2. SILK FIBROIN FUTURE TRENDS

As SF's use has increased over the last years, the material's sustainability could be compromised. The extraction, processing, and even waste are, in general, critical points for materials. Thus, it is necessary to avoid future problems from the beginning and ensure a whole natural-friendly life-cycle of the material.

Silk production (sericulture) is a non-industrialized process, mainly located in areas with limited technology access. Thus, to make SF a commercial material, it is mandatory to advance towards novel sericulture processes with significant production yields and control. This condition requires an increase in the current knowledge about production techniques, higher investment, and the elaboration of development plans. This requires well-controlled silk stocks to reproduce the achieved advances, facilitate comparisons across studies, and accelerate commercial application (especially in biomedicine).

There are today several strategies to modify, control, and even improve SF's properties. Still, there are some low explored techniques with great potential to produce sustainable materials. Among these techniques, transgenesis and feeding represent suitable options. Today the investigation around them is still limited, so advance towards this direction could be a reasonable step.

The study of materials manufacture represents a complementary strategy for the development of new devices. In this context, additive manufacturing represents an excellent option for obtaining new sustainable materials since it minimizes energy consumption and waste generation.

Sustainability is a collaborative process where many sectors must advance towards a common objective. There is not a single solution, so plenty of small, continuous and coordinated steps are required.

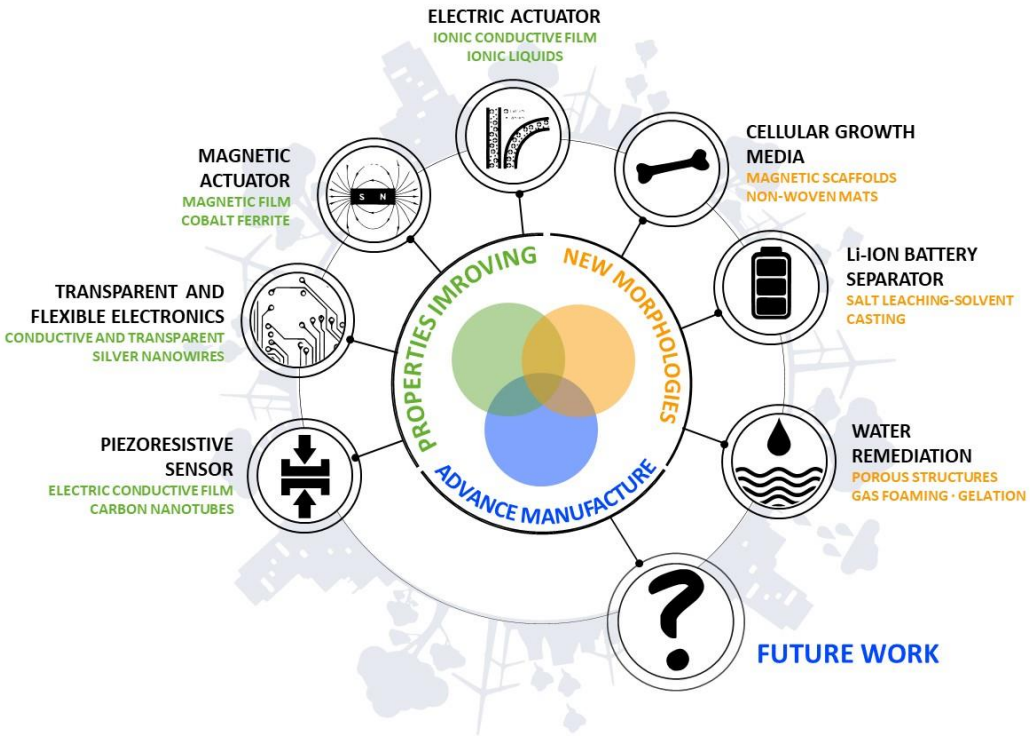

Figure 6. 2. *Graphical representation of developed SF based devices and future work*

Contributions

Part of the thesis:

- **A. Reizabal**, S. Gonçalves, R. Brito-Pereira, P. Costa, C. M. Costa, L. Perez-Alvarez, J.L. Vilas-Vilela, and S. Lanceros-Mendez., "*Optimized silk fibroin piezoresistive nanocomposites for pressure sensing applications based on natural polymers*," Nanoscale Adv., vol. 1, no. 6, pp. 2284–2292, 2019.
- **A. Reizabal**, S. Gonçalves, N. Pereira, C. M. Costa, Perez-Alvarez, J.L. Vilas-Vilela, and S. Lanceros-Mendez., "*Optically Transparent Silk Fibroin/Silver Nanowire Composites for Piezoresistive Sensing and Object Recognitions*," J. Mater. Chem. C, 2020.
- **A. Reizabal**, C. M. Costa, N. Pereira, L. Pérez-Álvarez, J.-L. Vilas-Vilela, and S. Lanceros-Méndez, "*Silk Fibroin Based Magnetic Nanocomposites for Actuator Applications*," Adv. Eng. Mater., vol. 22, no. 6, p. 2000111, Jun. 2020.
- **A. Reizabal**, D. M. Correia, C. M. Costa, L. Perez-Alvarez, J. L. Vilas-Vilela, and S. Lanceros-Méndez, "*Silk Fibroin Bending Actuators as an Approach Toward Natural Polymer Based Active Materials*," ACS Appl. Mater. Interfaces, vol. 11, p. 30197−30206, 2019.
- **A. Reizabal**, R. Brito-Pereira c , M.M. Fernandes, N. Castro, V. Correia, C. Ribeiro, C.M. Costa, L. Perez-Alvarez, J.L. Vilas-Vilela, and S. Lanceros-Mendez., "*Silk fibroin magnetoactive nanocomposite films and membranes for dynamic bone tissue engineering strategies*," Materialia, vol. 12, p. 100709, Aug. 2020.
- **A. Reizabal**, R. Gonçalves, A. Fidalgo-marijuan, C. M. Costa, P. Leyre, and J. Vilas, "*Tailoring silk fibroin separator membranes pore size for improving performance of lithium ion batteries*," J. Memb. Sci., vol. 598, no. 117678, 2020.
- **A. Reizabal**, C.M. Costa, P.G. Saiz, B. Gonzalez, L. Perez-Alvarez, R. Fernandez de Luis, A. Garcia, J.L. Vilas-Vilela, and S. Lanceros-Mendez., "*Processing Strategies to Obtain Highly Porous Silk Fibroin Structures with Tailored Microstructure and Molecular Characteristics and Their Applicability in Water Remediation*," J. Hazard. Mater., vol. 403, no. 123675, 2021.

Other articles:

- H. Salazar, P. M. Martins, B. Santos, M. M. Fernandes, **A. Reizabal**, and V. Sebasti, "*Photocatalytic and antimicrobial multifunctional nanocomposite membranes for emerging pollutants water treatment applications*," Chemosphere, vol. 250, no. 126299 Contents, 2020.
- J. C. Barbosa, **A. Reizabal**, D. M. Correia, R. Gonçalves, M. M. Silva, and C. M. Costa, "*Lithium-ion battery separator membranes based on poly(L-lactic acid) biopolymer*," Mater. Today Energy, p. 100494, 2020.
- E. Lizundia, **A. Reizabal**, C. M. Costa, A. Maceiras, and S. Lanceros-m, "*Electroactive γ-Phase, Enhanced Thermal and Mechanical Properties and High Ionic Conductivity Response of Poly (Vinylidene Fluoride)/Cellulose Nanocrystal Hybrid Nanocomposites*," Materials (Basel)., vol. 13, no. 743, 2020.
- P. G. Saiz, N. Iglesias, B. González Navarrete, M. Rosales, Y. Marcela Quintero, **A. Reizabal**, J. Orive, A. Fidalgo Marijuan, E. S. Larrea, C. Lopes, L. Lezama, A. García, S. Lanceros-Mendez, M. Isabel Arriortua, and R.Fernandez de Luis., "*Chromium Speciation in Zirconium-Based Metal–Organic Frameworks for Environmental Remediation*," Chem. - A Eur. J., 2020.
- **A. Reizabal**, J. M. Laza, J. M. Cuevas, L. M. León, and J. L. Vilas-Vilela, "*PCO-LLDPE thermoresponsive shape memory blends. Towards a new generation of breathable and waterproof smart membranes*," Eur. Polym. J., vol. 119, pp. 469–476, 2019.